Imperial College London
Department of Chemistry

Post-polymerisation Modification of Conjugated Polymers: Towards Novel Organic Semiconductor Materials

Charlotte Louise Rapley

Submitted in part fulfilment of the requirements
for the degree of Doctor of Philosophy in
Chemistry at Imperial College London

February 2022

“Out of clutter, find simplicity. From discord, find harmony. In the middle of difficulty lies opportunity.”

-Albert Einstein

Declaration

The work described in in this thesis was carried out in the Department of Chemistry, Imperial College London, from October 2017 to October 2021 under the supervision of Professor Martin Heeney. The content of this thesis is the author's original work, unless stated otherwise.

Charlotte Louise Rapley (2021)

Contributions

With the help and contributions from collaborators, the work presented in this thesis was made possible. I would like to recognise and thank the following collaborators for their hard work:

In Chapter 2-5, DOSY and high temperature ^{1}H and ^{19}F NMR experiments were carried out by Pete Haycock at Imperial College London.

In Chapter 3, polymer P3HT-TFB was synthesised and characterised by Hyunwoo Park (Professor Tae-Lim Choi's group) at Seoul National University.

Grazing-Incidence Wide-Angle X-ray Scattering (GIWAXS) experiments (Chapter 3 and 4) were carried out by Dr Edgar Gutiérrez Fernández (Dr Jaime Martín's group) at POLYMAT.

Atomic force microscopy (AFM) images (Chapter 3 and 4) were collected by Dr Flurin Eisner at Imperial college London.

Organic solar cell devices were fabricated and tested by Zhuoran Qiao and Dr Nicola Gasparini at Imperial College London.

Density field theory calculations (Chapter 4) were performed with guidance and assistance from Filip Aniés (Martin Heeney's group) at Imperial College London.

In chapter 4, photoelectron spectroscopy in air (PESA) measurements and organic thin film transistor (OTFT) device fabrication and testing were carried out by Dr Mohamad Insan Nugraha (Dr Thomas Anthopoulos' group) at King Abdullah University of Science and Technology (KAUST).

X-ray photoelectron spectroscopy sample fabrication and experiments (Chapter 5) were performed by Syuhada Binti Mohd Tahir (Dr David Payne's group) at Imperial College London.

Copyright Declaration

The copyright of this thesis rests with the author and is made available under a Creative Commons Attribution Non-Commercial No Derivatives licence. Researchers are free to copy, distribute or transmit the thesis on the condition that they attribute it, that they do not use it for commercial purposes and that they do not alter, transform or build upon it. For any reuse or redistribution, researchers must make clear to others the licence terms of this work.

Acknowledgments

I would like to start by thanking Professor Martin Heeney for the opportunity to work on my PhD within the Heeney group. I am very grateful for all the guidance, support and advice given that contributed to each project I worked on. I can honestly say that with your help, I have developed the skills to be a confident researcher.

For the funding to carry out this research, I would like to thank the Engineering and Physical Research Council (EPSRC).

I would like to thank the Centre of Plastic Electronics and management team who have welcomed me to seminars, symposiums, networking and social events, including the Winter School 2020, which provided a key pivot point in my personal development where I was able to learn how to confidently communicate scientific findings to fellow researchers and peers.

Throughout my PhD I have had the chance to work in two labs, the Harwood lab and the MSRH lab 402, meeting and working alongside exceptional researchers. I would like to thank members from these labs who made my time at Imperial a great one. When I first walked into the Harwood lab, Adam M. introduced me to the Heeney group. Adam C. took the time to introduce me to the lab and new synthetic techniques. Fei helped me to make my very first batch of P3HT. Tom was always the person to go to with a tricky synthesis query and also a shared appreciation of motivational rap music. Florian helped me to develop scientific communication skills, particularly in my writing and helped build my confidence to pursue a career in Science. Bowen has shown me the importance of patience, in the art of obtaining the highest quality analytical data. Martina has been a great support, generally keeping spirits up when times were hard, in particular with the 3 PM breaks where we could put the world to rights. Notina has been there through every ‘eureka’ moment and also the ‘why did this happen?’ moments, and even listened to all the cringy chemistry jokes I endeavoured to make. Petr, Qiao, Filip, Shengyu, Tingmang, Simeng, Wenmin, Tao, Ilknur... the most welcoming and most supportive group – a huge thank you, it was a pleasure to work with you all.

Working with people has always been incredibly enjoyable for me, and so I would like to thank my masters' students Toni and Nana. Your invaluable hard work has contributed to the developments of the projects presented in this thesis.

In the Harwood and the MSRH labs, members of the McCulloch, McLachlan and Fuchter group have been neighbours to the Heeney group and I would like to thank the members of these groups: James P., Mark, Iuliana, Matt, Max M., Adam, Helen, Maxime, Flo, Seán, Juan, Faisal, Ivy and Christina for their expertise, advice and friendly conversations.

For providing an excellent NMR service I must thank Peter Haycock for his patience and expertise. For an equally outstanding service in the mass spectrometry lab, I thank Lisa Haigh and Trevor Ferris, who have always gone over and above to help the researchers at ICL.

I would like to thank the collaborators Hyunwoo, Shyuhada, Nicola, Zhouran, Insan, Flurin, Jaime and Edgar for all the hard work, time, persistence, knowledge and expertise that has contributed to the work presented in this thesis.

Last, but not least, I would like to thank my incredibly supportive family for always cheering me on, with your unwavering love and support, this work was possible. Thanks to my Mum who has taught me to always keep a positive mindset even in the most difficult times. In my work, it is that positive mindset that made every challenge and complication one to relish and solve. Thanks to my Dad who has taught me to never give up and encouraged me to be the best I can be. With this encouragement I was able to persevere, keep learning and get to the finish line, with the best soundtracks to complete an epic task. Thank you to my Sister who took the time for lunchtime walks in Gunnersbury Park to break up the WFH days and for always reminding me that Psychology is a science. Thank you to my boyfriend Max, who has been by my side every step of the way, from the first year where we started the PhD journey together to the final chapter, writing side-by-side. With your love and support it was possible to complete this journey. Finally, thank you to Max's parents, Cristina and Ian, who welcomed me into their home and created a writing space to complete this work.

As this acknowledgement section shows, there are a lot of people who I have to thank along this journey of the PhD. Thank you to all for being a part of the journey and without further-a-do, I present to you the final findings.

Abstract

Organic conjugated polymer semiconductor materials have grasped the attention of many researchers, particularly in the last 10 years, for their use in electronic devices. In order to engineer materials for specific applications, it is essential to consider the polymer design and chemical structures. With thoughtful polymer design, it is possible to modify and manipulate physical and optoelectronic properties to optimise semiconductor materials for intended applications.

Post-polymerisation techniques have been widely explored as a useful tool to modify polymers with desired properties or specialised functionality. Nucleophilic aromatic substitution (S_NAr) has been identified as a useful reaction to facilitate the modification of conjugated polymers without introducing unwanted defects within the polymer backbone. In this thesis, S_NAr was used as technique to introduce conjugated polymer sidechains and various other functional groups along conjugated polymer backbones. Polymers were designed and synthesised for use in electronic devices such as; organic thin film transistors (OTFTs) and organic solar cell (OSC) devices, where physical and optoelectronic properties were evaluated for all polymers.

The work presented (Chapter 2-6) looks at polymers designed with a monofluorinated benzothiadiazole as a repeat unit within the backbone of a conjugated polymer. A range of nucleophiles were substituted onto the polymer backbones via S_NAr, directly onto the monofluorinated benzothiadiazole repeat unit, highlighting the versatility of this post-polymerisation modification method. In chapters 2 and 3, this method was used to develop graft co-polymers with an n-type conjugated polymer backbone and p-type conjugated polymer sidechains. In chapter 3, single-component graft co-polymer structures were shown to provide a comparatively similar solar cell device performance to the blended polymers, however, with higher recorded V_{oc} values.

Further exploration of the versatility of post-polymerisation modification requires the development of new conjugated backbone polymers that can readily undergo modification. Hence, in Chapter 4, the direct modification of two novel n-type conjugated polymer

backbones via S_NAr was demonstrated, including the quantitative incorporation of substituents along the polymer backbone. Unsubstituted polymers achieved an electron mobility of 0.16 $cm^2 V^{-1} s^{-1}$ in OTFT devices. After substitution, mobilities reduced by around one order of magnitude. Further developments looked at azide functionalised conjugated polymers, where polymer thin films were successfully thermally cross-linked or photo-patterned (high azide content polymer). Finally in Chapter 5, polymers were modified with increasing anionic content, for use as interlayers between active polymer layers and electrodes within OSCs, for example. Increasing the anionic content did not largely affect the electronic properties of the polymer, however, did modify the work function of indium tin oxide (ITO).

Table of contents

Declaration iii

Contributions iv

Copyright Declaration v

Acknowledgments vi

Abstract viii

Table of contents x

Publications xv

Abbreviations xvi

1 Introduction 1

1.1 Polymer semiconductors 1

1.2 Conjugated polymers 2

1.3 Organic thin film transistors 5

1.4 Organic solar cell devices 7

1.5 Using polymer design to optimise properties 10

1.5.1 Alkyl chains 10

1.5.2 Composition of the polymer backbone 11

1.6 Synthesis of conjugated polymers 14

1.7 Polymer characterisation 17

1.8 Post-polymerisation functionalisation 19

1.9 Functional polymers via nucleophilic aromatic substitution 21

1.9.1 End-functionalised polymers 22

1.9.2 Functionalised pendant groups 22
1.9.3 Functionalisation towards new polymer structures 23
1.10 Thesis aims and overview 25
2 Chapter 2: A novel synthetic method towards conjugated graft co-polymers utilising post-polymerisation modification 28
2.1 Introduction 28
2.2 Small molecule functionalisation 31
2.2.1 Synthesis of the monomers and polymers 31
2.2.2 Confirmation of substitution 33
2.3 Synthesis of end-functionalised P3HT (small scale) 35
2.3.1 P3HT starting polymer (P3HT-Br) 35
2.3.2 End-functionalised polymers (P3HT-PhOH and P3HT-PhSH) 38
2.4 Synthesis of graft co-polymer 41
2.4.1 Synthesis of graft co-polymer 41
2.4.2 Purification of F8BT-g-P3HT(OPh) 42
2.5 Characterisation of graft co-polymer 44
2.5.1 Confirmation of graft co-polymer structure by absorption spectroscopy 44
2.5.2 Confirmation of graft co-polymer structure by 1D and 2D NMR 45
2.5.3 Optical properties 47
2.5.4 Thermal properties 48
2.6 Limitations of using this method 50
2.6.1 Low grafting densities 50
2.6.2 Removal of un-grafted polymer 50
2.6.3 Scale up end-functionalisation of P3HT 51
2.6.4 Backbone and side chain selection 52
2.7 Conclusion 53

2.8 Experimental 54

2.9 Appendix Chapter 2 - list of figures 60

3 Chapter 3: Development of synthetic methods towards conjugated graft co-polymers utilising post-polymerisation modification 61

3.1 Introduction 61

3.2 Synthesis of end functionalised polymers 63

3.2.1 End-group analysis by MALDI 65

3.2.2 End group analysis by ^{1}H NMR 66

3.2.3 Molecular weight characterisation 67

3.3 Synthesis of graft co-polymer 69

3.4 Synthesis of graft co-polymer series 71

3.5 Optical properties 73

3.6 Electronic properties 75

3.7 Thermal properties 77

3.8 Thin film morphology 79

3.9 Photovoltaic properties 84

3.10 Conclusion 86

3.11 Experimental 88

3.12 Appendix Chapter 3 - list of figures 95

4 Chapter 4: Development of N-type Conjugated Polymer Backbones Engineered for Versatile Post-Polymerisation Modification towards Specifically Designed Functionalised Polymers 96

4.1 Introduction 96

4.2 Synthesis of monomers and polymer backbone structures 98

4.3 Hydrolysis of NDI core with stronger bases 100

4.4 Synthesis of substituted polymer structures 102

4.5 Optical properties 105

4.6 Electronic properties 107
4.7 Thermal properties 109
4.8 Thin film morphology 110
4.9 OTFT charge transport properties 112
4.10 Quantitative post-polymerisation substitution on PNDI-TBTT 114
4.11 Inclusion of azide functionality on PNDI-TfBTT 116
4.12 Crosslinking via the azide functionality on PNDI-TfBTT 119
4.12.1 Thermal crosslink 119
4.12.2 Photo-crosslink 121
4.12.3 Crosslinking summary 123
4.13 Thin film morphology post crosslinking 124
4.14 OTFT charge transport properties post crosslinking 127
4.14.1 Thermally annealed active layer 128
4.14.2 UV exposed active layer 128
4.15 Conclusion 130
4.16 Experimental 132
4.17 Appendix Chapter 4 - list of figures 142
5 Chapter 5: Design and progression of Anionic Conjugated Polyelectrolytes as interfacial layers 144
5.1 Introduction 144
5.2 Synthesis of anionic polymers 146
5.2.1 Confirmation of polymer structures by NMR 148
5.2.2 Confirmation of polymer structures by FTIR 150
5.2.3 Polymer composition by XPS 150
5.3 Optical properties 152
5.4 Electronic properties 154

5.5 X-ray photoelectron spectroscopy (XPS) analysis 156
5.6 Conclusion.....158
5.7 Experimental.....159
5.8 Appendix Chapter 5 - list of figures 163
6 General experimental.....164
7 References.....167
8 Appendix.....181
9 Permissions.....241

Publications

Shengyu Cong, Adam Creamer, Zhuping Fei, Sam A. J. Hillman, **Charlotte Rapley**, Jenny Nelson, Martin Heeney*, Tunable Control of the Hydrophilicity and Wettability of Conjugated Polymers by a Postpolymerization Modification Approach, *Macromolecular Bioscience*, 20, 2020, 2000087

Desiree Adamczak, Andrea Perinot, Hartmut Komber, Anna Illy, Sandra Hultmark, Bianca Passarella, Wen Liang Tan, Sebastian Hutsch, David Becker-Koch, **Charlotte Rapley**, Alberto D. Scaccabarozzi., Martin Heeney, Yana Vaynzof, Frank Ortmann, Christopher R. McNeill, Christian Müller, Mario Caironi, Michael Sommer*, Influence of synthetic pathway, molecular weight and side chains on properties of indacenodithiophene-benzothiadiazole copolymers made by direct arylation polycondensation, *Journal of Materials Chemistry C*, 9, 2021, 4597-4606.

Manuscripts for the work carried out in Chapters 3 and 4 are currently in the process of being drafted.

Abbreviations

°	Degree
δ	Chemical shift
µ	Micro
λ	Wavelength
AFM	Atomic Force Microscopy
BHJ	Bulk Heterojunction
BT	2,1,3-benzothiadiazole
CB	Chlorobenzene
CF	Chloroform
COSY	Correlated Spectroscopy
CV	Cyclic Voltammetry
CPE	Conjugated Polyelectrolyte
Đ	Dispersity Index
DCM	Dichloromethane
DFB	Difluorobenzene
DFBP	Decafluorobiphenyl
DFT	Density Functional Theory
DMAc	Dimethylacetamide
DMF	*N,N*-dimethylformamide
DMSO	Dimethyl Sulfoxide
DOSY	Diffusion Ordered Spectroscopy
DSC	Differential Scanning Calorimetry
E_g	Band Gap
$E_{g,opt}$	Optical Band Gap
ETL	Electron Transport Layer
eV	Electron Volt
FF	Fill Factor

FTIR	Fourier-Transform Infrared Spectroscopy
GCMS	Gas Chromatography Mass Spectrometry
GIWAXS	Grazing-Incidence Wide-Angle X-ray Scattering
GPC	Gel Permeation Chromatography
h	Hour
HFB	Hexafluorobenzene
HOMO	Highest Occupied Molecular Orbital
HTL	Hole Transport Layer
ICL	Imperial College London
ICT	Intramolecular Charge Transfer
IP	In-plane
ITO	Indium Tin Oxide
J_{MP}	Current when the power output is maximised
J_{SC}	Short Circuit Current
KCTP	Kumada catalyst-transfer polycondensation
kDa	Kilodalton
LUMO	Lowest Occupied Molecular Orbital
MALDI	Matrix-assisted laser desorption/ionization
M_n	Number Average Molecular Weight
M_w	Weight Average Molecular Weight
min	Minute
nm	Nanometre
NMP	*N*-methyl-2-pyrrolidone
NMR	Nuclear Magnetic Resonance
NOESY	Nuclear Overhauser Effect Spectroscopy
OFET	Organic Field-Effect Transitor
OLED	Organic Light Emitting Diode
OOP	Out-of-plane
OPV	Organic Photovoltaic
OSC	Organic Solar Cell
OTFT	Organic Thin Film Transistor

PCE	Power Conversion Efficiency
$Pd(PPh_3)_4$	Tetrakis(triphenylphosphine)palladium(0)
PDI	Polydispersity Index
PESA	Photoelectron Spectroscopy in Atmosphere
PFB	Pentafluorobenzene
PL	Photo Luminescence
PPM	Parts per million
RFID	Radio-frequency identification
RMS	Root-mean square
SEC	Size Exclusion Chromatography
S_NAr	Nucleophilic Aromatic Substitution
TCE	Tetrachloroethane
TFB	Trifluorobenzene
THF	Tetrahydrofuran
TLC	Thin Layer Chromatography
TOF	Time of Flight
UPS	Ultraviolet Photoelectron Spectroscopy
UV-Vis	Ultraviolet-Visible
v:v	Volume ratio
V_D	Drain Voltage
V_S	Source Voltage
V_{MP}	Voltage when the power output is maximised
V_{OC}	Open Circuit Voltage
XPS	X-ray Photoelectron Spectroscopy

1 Introduction

In our world today, we see plastics in almost all aspects of our lives. Utilising plastics in the place of other materials provides cheap, versatile and effective solutions for an extensive range of applications. We are constantly gaining better understanding where these versatile materials are useful to us and where they are unnecessary. In our daily lives, packaging, clothing, building materials and household appliances are a few common places where we see the flexible and durable materials. If we delve a little deeper, we can observe the use of these materials in electronic devices, in newly developed technology today.

1.1 Polymer semiconductors

Plastics are synthetic organic compounds, made from polymers, with properties that depend on the chemical structure, polymer length and tacticity. With design of the chemical structure and control of synthetic techniques, it is possible to optimise polymer properties for specific applications.

The first discovery of conductive polymers was made in 1976 by Heeger, MacDiarmid and Shaiakawa. For the discovery and characterisation of doped poly(acetylene), they were awarded the Nobel prize in chemistry in 2000.[1,2] This discovery prompted much research into new classes of conducting and semiconducting materials. Researchers have since continued to develop such materials for use in a wide range of applications in organic electronic devices.[3,4] Applications of organic semiconducting polymers include, but are not limited to; organic light emitting diodes (OLEDs) [5–8], organic photovoltaic (OPVs) cells[9–11], organic field effect transistors (OFETs)[12,13], organic thin film transistors (OTFTs)[14–16], organic electrochemical transistors (OECTs)[17], sensors[18–20], supercapacitors[21,22] and lithium ion batteries[23–25].

Interest in organic semiconducting polymers can be derived from the unique properties these materials have. Electrical properties of a semiconductor are described as: displaying partial conductivity somewhere between the conductivity of a pure conductor (e.g. copper) and an insulator (e.g. glass). Modifying the electrical properties of a polymer semiconductor can be

achieved by doping (with organic small molecules for example) or engineered by polymer design.[26,27] Key advantages over inorganic semiconductors lies within their easy processability. With good solubility in organic solvents, polymer semiconducting materials can be deposited through reel-to-reel processing, via screen printing, inkjet printing or spray coating, directly onto flexible substrates.[28–30] Fabricating devices through reel-to-reel processes enables the delivery of lightweight and cost-effective flexible electronic devices, with reduced industrial manufacturing costs.[31,32]

Polymer design is paramount to developing these materials for specific applications. By modifying the repeat units along the chain, it is possible to adapt and tune optoelectronic, physical and mechanical properties of the polymers. In the following sections, the composition of polymer materials, how materials can be designed for specific applications and examples of polymers in organic electronic devices are discussed. Through the eyes of a chemist, synthetic routes towards conjugated polymers are presented, with a short introduction on the characterisation of these materials. Finally leading onto more specific overview of post-polymerisation modification techniques, where significant advantages of these techniques from reported literature are identified.

1.2 Conjugated polymers

Conjugated polymers are long chain organic molecules comprised of conjugated organic repeating units. The term 'conjugated' refers to a system with a continuous array of aligned p-orbitals that creates a π overlap within the system. Examples of both non-conjugated and conjugated molecules, as isolated and extended systems, are shown in Figure 1.1.

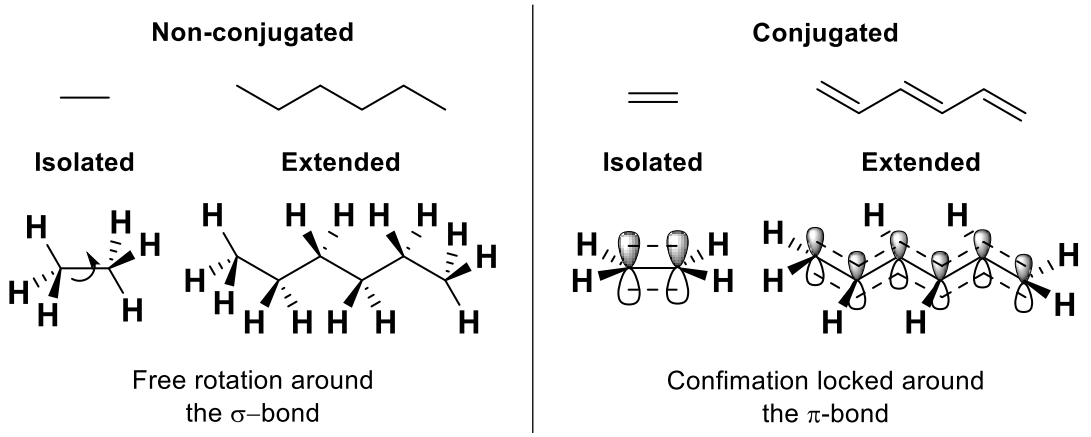
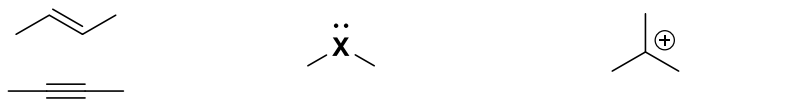


Figure 1.1. Examples of non-conjugated isolated and extended molecules (left) and conjugated isolated and extended molecules (right).

Non-conjugated molecules with single bonds (σ-bonds) have no overlapping orbitals and therefore there is free rotation about the C-C bond. Conversely for conjugated molecules, due to the double bonds (π-bonds) the adjacent p-orbitals overlap, hence, these molecules experience limited rotation about the C=C bonds. Whilst the structural confirmation is locked in place, it is still possible to observe some twisting or bending due to steric reasons.

Alternating double and single bonds form the extended conjugated systems, with a network of overlapping p-orbitals where electrons are delocalised along the chain. Structural elements of delocalised π-systems use building blocks with multiple bonds, heteroatoms with lone pairs (sp or sp^2 hybridised) or carbocations, as shown in Figure 1.2. Delocalised π-systems are made up of directly connected structural elements in a series of three or more overlapping p-orbitals. For double and triple bonds, unhybridised p-orbitals in the z-direction (P_z orbital) overlap, with additional overlapping of unhybridised p-orbitals in the y-direction for triple bonds (P_y orbital), where each carbon contributes one π-electron into the delocalised system. Alternatively, for heteroatoms the lone pair or unpaired π-electron (depending on hybridisation) on a heteroatom occupies the overlapping p-orbital. In the case of the carbocation, the empty orbital is associated with an unhybridised overlapping p-ortbital.

In a simple ethylene molecule, two overlapping p_z orbitals generate a π-bonding orbital (occupied by two electrons) and a π*-antibonding orbital (unoccupied). These orbitals are referred to as the highest occupied molecular orbital (HOMO) and the lowest occupied molecular orbital (LUMO) respectively. The energy difference between the HOMO and LUMO is known as the band-gap. Increasing the conjugation by adding more repeat units results in additional overlapping p-orbitals, hence, more π bonding and antibonding energy levels, as shown in Figure 1.3. As the degree of conjugation is extended, the energy gap between the HOMO and LUMO energy levels decreases, thus, the energy required to promote an electron to the excited state is reduced.



Double or triple bonds | **Hetroatom e.g. O, N, S (sp, sp^2 hybridised)** | **Carbocation (six e^- building blocks)**

Figure 1.2. Structural elements of delocalised π-systems.

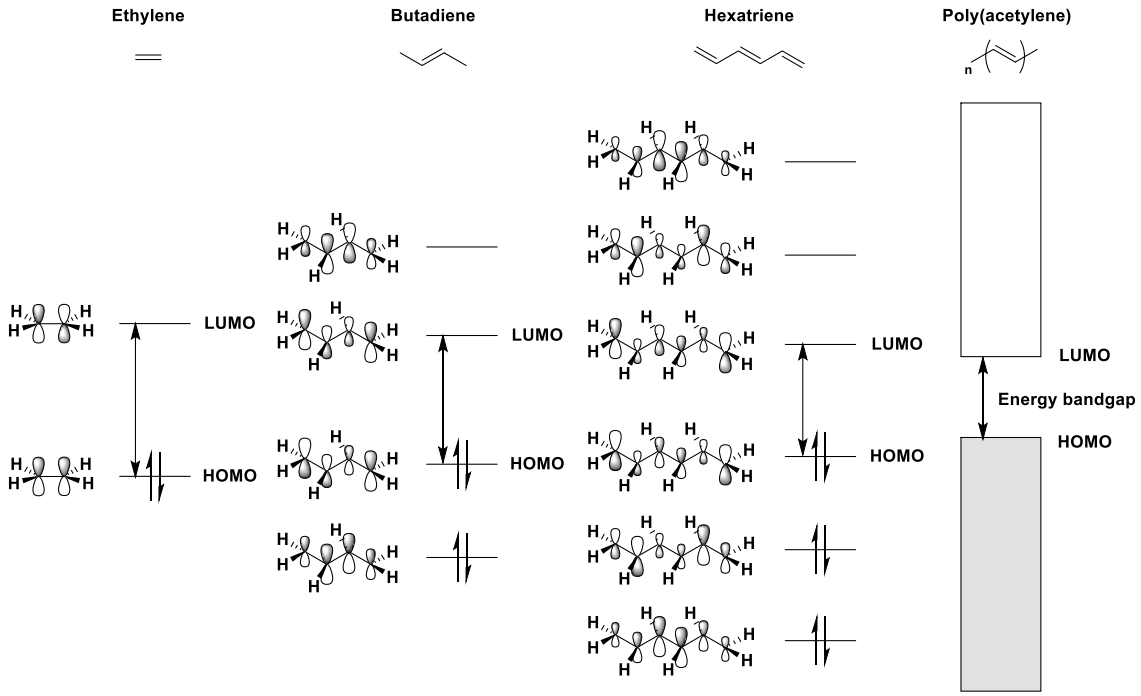


Figure 1.3. Energy level diagram for ethylene, butadiene, hexatriene and polyacetylene showing the decreasing energy band gap with increasing conjugation length.

Conjugated polymers are largely extended delocalised π-systems composed of many overlapping p-orbitals. The extensive π-network results in a reduced bandgap as chain length is extended, until it reaches an effective conjugation length where the band-gap does not continue to reduce and remains fixed even as the molecular length increases.[33] Due to the lowered energy bandgap, there is a potential for electrons to be promoted across the band gap by absorption of visible light, which gives rise to coloured materials with semiconductor properties. Some examples of well-known polymers that have been implemented in electronic devices, selected for their semiconductor properties are shown in Figure 1.4.

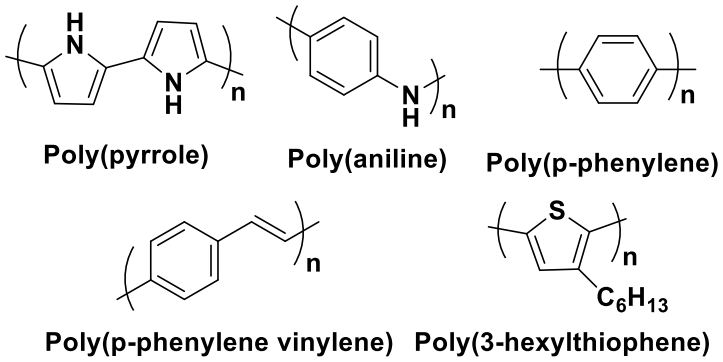


Figure 1.4. Examples of conjugated polymers.

1.3 Organic thin film transistors

Organic thin film transistors (OTFTs) are a well-established principal building block for flexible, reel-to-reel processable electronic devices, displays and sensors.[34] Typical OTFT device architectures, shown in Figure 1.5, are comprised of an organic semiconductor thin film (active layer), a dielectric film, and three electrodes; the source (S), the drain (D) and the gate (G).[35] Figure 1.5 shows staggered and co-planar device structures. In a staggered device structure, the source and drain electrodes are positioned opposite the dielectric layer. Conversely for the co-planar device structure, the source and drain electrodes are positioned adjacent to dielectric layer. Finally, device structures can be identified as top-gate or bottom-gate (inverted structure) which refers to the position of the gate electrode.

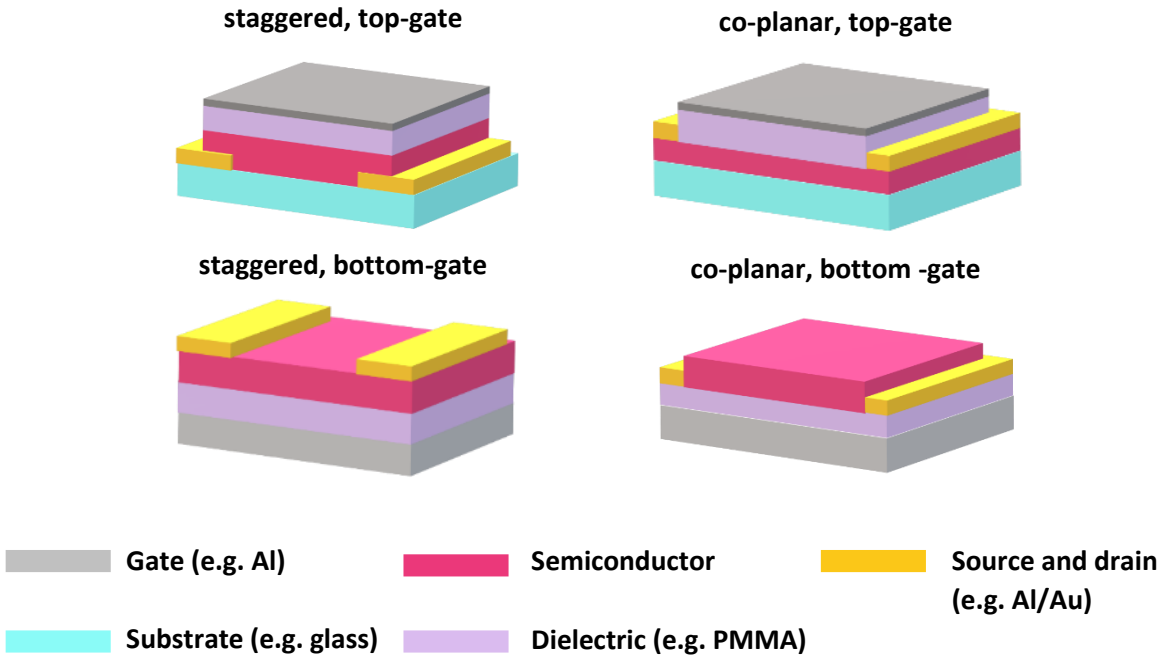


Figure 1.5. General device architectures of OTFTs.[35]

It is important to consider device architecture for both the optimisation of device performance and fabrication of the device. With some device architectures processing limitations may arise. For example, in the bottom-gate device architecture, the semiconductor layer must be deposited after the dielectric layer. Depositing the semiconductor layer in the later stages of device fabrication may result in limited solvents that can be used for film deposition or restricted annealing temperatures where lower temperatures are required to maintain other components within the device.

Organic semiconductors can be identified by the predominant charge carrier it transports; hole carrier (p-type), electron carrier (n-type) or a balanced hole and electron carrier (ambipolar). The HOMO and LUMO energy levels, relative to the work function of the electrodes, determines whether a semiconductor is p-type or n-type. An energy level diagram for a general OTFT device containing p- and n-type materials is shown in Figure 1.6. For p-type materials the valence band (HOMO) is close to the Fermi level of the electrode and the hole injection barrier is small ($f_p < f_n$). On the other hand, for n-type materials the conduction band (LUMO) has a lower energy and is close to the Fermi level of the electrode, therefore, the electron injection barrier is small ($f_n < f_p$).[36]

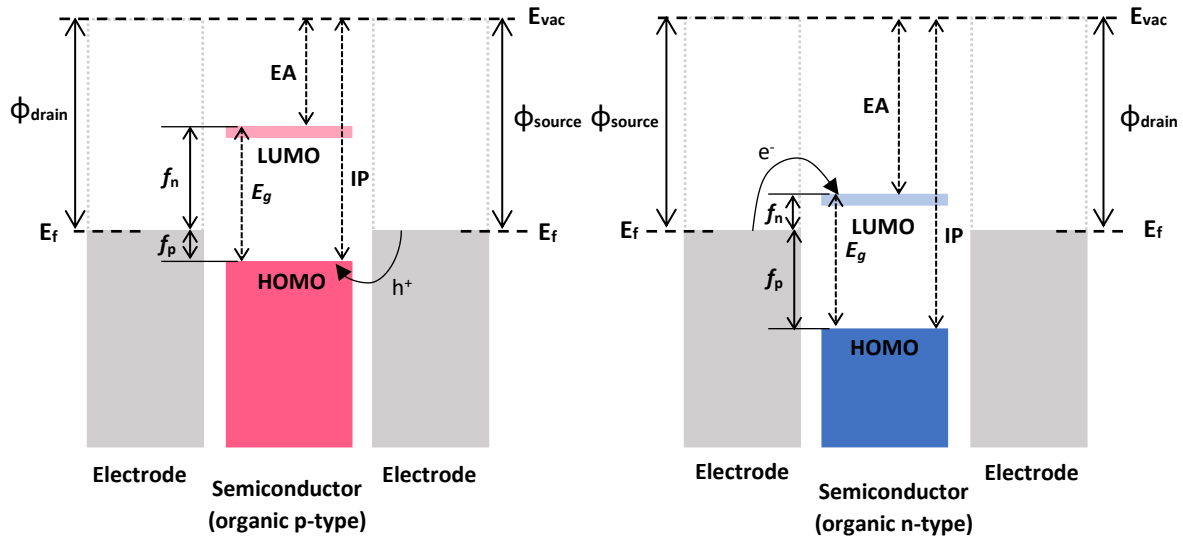


Figure 1.6. General energy level diagram of a p-type (left) and an n-type (right) OTFT.[36] E_f represents the Fermi level of the electrode, E_{vac} represents the vacuum level, ϕ_{drain} and ϕ_{source} represent the work function of the drain and source electrodes respectively, f_p and f_n represent the hole and injection barriers respectively, EA is the electron affinity, IP is the ionisation potential and E_g represents the bandgap of the material.

In 1986, the first examples of OTFTs fabricated with conjugated polymers used the p-type polymer poly(thiophene) in the semiconductor layer. These initial devices were reported to have a charge carrier mobility of ca. 10^{-5} $cm^2V^{-1}s^{-1}$.[37] Polythiophene was found to be relatively insoluble and air sensitive. Further developments in the design of the poly(thiophene) saw the introduction of solubilising alkyl chains to afford poly(3-hexylthiophene) (P3HT).[38] The modified material, P3HT, was highly soluble in a range of organic solvents including THF, chloroform and chlorobenzene. Soluble conjugated polymers can be easily deposited as thin films by spin coating, spray coating, screen printing and inkjet printing, for example. In recent reports, OTFT devices fabricated with an active P3HT semiconductor layer can achieve ca. 10^{-2} $cm^2V^{-1}s^{-1}$.[39–41] Regioregularity, molecular weight of the polymer and consequently thin

film morphology of the semiconductor layer was found to greatly influence the charge carrier mobility of the device.[42–44] Development of p-type polymer materials for OTFT devices has seen high hole mobilities in the range of ca. 10 to 20 $cm^2V^{-1}s^{-1}$.[45,46]

It is well known that the development of n-type semiconducting materials has been relatively slower than that of p-type materials, where the highest electron mobilities for devices fabricated with n-type conjugated polymers are reported below 10 $cm^2V^{-1}s^{-1}$.[47,48] A key challenge that hinders the development of n-type conjugated polymers for OTFT devices is the requirement for the polymer to be electron deficient with low lying LUMO energy levels. To ensure device stability in ambient environments the LUMO energy level of the conjugated polymer should be around or below -4 eV.[49,50]

To maximise charge carrier mobility in OTFT devices, optimised polymer design, synthesis and purification is essential. Depending on the charge carrier mobility of a polymer, the application of the OTFT devices will vary. Considered applications include electronic paper, flexible displays, sensors and radio frequency identification devices (RFIDs). [47,51,52]

1.4 Organic solar cell devices

Organic solar cell (OSC) devices are an example of a photovoltaic device that incorporates organic semiconducting materials, both p-type and n-type, in an active layer to convert energy from sunlight to electrical energy. OSCs have particularly gained the interest of researchers in recent years as these devices provide a gateway to producing large scale, light weight solar panels to deliver renewable energy.[35] Utilising organic semiconducting materials that are soluble in organic solvents enables facile processability of solutions to thin films, hence, the possibility to easily up-scale fabrication of devices with reel-to-reel techniques.[53]

Recent reports confirm that efficiencies up to 18% have been achieved for OSCs with polymer and small molecule blends.[54,55] For OSCs fabricated with all-polymer semiconductor materials, efficiencies over 15% have been reported.[56–58] It should be noted that these higher efficiencies have been achieved with lab-scale devices. For larger-area OSCs, reported efficiencies are lower, with maximum values around 9%.[59,60] Figure 1.7 shows a diagram of a typical OSC device architecture, composed of two blended organic semiconductor materials (p- and n-type) in active layer, an electron transport layer (ETL), a hole transport layer (HTL) and two electrodes; the cathode (e.g. Ag) and the anode (e.g. ITO).

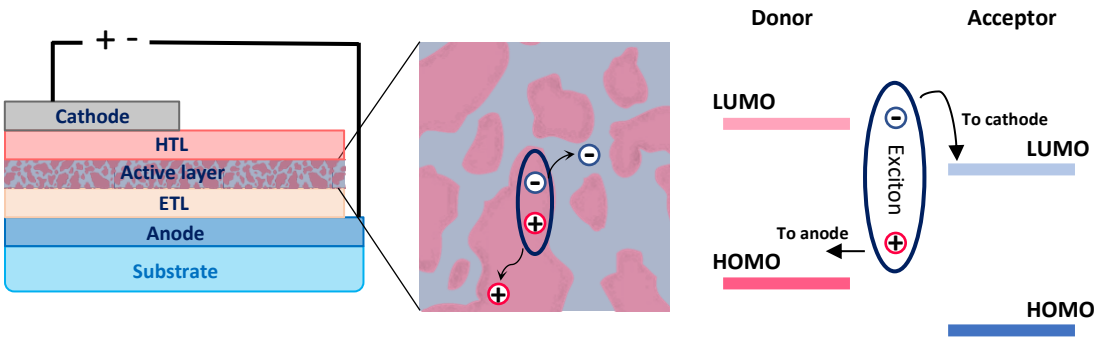


Figure 1.7. General device architectures of OSC devices (left) and illustration of exciton formation and extraction in the semiconductor active layer (right).

When the device is exposed to light, an incident photon has sufficient energy to promote an electron from the HOMO to the LUMO of a semiconductor material. The promotion of an electron generates an exciton: an electrostatically bound electron and hole which can diffuse within the material to the interface of p-type (donor) and n-type (acceptor) materials. Once at the polymer interface, the exciton dissociates into the separate charge carriers transported by the respective donor material (transports holes) to the anode and acceptor material (transports electrons) to the cathode. Finally, the charges are collected at the anode and cathode and the performance of the OSC can be determined.

OSC device performance can be determined from the calculated power conversion efficiency (PCE), shown in Equation 1.1. Considering the ratio of the useful power output (P_{out}) of the device compared to the power input (P_{in}), it is possible to evaluate the PCE percentage of a device. Three parameters; short circuit current (J_{sc}), open circuit voltages (V_{oc}) and fill factor (FF) make up the power output of the device.

$$PCE\ (\%) = \frac{P_{out}}{P_{in}} = \frac{J_{SC} \times V_{OC} \times FF}{P_{in}} \tag{1.1}$$

When no voltage is applied, the short circuit current is measured (J_{sc}). On the contrary, the open circuit voltage (V_{oc}) is measured where the current is zero. To promote the PCE of an organic solar cell device, it is important to maximise J_{sc}, V_{oc} and FF. Figure 1.8 depicts the ratio between the maximum power, at J_{MP} and V_{MP}, and the maximum potential power of the device, at J_{SC} and V_{OC} of the device, that is used to calculate the FF, shown in Equation 1.2.

$$FF = \frac{J_{MP}V_{MP}}{J_{SC}V_{OC}} \tag{1.2}$$

Two components, J_{sc} and V_{oc}, are mostly influenced by the energy levels of the absorbing semiconducting materials. The third component, FF, is instead associated more with the efficiency of charge extraction from the cell, determined by the charge carrier mobility and the rate of charge recombination.[61] Figure 1.8 shows a typical energy level diagram for an organic solar cell. Through polymer design it is possible to modify the HOMO and LUMO energy levels of the semiconducting material as well as tune the bandgap. Control over energy levels and the bandgap enables researchers to minimise J_{sc} and V_{oc} losses, thus, making it possible to improve device efficiencies.[62,63]

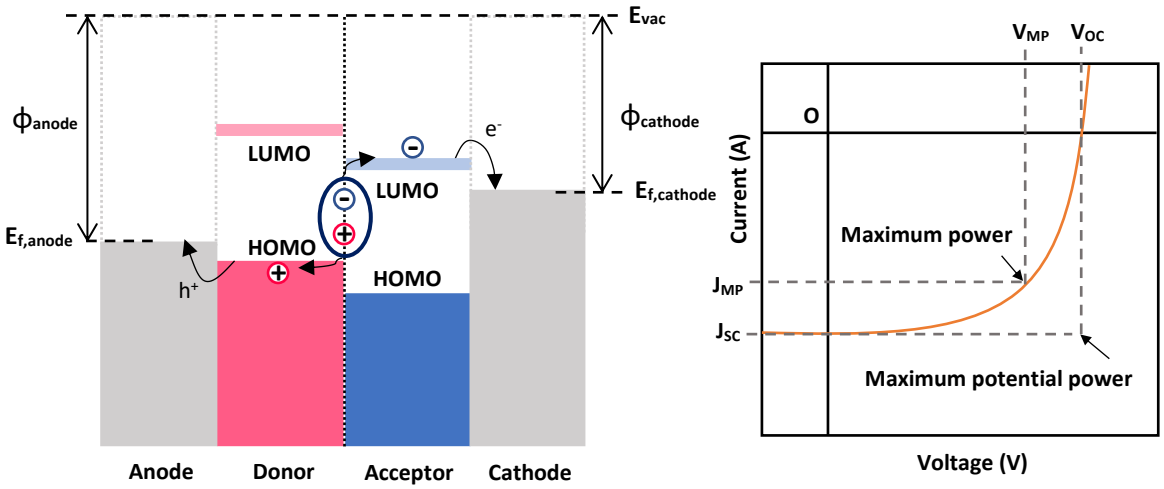


Figure 1.8. General energy level diagram of a photovoltaic cell.[36] (left) $E_{f,anode}$ and $E_{f,cathode}$ represents the Fermi level of the anode and cathode respectively, E_{vac} represents the vacuum level and ϕ_{anode} and $\phi_{cathode}$ represents the workfunction of the anode and cathode electrodes respectively. General J-V curve of a OSC under illumination. (right)

1.5 Using polymer design to optimise properties

In previous sections, the importance of polymer design to modify the properties semiconductor materials for specific applications has been established. This section details how particular design features can affect physical properties of a polymer, as well as, electronic properties. Good control over these properties enables the modification of certain characteristics of a polymer such as; solubility, thermal stability, mechanical flexibility, absorption range, HOMO and LUMO energy levels, therefore, the all-important bandgap of a semiconductor material.

1.5.1 Alkyl chains

Key advancements of semiconducting conjugated polymers were made in the 1980's with the introduction of alkyl chains onto the polymer backbone to give more air stable and solution processable polymers. One example, previously highlighted, was the development of poly(thiophene) to poly(hexylthiophene), where introduction of hexyl side chains was found to be essential to improving air stability and solubility.[38] Interest in these polymers was derived not only for the excellent solubility of the polymers but for the long-range order and crystalline ordering of the polymers in a thin film.[64] Savagatrup *et.al.* investigated the effect of extending poly(3-alkylthiophene) with butyl, hexyl, octyl and dodecyl side chains.[65] It was found that the brittleness of the thin film decreased with increasing alkyl chain length, therefore, demonstrating the effect of alkyl chain extension on the mechanical properties of a polymer.

Further considerations, with respect to inclusion of alkyl chains within a polymer backbone, focuses on the arrangement of these chains. Continuing with the poly(3-alkylthiophene) example, the importance of alkyl chain position can be understood by comparing regiorandom-P3HT with regioregular-P3HT. In a regioregular-P3HT structure the polymer chains are arranged in a head-to-tail configuration, whereas, in a regiorandom-P3HT structure there is a mixture of head-to-head, tail-to-tail and head-to-tail configurations. For regiorandom-P3HT a higher degree of morphological disorder was observed compared to regioregular-P3HT, as a result, the electronic properties of the semiconducting polymer were directly affected, such as charge carrier mobility and current-voltage characteristics.[66]

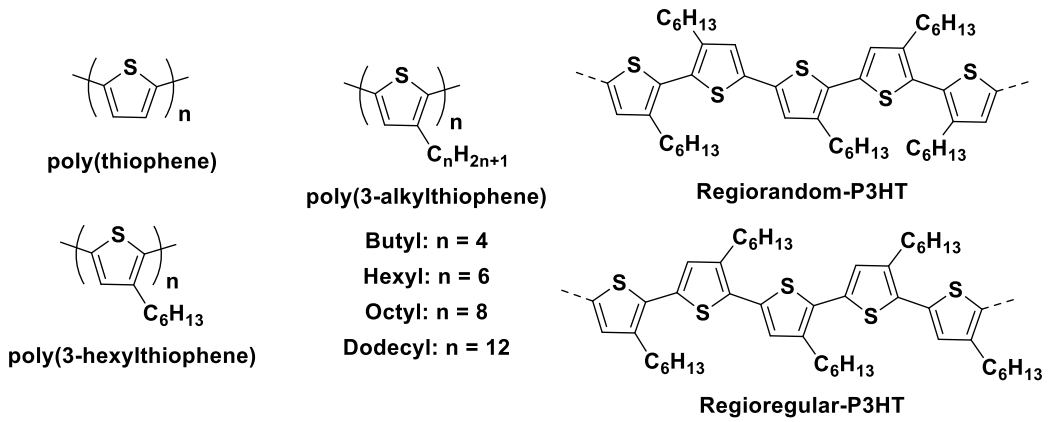


Figure 1.9. Structures of poly(3-alkylthiophenes) with the introduction of alkyl chains, the extension of alkyl chains and the arrangement of alkyl chains (regiorandom and regioregular) along the polymer backbone.

1.5.2 Composition of the polymer backbone

The backbone of a conjugated polymer, made up of repeating units, can determine how the semiconducting material might behave. For example, if the polymer is an electron rich donor (p-type) or an electron poor acceptor (n-type). In some cases, it can be easily understood if a polymer behaves as an acceptor or a donor by evaluating the repeat unit of the polymer chain. For donor polymers, the presence of electron donating groups within the polymer backbone influences the semiconducting material to behave as a p-type material. Considering the polymer P3HT with the alkylated thiophene repeating unit. In thiophene, the lone pair on the is delocalised within the 5-membered ring, resulting in six π-electrons being shared over five atoms, hence, the heterocycle is electron rich. P3HT is a well-known donor polymer and can effectively transport holes. Other examples of donor polymers, shown in Figure 1.10, include poly(2-methoxy-5-(2'-ethylhexyloxy)-1,4-phenylene vinylene) (MEH-PPV) and poly(2,5-dimethoxy-1,4-phenylene-1,2-ethenylene-2-methoxy-5-(2-ethylhexyloxy)–(1,4-phenylene-1,2-ethenylene)) (M3EH-PPV). Polymers MEH-PPV and M3EH-PPV have alkoxy (-O-R) electron donating groups on the phenyl ring in the repeat unit, effectively raising the HOMO energy

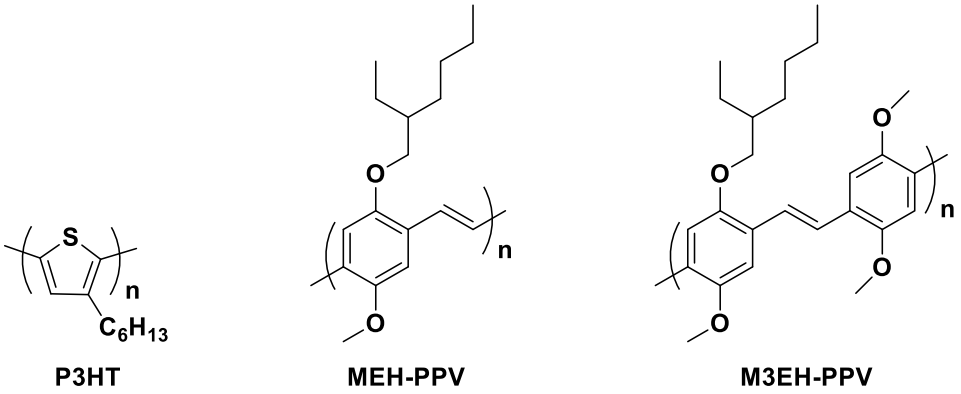


Figure 1.10. Examples of donor polymers.[67]

level.[67] Polymers P3HT, MEH-PPV and M3EH-PPV all behave as donor polymers and can effectively transport holes.

For acceptor polymers, the presence of electron withdrawing groups within the polymer backbone influences the material to behave as a n-type material. Polymers poly(1,4-dioctyloxyl-p-2,5-dicyanophenylenevinylene) (CNPh-PPV) and poly(oxa-1,4-phenylene-1,2-(1-cyano)-ethenylene-2,5-dioctyloxy-1,4-phenylene-1,2-(2-cyano)-ethenylene-1,4-phenylene) (CN-ether-PPV) have an electron withdrawing cyano (-C≡N) group introduced within the polymer backbone. In the case of poly((9,9-di-n-octylfluorenyl-2,7-diyl)-alt-(benzo[2,1,3] thiadiazol-4,8-diyl)) (F8BT) the carbon-nitrogen double bond (C=N) within the benzothiadiazole (BT) unit is the electron withdrawing component in the building block.[67] Polymers CNPh-PPV, CN-ether-PPV and F8BT all behave as acceptor polymers and can effectively transport electrons.

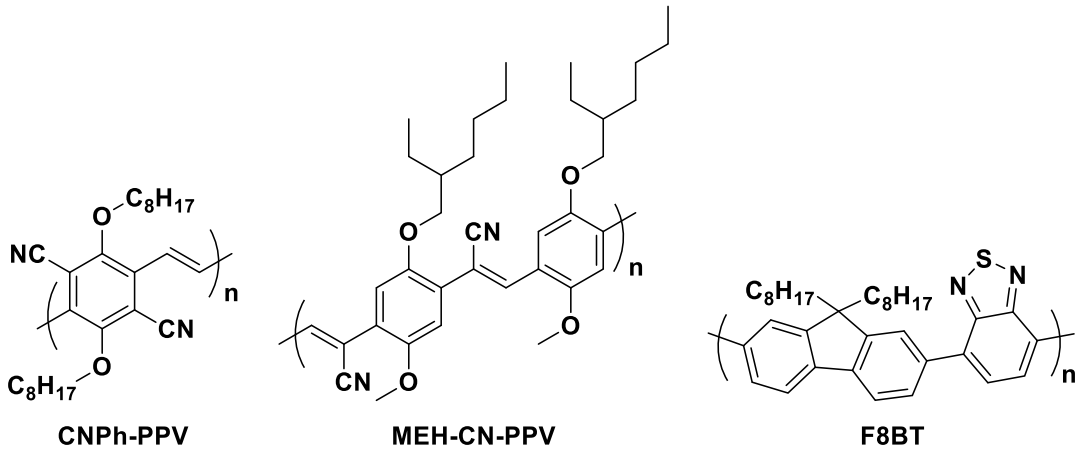


Figure 1.11. Examples of acceptor polymers.[67]

To effectively narrow the bandgap of polymers, donor-acceptor polymers have been designed with co-polymerised electron-rich (donor) and electron-poor (acceptor) monomers.[68] Donor-acceptor polymers show orbital mixing of the HOMO-LUMO energy levels from the donor unit and HOMO-LUMO energy levels from the acceptor unit to form hybrid molecular orbitals, as shown in Figure 1.12.[68] The resulting mixed hybrid orbitals give rise to a higher HOMO and a lower LUMO energy level for the polymer and the overall band gap (E_g) of the polymer is effectively reduced. The structure of poly((N,N'-bis(2-octyldodecyl)-naphthalene-1,4,5,8-bis(dicarboximide)-2,6-diyl)-alt-5,5'-(2,2'-bithiophene)) (N2200) is shown as an example of a polymer with alternating donor-acceptor repeat units.[48]

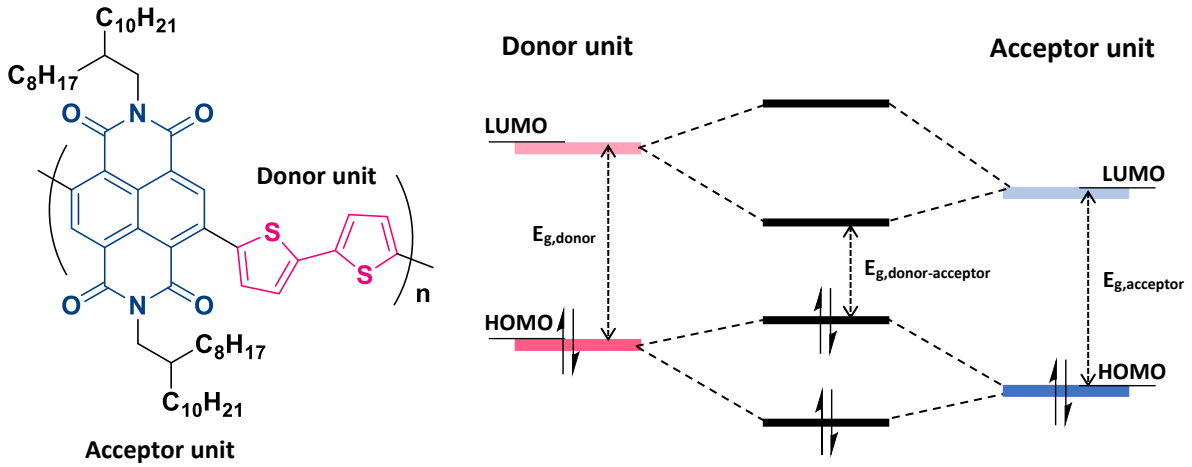


Figure 1.12. Structure of N2200 (left) and a general energy level diagram showing orbital mixing experienced in donor-acceptor polymers (right).[48, 68]

Alternating donor and acceptor units can result in an increased double bond character for the connecting bonds, therefore, the planarity of the polymer chain is increased (more planar). Increased planarity can also contribute to a reduction in the band gap, due to the increased conjugation along the backbone. Narrow band gap materials have been shown to improve device performance in electron devices such as OSCs.[69]

Planarity of a polymer can also be modified by introduction of an vinylene group into the polymer backbone.[70–72] Fei *et.al.* demonstrated the planarisation effect observed in thiophene-NDI-thiophene (T-NDI-T) compared with the vinylene containing analogue (T-V-NDI-V-T) using DFT calculations, shown in Figure 1.13.[70] From energy minimised structures, the dihedral angles between the thiophene and the NDI unit were reduced from 48° (T-NDI-T) to 0.3° and 18° (T-V-NDI-V-T) upon inclusion of the vinylene groups. The motivation for these polymer modifications arises from the correlation between increased planarity and better π-π stacking of the polymer chains thin films.[71] Improved π-π stacking can ultimately lead to higher device performances.

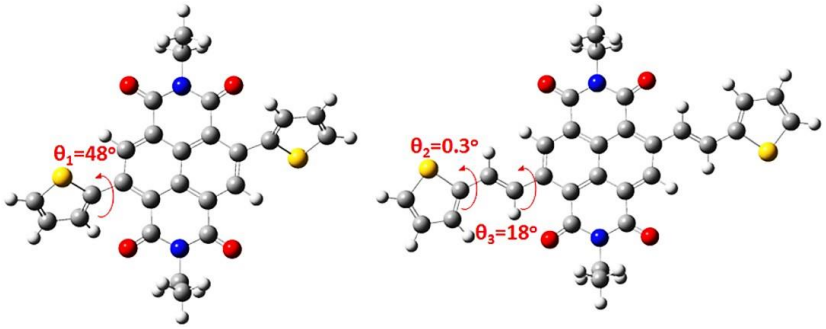


Figure 1.13. DFT results showing the energy-minimised structures of T-NDI-T (left) and T-V-NDI-V-T (right) calculated using at the B3LYP/6.31G* level.[70]

1.6 Synthesis of conjugated polymers

When designing novel conjugated polymers as semiconductors, it is important to consider the synthetic methods used. Synthetic methods can influence the molecular weight and polydispersity of the polymer, therefore, can affect the properties of the polymer. To synthesise conjugated polymers the most common methods used are transition-metal catalysed polymerisations, which proceed via two mechanisms: (a) step-growth or (b) chain growth.[73] Here, both polymerisation methods via step-growth and chain-growth mechanisms are discussed.

Before delving into the specific polymerisation mechanisms, the general mechanism for transition-metal catalysed polymerisations should be understood. Polymeric structures are accessed from the formation of C-C bonds between repeating monomer units. Figure 1.14 shows how these bonds can be formed with; an organic molecule fuctionalised with an effective leaving group (e.g. halide, R-X), an organic molecule functionalised with a non-noble metal-based group (e.g. boronic acid, R-M) and a transition metal catalyst (e.g. palladium(0)). As shown below, the process occurs via three key steps; oxidative addition (OA), transmetallation (TM) and reductive elimination (RE). Oxidative addition involves in insertion of the metal catalyst, for this example Pd(0)(L_2) is considered, between the carbon-halide (R'-X) bond where the metal centre oxidises from Pd(0) to Pd(II). Following oxidative addition, transmetallation takes place where the halide coordinated to the palladium catalyst is displaced by the R- group from the organic molecule with a non-noble metal-based group (R-M), producing an R-Pd(L_2)-R' complex. Finally, the reductive elimination step involves the regeneration of the Pd(0)(L_2) catalyst and the elimination of the product R-R'.

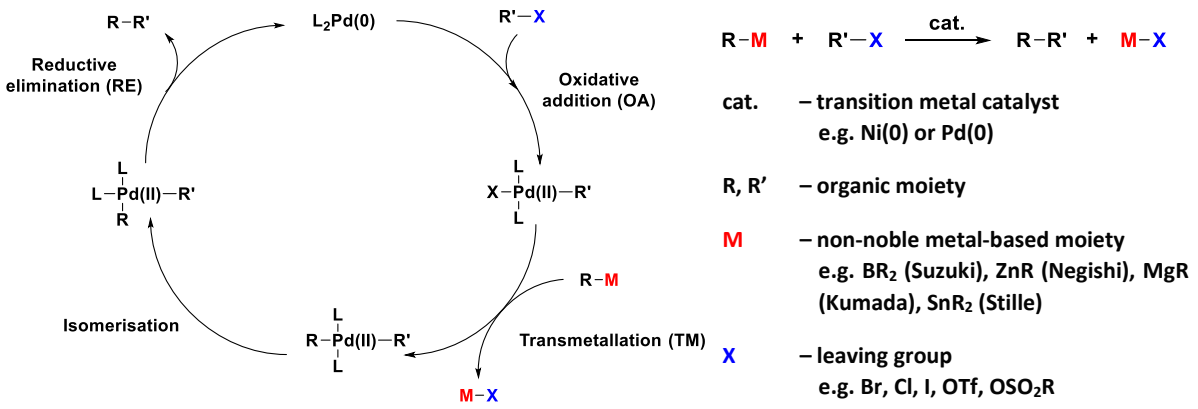


Figure 1.14. General mechanism for a transition-metal catalysed cross coupling reactions.

In a transition-metal catalysed polymerisation, monomers are functionalised with both leaving group (X) and non-noble metal groups (M) functionalities, either on the same monomer or two di-functionalised monomers. Designing monomers with both functional groups present at either end of the monomer allows the catalytic cycle to propagate, hence, enabling the construction of polymeric structures. Examples of the monomers functionalised with both X and M and di-functionalised monomers are shown in Figure 1.15.

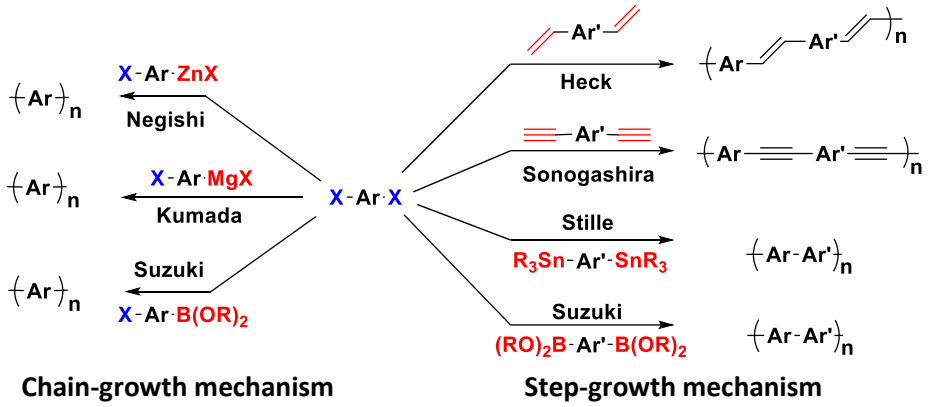


Figure 1.15. Examples of monomers used for transition-metal catalysed polymerisations.

For organic electronic applications, conjugated polymers are often synthesised from two di-functionalised monomers in a transition-metal catalysed reaction.[73] Using di-functionalised monomers, the transition-metal catalysed reaction proceeds via a step-growth mechanism to afford the conjugated polymers. Some examples of reactions that proceed via step-growth polymerisation, such as Suzuki and Stille reactions, are highlighted in Figure 1.15.

In a step-growth mechanism the polymer molecular weight increases slowly as the monomer initially couples to give dimers and trimers, as the reaction progresses longer oligomers are formed and eventually polymers. Most high-performing polymers reported in literature are synthesised using step-growth polymerisations.[58,74] Whilst these reactions are excellent for synthesising complex polymers, such as alternating donor-acceptor polymers, the nature of step-growth means it is often difficult to form high molecular weight materials and the polydispersity is typically high. Such polymerisations can also exhibit batch-to-batch variation.

Polymerisation techniques that proceed via chain-growth mechanism, instead form polymer chains by sequential addition of one monomer to the end of the growing chain. The chain-growth mechanism, shown in Figure 1.16, usually enables the formation of higher molecular weight material, as the polymer grows from the abundant monomer. If termination processes can be reduced, chain-growth polymerisations can give good control of the polymers molecular weight, polydispersity and end-group termination.

Considering transition metal-catalysed reactions, only a few conjugated polymers have been shown to grow by chain-growth processes. In these examples, the catalyst stays associated with the growing polymer chain, often via the process of ring-walking, where a metal-polymer π-bound intermediate exists. The π-bound intermediate migrates to the terminal carbon-halide bond (C-X) and the catalytic cycle repeats via intramolecular oxidative addition.[75,76] Using this mechanism the polymer grows sequentially by one monomer unit. By varying the reaction time it is possible to synthesise polymers with targeted molecular weights and narrow polydispersities.[77] In 1992 McCullough demonstrated a nickel catalysed polymerisation technique, via chain growth polymerisation, to give highly regioregular poly(3-hexylthiophene) polymers.[77] The chain growth mechanism was later confirmed by McCullough and Yokozawa in 2004.[78,79] These methods have since been developed to afford polymers with excellent control over molecular weight, polydispersity and high end-group fidelity.[80] Whilst these reactions have been typically limited to polymerising electron rich monomers, recently, there have been reported examples of more complex donor-acceptor polymers synthesised from chain-growth mechanisms with Suzuki-Miyaura Catalyst-Transfer polycondensation (SCTP) reactions.[81,82]

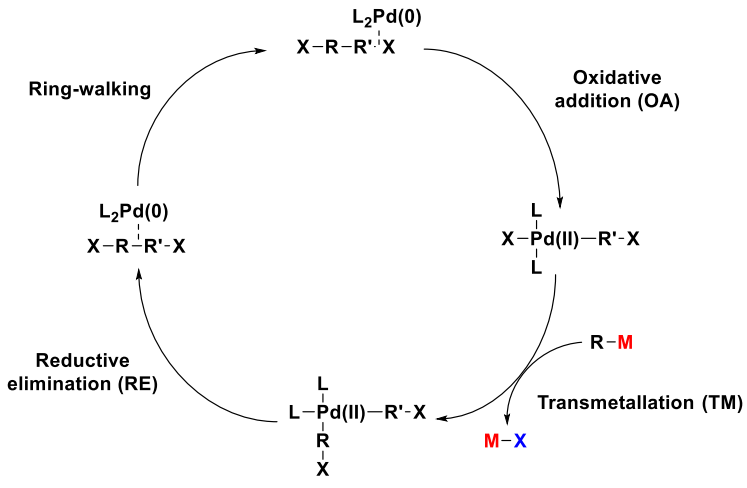


Figure 1.16. Chain-growth mechanism for transition-metal catalysed cross coupling reactions.[72]

1.7 Polymer characterisation

When synthesising conjugated polymers, it is essential to verify the formation of the polymer structures once the final product is obtained. Verification of polymer structures can be achieved from a combination of characterisation techniques such as gel permeation chromatography (GPC) and nuclear magnetic resonance (NMR), which will be discussed in this section. These techniques provide key information about the polymer, for example; molecular weight, polydispersity, regioregularity and end-group termination, that can influence the overall properties of the conjugated polymer.

The degree of polymerisation present in a polymeric material can be evaluated with analytical GPC techniques. Depending on the methods and conditions used for polymerisation, the degree of polymerisation can vary, consequently, a distribution of molecular weights corresponding to the polymer chains is measured. With step-growth polymerisation methods there can be significant batch-to batch variations, as discussed in Section 1.6, where high molecular weights can be achieved, however, with broad polydispersities. On the other hand, for living chain-growth polymerisations targeted molecular weights can be acquired with narrow polydispersities. In order to characterise the molecular weight of a polymer material, an average of the molecular weights from the polymer chains present is measured. Two important averages are considered: (a) 'number average molecular weight' (M_n) and (b) 'weight average molecular weight' (M_w).

The first average, M_n, takes into consideration the mole fraction distribution of the polymer chains in the sample, as shown in Equation 1.3. In this equation, n_i is defined as the number of molecules with molecular weight M_i.

$$M_n = \frac{\sum_{i=1}^{\infty} n_i M_i}{\sum_{i=1}^{\infty} n_i} \tag{1.3}$$

Instead, the M_w average takes into consideration the weight fraction distribution of the polymer chains in the sample, as shown in Equation 1.4. Average M_w values are greater the M_n values as the longer polymer chains have a higher weight compared with shorter chains.

$$M_w = \frac{\sum_{i=1}^{\infty} n_i {M_i}^2}{\sum_{i=1}^{\infty} n_i M_i}$$

(1.4)

For polymer materials with narrow polydispersities, the value for M_w approaches the value for M_n. The polydispersity index (PDI) is calculated from the ratio of the weight average of the polymer to the number average, as shown in Equation 1.5. Measured PDI values that are close to one indicates a narrow polydispersity. It should be noted that it is not possible for a PDI value to be less than one, as $M_w > M_n$.

$$PDI(Đ) = \frac{M_w}{M_n}$$

(1.5)

It is also important to characterise the structure of the polymer using techniques such as NMR. From an NMR spectrum, it is possible to assign signals to atoms both along the polymer backbone and within sidechains. In an NMR spectrum for a polymer, signals will typically be broad, as the signals are an averaged from the repeating unit of the polymer chain. Types of NMR experiments used to characterise polymers include ^{1}H, ^{19}F NMR, ^{31}P NMR and ^{11}B NMR. From ^{1}H NMR spectra, the assignment of signals to the end-groups of a polymer chain enables the quantification of molecular weight, by considering the ratio of protons assigned to the end group signal to the protons assigned to the polymer repeat unit.[83] To carry out this evaluation of the molecular weight by ^{1}H NMR, the molecular weight of the polymer must be low, to be able to resolve the end group signals. It is also important that the mechanism of the polymerisation is known (e.g. living chain-growth), such that the end-group can be clearly identified. Additionally, the regioregularity of a polymer can also be determined by ^{1}H NMR.[84]

In addition to 1D NMR techniques, 2D NMR techniques such as correlated spectroscopy (COSY), nuclear overhauser effect spectroscopy (NOESY) and diffusion ordered spectroscopy (DOSY) can be used to better understand the structure of a polymer. Measuring the diffusion coefficients from a polymer species, using DOSY experiments, can give an insight into the molecular weight of a polymer sample for example.[85] The diffusion coefficient of a polymer species can vary with the solvent and temperature used, thus, it can be difficult to quantify molecular weight of a polymer with DOSY alone. A combination of results from DOSY and ^{1}H

NMR (end group analysis) could be used for a more accurate quantification of molecular weight.[85]

1.8 Post-polymerisation functionalisation

Post-polymerisation modification (PPM) is a method used to introduce complex functionality onto a polymer backbone. PPM techniques involve performing reactions directly onto a polymer backbone; designed with a functional group that can selectively undergo further functionalisation. Often PPM is challenging, since there are multiple functional groups on a polymer, and therefore complex mixtures can arise if the functionalisation chemistry is not very high yielding with no side products. However, the use of optimised PPM techniques can enable the introduction of sensitive functional groups onto the polymer backbone, without the introduction of unwanted side products or polymer defects. Furthermore, by performing PPM reactions on the same batch of starting polymer the ability to create highly comparable polymer libraries is available, providing an excellent way to better understand structure-property relationships.[86]

In literature, reported PPM reactions have been widely explored for non-conjugated polymers, since the 1920s when Staudinger initially started exploring PPM techniques.[87–89] Following initial explorations of these reactions, since the 1990's, there was a rapid acceleration of research into PPM techniques for non-conjugated polymers.[86,90,91] Understandably, developments of PPM techniques towards conjugated polymers started much later, where a range of techniques have been explored.[92–96] There is however, a distinct development lag of reported PPM examples for conjugated polymers, compared to non-conjugated polymers, which can be owed to issues with selectivity and incomplete reactions.[97] In this section, recently reported PPM reactions towards conjugated polymers are presented. Reactions ideal for PPM should fulfil the following criteria: (a) can be carried out in one step, (b) can react with high efficiency and (c) are widely applicable to produce a range of polymers with a variety of functional groups. It is essential to ensure high efficiency without the formation of unwanted side products, as these can cause defects along the backbone and impurities can be difficult and complicated to remove.

Click reactions are the ideal candidate for PPM reactions as they proceed with high efficiency, with little or no side-reactions, where a wide range of functional groups can be introduced.[98] Copper-catalysed azide-alkyne cycloadditions (CuAAC) are a leading example of click reaction used to synthesise new conjugated polymer materials via PPM.[99] These reactions have been used to prepare complex polymer structures such as block co-polymers, non-linear conjugated polymers, graft co-polymers and high molecular weight organogels, shown in Figure 1.17. [100–103]

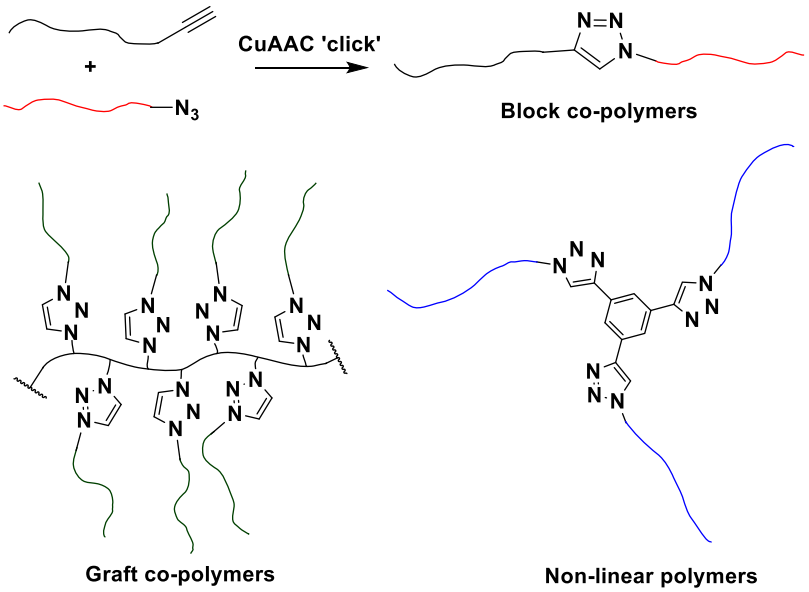


Figure 1.17. An illustration of polymer structures from CuAAC click reactions.[100–102]

Nucleophillic aromatic substitution (S_NAr) has been reported in literature as another ideal PPM reaction towards new conjugated polymer materials.[97,104,105] S_NAr reactions present high reaction efficiencies; with the displacement of halide group (typically fluorine), attached to an electron withdrawing aromatic unit, with a range of thiol (-SH), thioacetate (-S) and alcohol (-OH) terminated nucleophilic reagents. The displacement reaction has been shown to be highly versatile where final polymer products can be obtained in one synthetic step after polymerisation. Creamer *et.al.* demonstrated the versatility of S_NAr reactions onto poly(9,9'-dioctylfluorene-5-fluoro-2,1,3-benzothiadiazole) (F8fBT) with a wide range of nucleophiles, shown in Figure 1.18.[97]

Other examples of PPM click reactions on conjugated polymers include: strain-promoted azide-alkyne[106,107], alkyne-acceptor addition[108], and Diels-Alder reactions[109,110]. Introduction of new functionality by PPM that do not use click reactions to modify conjugated backbones

have also been explored using techniques such as; oxidation and reduction[111–114], doping[115,116] and transition-metal catalysed cross-coupling[117,118].

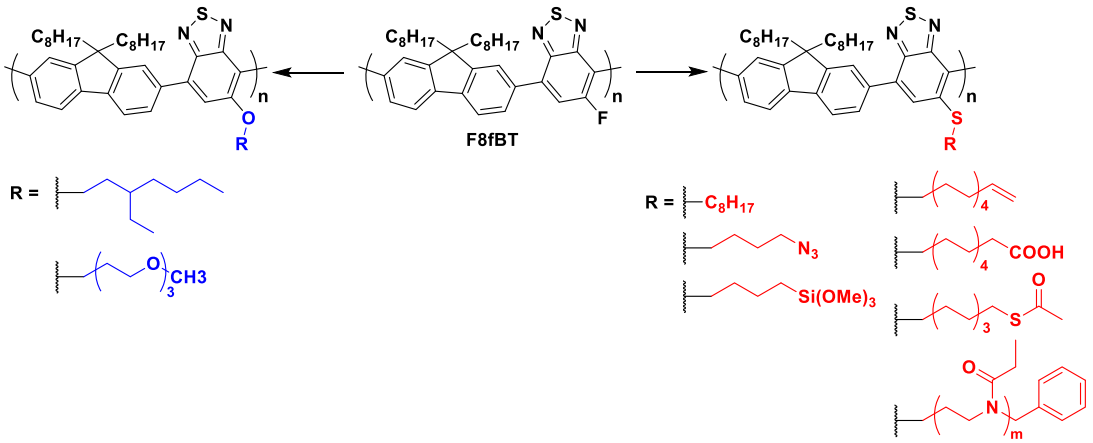


Figure 1.18. Polymer products from nucleophilic aromatic substitution reactions onto F8fBT.[97]

1.9 Functional polymers via nucleophilic aromatic substitution

Post-polymerisation modification methods have been used to synthesise a wide range of polymers,[119] from end-functionalised polymers to polymers functionalised along the backbone (within the repeating unit). These functionalised polymers can then be utilised to synthesise new and interesting polymeric structures such as graft, brush, star and double-cable polymers. This thesis focuses on (a) using nucleophilic aromatic substitution (S_NAr) as a PPM method to acquire conjugated polymers and (b) development of new polymer backbones capable of undergoing S_NAr. As previously discussed, S_NAr reactions have been shown to be an efficient, simple and versatile PPM technique. In this section, functional polymers synthesised from S_NAr reactions are presented. In an S_NAr reaction, a nucleophile (Nu^-), typically a reactant with a terminal thiol (-SH), alcohol (-OH) or amine ($-NH_2$) group, attacks an electron-deficient aromatic group and displaces a leaving group, typically a halide (-F or -Cl). Examples of electron-deficient aromatic moieties, with a leaving group, used in S_NAr reactions for PPM are shown in Figure 1.19.

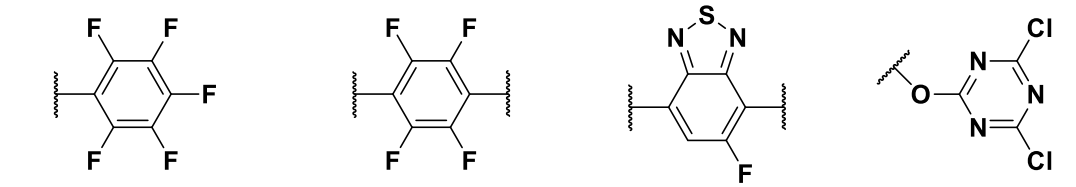


Figure 1.19. Electron-deficient aromatic moieties suitable for nucleophilic aromatic substitution.

1.9.1 End-functionalised polymers

Boufflet *et.al.* demonstrated the use of S_NAr reactions on poly(3-alkylthiophenes), end-functionalised with an electron-deficient pentafluorobenezene (PFB) group. The end-fuctionalised polymer was obtained from *in situ* end-capping, of the Kumada catalyst-transfer polymerisation (KCTP), with a PFB-MgCl Grignard reagent. The PFB end-capped polymer was reacted with a range of thiols, via S_NAr, to afford end-functionalised polymers suitable for surface functionalisation, crosslinking, energy transfer and biolabeling applications. Additionally, the PPM technique was used to attach thiol-terminated PEG chains, indicating the use of S_NAr towards diblock co-polymer structures.[120] This work highlights the high selectivity and efficiency of S_NAr reactions at the end of polymeric chains. Whilst a wide range of thiol terminated reactants were shown to fully substitute onto the polymer end-chains, substitution with alcohol and amine terminated reactants showed no reaction via S_NAr onto the PFB end-group.

Lee *et.al.* synthesised end-functionalised polymers from a nucleophilic aromatic substitution polymerisation with a telechelic phenoxide end-group. In a PPM reaction hexafluorobenzene (HFB) or decafluorobiphenyl (DFBP) was substituted onto the phenoxide end-group by S_NAr. Di-funtionalised polymers were then used in a further PPM reaction to afford tough and ductile di-block co-polymers for applications in fuel cells.[121]

1.9.2 Functionalised pendant groups

Using S_NAr reactions, the possibility to incorporate functional groups along a polymer backbone, within the repeating unit, has been established by means of including electron-deficient groups within the polymer backbone. Shao *et.al.* synthesised non-conjugated poly(pentafluorostyrene) with a PFB group included in each repeat unit along the polymer backbone. Sodium trifluoromethanesulfonamide was substituted onto the PFB group, via S_NAr, where the degree of substitution could be controlled by the molar quantity of reactant added. Polymers functionalised with lithium (N-perfluorophenyl)trifluoromethanesulfon-amide pendant groups were designed for use as solid single-ion conducting electrolytes, where physical and electronic properties could be tuned by controlling the percentage of the pendant group present along the backbone.[122] Also using a fluorinated aromatic repeating unit (tetrafluorobenzene (TFB)), Shida *et.al.* presented the use of S_NAr directly onto a

conjugated polymer backbone (poly(9,9-dioctylfluorene-alt-tetrafluoro-p-phenylene)) towards the diversification of conjugated polymers. This work specifically looked at how optical and electrochemical properties can be directly influenced by varying the pendant groups attached to the polymer backbone.[105]

Creamer et. al. highlighted the use of a monofluoro-benzothiadiazole repeat unit within conjugated polymer (F8fBT), an alternative to fluorinated benzene, as an electron deficient unit for S_NAr reactions. The highly electron-withdrawing benzothiadiazole moiety allowed facile displacement of the fluorine group with thiols, thioacetates and alcohol terminated reactants. From the polymer functionalised with pendant azide and carboxylic groups, emissive nanoparticles were made. Further post-polymerisation functionalisation using strain-promoted azide-alkyne cycloaddition (SPAAC) was conducted onto the functionalised nanoparticles, highlighting the extensive and valuable uses of post-polymerisation modification techniques.[97] It is important to note that S_NAr reactions can also proceed with alternative leaving groups, such as chlorine. Kubo *et.al.* showed electron-deficient trichloro-triazine groups, along a non-conjugated polymer backbone, could be functionalised with thiol or amine terminated reactants by displacement of the chlorine via S_NAr. The sequential addition of different nucleophiles was used to obtain multifunctional polymers, also highlighting the complex polymeric structures that can be prepared using S_NAr.[123]

1.9.3 Functionalisation towards new polymer structures

As shown above, there are a number of examples of nucleophilic aromatic substitution onto the end of the polymer backbone and along the polymer chain (within the repeating unit). Using end-functionalised polymers di-block co-polymer structures have been achieved.[121] Another interesting polymer structure afforded from S_NAr includes graft co-polymer structures. Graft co-polymers can be synthesised from a range of methods that can be categorised as; grafting through, grafting from and grafting onto methods, as shown in Figure 1.20. The method chosen depends on the required application, or structure of the graft co-polymer. The grafting onto method allows utilisation of S_NAr to produce well-defined graft co-polymer structures. Considering the high versatility of click reactions, the grafting onto method is an attractive approach to synthesise graft co-polymers.

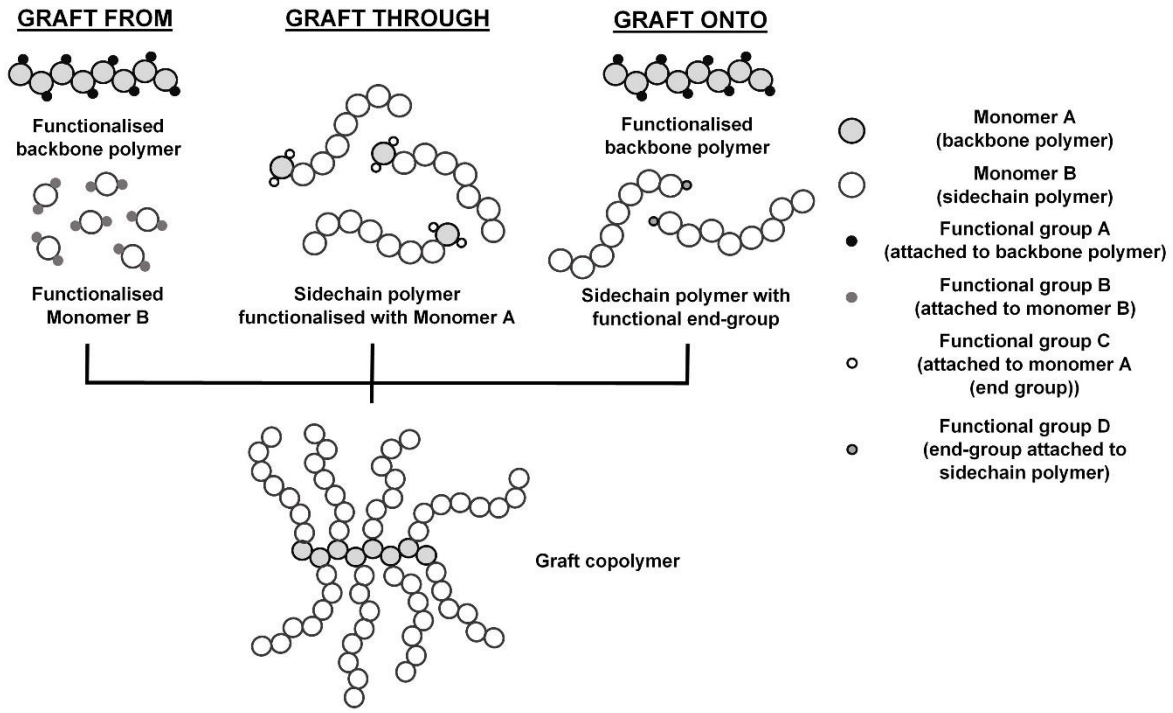


Figure 1.20. The different methods; graft from, graft through and graft onto methods that can be used to synthesise graft co-polymer structures.

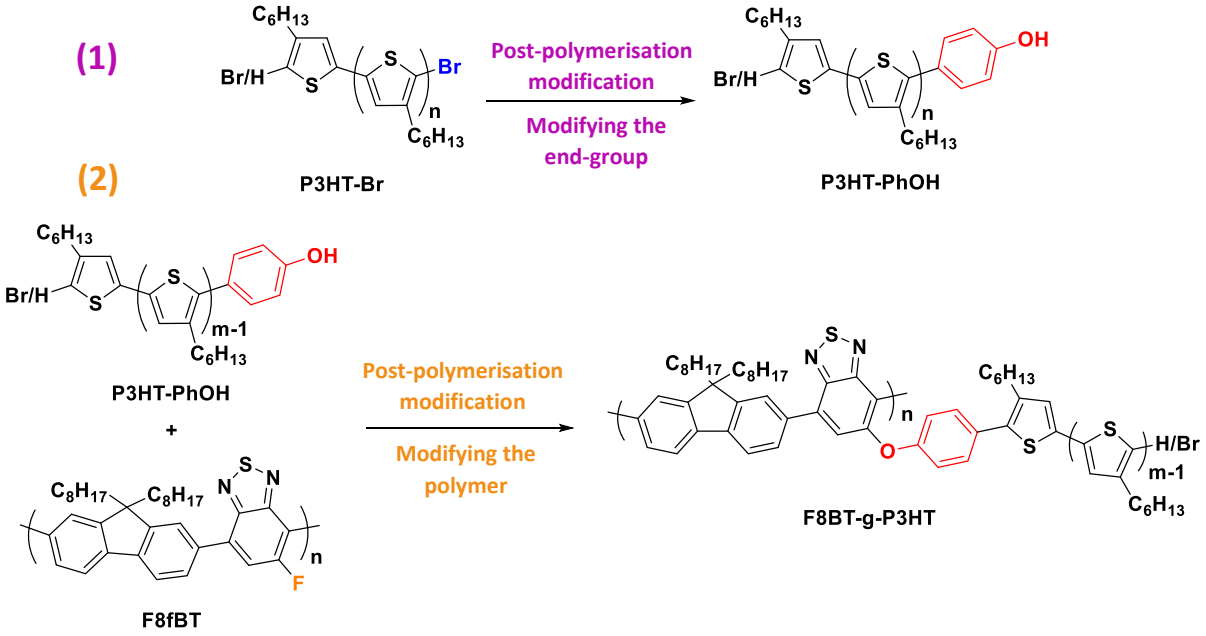
Cong *et.al.* reported the synthesis of graft co-polymer structures by substitution of alcohol terminated poly(ethyleneglycol) (PEG) sidechains onto the electron-deficient monofluoro-benzothiadiazole repeat unit within the F8fBT polymer backbone. By varying the length of the sidechain, the solubility of the polymer in polar solvents and the surface wettability of the polymer was modified. It was concluded that the solubility and wettability of conjugated polymer materials could be easily modulated by varying the PEG sidechain length on the graft co-polymer, via S_NAr. In addition, the properties of the graft co-polymers were highly comparable as the polymers were synthesised from the same batch of F8fBT, hence, the backbone chain lengths were the same for all graft co-polymer derivatives.[104]

In the past ten years, there has been a growing interest into using nucleophilic aromatic substitution methods to synthesise new conjugated polymers. This thesis reports a further expansion of this research area by consideration and development of novel end-functionalised conjugated polymers and conjugated polymer backbones towards semiconductor materials for use in electronic devices.

1.10 Thesis aims and overview

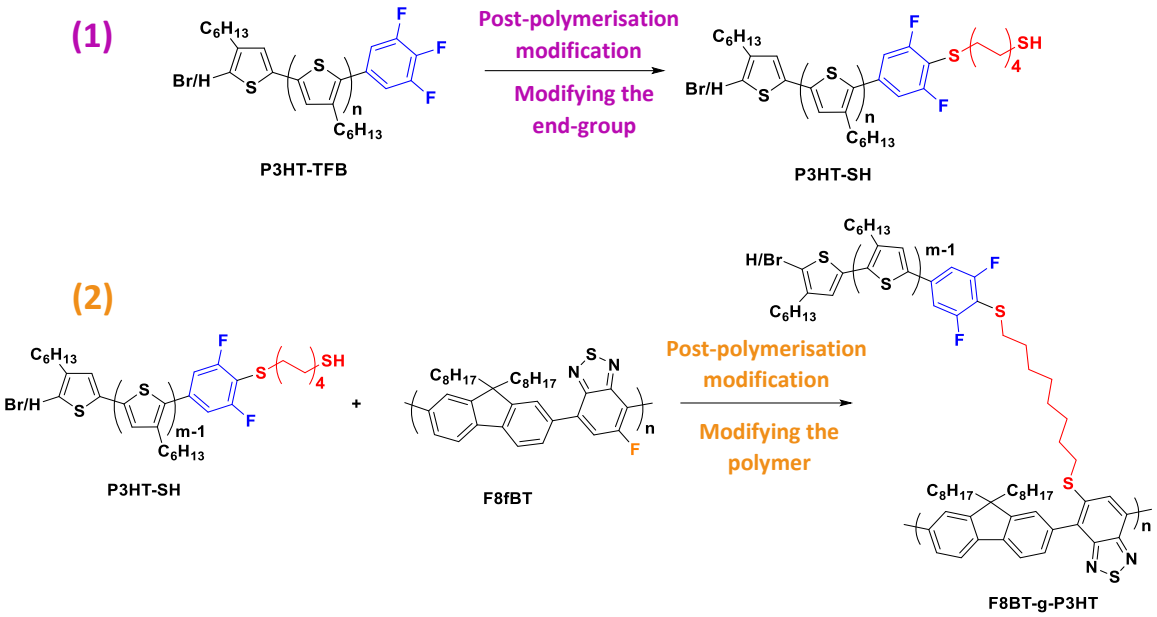
Post-polymerisation modification by nucleophilic aromatic substitution comprises the backbone of this thesis, presented in Chapters 2 to 5. Both end-group functionalisation and functionisation within the repeat unit of a polymer was explored to afford a variety of conjugated polymer structures. Physical and optoelectronic properties of all synthesised polymers were investigated, hence, it was possible to gain a good understanding of how the chemical structure could influence the performance in OTFT or OSC devices. Particularly in this work, the versatility of the S_NAr reaction to yield partially substituted conjugated polymers (along the polymer backbone) was demonstrated, thus, enabling access to polymer series with varied sidechain/group densities. Previously reported synthetic techniques were utilised and developed to establish an effective and efficient method towards novel conjugated polymer materials.[97,120]

Chapters 2 and 3 present the successful synthesis of graft co-polymer structures, via S_NAr, with an n-type backbone and p-type sidechains. In both Chapters, after polymerisation, a two-step method was used to assemble the graft co-polymer structures; (a) PPM modification of the polymer end-group and (b) PPM modification of the repeat unit along the polymer backbone, as shown in Schemes 1.1 and 1.2. The graft co-polymer structures were confirmed by GPC and various NMR techniques. Advantages and limitations of each method were discussed.



Scheme 1.1. Synthetic route (1) towards graft co-polymer structures.

Additionally, Chapter 3 looks at a graft co-polymer series, in which the grafted density of the p-type sidechains attached to the n-type backbone polymer was varied. For the graft co-polymer series optical, electronic and thermal properties were investigated. In addition, thin films of the graft co-polymers were characterised by GIWAXS and AFM before testing their performance in organic solar cell devices.



Scheme 1.2. Synthetic route (2) towards graft co-polymer structures.

In Chapter 4, two novel n-type polymer backbones were designed and synthesised. Designed polymers incorporated a fluorinated 2,1,3-benzothiadiazole repeat unit within the polymer backbone, capable of undergoing S_NAr to attach a range of thiol-terminated pendant groups, as shown in Figure 1.21. Complete substitution along the polymer backbone with a thiol terminated alkylchain was demonstrated, confirming the ability for the polymers to undergo S_NAr. The effect of substitution on the optical, electronic and thermal properties of the polymer were analysed. Further exploration looked at functionalising the polymer backbone with a crosslinkable azide pendant group. For polymers fuctionalised with the crosslinkable azide group, thin film immobalisation (and patterning) was investigated by thermal and photochemical methods. All new n-type polymers were tested within OTFT devices, where it was possible to determine their ability to transport electrons by evaluating the charge carrier mobility.

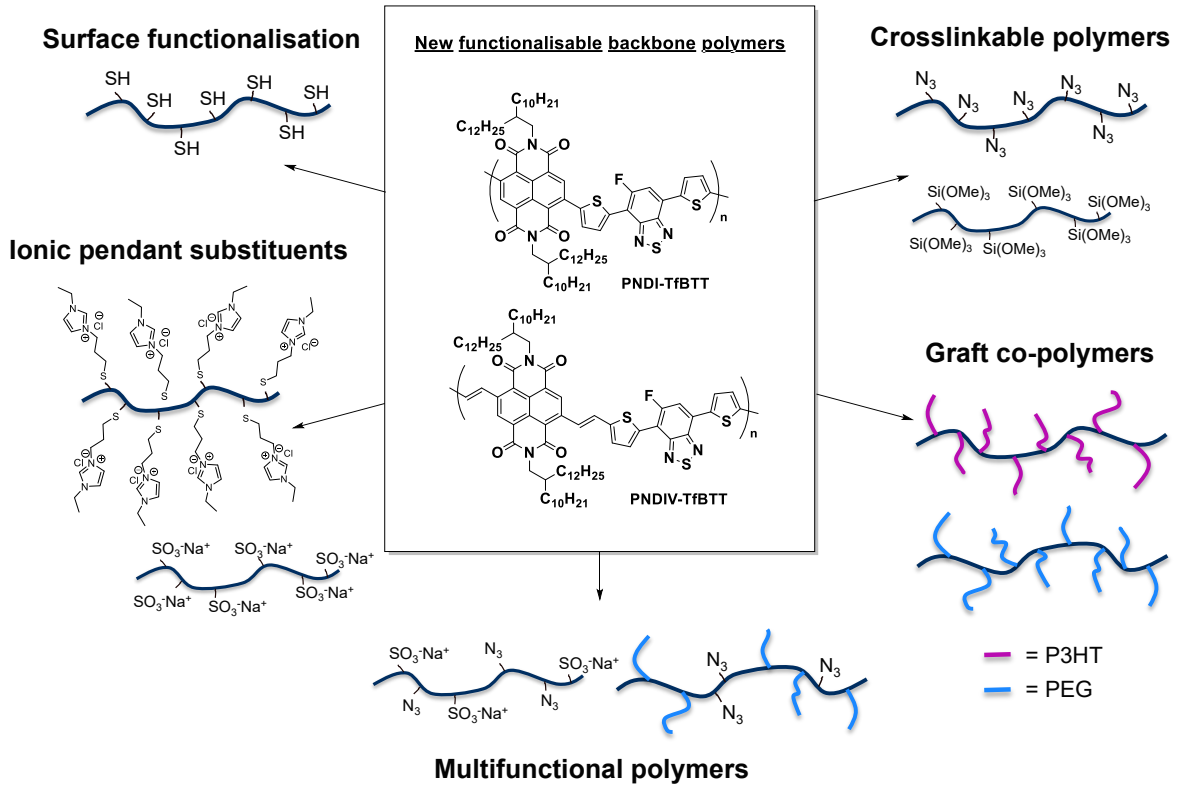


Figure 1.21. Potential post-polymerisation functionalisation products from PNDI-TfBTT and PNDIV-TfBTT backbone polymers.

In Chapter 5, a series of conjugated polyelectrolytes (CPEs) were synthesised with increasing ionic density along the polymer backbone, shown in Figure 1.22, designed as interlayers for electronic devices such as OSCs. Use of CPEs as interlayers the enables the possibility to modify the energy barrier for charge carrier transport from the active layer to the electrode, hence, fine-tuning the work function of the electrode.[124,125]

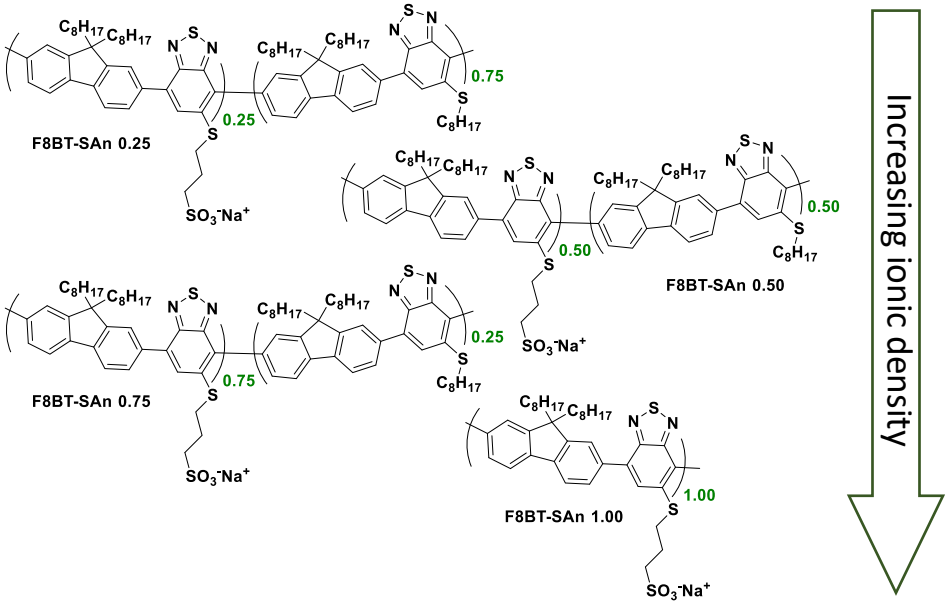


Figure 1.22. Conjugated polyelectrolytes with increasing anionic density.

2 Chapter 2: A novel synthetic method towards conjugated graft co-polymers utilising post-polymerisation modification

2.1 Introduction

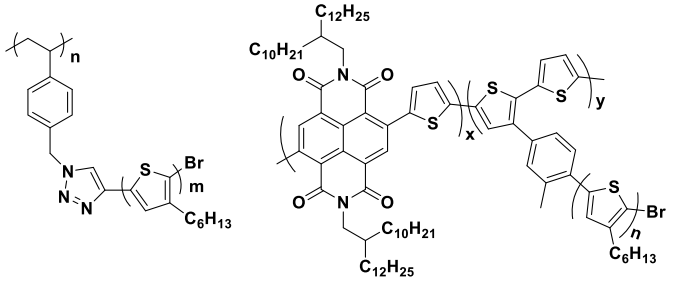
Conjugated polymers have received considerable attention in recent years for a range of applications including; organic light emitting diodes (OLEDs)[126–128], organic thin film transistors (OTFTs)[46,129] and organic photovoltaic (OPV)[130–132] devices. Use of these organic conjugated polymer semiconducting materials, enables the development of devices with effective flexibility, impact resistance and optical transparency.[133–135] Industrial scale production of devices, containing polymer semiconductor materials, may see benefits such as; reduced production costs and increased rates of processability, therefore, leading to broader scope of potential applications.[136–138]

It has been shown for devices that incorporate conjugated polymers in an active layer, the morphology of the active layer can affect the efficiency and stability of an electronic device.[139] In addition, reports have identified the use of a bulk heterojunction (BHJ) morphology can improve overall power conversion efficiency (PCE) in OPV devices. BHJ morphologies are typically achieved from a blended acceptor and donor active layer, where the blended photoactive layer enables fast charge transfer and efficient separation of charges.[140,141] Diffusion length of an exciton (a bound state of an electron and a hole) is approximately limited to 10-20 nm.[142] Therefore, it is understood that active layer morphology should be carefully considered to improve efficiency in OPV devices.[143,144] Photoactive polymer blends with a variety of architectures have been explored including: all polymer blends, block co-polymer structures (with alternating donor and acceptor units) and more recently graft/brush co-polymer structures (with acceptor and donor polymer chains).[145–149]

All-polymer blends are a mixture of two partially immiscible polymers in an organic medium, which are deposited to form a thin film photoactive layer. Blended polymer active layers may undergo macro-phase separation, where morphologies can be difficult to predict, affected by factors such as polymer ratios, solvent type, and temperature. Macro-phase separation may be observed due to a diffusion of one or both of the polymer types.[150,151] Control of the phase

separation of blended polymers is essential to achieve a stable BHJ layer. One method to address issues of macro-phase separation saw the implementation of covalently bound block co-polymer structures, that incorporate donor and acceptor polymers covalently bound at the polymer ends. Ordered microphase separated structures can be achieved by varying the chain-length of the donor and acceptor polymer blocks in a controlled living polymerisation.[152,153]

Further development of polymer structures led to graft co-polymer structures, where donor and acceptor polymers are covalently bound with a polymer backbone and grafted polymer sidechains. Conjugated graft co-polymers are structurally interesting materials for use as an active layer in photovoltaic devices, as they could resolve issues related to stability of thin film morphology and thermal stability.[154] Thelakkat and Heinrich reported a series of 'grafted bottled brushes' polystyrene-graft poly(3-hexyl-thiophene) (PS-g-P3HT), synthesised via a grafting onto method, in OFET devices.[155] With high molecular weight sidechains (approx. 17.4 kDa) a charge carrier mobility of 5.0 x 10^{-2} $cm^2V^{-1}s^{-1}$ was found, comparable with linear P3HT. PS-g-P3HT showed improved thermal stability and wetting behaviour in comparison to linear P3HT.[155] Wang *et al.* reported a series of all conjugated graft co-polymer structures for OFET devices comprising of a donor/acceptor block co-polymer backbone and donor side chains.[156] The polymer backbone was composed of naphthalene diimide (NDI) co-polymerised with 3-(4'-chloro-3'- tolyl)thiophene (CTT), to form the acceptor section of the backbone and poly(3-(4'-chloro-3'-tolyl)thiophene-alt-thiophene) (PCTT), to form the donor section of the backbone. To the $PNDICTT_{xy}$ backbone, P3HT (donor) side chains were grafted, via a grafting from method, to afford $PNDICTT_{xy}$-g-P3HT. This work concluded $PNDICTT_{xy}$-g-P3HT showed an overall p-type characteristic with a mobility in the order of 10^{-4} $cm^2V^{-1}s^{-1}$. Microphase separation of the PNDICTT and P3HT was observed where P3HT domains exhibited 'nanofibril-



PS-*g*-P3HT **$PNDICTT_{xy}$-*g*-P3HT**

Figure 2.1. Examples of graft co-polymers reported.[155,156]

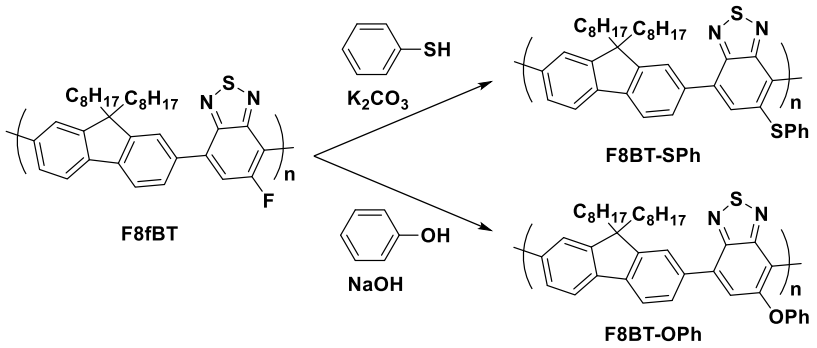
like' morphology within 10-20 nm.[156] In another report Wang *et al.* indicates PNDICTT$_{xy}$-g-P3HT shows high thermal stability.[157]

Conjugated graft co-polymer structures pique the interest of researchers as single component active layers in photovoltaic devices, where charge transfer processes occur intramolecularly, as opposed to the intermolecular processes observed in active layer polymer blends. However, few examples of conjugated graft co-polymers are reported in the literature, likely due to the complexity of the polymer structures and limited synthetic routes towards such structures. Synthetically, graft co-polymers can be achieved via grafting through, grafting from or grafting onto methods. Grafting onto methods are particularly advantageous as they provide a straight-forward approach, in a one-step synthesis (post-polymerisation), to afford graft co-polymer structures. Grafting onto methods require the reaction of end-functionalised conjugated polymers with conjugated polymers functionalised along the polymer backbone.

Adam Creamer *et al.* reported a post-polymerisation modification method involving Nucleophilic Aromatic Substitution (S_NAr) onto a poly(9,9'-dioctylfluorene-5-fluoro-2,1,3-benzothiadiazole) (F8fBT) functionalised polymer backbone.[97] S_NAr reactions were demonstrated with a variety of groups functionalised with a thiol (-SH), thioacetate () or alcohol (-OH) end-group. The main aim of this work was to demonstrate the ability to tune the physical and optoelectronic properties of the backbone polymer, F8fBT. Direct comparison of the polymers was possible as there was very little variation in the molecular weight of the modified polymers, where the same batch of starting polymer was used for all substitutions.[97] Full substitution, with 100% graft efficiency, was achieved via this grafting onto method making it a highly desirable method to explore further. Development of fully conjugated graft co-polymers using grafting onto techniques has expectedly been limited, due to the reduced number polymer building blocks available to undergo grafting onto reactions. In this Chapter, the synthesis of a fully conjugated graft co-polymer via post-polymerisation modification (grafting onto) method is reported. The fully conjugated graft co-polymer reported here comprised of a functionalised acceptor polymer backbone (F8fBT) with end-functionalised donor polymer side chains (P3HT-PhOH).

2.2 Small molecule functionalisation

When considering end-group functionalisation of the sidechain polymer it was important to first demonstrate the substitution of solely the end-group onto the F8fBT backbone. F8fBT was synthesised via a palladium-catalysed Suzuki polymerisation reported in the literature.[97] Thiophenol (PhSH) and phenol (PhOH) were considered as functional groups that could be incorporated onto the end of P3HT chain and could undergo S_NAr directly onto the F8fBT backbone, shown in Scheme 2.1. Thiophenol and phenol groups were selected to maintain full conjugation within the graft co-polymer structure.

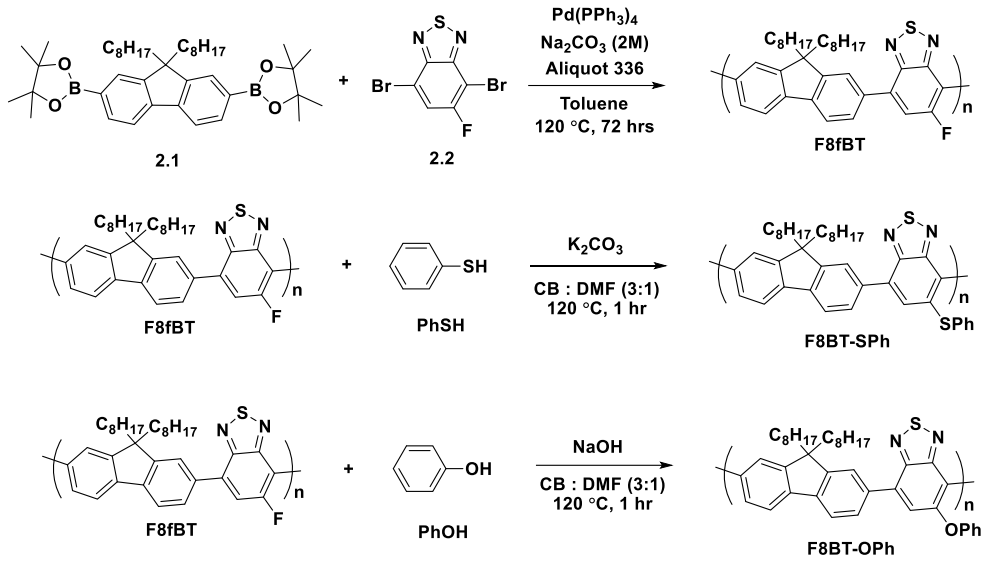


Scheme 2.1. Post-polymerisation modification of F8fBT with thiophenol (top) and phenol (bottom) to give F8BT-SPh and F8BT-OPh respectively.

2.2.1 Synthesis of the monomers and polymers

F8fBT was synthesised via a Suzuki polymerisation, where stoichiometric amounts of monomer 2.1 and 2.2 were reacted in the presence of a palladium(0) catalyst and base in toluene (shown in Scheme 2.2). The mixture was heated to 120 °C and maintained at this temperature for 72 hours under argon. The mixture was then cooled, precipitated into methanol and filtered before purification by Soxhlet extraction. This purification involved washing of the polymer in hot methanol, acetone and hexane to remove any residual catalyst and low molecular weight impurities. Hot chloroform was used to extract the purified polymer from the Soxhlet thimble. Finally, the solvent was removed and the polymer redissolved, precipitated, filtered and dried to give the polymer F8fBT, a fibrous yellow solid (yield 70-99%). F8fBT was found to be soluble in a wide range of solvents including toluene, THF, chloroform and chlorobenzene at room temperature. Polymers F8BT-SPh and F8BT-OPh were synthesised via post-polymerisation modification from F8fBT.

In the case of F8BT-SPh, F8fBT was reacted with thiophenol, in the presence of base, in a 3:1 mixture of chlorobenzene and DMF respectively (shown in Scheme 2.2). The mixture was heated to 120 °C and maintained at this temperature for 1 hour in a microwave reactor. The mixture was then cooled, precipitated into methanol and filtered before purification by Soxhlet extraction. Purification by Soxhlet extraction involved washing of the polymer in hot methanol and acetone. Hot chloroform was used to extract the purified polymer from the Soxhlet thimble, the solvent was removed and the polymer was redissolved, precipitated, filtered and dried to give the polymer F8BT-SPh, a fibrous yellow solid. This polymer was soluble in the same range of solvents as F8fBT. The polymer F8BT-OPh was synthesised via the same method as F8BT-SPh, where instead, F8fBT was reacted with excess phenol, in the presence of base, in a 3:1 mixture of chlorobenzene and DMF respectively (also shown in Scheme 2.2). The dried polymer F8BT-OPh was a fibrous yellow solid. F8fBT, F8BT-OPh and F8BT-SPh were all characterised by GPC, ^{1}H NMR and ^{19}F NMR.



Scheme 2.2. Synthesis of backbone polymer F8fBT and polymers F8BT-SPh and F8BT-OPh.

2.2.2 Confirmation of substitution

The substitution of thiophenol and phenol onto the F8fBT polymer backbone was confirmed by ^{1}H NMR and ^{19}F NMR. From the ^{1}H NMR of F8fBT (Figure 2.2), a multiplet in the aromatic region, δ 8.20-7.70 ppm, was observed corresponding to the seven aromatic protons along the polymer backbone. Additionally, a broad signal at δ 2.30-1.90 ppm, corresponding to the four aliphatic protons (closest to the backbone) on the alkyl chain, and a multiplet at δ 0.90-0.70 ppm, corresponding to the six aliphatic protons at the end of the alkyl chain, was identified. Finally, the remaining 24 aliphatic protons on the alkyl chain were assigned to the signal at δ 1.30-0.90 ppm.

Figure 2.2 shows the ^{1}H NMR for F8BT-SPh, where a complex multiplet (3H), three broad signals (3H, 2H, 3H) and a triplet (1H) in the aromatic region at δ 8.05-7.35 ppm were assigned to twelve aromatic protons. Seven protons from the F8fBT and five protons from the thiophenol pendant group. As previously, the broad signal at δ 2.30-1.70 ppm corresponding to the four aliphatic protons was observed and the remaining signals from aliphatic protons reside at the same chemical shift as observed in the ^{1}H NMR of F8fBT. The ^{1}H NMR for F8BT-OPh displayed a complex multiplet (7H) at δ 8.05-7.60 ppm and two broad signals (2H, 3H) at δ 7.35-7.28 and δ 7.10-7.00 ppm respectively. The broad signal at δ 2.15-1.70 ppm corresponding to the four aliphatic protons was observed and the remaining signals from aliphatic protons reside at the same chemical shift as observed in the ^{1}H NMR of F8fBT. For both polymers, F8BT-SPh and F8BT-OPh, the signals from the protons in both aromatic and

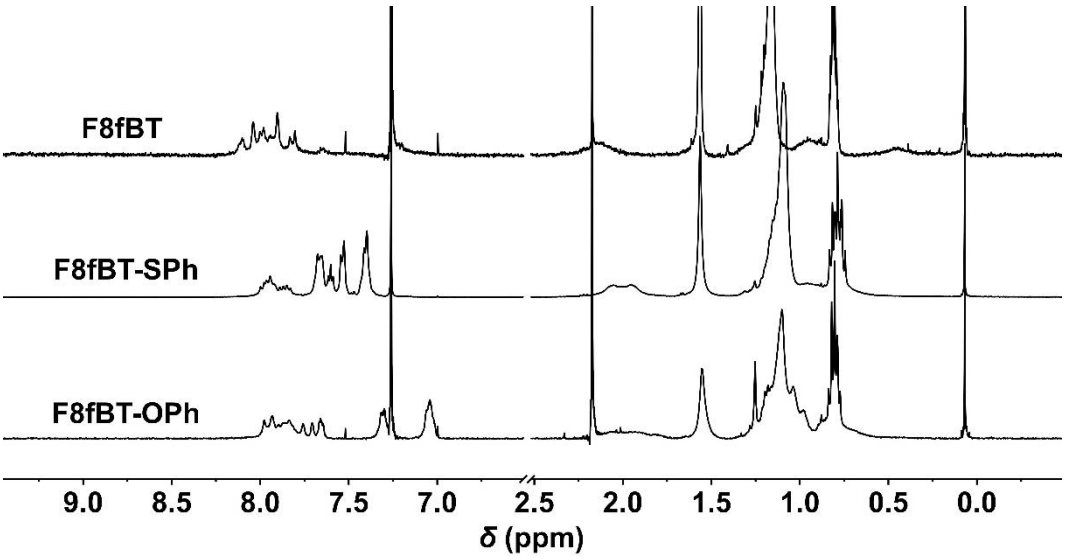


Figure 2.2. ^{1}H NMR of F8fBT (top) F8BT-SH (middle) and F8BT-OPh (bottom).

aliphatic regions (for signals of protons closer to the backbone) were observed at a slightly lower chemical shift. The observed shift upfield (shielded) can relate to the replacement of the inductively withdrawing F group with a donating ether or thioether.

From the ^{19}F NMR, shown in Figure 2.3, F8fBT displayed strong signal at δ - 114.50 ppm. For both polymers, F8BT-SPh and F8BT-OPh, the absence of this peak was noted indicating the complete displacement of the fluorine on the backbone polymer. A summary of the molecular weight data for each polymer is detailed in Table 2.1. F8fBT, F8BT-SPh and F8BT-OPh had similar M_n values of 43.5, 36.8 and 43.6 KDa as F8BT-SPh and F8BT-OPh synthesised from the same batch as F8fBT. Here it has been shown, that both thiophenol and phenol are good candidates for P3HT end groups, as these groups can successfully undergo S_NAr onto the F8fBT backbone.

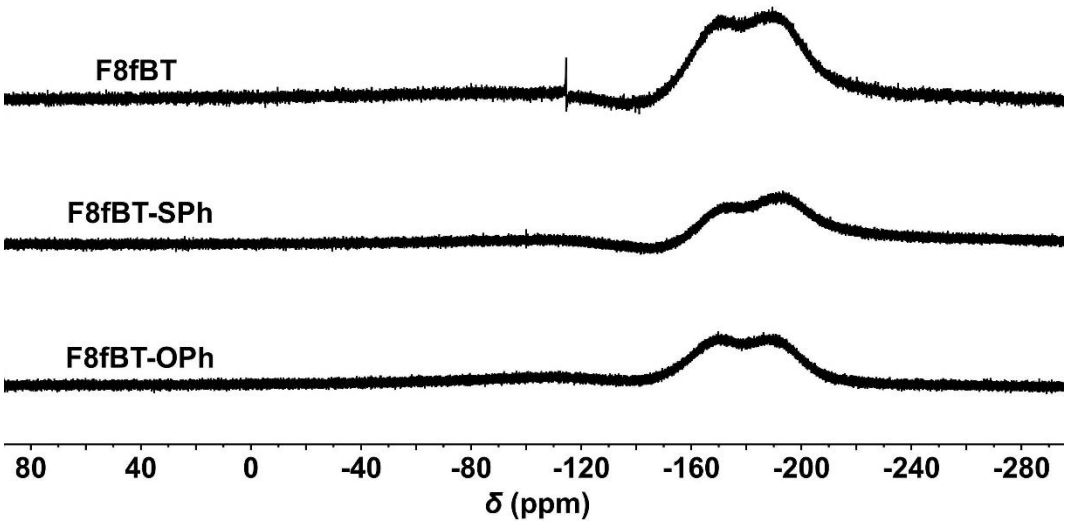


Figure 2.3. ^{19}F NMR of F8fBT (top) F8BT-SH (middle) and F8BT-OPh (bottom).

Table 2.1. GPC data of F8fBT, F8BT-SPh and F8fBT-OPh.

Polymer	M_n (kDa)	M_w (kDa)	DP_n[a]	DP_w[b]	Đ[c]
F8fBT	43.5	76.9	80	142	1.80
F8BT-SPh	36.8	83.4	58	132	2.30
F8BT-OPh	43.6	86.3	71	140	1.98

[a]Degree of polymerisation calculated from M_n
[b]Degree of polymerisation calculated from M_w
[c]Polydispersity index M_w/M_n

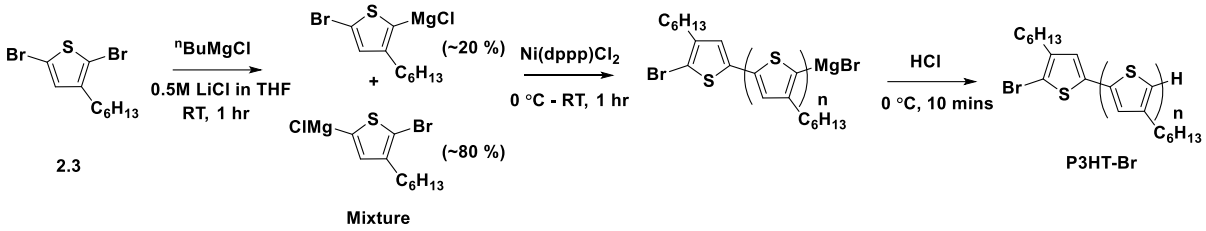
2.3 Synthesis of end-functionalised P3HT (small scale)

In order to synthesise graft co-polymers via a 'grafting onto' method, end-functionalised P3HT sidechains were designed and functionalised with a nucleophilic group (containing -SH or-OH) for subsequent reaction with F8fBT. The synthesis of P3HT terminated with thiophenol (P3HT-PhSH) and phenol (P3HT-PhOH) was investigated. These polymers were synthesised from mono-bromo terminated P3HT (P3HT-Br). All syntheses of end functionalised P3HTs are discussed in this section.

2.3.1 P3HT starting polymer (P3HT-Br)

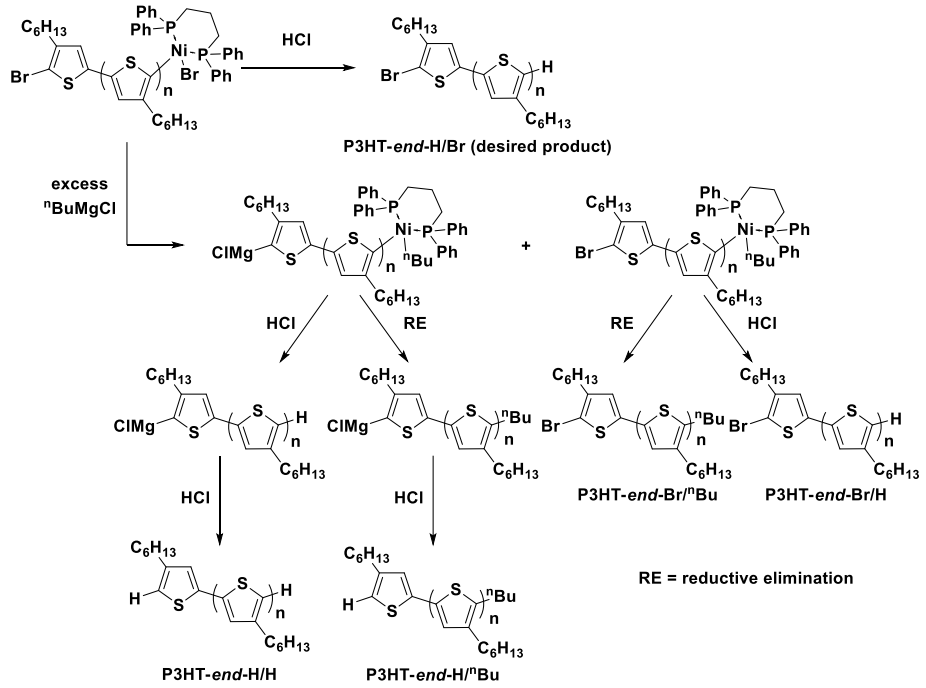
Reported Grignard Metathesis Method (GRIM) and Kumada Catalyst Transfer Polycondensation (KCTP) were used to synthesise end-functionalised P3HTs.[158–160] A modified procedure from Thelakkat *et. al.* was used to afford P3HT with defined hydrogen and bromine end groups (P3HT-Br), utilising GRIM and KCTP methods, as shown in Scheme 2.3.[161] This synthetic method used monomers that are widely commercially available, hence, provides a scalable route towards end-functionalised P3HTs.

Monomer 2.3 was reacted with n-butylmagnesium chloride in 0.5 M LiCl in THF solution (^{n}BuMgCl) to form a mixture of active monomers: 2-bromo-5-chloromagnesio-3-hexylthiophene (approx. 80%) and 5-bromo-2-chloromagnesio-3-hexylthiophene (approx. 20%). The formation of the active monomers was monitored by GCMS, where an internal standard (hexadecane) was used to quantify the degree of conversion to the active monomers. The polymerisation was initiated by addition of nickel catalyst to the reaction mixture at 0 °C, the reaction was left to warm to room temperature and stirred for one hour. Termination of the polymerisation reaction was carried out at 0 °C, where HCl was added and stirred for 10 minutes. The mixture was precipitated into methanol and filtered before purification by Soxhlet extraction. Purification by Soxhlet extraction involved washing the polymer with hot methanol, acetone and hexane to remove any residual catalyst and low molecular weight impurities. Finally, the polymer was extracted from the Soxhlet thimble with hot chloroform, the solvent was removed, the polymer redissolved, precipitated, filtered and dried to give the product, P3HT-Br, a powdered purple solid (yield 80%).



Scheme 2.3. Reaction scheme for the synthesis of P3HT-Br.

Following the procedure described above, H/Br end-functionalised P3HT (P3HT-Br) was prepared from carefully monitored and optimised GRIM and nickel catalysed KCTP reactions. Homocoupling to afford the unwanted polymer product, with Br/Br end-groups, was avoided by using a low polymerisation temperature (0 °C). The presence of Br/Br terminated P3HT in the final product, even in very low quantities, would lead to cross-linking reactions in the synthesis of the final graft co-polymer. Therefore, it was essential to optimise the synthesis to eliminate the formation of Br/Br terminated P3HT. It was important, when synthesising the active Grignard monomer (monomer 2.3), to ensure Grignard reagent was not present in excess. If an excess of the Grignard reagent resided in the reaction mixture, the subsequent KCTP reaction and HCl quench would yield undesired polymer products such as; H/H, H/^{n}Bu and Br/^{n}Bu terminated P3HT, as shown in Scheme 2.4.[161]



Scheme 2.4. Potential routes towards unwanted side products formed during the synthesis of P3HT-Br.[161]

To avoid obtaining the undesired polymer products, an offset stoichiometry of 0.96 equivalents of titrated ^{n}BuMgCl was added. This offset ensured there was not an excess of the Grignard reagent present in the reaction mixture. An accurate concentration of ^{n}BuMgCl solution was determined by titration against iodine in THF solution with 0.5 M lithium chloride.[162] The reaction was monitored by GCMS, where a small sample (one drop) was quenched with hydrochloric acid, extracted with chloroform, filtered and analysed by GCMS. Less than 2% of starting material (2,5-dibromo-3-hexylthiophene) was measured, and an absence of 3-hexylthiophene, indicating that ^{n}BuMgCl was not present in excess. Using these conditions, a small amount of H/H terminated P3HT was formed, as well as, the major product, H/Br terminated P3HT.

P3HT-Br was analysed by MALDI, shown in Figure 2.4, where both H/H and H/Br terminated P3HT chains (P3HT-*end*-H/Br and P3HT-*end*-H/H) were observed. The higher intensity peaks, labelled with a circle, correspond to P3HT-*end*-H/Br chains. The peak at 1746 gmol^{-1} relates to a decamer of the repeat unit molecular weight (166.3 g mol^{-1}), plus the molecular weight of the end-groups; a proton and a bromine. The lower intensity peaks, labelled with a triangle, correspond to P3HT-*end*-H/H chains. The peak at 1666 gmol^{-1} relates to a decamer of the repeat unit molecular weight, plus the end-group molecular weight of two protons. In addition, the MALDI spectra confirmed low molecular weight P3HT chains, approximately 1-4 kDa, were achieved with the ratio of catalyst (0.05 eq.) and reaction conditions used.

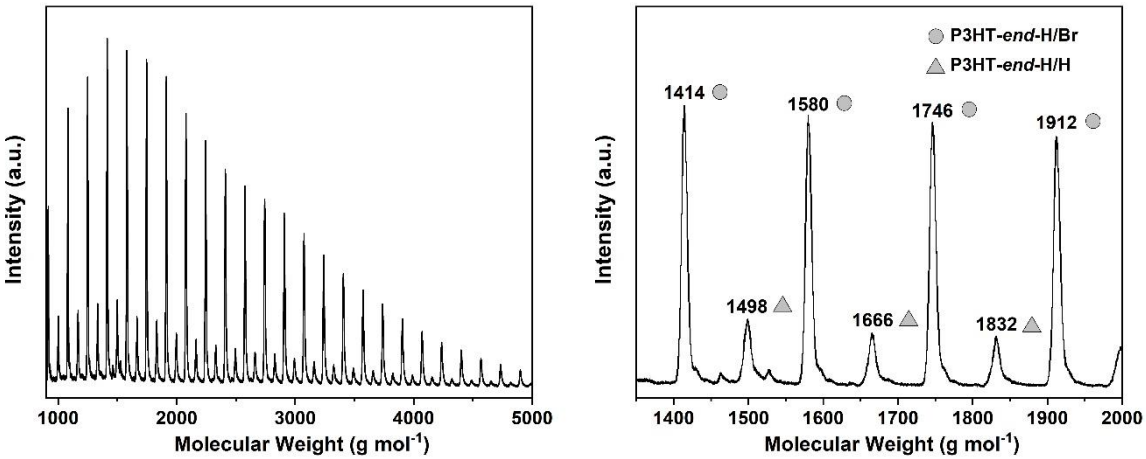


Figure 2.4. MALDI of P3HT-Br, full spectra (left) and zoomed in (right).

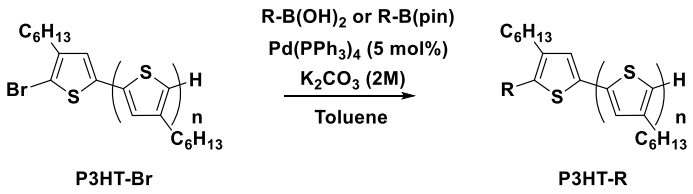
The formation of P3HT-*end*-H/H may have been due to complex reactions occurring with the presence of 2,5-dibromo-3-hexylthiophene in the reaction mixture. As P3HT-*end*-H/H was a minor product and was not reactive in subsequent reactions, elimination/separation of P3HT-

end-H/H was not considered. P3HT-*end*-H/Br polymer chains, within the P3HT-Br polymer product, were further modified to introduce a nucleophilic end-group functionality.

From the ^{1}H NMR, shown in Figure S2.7, it was possible to confirm the P3HT polymer structure, where signal associated with the aromatic proton from the thiophene (1H) appears at δ 6.98 ppm. Another characteristic peak of P3HT, at δ 2.80 ppm, comes from the methylene group (2H) closest to the polymer backbone. The very low intensity peak at δ 2.58 ppm and narrow peaks in the ^{1}H NMR spectra suggest the P3HT-Br product had a predominantly regioregular structure.[84]

2.3.2 End-functionalised polymers (P3HT-PhOH and P3HT-PhSH)

In situ end-capping methods have previously been reported to modify the end groups on P3HT chains.[163] However, these methods can produce a mixture of end-capped polymer products and can be difficult to control. As mentioned before, precise control of the end-groups on the polymer was of utmost importance for later grafting onto processes, to avoid crosslinking of the polymers. Therefore, post-polymerisation modification techniques were considered to introduce the desired functionality at the end of the P3HT polymer chains. Further functionalisation of well-defined P3HT-Br proceeded via a palladium catalysed Suzuki cross-coupling reaction, shown in Scheme 2.5, to incorporate -PhSH and -PhOH groups.



Scheme 2.5. General reaction scheme for end-funcionalisation of P3HT-Br.

P3HT-Br was reacted with an excess of 4-mercaptophenylboronic acid or 4-hydroxyphenylboronic acid pinacol ester, in toluene, in the presence of a palladium catalyst and K_2CO_3 to afford P3HT-PhSH and P3HT-PhOH respectively. Progression of the substitution reaction was monitored by MALDI. Upon completion of the substitution reaction, the mixture was precipitated into methanol and filtered before purification by Soxhlet extraction. Purification by Soxhlet extraction involved washing with hot methanol before the polymer was extracted from the Soxhlet thimble with hot chloroform. The solvent was removed, the polymer redissolved, precipitated, filtered and dried to give a powdered purple solid. In the case for both P3HT-PhSH and P3HT-PhOH, the product was obtained as a powdered purple

solid. MALDI was used to analyse the collected products, where successful substitution of bromide with the -PhSH or -PhOH was evaluated.

P3HT-PhSH

MALDI analysis confirmed that the conversion of P3HT-Br to P3HT-PhSH did not occur after reacting for over 72 hours, as shown in Figure 2.5. The highest intensity peaks correspond to P3HT-*end*-H/Br chains and the lower intensity peaks correspond to P3HT-*end*-H/H chains. The emergence of a new peak, labelled with a star, corresponding to P3HT-*end*-H/PhSH chains was present, however, in very low concentrations. The peak at 1445 g mol^{-1} represents an octamer of the repeat unit (166.3 g mol^{-1}), plus the molecular weight of the end groups; a proton and thiophenyl group. After extending the reaction time beyond one week and addition of excess 4-mercaptophenylboronic acid, the reaction did not go to completion. It was possible that oxidation of the thiol to the disulfide hindered the progression of the reaction, but perhaps more likely, was the poisoning of the Pd catalyst by the presence of an thiol group (4-mercaptophenylboronic acid).[164] These complications could be avoided by protecting the aryl thiol, however, with the addition of considerable complexity to the synthetic route.[164] Therefore, further investigation proceeded with attempts to end-functionalise P3HT with 4-hydroxyphenylboronic acid pinacol ester.

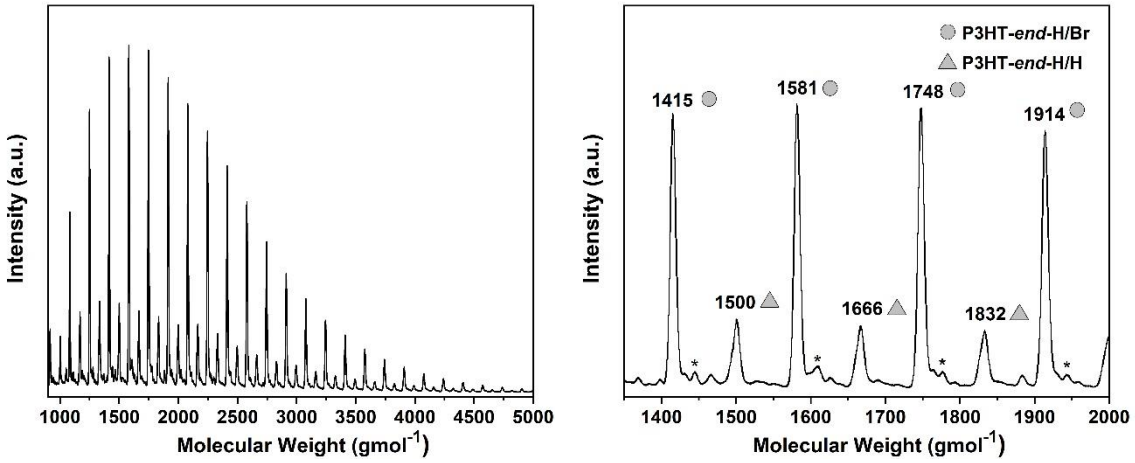


Figure 2.5. MALDI of P3HT-PhSH, full spectra (left) and zoomed in (right).

P3HT-PhOH

MALDI was used to confirm the complete conversion of P3HT-Br to P3HT-PhOH after 12 hours. MALDI-TOF MS spectra (Figure 2.6) showed the conversion of P3HT-*end*-H/Br chains to P3HT-*end*-H/PhOH and the presence of unreacted P3HT-*end*-H/H. The higher intensity peaks, labelled with squares, correspond to P3HT-*end*-H/PhOH chains. The peak at 1762 $gmol^{-1}$ represents a decamer of the repeat unit (166.3 $gmol^{-1}$), plus the molecular weight of a proton and a phenol end group. The lower intensity peaks corresponded to P3HT-*end*-H/H chains, where peak at 1669 $gmol^{-1}$ relates a decamer of the repeat unit (166.3 g mol^{-1}), plus the molecular weight of two proton end groups.

Figure S2.8 shows the ^{1}H NMR for P3HT-PhOH, where signal from the aromatic proton on the thiophene repeat unit (1H) appears at δ 6.98 ppm and the signal from the allylic protons on the methylene group (2H) closest to the polymer backbone appear at δ 2.80 ppm. Furthermore, in the ^{1}H NMR the emergence of two small peaks at δ 7.32 and δ 6.89 ppm was observed. These new peaks correspond to the aromatic protons on the phenol end-group.

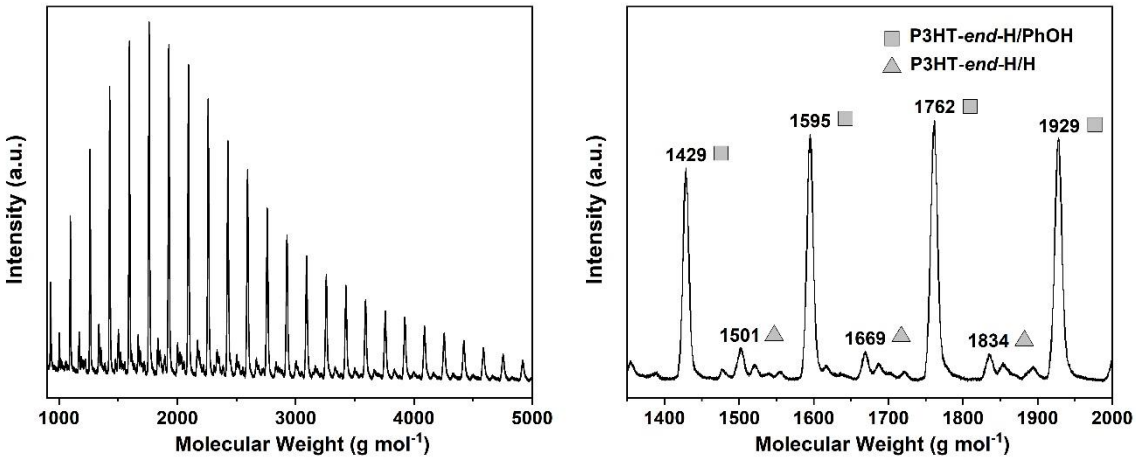


Figure 2.6. MALDI of P3HT-PhOH, full spectra (left) and zoomed in (right).

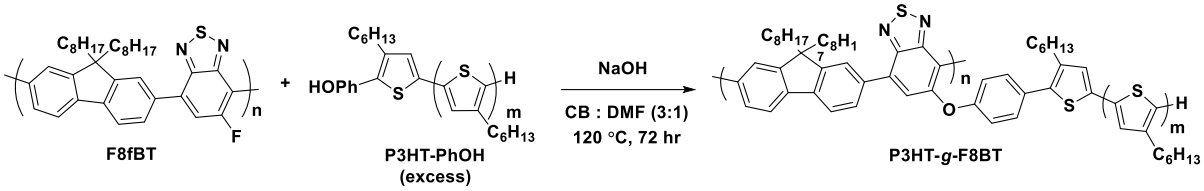
P3HT-PhOH was utilised in subsequent nucleophilic aromatic substitution (S_NAr) reactions, where the nucleophilic hydroxy group on the polymer, stabilised by the phenyl ring, can displace each fluoride atom on a benzothiadiazole (BT) repeat unit in F8fBT.

2.4 Synthesis of graft co-polymer

As mentioned previously, conjugated polymer acceptor, F8fBT, contains a fluorinated benzothiadiazole repeat unit along the backbone. The highly electron withdrawing nature of the benzothiadiazole repeat unit enables the successful displacement of fluorine with nucleophiles in the presence of base, via an S_NAr reaction.[97] In this section, the process of grafting end-functionalised P3HT-PhOH onto F8fBT, to form a fully conjugated graft co-polymer (F8BT-g-P3HT(OPh)), was explored. The graft co-polymer, F8BT-g-P3HT(OPh), comprised of an acceptor polymer backbone (F8BT) and donor polymer sidechains (P3HT).

2.4.1 Synthesis of graft co-polymer

F8BT-g-P3HT(OPh) was synthesised from a base catalysed S_NAr reaction, as shown in Scheme 2.6. Starting polymers F8fBT and an excess of P3HT-PhOH were dissolved in a mixture of chlorobenzene and DMF (3:1) and reacted in presence of 10 equivalents of base (sodium hydroxide) in an inert argon atmosphere at 120 °C for 72 hours. P3HT-PhOH was added in slight excess to encourage maximum displacement of the fluoride along the F8fBT backbone. Progression of the reaction was tracked by periodic GPC measurements. Completion of the reaction was indicated when no change in the measured GPC trace (from the previous measurement) was recorded. Upon completion, the reaction mixture was cooled, precipitated into methanol and filtered before purification by Soxhlet extraction. The polymer was washed with hot methanol and extracted from the Soxhlet thimble by washing with hot chloroform. The solvent was removed, the polymer redissolved, precipitated, filtered and dried to give the crude polymer. Purification by preparative gel permeation chromatography was used to remove excess P3HT-PhOH polymer. After purification, the fractions with isolated polymer product were collected, concentrated down, and reprecipitated to give a fibrous crimson polymer.



Scheme 2.6. General reaction scheme for the synthesis of F8BT-g-P3HT(OPh).

2.4.2 Purification of F8BT-g-P3HT(OPh)

GPC analysis of the crude polymer product showed a bimodal peak, indicating the presence of a high molecular weight and a lower molecular weight polymer. Combined characterisation by GPC and UV-Vis was carried out to identify the composition of the crude polymer, where the GPC trace and corresponding absorption spectra are shown in Figure 2.7. The GPC trace showed two distinct peaks at 14.1 and 16.2 minutes respectively, where a maximum refractive index signal was measured. Recorded elution time range was between 12.8 to 15.2 minutes for the initial signal, and 14.9 to 17.3 minutes for the second signal. Solution absorption spectra was collected for the material at periodic elution times; 13, 14, 15 and 16 minutes. The sample eluted first, at 13 and 14 minutes, displayed an absorption maximum at 450 nm and an additional absorption peak at 320 nm. The measured absorption spectra indicated a modified F8fBT backbone, therefore was assigned as the graft co-polymer F8BT-g-P3HT(OPh). The sample eluted later, at 16 minutes, showed an absorption maximum at 450 nm with no other absorption peaks, indicative of excess P3HT-PhOH. The absorption spectra measured at 15 minutes was found to be a result of the two polymer species eluting at the same time, hence, a superposition of the two spectra measured at 14 and 16 minutes was observed. Further analysis, after purification, was collected to confirm the formation of F8BT-g-P3HT(OPh) and the presence of excess P3HT-PhOH.

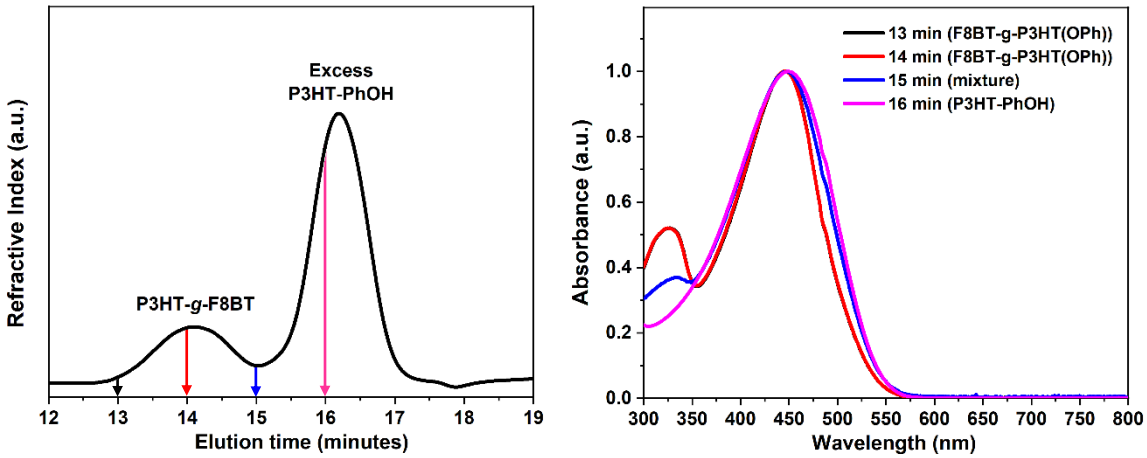


Figure 2.7. GPC trace of crude reaction mixture (left) and corresponding UV-VIS traces of eluted materials (right).

A limited number of methods were available to purify the polymer mixture, compared to purification techniques typically used to purify monomer mixtures. As the mass and overall size of the graft co-polymer was considerably larger than the excess P3HT-PhOH, size exclusion techniques by preparative gel permeation chromatography were considered to

purify the polymer mixture. The crude polymer mixture in chloroform was injected onto the preparative GPC column and cycled once allowing for sufficient separation of the two polymers. Three polymer fractions were collected, the solvent was removed, redissolved, precipitated, filtered and dried to give a fibrous crimson solid (fraction one) and a powdered purple solid (fraction three). The separated polymer fractions were reanalysed by analytical GPC, results are detailed in Table 2.2 and GPC traces are shown in Figure S2.14 and S2.15. The observed M_n for starting polymer F8fBT (43.5 KDa) was found to be slightly higher compared to polymer fraction one (35.4 KDa), containing the graft co-polymer F8BT-g-P3HT(OPh). The observed decrease in M_n could be due to an initial aggregation of F8fBT in chlorobenzene which was reduced after substitution of the P3HT side chains.

Table 2.2. GPC data of starting polymers F8fBT and P3HT-PhOH and polymer fractions post-substitution reaction.

Polymer	M_n (kDa)	M_w (kDa)	DP_n[a]	DP_w[b]	Đ[c]
F8fBT	43.5	76.9	80	142	1.80
P3HT-PhOH	4.2	6.0	25	36	1.42
Polymer fraction 1	35.4	37.6	-	-	1.06
Polymer fraction 2	7.0	7.8	-	-	1.12

[a]Degree of polymerisation calculated from M_n
[b]Degree of polymerisation calculated from M_w
[c]Polydispersity index M_w/M_n

2.5 Characterisation of graft co-polymer

This section details the successful isolation of the graft co-polymer F8BT-g-P3HT(OPh). Successful isolation of the product was confirmed by the comparison of absorption spectra, ^{1}H, ^{19}F and DOSY NMR of starting polymers (un-grafted) polymer with those of the grafted co-polymer. In addition, the electronic and thermal properties of the grafted co-polymer material were evaluated.

2.5.1 Confirmation of graft co-polymer structure by absorption spectroscopy

The UV-Vis absorption spectra for the blended P3HT and F8fBT chains (P3HT:F8fBT (3:1 molar ratio)) and for the graft co-polymer (P3HTg-F8BT(OPh)) were collected. The two absorption spectra, labelled P3HT:F8fBT blend and F8BT-g-P3HT(OPh), are shown in Figure 2.8. It should be noted, the UV-Vis absorption measurements of the crude graft co-polymer mixture (before purification by preparative GPC) was used to compare to the blended mixture, where a known molar ratio of 3:1 was used in the reaction. The absorption spectra for the P3HT:F8fBT blend, showed an absorption maximum at 447 nm and a high energy band absorption with a similar intensity to the maxima at 320 nm. Similarly, the absorption spectra of the crude F8BT-g-P3HT(OPh) showed an absorption maximum at 447 nm. The observed peak at 447 nm appeared broader for F8BT-g-P3HT(OPh), indicating the grafted P3HT chains may provide wider range of absorption. Additionally, the high energy band absorption was also observed at 320 nm, where a reduced intensity compared to the P3HT:F8fBT blend was observed. The reduction in the high energy absorption band can be owed to the displacement of the electron deficient fluoride, on the benzothiadiazole, by the electron donating ether linkage after

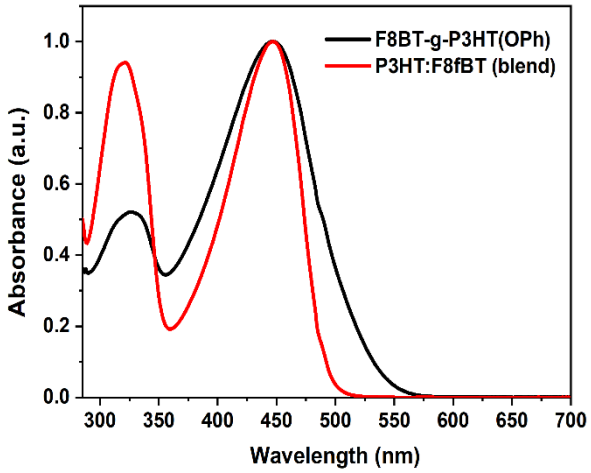


Figure 2.8. UV-VIS absorption spectra of P3HT:F8fBT (blend) and F8BT-g-P3HT(OPh) (crude) in chloroform solution.

substitution of the P3HT-PhOH. After substitution, the benzothiadiazole acceptor unit becomes less electron deficient overall. From the comparison of the two spectra of P3HT:F8fBT blend and F8BT-g-P3HT(OPh) it was clear that the crude mixture was not simply a blended mixture of the two polymers. Preparative GPC was used to purify the polymer mixture, as outlined in Section 2.4.2, to give the graft co-polymer product F8BT-g-P3HT(OPh).

2.5.2 Confirmation of graft co-polymer structure by 1D and 2D NMR

Three NMR techniques were used to confirm the substitution of P3HT sidechains onto F8fBT; ^{1}H and ^{19}F NMR (1D techniques) and DOSY NMR (2D technique). ^{1}H NMR spectra were collected for the starting polymers F8fBT and P3HT-PhOH (referred to as P3HT from the section onwards) and the graft polymer product labelled F8BT-g-P3HT(OPh), shown in Figure 2.9.

For the starting polymer F8fBT, the ^{1}H NMR spectra showed a multiplet signal at δ 7.70 – 8.20 ppm corresponding to the aromatic protons (7H) along the polymer backbone. Additionally, a series of peaks were observed in the aliphatic region corresponding to the alkyl sidechains (34H). The fully assigned spectra can be found in Figure S2.1. For the starting polymer P3HT, a singlet signal at δ 7.00 ppm corresponding to an aromatic proton (1H) along the polymer backbone was observed. Similarly, a series of peaks in the aliphatic region were observed corresponding to the alkyl sidechains (13H). Comparison of the ^{1}H NMR spectra for the starting polymers (F8fBT and P3HT) with F8BT-g-P3HT(OPh) enabled the assignment of the peaks from the F8BT backbone and the P3HT side chains. For the graft co-polymer F8BT-g-

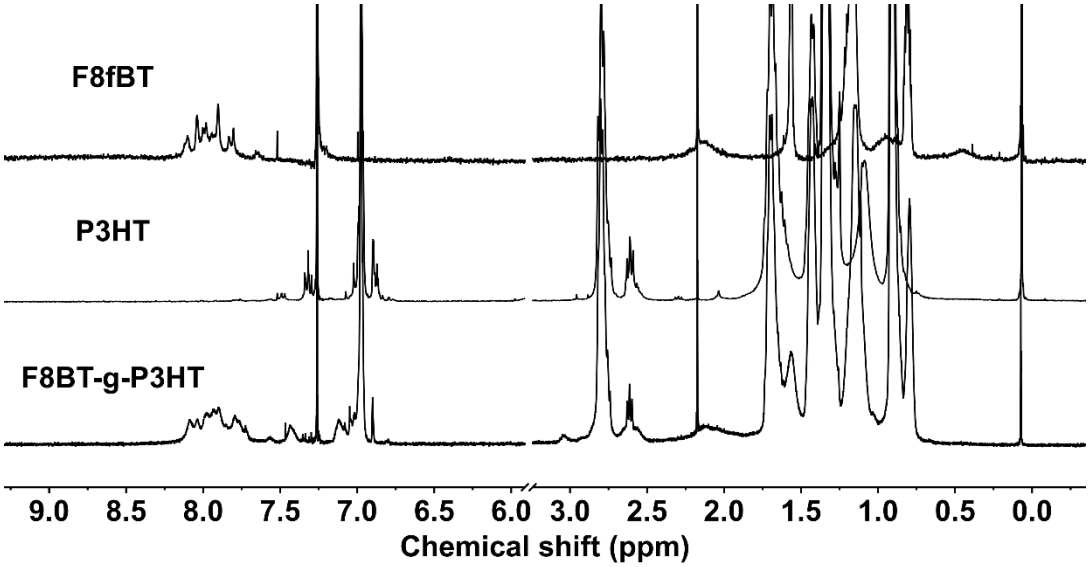


Figure 2.9. ^{1}H NMR of F8fBT, P3HT and F8BT-g-P3HT(OPh).

P3HT(OPh), both multiplet and singlet signals were observed at δ 7.65 – 8.20 ppm and δ 7.00 ppm, corresponding to the aromatic protons along the F8BT backbone (7H) and the P3HT side chains respectively. Low intensity peaks in the aromatic region at δ 7.10 (2H) and 7.45 (2H) ppm, correspond to the -PhO- linker. Using this identifier, it was possible to estimate the grafting efficiency of the reaction. Measured integral values of the signals assigned to the aromatic protons on the -PhO- linker (0.91H and 0.92H) were compared to the theoretical integral values (2H and 2H), hence, the grafting efficiency was estimated to be ca. 46%.

Figures S2.2 and S2.10 show the ^{19}F NMR spectra of starting polymer F8fBT and the graft co-polymer product F8BT-g-P3HT(OPh) respectively. Post-substitution, the signal at δ -114 ppm remained present, confirming the grafting efficiency was below 100%. It was possible that the reaction reached a stage where steric hinderance, from the P3HT chains that are already grafted, becomes so large that new chains cannot access the reactive -F site on the acceptor polymer backbone.[165–167]

Diffusion Ordered Spectroscopy (DOSY) was used to confirm the isolation of F8BT-g-P3HT(OPh) and the successful removal of excess P3HT. From the 2D spectra it was possible to identify the number of polymers species present by evaluating the diffusion coefficient.[85] DOSY spectra, Figure 2.10, shows the DOSY spectra for the P3HT:F8fBT blend and F8BT-g-P3HT(OPh). Defined ^{1}H NMR peaks in the aromatic region were used to analyse the DOSY spectra. For the P3HT:F8fBT blend, peaks associated with the aromatic proton peaks from the P3HT polymer chains and the aromatic proton peaks from the F8fBT polymer chains do not diffuse at the same rate, thus, two diffusion peaks were observed indicating the mixture of P3HT and F8fBT polymer chains. For F8BT-g-P3HT(OPh), the DOSY spectra displayed diffusion

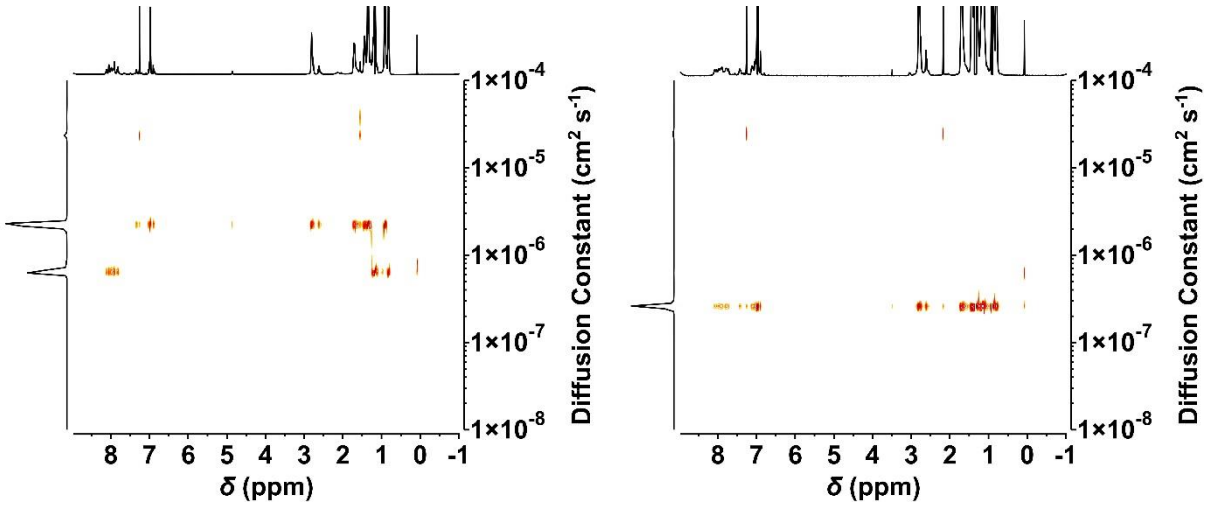


Figure 2.10. DOSY NMR of P3HT:F8fBT blend (left) and F8BT-g-P3HT(OPh) (right).

of the peaks associated with aromatic protons from the P3HT side chains and the F8BT backbone with the same rate as one defined diffusion peak. Furthermore, the measured diffusion constant for F8BT-g-P3HT(OPh) (2.6 x 10^{-7} cm^2s^{-1}) was lower compared to P3HT (2.3 x 10^{-6} cm^2s^{-1}) and F8fBT (6.25 x 10^{-7} cm^2s^{-1}), due to the higher molecular weight of the polymer.[85]

After analysis using combined characterisation techniques: GPC, absorption spectra, ^{1}H NMR, ^{19}F NMR and DOSY NMR, the successful synthesis and isolation of the graft co-polymer structure F8BT-g-P3HT(OPh) was confirmed.

2.5.3 Optical properties

Solution and film absorption spectra were measured for F8BT-g-P3HT(OPh) and the starting polymers P3HT and F8fBT, shown in Figure 2.11. Firstly, the absorption of the polymers in chloroform solutions were evaluated. The starting polymer F8fBT, displayed a maximum absorption at 447 nm and a high energy band absorption at 320 nm. The high energy absorption was assigned to the π- π* transition and the lower energy absorption to intramolecular charge transfer (ICT).[168] For starting polymer P3HT, a maximum absorption at 460 nm, over a wide range from 325 to 580 nm, was measured corresponding to the π- π* intraband transition.[169,170] For the graft co-polymer F8BT-g-P3HT(OPh), a superposition of the two spectra of the starting polymers, F8fBT and P3HT, was observed with a maximum absorption at 441 nm. There was a broadening of the peak at 441 nm compared to F8fBT due to the addition of P3HT sidechains that widen the absorption range of the peak. The high energy band absorption at 320 nm reduced in intensity for F8BT-g-P3HT(OPh) compared to F8fBT due to the increased electron deficiency of the benzothiadiazole acceptor unit.

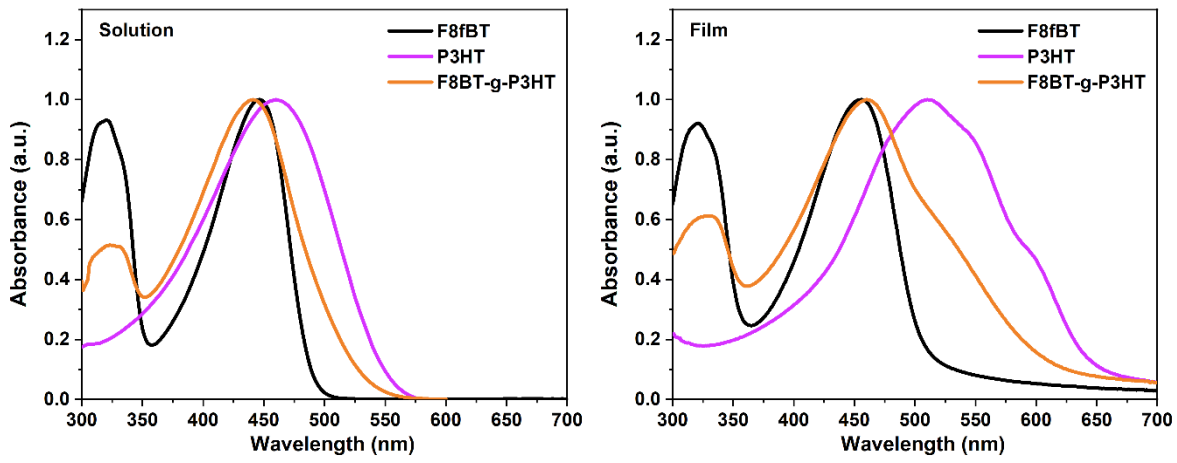


Figure 2.11. UV-VIS absorption spectra of F8fBT, P3HT and F8BT-g-P3HT(OPh) in chloroform solution (left) and as thin films deposited by spin coating onto glass (right).

Thin films of F8fBT, P3HT and F8BT-g-P3HT(OPh) were fabricated from spin casted polymer solutions (in chloroform) onto a glass substrate. Absorption spectra for the polymer thin films were measured, shown in Figure 2.11. A red-shift in the spectra was observed for all three polymers, F8fBT, P3HT and F8BT-g-P3HT(OPh), highlighted by the shift of the λ_{max} to higher wavelengths by 10, 50 and 21 nm respectively, indicative of the solid-state packing. The onset of absorption, from the absorption spectra of the thin films, was used to determine the optical energy bandgap. For F8fBT, P3HT and F8BT-g-P3HT(OPh) the onset of absorption was found to be 509, 642 and 602 nm, corresponding to an optical energy band gap of 2.44, 1.93 and 2.06 eV, respectively. As in the solution absorption spectra, the thin film absorption spectra for F8BT-g-P3HT(OPh) presents as a superposition of the thin film spectra for the starting polymers (F8fBT and P3HT). For this reason, we observe an onset absorption for F8BT-g-P3HT(OPh) (602 nm) between that of F8fBT (509 nm) and P3HT (642 nm), therefore, the optical bandgap energy for F8BT-g-P3HT(OPh) also lies between that of F8fBT and P3HT.

Table 2.3. Optical properties for F8fBT, P3HT and F8BT-g-P3HT(OPh).

Polymer	$\lambda_{abs,max}$ (nm), solution	$\lambda_{abs,max}$ (nm), film	λ_{onset} (nm), film	$E_{g,opt}$[a] (eV)
F8fBT	320, 445	320, 455	509	2.44
P3HT	460	510	642	1.93
F8BT-g-P3HT(OPh)	322, 441	330, 462	602	2.06

[a]Estimated from the onset of absorption from the measured UV-VIS spectra where E = hc/λ

2.5.4 Thermal properties

Thermal Gravimetric Analysis (TGA) and Differential Scanning Calorimetry (DSC) were used to characterise the starting polymers, F8fBT and P3HT, and the graft co-polymer, F8BT-g-P3HT(OPh). For TGA measurements, powdered samples (approx. 2mg) of each polymer were heated in a nitrogen atmosphere from 25 – 750 °C at a rate of 5 °C/min. The thermal stability was determined by the onset of degradation. From the TGA curves, shown in Figure 2.12, the onset of degradation of F8fBT, P3HT and F8BT-g-P3HT(OPh) was found to be 440, 420 and 429 °C respectively. The thermal stability of F8BT-g-P3HT(OPh) (429 °C) was slightly improved in comparison to the starting polymer F8fBT (420 °C). This slight increase could be due to the greater thermal stability of the P3HT side chains and the increased molecular weight of the graft co-polymer.

For DSC analysis, powdered polymer samples (approx. 2 mg) were heated and cooled for three cycles, at a rate of 10 °C/min, in the range of 40 to 400 °C for P3HT and F8BT-g-P3HT(OPh) and 40 to 350 °C for F8fBT. To avoid contamination of the DSC sample chamber a lower temperature maximum of 350 °C was selected for F8fBT, as the TGA showed 5% mass loss below 400 °C. Figure 2.12 shows the DSC curves (cycle 2) for all three polymers.

For P3HT, a broad endotherm was observed in the DSC curve upon heating with a peak value at approximately 145 °C. From previous reports of low molecular weight P3HT, this transition was attributed to a polymer melt.[171] The broad nature of the transition reflects a relatively high dispersity for the low molecular weight P3HT.[172] No clear crystallisation upon cooling was observed under these measurement conditions. For F8fBT, two broad transitions were observed in the DSC curve upon heating at 113 and 248 °C. The first transition at 113 °C was assigned as a glass transition, in agreement with previously reported T_g values for this polymer.[173] The glass transition temperature signifies a phase transition where the polymer properties change of the polymer from brittle to flexible. The broad endothermic transition at 248 °C was indicative of a melting transition.[173] Recrystallisation upon cooling was not observed under these measurement conditions. For the F8BT-g-P3HT(OPh), no endothermic or exothermic transitions were observed representative of an amorphous polymer material.

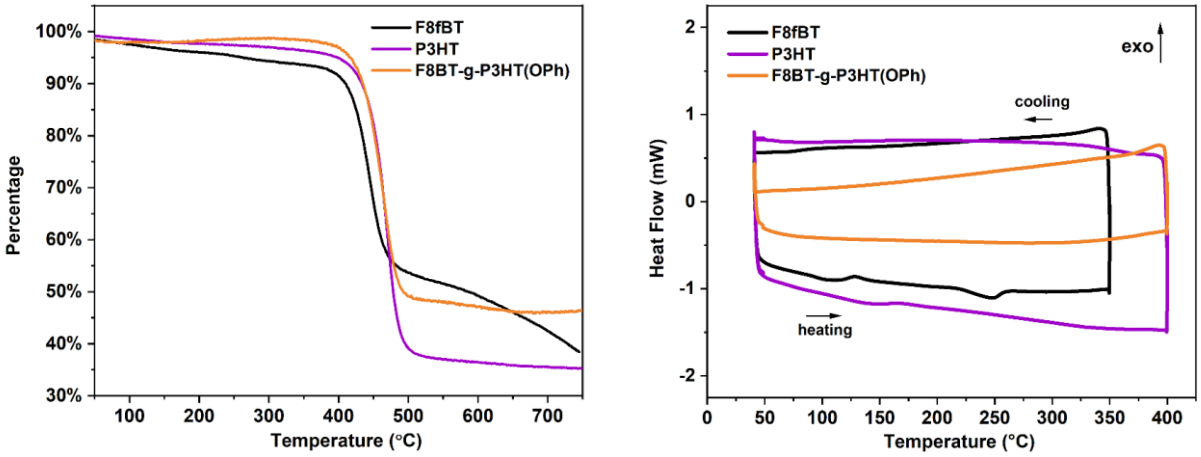


Figure 2.12. TGA (left) and DSC (right, 2nd cycle at 10 °C/min) trace of F8fBT, P3HT and F8BT-g-P3HT(OPh).

2.6 Limitations of using this method

Thus far, successful small-scale synthesis of the graft co-polymer F8BT-g-P3HT(OPh) with a grafting efficiency of approximately 46% has been demonstrated. This section describes some limitations and challenges of developed synthetic method towards graft co-polymer products reported in this chapter.

2.6.1 Low grafting densities

Using the grafting onto synthetic method, a grafting efficiency of approximately 46% was achieved. Two possible reasons for low grafting efficiencies were considered: (a) reduced reactivity of the -PhOH end group or (b) steric strain from the already grafted P3HT chains. To further investigate the reactivity of the -PhOH end group, with hope to improve the grafting efficiency, increasing reaction time and the concentration of base was explored. Both reacting for a longer time and increasing concentration led to lower graft efficiencies or no graft co-polymer formation at all. This was likely due to unwanted side product formation from the decomposition of DMF at high temperatures in the presence of strong base, where the post-polymerisation modification reaction was carried out in DMF in the presence of a NaOH (strong base) at the high temperature of 150 °C. To avoid the degradation of DMF, the use of an alternative polar aprotic solvent such as DMAc was considered, hence, experiments were carried out with a CB:DMAc (3:1) solvent mixture. From the NMR a similar grafting efficiency of approximately 40% was achieved. This observation led to the consideration of alternative end groups for P3HT, allowing the ability to explore milder reaction conditions, as reported in Chapter 3.

2.6.2 Removal of un-grafted polymer

Whilst grafting onto methods towards graft co-polymer structures have many advantages, such as producing polymers with consistent molecular weight in a one-step reaction post-polymerisation, it was important to also consider the disadvantages. The main disadvantage to using a grafting onto method was the purification processes required the removal of unreacted polymer side chains. In this chapter, the successful purification of the graft co-polymer F8BT-g-P3HT(OPh) by preparative GPC separation techniques was reported. Whilst this was a highly effective technique to purify the graft co-polymer on a small scale, purification using preparative GPC would limit the scalability of the synthesis. Solutions to

avoid complex purification methods could consider stoichiometric addition of the polymer side chain, where the polymer is not present in excess and is fully consumed in the reaction. Other routes to avoid complex purification processes include use of other grafting methods: grafting from or grafting through. These methods, however, do also have drawbacks to consider such as lower control over molecular weight distribution and potential formation of other side products that may be difficult to remove.

2.6.3 Scale up end-functionalisation of P3HT

One of the most difficult challenges when using grafting onto methods resides in the circumvention of crosslinking side reactions. Crosslinking reactions result in an insoluble gel with extremely high molecular weight that cannot be processed any further. In this chapter, the small-scale synthesis of F8BT-g-P3HT(OPh) without any crosslinked impurities has been demonstrated. Attempts to synthesise P3HT-Br on larger scales, however, led to the formation of small amounts of Br/Br terminated P3HT, which could not be removed by conventional methods. If the polymer were end-functionalised with a phenol group; the presence of the respective PhOH/PhOH terminated P3HT would result in the initiation of crosslinking reactions, illustrated in Figure 2.13. To eliminate the formation of di functionalised polymer impurities, synthetic routes using end-group initiators could be considered.

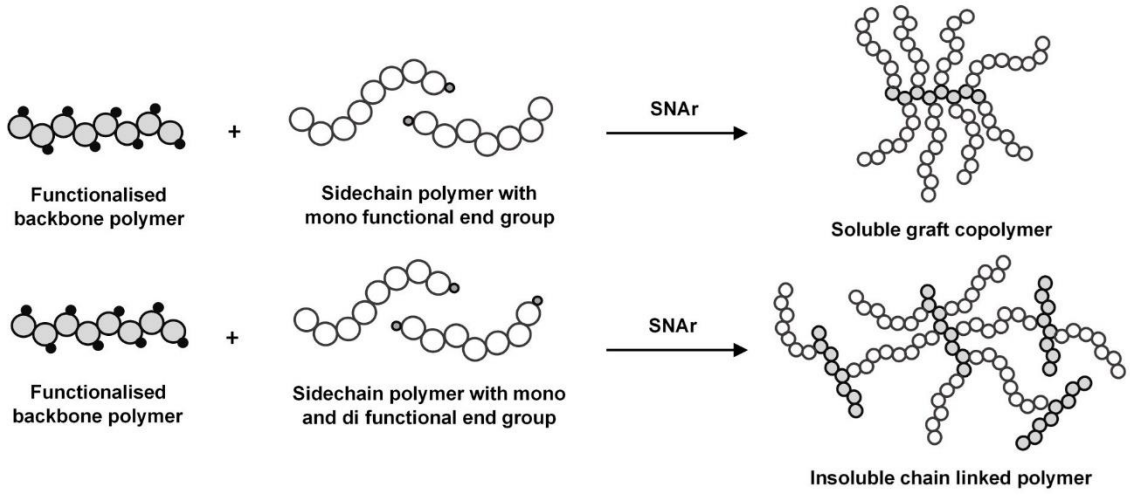


Figure 2.13. Illustration of crosslinking side reactions that could lead to insoluble chain-linked polymers.

2.6.4 Backbone and side chain selection

Formation of a graft co-polymer structures were successfully demonstrated using an F8fBT backbone capable of undergoing S_NAr reactions. The main purpose of this work, to investigate the use of this post-polymerisation modification method to introduce donor polymer sidechains, was achieved. Progression of this work would consider the use of these graft co-polymer materials in OPV devices. Depending on the device application, the properties of the graft co-polymer could be finely tuned by modification of the backbone polymer or the side chain polymer.

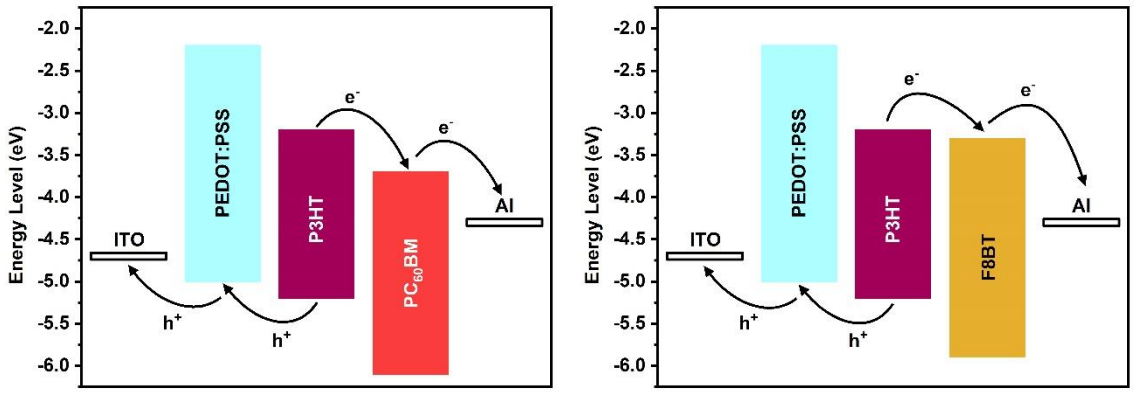
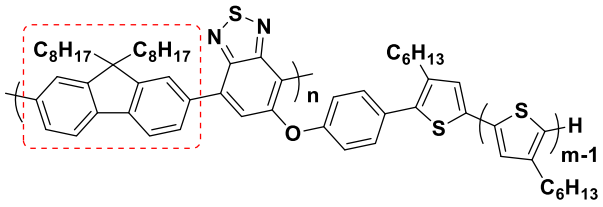


Figure 2.14. Energy level diagram of a generic photovoltaic device with P3HT:PC60BM active layer (left) and with P3HT:F8fBT active layer (right).

Figure 2.14 shows an approximation of energy levels of the materials within a general photovoltaic device with a P3HT:PC_{60}BM active layer and with P3HT:F8fBT active layer. To ensure optimal charge separation in a device, the HOMO and LUMO levels of the acceptor and donor polymers should allow effective transport of holes and electrons respectively, whilst also preventing recombination reactions. In a conventional photovoltaic device, the LUMO of the acceptor material would be lower than the LUMO of donor allowing effective separation of the electrons to the cathode. For the P3HT:PC_{60}BM active layer, the LUMO levels of the materials are approximately -3.2 and -3.7 eV, for P3HT and PC_{60}BM respectively. In comparison for the graft co-polymer, comprised of P3HT side chains and an F8BT backbone, the LUMO levels are approximately -3.2 and -3.3 eV respectively. From this evaluation, it was understood that F8BT may not be an ideal acceptor material in such devices, where the LUMO level is not well aligned at 3.3 eV compared with PC_{60}BM at -3.7 eV. Therefore, future work would consider modifications to the acceptor backbone, for example replacing the 9,9-dioctylfluorene unit, highlighted in Figure 2.15, with a more electron deficient unit.



F8BT-g-P3HT(OPh)

Figure 2.15. Potential co-monomer modification of F8fBT to synthesise new graft co-polymers.

In addition to improving the electronic properties, the backbone or side chain polymers can be modified to optimise properties such as absorbance range, solubility or morphology, for specific applications.

2.7 Conclusion

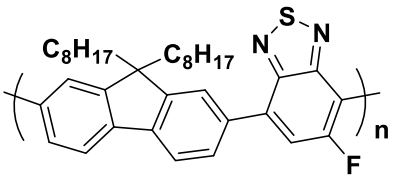
In summary, this Chapter presents a 'grafting onto' method that was used to synthesise a fully conjugated graft co-polymer, containing an acceptor backbone with donor side chains, on a small scale. Using analytical techniques such as: GPC, UV-VIS and DOSY NMR, graft co-polymer structures were confirmed, indicating the successful synthesis and isolation of F8BT-g-P3HT(OPh). A grafting efficiency of 46% was achieved, representative of a 46% substitution of P3HT-PhOH side chains onto an F8fBT polymer backbone. On larger synthesis scales, the emergence of unwanted side products that could potentially initiate crosslinking reactions was observed. This observation highlighted the synthetic route towards P3HT-PhOH was not a trivial route. Considerable optimisation of the synthetic route and purification process should be explored to ensure the elimination of unwanted impurities.

F8BT-g-P3HT(OPh) was comprised of P3HT donor chains and an F8BT acceptor backbone, hence, could be considered for use in applications in solar cell, OLED and OFET devices, where the material can act as an all-polymer organic photovoltaic active layer. Some potential limitations of the material F8BT-g-P3HT(OPh) as an active layer in an OPV device have been identified and simple modifications to tune the properties of the graft co-polymer have been briefly discussed. Post-polymerisation modification via S_NAr has the potential to be used with a range of backbone polymers, with a monofluoro benzothiadiazole (BTf) moiety, and side chain polymers, with a thiol, thioacetate or alcohol end group, to synthesise a wide range of graft co-polymer structures via a 'graft onto' method. Therefore, it is of strong interest to continue exploration of this synthesis towards new graft co-polymer structures.

2.8 Experimental

Synthesis of F8fBT polymer

as prepared according to a modified procedure of Adam Creamer et al.[97]

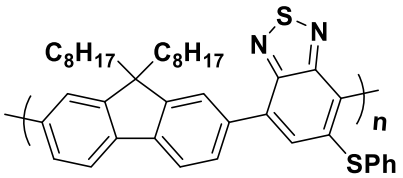


In a dry 100 mL round bottom flask under nitrogen, 9,9-dioctylfluorene-2,7-diboronic acid bis(pinacol) ester (2.39 g, 3.72 mmol), 4,7-dibromo-5-fluoro-2,1,3-benzothiadiazole (1.16 g, 3.72 mmol) and tetrakis(triphenylphosphine) palladium(0) (86 mg, 0.07 mmol) were added and degassed with nitrogen. To the solid mixture degassed toluene (32 mL) with on drop of aliquot 336 and degassed aqueous 2 M Na_2CO_3 (20 mL) were added before the solution was heated to reflux for 72 h. After the reaction was cooled to room temperature and the mixture was precipitated into methanol. The precipitate was filtered into a Soxhlet thimble and washed (Soxhlet) with methanol, acetone and hexane (in that order) and the final product was extracted into chloroform. After extraction, the solvent was removed using a rotary evaporator. The product was dissolved in the minimum amount of chlorobenzene (approx. 5 mL) and precipitated into methanol (approx. 500 mL). The precipitate was collected by vacuum filtration through a nylon pad (pore size 20 µm), washed with methanol and acetone then dried. The dry product was collected in a vial and further dried under vacuum. The product obtained was a yellow solid (1.41-1.99g, 70–99% yield).

^{1}H NMR (400 MHz, $CDCl_3$): δ 8.20-7.80 (m, 7H, H_{ar}), 2.13(m, 4H, CH2), 1.20–1.15 (m, 20H, CH2), 0.96 (s, 4H, CH2), 0.85–0.75 (m, 6H, CH3) ppm. ^{19}F NMR (377 MHz, $CDCl_3$): δ -114.51 ppm. GPC (80 °C, chlorobenzene, vs PS): M_n = 43 kDa, M_w = 76 kDa, PDI = 1.8.

Synthesis of F8(SPh)BT polymer

as prepared according to a modified procedure of Adam Creamer et al.[97]

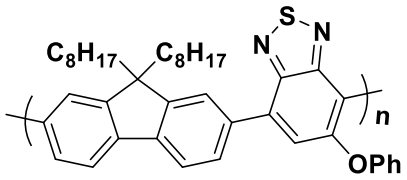


To a 20 mL microwave vial under nitrogen, F8fBT (10 mg, 0.018 mmol), thiophenol (5 uL, excess) and K_2CO_3 (25 mg, 0.18 mmol) were added, sealed with a septum, and degassed. To the degassed solid mixture anhydrous chlorobenzene (1.5 mL) and DMF (0.5 mL) were added and degassed for a further 10 minutes. The solution was heated to 120 °C and stirred at this temperature for 72 hours. After cooling to room temperature, the mixture was precipitated into methanol and filtered into a Soxhlet thimble. The product was washed (Soxhlet) with methanol, acetone and hexane (in that order) before the product was extracted into chloroform. After extraction, the solvent was removed using a rotary evaporator. The product was dissolved in the minimum amount of chlorobenzene (approx. 5 mL) and precipitated into methanol (approx. 500 mL). The precipitate was collected by vacuum filtration through a nylon pad (pore size 20 µm), washed with methanol and acetone then dried. The dry product was collected in a vial and further dried under vacuum. The product obtained was a yellow solid.

^{1}H NMR (400 MHz, $CDCl_3$): δ 8.10-7.30 (m, 12H, H_{ar}), 2.30-1.70(m, 4H, CH2), 1.30–0.85 (m, 24H, CH2), 0.85–0.70 (m, 6H, CH3) ppm. ^{19}F NMR (377 MHz, $CDCl_3$): No signal observed. GPC (80 °C, chlorobenzene, vs PS): M_n = 36.8 kDa, M_w = 83.4 kDa, PDI = 2.3.

Synthesis of F8(OPh)BT polymer

as prepared according to a modified procedure of Adam Creamer et al.[97]

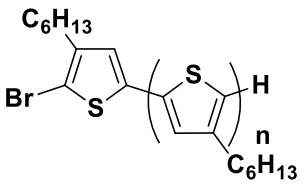


To a 20 mL microwave vial under nitrogen, F8fBT (10mg, 0.018 mmol), phenol (6mg, 0.054 mmol) and NaOH (7.2 mg, 0.18 mmol) were added, sealed with a septum, and degassed. To the degassed solid mixture anhydrous chlorobenzene (1.5 mL) and DMAc (0.5 mL) were added and degassed for a further 10 minutes. The solution was heated to 120 °C and stirred at this temperature for 72 hours. After cooling to room temperature, the mixture was precipitated into methanol and filtered into a Soxhlet thimble. The product was washed (Soxhlet) with methanol, acetone and hexane (in that order) before the product was extracted into chloroform. After extraction, the solvent was removed using a rotary evaporator. The product was dissolved in the minimum amount of chlorobenzene (approx. 5 mL) and precipitated into methanol (approx. 500 mL). The precipitate was collected by vacuum filtration through a nylon pad (pore size 20 µm), washed with methanol and acetone then dried. The dry product was collected in a vial and further dried under vacuum. The product obtained was a yellow solid.

^{1}H NMR (400 MHz, $CDCl_3$): δ 8.00-7.60 (m, 7H, H_{ar}), 7.31 (d, 2H, $H_{Ph(a)}$), 7.04 (m, 3H, $H_{Ph(b)}$), 2.10-1.70(m, 4H, CH2), 1.20–1.15 (m, 20H, CH2), 0.96 (s, 4H, CH2),0.85–0.75 (m, 6H, CH3) ppm. ^{19}F NMR (377 MHz, $CDCl_3$): No signal observed. GPC (80 °C, chlorobenzene, vs PS): M_n = 43.6 kDa, M_w = 86.3 kDa, PDI = 2.0.

Synthesis of P3HT-Br polymer

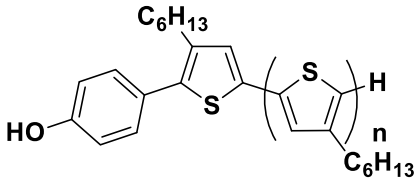
as prepared according to a modified procedure of Mukundan Thelakkat et al.[161]



To a 100mL dry 2-neck flask under argon, 2,5-dibromo-3-hexylthiophene (6.0 g, 18.4 mmol) an internal standard (hexadecane) and 0.5M LiCl in THF (40 mL) at room temperature was added and degassed before adding 1.4M ^{n}BuMgCl in THF (12.8 mL, 17.9 mmol). The reaction mixture was stirred at room temperature for 2-3 hours. Every hour an aliquot (<0.1 mL) was taken out and directly quenched into water before ethyl acetate as added. The organic phase was collected and filtered before analysis by GCMS, was used to quantify the degree of conversion to the active monomer, where the unreacted starting monomer (2,5-dibromo-3-hexylthiophene) was found to be present in quantities approximately less than 5%. Ni(dppp)Cl_2 (50 mg, 0.9 mmol) was added 0 °C and the reaction proceeded for 1 hour. The reaction was quenched with 5M HCl (20 mL) before the mixture was brought to room temperature, precipitated in methanol and filtered into a Soxhlet thimble. The filtered product was washed (Soxhlet) with methanol and acetone, and the final product was extracted into chloroform. After extraction the solvent was removed using a rotary evaporator. The product was dissolved in the minimum amount of chlorobenzene (approx. 10 mL) and precipitated into methanol (approx. 500 mL). The precipitate was collected by vacuum filtration through a nylon pad (pore size 20 μm), washed with methanol and dried. The dry product was collected in a vial and further dried under vacuum. The product obtained was a dark purple solid (2.46 g, 80% yield).

^{1}H NMR (400 MHz, $CDCl_3$): δ 6.98 (s, 1H, H_{ar}), 2.80 (t, *J* = 7.56 Hz, 2H, α-CH2), 1.80-1.50 (m, 2H, β-CH2), 1.50-1.20 (m, 6H), 1.0-0.8 (m, 3H, CH3) ppm. GPC (80 °C, chlorobenzene, vs PS): M_n = 2930 Da, M_w = 3908 Da, PDI = 1.3.

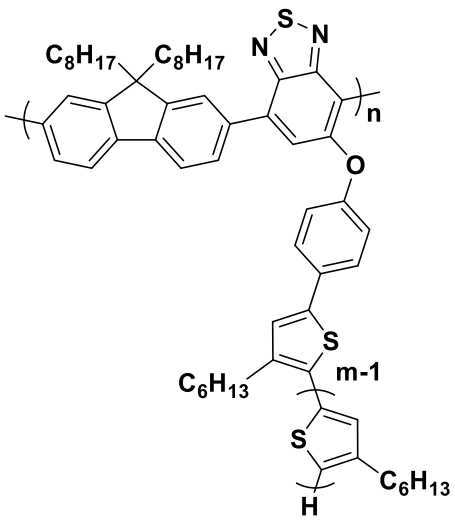
Synthesis of P3HT-PhOH polymer



In a 100 mL dry 2-neck flask under argon P3HT-Br (210 mg, 0.05 mmol), 4-hydroxyphenylboronic acid pinacol ester (288 mg, 1.33 mmol) and tetrakis(triphenylphosphine)palladium(0) (15 mg, 0.013 mmol) were added and degassed. To the solid mixture, toluene (25 mL) with one drop of aliquat 336 was added and degassed for a further 10 minutes. The solution was heated to 110 °C and an aqueous solution of 2M K_2CO_3 (6mL) was added dropwise. The reaction was stirred at 110 °C for 12 hours. The mixture was cooled to room temperature, precipitated in methanol and filtered into a Soxhlet thimble. The filtered product was washed (Soxhlet) with methanol before the product was extracted into chloroform. After extraction the solvent was removed using a rotary evaporator. The product was dissolved in the minimum amount of chlorobenzene (approx. 1 mL) and precipitated into methanol (approx. 50 mL). The precipitate was collected by vacuum filtration through a nylon pad (pore size 20 µm), washed with methanol and dried. The dry product was collected in a vial and further dried under vacuum. The product obtained was a dark purple solid (203 mg, 96% yield).

^{1}H NMR (400 MHz, $CDCl_3$): δ 6.98 (s, 1H, H_{ar}), 2.80 (t, *J* = 7.56 Hz, 2H, α-CH2), 1.80-1.50 (m, 2H, β-CH2), 1.50-1.20 (m, 6H), 1.0-0.8 (m, 3H, CH3) ppm. GPC (80 °C, chlorobenzene, vs PS): M_n = 3670 Da, M_w = 5390 Da, PDI = 1.5.

Synthesis of F8BT-g-P3HT(OPh) polymer



To a 20 mL microwave vial under argon, P3HT-PhOH (177 mg, 0.04 mmol), F8fBT (20 mg, 0.037 mmol) and NaOH (92 mg, 2.30 mmol) were added and degassed with argon for 20 minutes. To the solid mixture chlorobenzene (6 mL) and DMF (2 mL) were added and degassed for a further 10 minutes. The solution was heated to 120 °C and stirred at this temperature for 72 hours. The reaction was cooled to room temperature, precipitated in methanol and filtered into a Soxhlet thimble. The filtered product was washed (Soxhlet) with methanol and acetone before the product was extracted into chloroform. After extraction the solvent was removed using a rotary evaporator. The product was dissolved in the minimum amount of chlorobenzene (approx. 0.5 mL) and precipitated into methanol (approx. 100 mL). The precipitate was collected by vacuum filtration through a nylon pad (pore size 20 µm), washed with methanol and dried. The crude product was dissolved in chloroform (< 5 mL), purified by preparative GPC, collected, concentrated down, precipitated into methanol, collected in a vial and dried under vacuum. The product obtained was a deep red solid (53 mg, undetermined% yield).

^{1}H NMR (400 MHz, $CDCl_3$): δ 8.20-7.80 (m, 7H, F8BT-H_{ar}), 6.98 (s, 8H, P3HT-H_{ar}), 2.90-2.50 (m, 14H, P3HT-α-CH2), 1.75-0.70 (m, 111 H, P3HT and F8BT alkyl chain protons) ppm. ^{19}F NMR (377 MHz, $CDCl_3$): -114.51 ppm. GPC (80 °C, chlorobenzene, vs PS): M_n = 35.4 kDa, M_w = 37.6 kDa, PDI = 1.1.

2.9 Appendix Chapter 2 - list of figures

All supplementary figures for Chapter 2 are presented in the Appendix (Chapter 8).

Figure S2.1. ^{1}H NMR of F8fBT.

Figure S2.2. ^{19}F NMR of F8fBT.

Figure S2.3. ^{1}H NMR of F8BT-SPh.

Figure S2.4. ^{19}F NMR of F8BT-SPh.

Figure S2.5. ^{1}H NMR of F8BT-OPh.

Figure S2.6. ^{19}F NMR of F8BT-OPh.

Figure S2.7. ^{1}H NMR of P3HT-Br.

Figure S2.8. ^{1}H NMR of P3HT-PhOH.

Figure S2.9. ^{1}H NMR of F8BT-g-P3HT(OPh).

Figure S2.10. ^{19}F NMR of F8BT-g-P3HT(OPh).

Figure S2.11. GPC trace of P3HT-Br.

Figure S2.12. GPC trace of P3HT-PhOH.

Figure S2.13. GPC trace of F8BT-g-P3HT(OPh) crude.

Figure S2.14. GPC trace of F8BT-g-P3HT(OPh) fraction 1, post-purification.

Figure S2.15. GPC trace of F8BT-g-P3HT(OPh) fraction 3, post-purification.

Figure S2.16. UV-Vis absorption spectra for F8fBT, F8BT-SPh, F8BT-OPh, P3HT and F8BT-g-P3HT(OPh) in solution (left) and thin film (right).

Figure S2.17. TGA curve of F8fBT.

Figure S2.18. TGA curve of P3HT-PhOH.

Figure S2.19. TGA curve of F8BT-g-P3HT(OPh).

Figure S2.20. DSC curve of F8fBT.

Figure S2.21. DSC curve of P3HT-PhOH.

Figure S2.22. DSC curve of F8BT-g-P3HT(OPh).

3 Chapter 3: Development of synthetic methods towards conjugated graft co-polymers utilising post-polymerisation modification

3.1 Introduction

A wide range of all-polymer organic solar cells (OSCs) have been explored in recent years.[11,58,174] Advantages to using all-polymer OSCs, rather than blends of polymers and small molecules, can include improved blend stability, good ink rheology as well as their lightweight and flexible properties.[32,175,176] Photovoltaic devices have been designed, investigated and developed with a variety of different polymer compositions and architectures. Examples of all-polymer OSCs have been reported using blends of p- and n-type polymers, block co-polymers comprising chemically linked p- and n-type polymers and brush or graft co-polymers.[6,177–180] The many examples of all-polymer OSCs highlight the importance of controlling the thin film morphology of the active layer, in order to maximise device performance, where exciton diffusion is limited to approximately 10-20 nm.[142] Researchers have investigated graft and brush co-polymer structures with the aim to minimise instability associated with thin film morphology, due to macro/microphase separation or unpredictable morphology formations.[180] Furthermore, graft co-polymer structures have been shown to improve overall stability within electronic devices.[181]

All-polymer graft co-polymer structures typically consist of a backbone polymer with covalently attached polymer sidechains. Typically polymer designs with an acceptor backbone and donor polymer grafts have been explored.[154] Graft co-polymers can be synthesised via three main strategies; grafting through, grafting from and grafting onto. Whilst there are many examples of non-conjugated or partially conjugated (backbone or side chain) graft co-polymers synthesised via all three strategies, there are only few examples of conjugated (both backbone and sidechain) all-polymer graft co-polymers.[154] Grafting through and grafting from methods have been largely employed to synthesise all-polymer conjugated graft co-polymer structures.[156,179,180,182] Utilising these methods it is possible to synthesise well-defined and intricate polymeric structures, however, challenges such as complexity of reactions and versatility are often associated with grafting through and grafting from methods. Alternatively

grafting onto methods could be used as a straight-forward approach towards conjugated all-polymer graft co-polymer structures. Additionally grafting onto methods allows access to graft co-polymer series synthesised from backbone polymers and sidechains with consistent molecular weight and dispersity, hence, providing the possibility to tune physical and optoelectronic properties with good control. Despite the key benefits of the grafting onto methods, it is not yet widely used due to limited examples of conjugated backbone polymers and end-functionalised conjugated sidechain polymers that can undergo further post-polymerisation modification towards graft co-polymers.

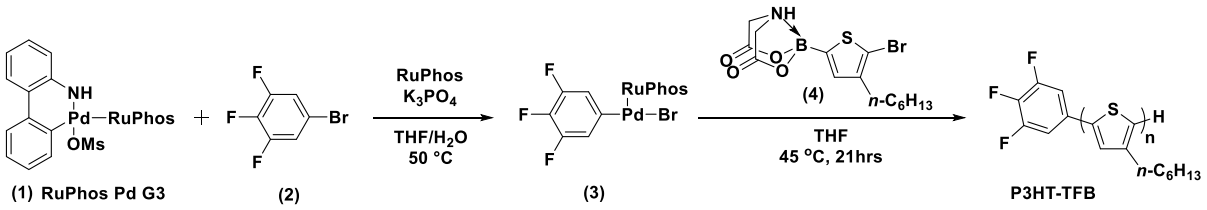
Poly(3-hexylthiophene) (P3HT) has persistently grasped the interest of researchers and has been broadly studied due to a range of properties, including its relative high hole-mobility, stability and visible light absorption range. [183–186] As P3HT has been so widely studied for a range of applications there are many examples reporting selectively end-functionalised P3HT.[80,159,161,187,188] Tae-Lim Choi's group have developed a unique synthesis of P3HT via Suzuki-Miyaura catalyst-transfer polycondensation (SCTP).[80] The optimised synthesis utilises a carefully designed monomer 5-bromo-4-n-hexylthien-2-yl-MIDA-boronate and precatalyst RuPhos Pd G3 to obtain P3HTs with excellent molecular weight control and high degree of polymerisation (DP) in respectable yields.[188] Furthermore, using externally initiated SCTP methods gave access to a wide range of end-functionalised P3HTs with high fidelity. End-fuctionalised P3HTs have been developed and further functionalised towards bio-sensors, crosslinkable polymers, diblock co-polymers or graft co-polymers for example.[120,189,190]

Grafting onto methods typically involve the use of 'click-reactions' that minimise the formation of unwanted byproducts. Copper catalysed azide-alkyne cycloaddition (CuAAC) has been the predominantly reported click-reaction towards conjugated all-polymer graft co-polymers.[95,191,192] Previous reported work, conducted within the group, used nucleophilic aromatic substitution (S_NAr) as a post-polymerisation modification technique towards a wide range of functional polymers.[97] Reports include examples of non-conjugated all-polymer graft co-polymer synthesised via S_NAr.[104] Herein, further investigation of post-polymerisation modification via S_NAr is reported as a straightforward method to synthesise graft co-polymers with an n-type backbone and p-type sidechains. The flexibility of S_NAr was explored as a grafting onto technique, as well as, a technique to further end-functionalise polymer sidechains. The work endeavored to expand the library of end-functionalised P3HTs, using

SCTP enabled control over chain end-groups, molecular weight, regioregularity and polydispersity index. Moreover, the versatility of the grafting onto technique and the ability to straight-forwardly tune physical and optoelectronic properties was explored.

3.2 Synthesis of end functionalised polymers

Previously reported research conducted by Boufflet *et.al.* showed P3HT end-capped with a pentafluorobenzene (PFB) end-group could be prepared via the Grignard Metathesis (GRIM) polymerisation.[120] In this case, a mixture of 2,5-dibromo-3-hexylthiophene was treated with one equivalent of an alkyl Grignard reagent, and the resulting mixture of aryl Grignards was polymerised by the addition of a Ni(II) initiator and catalyst. Termination of the polymerisation by the addition of perfluorophenylmagnesium bromide led to a predominately PFB end-capped polymer. Although subsequent fluoride displacement reactions were demonstrated, the end-capping procedure was imperfect and resulted in approximately 35% of polymer without a PFB group. As such, alternative polymerisation procedures based on Suzuki-Miyaura catalyst-transfer (SCTP) were investigated. Furthermore, multiple fluoride displacements on the PFB end group with reactive thiols were demonstrated with specific reaction conditions. Trifluorobenzene (TFB) was selected as an end-group for fluoride displacement reactions to avoid multiple fluoride displacement reactions. So far, end-capped P3HT with TFB has not been reported in the literature.

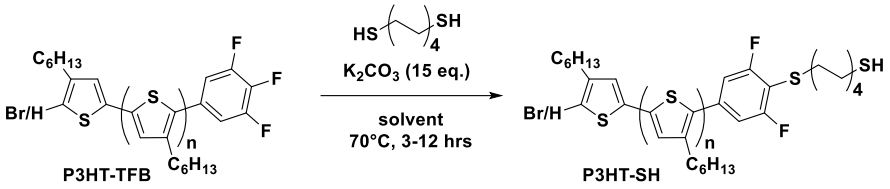


Scheme 3.1. Synthesis of P3HT-TFB via SCTP.

Initiator RuPhos-Pd(II)-(1,2,3-trifluorobenzene)-Br (3), monomer 5-bromo-4-n-hexylthien-2-yl-MIDA-boronate (4) and polymer P3HT-TFB were synthesised by collaborator Hyunwoo Park. Initiator RuPhos-Pd(II)-(1,2,3-trifluorobenzene)-Br (3) was synthesised according to the modified reported procedure.[80] Monomer 5-bromo-4-n-hexylthien-2-yl-MIDA-boronate (4) was synthesised according to a previously reported procedure.[80]

Using an SCTP procedure, P3HT-TFB was synthesised by reaction of initiator (3) with monomer (4). Initiator RuPhos-Pd(II)-(1,2,3-trifluorobenzene)-Br (3) was generated by reacting catalyst

RuPhos Pd G3 (1) with 1-Bromo-3,4,5-trifluorobenzene (2), RuPhos and tripotassium phosphate at 50 °C for 1 hour in THF/water. Initiator RuPhos-Pd(II)-(1,2,3-trifluorobenzene)-Br (3) was used in-situ, where a solution 5-bromo-4-n-hexylthien-2-yl-MIDA-boronate (4) (M/I ratio 15/1) in THF was added to the reaction mixture and heated to 45 °C for 21 hours. The polymerisation reaction was complete after 21 hours and the reaction mixture was precipitated into methanol, collected by filtration, washed with methanol, and dried to afford a deep purple solid in a yield of 88%. Optimised conditions for the controlled polymerisation of P3HT via SCTP used a monomer to initiator (M/I) ratio of 15/1 to afford P3HT-TFB with: M_n of 2.1 kDa, high yield (88%), narrow PDI (1.3) and good control of the end-groups (TFB/H).



Scheme 3.2. Post-polymerisation modification of P3HT-TFB with 1,8-octanedithiol.

With end-functionalised P3HT-TFB in hand, selective conversion to an end-group bearing a free thiol group was required. Therefore, nucleophilic aromatic substitution reactions (S_NAr) on the trifluorobenzene end-group (TFB) were investigated. Typically, S_NAr reactions on fluorinated aromatics are activated by the adjacent (*ortho*-position) fluorine substituents. Therefore, it was expected that the fluorine in the *para*-position would be most reactive, activated by two adjacent fluorine groups.[193] It was noted that similar reactions on poly(3-octylthiophene) end-capped with PFB have demonstrated mono substitution in the *para*-position.[120]

Therefore P3HT-TFB was reacted with an excess of commercially available 1,8-octanedithiol in the presence of K_2CO_3 in THF/DMF (4:1) at 70 °C under an inert nitrogen atmosphere. The reaction progress was monitored by MALDI-TOF, where a small sample was extracted, precipitated, washed with acetone and redissolved in the matrix (terthiophene in THF (10mg/mL)). The reaction was complete after three hours and the mixtures were precipitated into methanol and washed immediately with hot acetone to remove excess 1,8-octanedithiol, which could polymerise upon oxidation. Further purification by preparative Size Exclusion Chromatography was performed to ensure the removal of residual 1,8-octanedithiol. Finally, the polymer was reprecipitated from chloroform into methanol, filtered and dried to afford a deep purple solid, P3HT-SH, in a yield of 74%.

The S_NAr reaction was found to be sensitive to the DMF concentration where the TFB end-group was susceptible to multiple substitutions. Boufflet *et. al.* previously reported the use of DMF to promote similar S_NAr reactions, where changing solvents from THF to DMF was shown to promote tri-substitution onto the PFB end-group instead of mono-substitution.[120] Performing the S_NAr reaction on P3HT-TFB in pure THF led to an incomplete reaction after 12 hours, where peaks corresponding to P3HT-TFB were observed in the MALDI spectra. Increasing the DMF content to 1:1 THF/DMF resulted in the formation of mono-substituted and di-substituted polymer products, observed in the MALDI spectra, within 3 hours of reaction. When the quantity of DMF was lowered to 4:1 THF/DMF, where selective mono-substituted polymer products were observed in the MALDI spectra within 3 hours of reaction. Under the optimised S_NAr reaction conditions, after careful degassing of the reaction mixture with nitrogen, the P3HT-SH appeared stable to oxidation and subsequent disulfide bond formation, where P3HT-S-S-P3HT was not observed in the MALDI spectra or GPC trace of the final product.

3.2.1 End-group analysis by MALDI

Full conversion of P3HT-TFB to P3HT-SH was initially confirmed by MALDI-TOF, as shown in Figure 3.1. The signals were shifted by approximately 158.3 $gmol^{-1}$ corresponding to the displacement of fluoride on the TFB end group with 1,8-octanedithiol. For P3HT-TFB, the signal at 1790.7 $gmol^{-1}$ is associated with a decamer of the P3HT repeat unit (166 $gmol^{-1}$) plus a proton and TFB end group. For P3HT-SH, the signal at 1946.9 $gmol^{-1}$ is associated with an decamer of the P3HT repeat unit (166 $gmol^{-1}$) plus the proton and 8-((2,6-

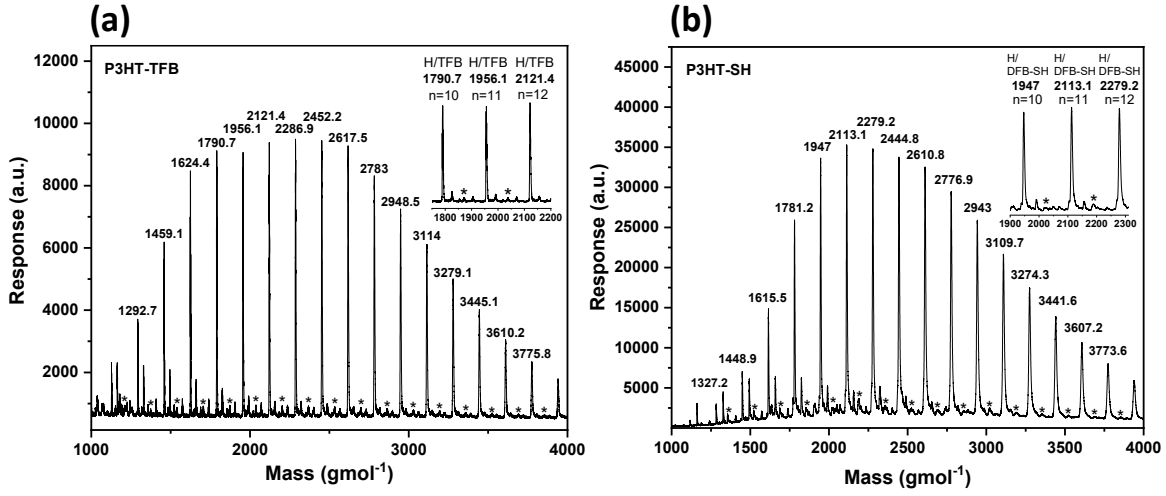


Figure 3.1. MALDI-TOF spectra of (a) P3HT-TFB and (b) P3HT-SH.

difluorophenyl)thio)octane-1-thiol (DFB-SH) end group. A closer look at the lower molecular weight region in the MALDI spectra for P3HT-TFB reveals lower intensity peaks related to P3HT terminated with H/H and H/Br. Polymers terminated with H/H and H/Br did not react under S_NAr conditions and identical peaks were observed in the MALDI spectra for P3HT-SH. Additionally, small amounts of P3HT terminated with Br/TFB were found where the end groups were converted to Br/DFB-SH when reacted under S_NAr conditions. Peaks corresponding to P3HT terminated with Br/TFB and Br/DFB-SH are highlighted with an Asterix (*) in the MALDI spectra (Figure 3.1) for P3HT-TFB and P3HT-SH respectively. Most importantly no di-funtionalised polymer chains, with TFB/TFB or DFB-SH/DFB-SH were observed in the MALDI data.

3.2.2 End group analysis by ^{1}H NMR

Successful substitution onto the TFB end group was further confirmed by ^{1}H NMR, shown in Figure 3.2. In the spectra for P3HT-TFB, the multiplet found at δ 7.15-7.20 ppm corresponds to the two protons (H_{TFB}) on the TFB end-group, which couple to the fluoro substituents. The signal from the aromatic proton (H_e) from the 3-hexylthiophene repeat unit directly adjacent to the TFB end-group appeared as a singlet at δ 7.09 ppm. On the other side of the polymer chain, the terminal proton (H_a) on the end 3-hexylthiophene unit has a signal at δ 6.92 ppm. The final key identifying signal for the terminal 3-hexylthiophene was the signal from the α-methylene protons at δ 2.61 ppm. In the ^{19}F NMR two distinct signals were observed, a doublet at δ -133.79 ppm and a triplet at δ -161.79 ppm.

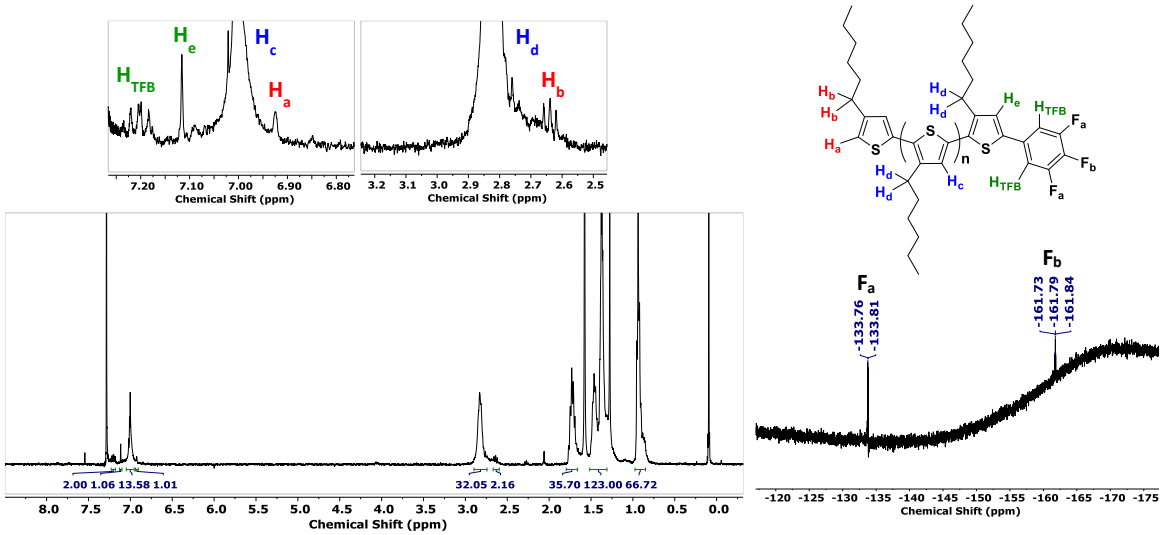


Figure 3.2. ^{1}H NMR (left) and ^{19}F NMR (right) of P3HT-TFB.

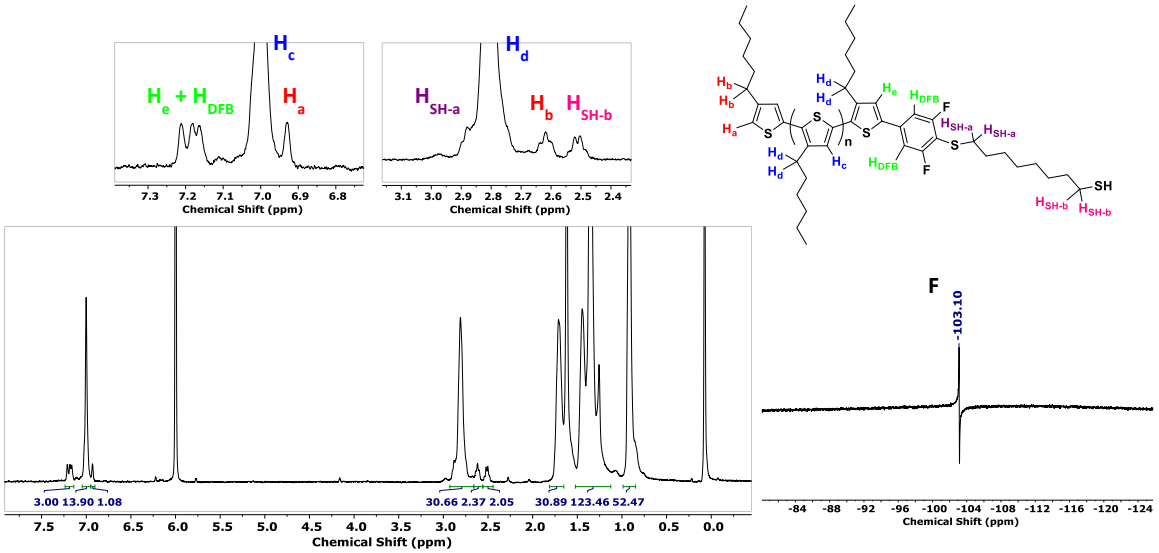


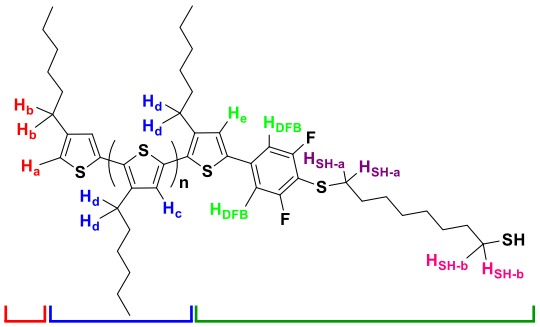
Figure 3.3. ^{1}H NMR (left) and ^{19}F NMR (right) of P3HT-SH.

Upon displacement of the fluoride on the TFB end-group with 1,8-octanedithiol, signals at δ 7.15-7.20 ppm and δ 7.09 ppm, corresponding to the two protons (H_{DFB}) on the DFB-SH end group and the proton (H_e) on the 3-hexylthiophene repeat unit directly adjacent to the DFB-SH end-group were observed in the ^{1}H NMR spectra for P3HT-SH (Figure 3.3). Post-substitution, the signals from H_{DFB} and H_e in the ^{1}H NMR spectra for P3HT-SH were shifted slightly downfield compared to the signals from H_{TFB} and H_e in the ^{1}H NMR spectra for P3HT-TFB. Another key indication of the substitution was the emergence of new peaks at δ 2.87 and δ 2.81 ppm associated with the α- and θ-methylene protons (H_{SH-a} and H_{SH-b}) on the dithiol end-chain. The ^{19}F NMR for P3HT-SH showed only one singlet peak at δ -103.10 ppm indicating mono-substitution at the *para*-position of dithiol onto the TFB end group.

3.2.3 Molecular weight characterisation

Thus far, in this section, the use of a lower molecular weight P3HT batch has been shown to facilitate the use of end-group analysis by ^{1}H NMR and mass spectrometry (MALDI). Furthermore, due to the low molecular weight and narrow polydispersity of the P3HT materials, it was possible to estimate average molecular weight values for P3HT-TFB and P3HT-SH from ^{1}H NMR and MALDI data as well as size exclusion chromatography (SEC).[83,194] All molecular weight data has been summarisied in Table 3.1.

From ^{1}H NMR spectra, M_n values of P3HT-TFB and P3HT were estimated by comparison of the integration values for the signals associated with identifiable end-group protons with those from the repeating monomer unit. Using the measured integration values, it was possible to



terminal proton + n(P3HT rep. unit) + terminal thiophene unit and DFB-SH

Formula:	**1.01**	**+**	**n(166.30)**	**+**	**423.65**	**gmol^{-1}**
M_n (P3HT-SH):	**1.01**	**+**	**13.90(166.30)**	**+**	**423.65**	**gmol^{-1}**

Figure 3.4. Formula used for the estimation of M_n for P3HT-SH by the molecular weight sum of end groups plus the average number of repeat units, determined by ^{1}H NMR.

estimate the M_n for each polymer. An example of the formula used to estimate the M_n for P3HT-SH is outlined in Figure 3.4. In this example, integration values of the signals in the ^{1}H NMR corresponding to H_a, H_{DFB} and H_e (end-group protons) were compared with those of H_c (repeating monomer unit protons) to estimate the average number of repeat units within the polymer batch. The average number of repeat units was found to be 13.90, hence, the M_n for P3HT-SH was estimated as 2700 gmol^{-1}. Post-substitution M_n values, determined by NMR, showed a slight increase from 2.6 to 2.7 kDa for P3HT-TFB and P3HT-SH respectively, as expected from the inclusion of thiol group.

From MALDI spectra, data points from the normalized spectra provide the information for mass distribution calculations, shown in Equation 3.1 and 3.2, where n_i was defined as the number of molecules with molecular weight M_i.

$$M_n = \frac{\sum_{i=1}^{\infty} n_i M_i}{\sum_{i=1}^{\infty} n_i} \tag{3.1}$$

$$M_w = \frac{\sum_{i=1}^{\infty} n_i {M_i}^2}{\sum_{i=1}^{\infty} n_i M_i} \tag{3.2}$$

From mass distribution calculations, M_n values for P3HT-TFB and P3HT-SH were found to increase from 2.5 to 2.6 kDa respectively, denoting the slight expected growth of the polymer chains upon inclusion of thiol group.

From SEC data, the measured M_n values were 2.1 KDa and 3.3 kDa for P3HT-TFB and P3HT-SH respectively; SEC traces are shown in Figure S3.6. The molecular weight for the starting P3HT-TFB measured by SEC against polystyrene standards was in reasonable agreement with those calculated by ^{1}H NMR and MALDI. After reaction with 1,8-octanedithiol the M_n, determined by SEC, increased significantly from 2.1 kDa (P3HT-TFB) to 3.3 kDa (P3HT-SH), in disagreement with the NMR and MALDI data, which only shows the expected modest increase. This discrepancy may arise from changes in the hydrodynamic volume of the thiolated material, perhaps due to changes in the polarity of the end-group upon inclusion of the thiol group.

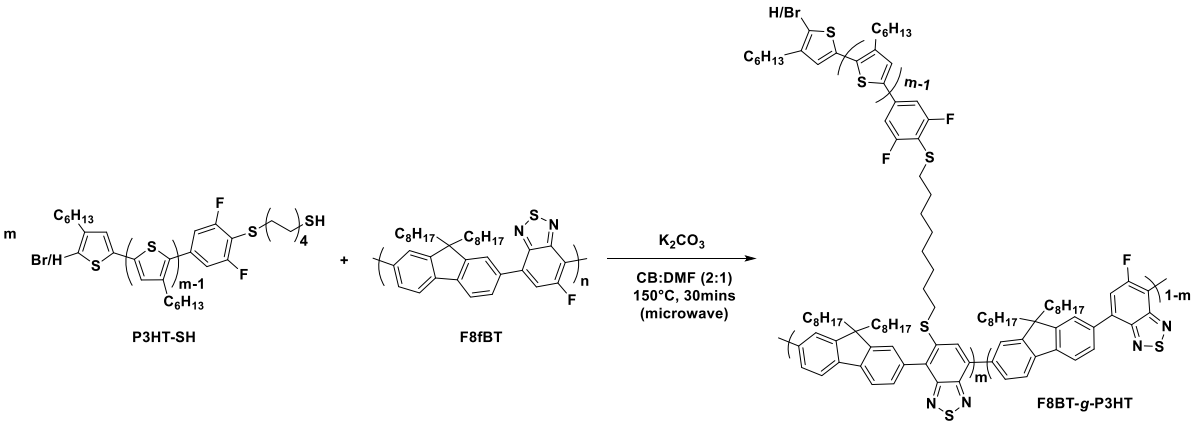
Table 3.1. Summary of GPC data for P3HT-TFB and P3HT-SH.

Technique	NMR	MALDI			SEC		
Polymer	**M_n (kDa)**	**M_n (kDa)**	**M_w (kDa)**	**Đ[a]**	**M_n (kDa)**	**M_w (kDa)**	**Đ[a]**
P3HT-TFB	2.6	2.5	2.7	1.1	2.1	2.7	1.3
P3HT-SH	2.7	2.6	2.8	1.1	3.3	3.8	1.1

[a]Polydispersity index M_w/M_n

3.3 Synthesis of graft co-polymer

Nucleophillic aromatic substitution (S_NAr) was further investigated to substitute P3HT-SH side chains along F8fBT via a 'grafting onto' method. The backbone polymer, F8fBT, was synthesised via a Suzuki coupling reaction under previously reported conditions to afford a polymer with M_n 59.7 kDa and M_w 109.7 kDa by SEC.[97] Creamer et.al. reported successful incorportation of the non-conjugated polymer poly(2-ethyl-2-oxazoline) (PEtOx) side chain onto F8fBT via S_NAr. Utilising the grafting onto method, the thiol terminated PEtOx side chain displaced the fluoride on the 5-fluorobenzo-2,1,3-thiadiazole (fBT) repeat unit to afford the



Scheme 3.3. Post-polymerisation modification of F8fBT with P3HT-SH towards graft co-polymer F8BT-g-P3HT.

graft co-polymer.[97] Here, thiol terminated conjugated P3HT-SH side chains were designed to displace the fluoride on the fBT repeat unit of F8fBT towards graft co-polymer F8BT-g-P3HT.

Initial experiments were performed with an excess of P3HT-SH in order to achieve the maximum grafting efficiency. Both polymers P3HT-SH and F8fBT were reacted in the presence of K_2CO_3 in a chlorobenzene/DMF solvent mixture. The reaction was carried out in a microwave reactor at 150 °C for 30 minutes. Extending the reaction time to 60 minutes, saw no change in the GPC trace or the UV-Vis Spectra of the sample taken at 60 minutes compared with the sample take at 30 minutes, suggesting that the maximum substitution had been reached, as shown in Figure S3.1. After reaction, the excess P3HT was removed by multiple washes with hot hexane and the final polymer, F8BT-g-P3HT, was filtered, collected and dried to give a deep purple solid in a yield of 60.2%. After purification the ^{1}H NMR of F8BT-g-P3HT clearly shows the aromatic peaks from the F8BT polymer backbone, from the P3HT side chain repeat unit and the H/DFB-SR linker on the P3HT side chain. Theoretical integral values within the aromatic region were calculated as: (a) the F8BT polymer backbone (δ 7.58-8.20 ppm, 7H) and (b) DFB-SR linker plus and the proton from the 3-hexylthiophene repeat unit directly adjacent to the DFB-SR linker from the P3HT side chain (δ 7.02-7.20 ppm, 3H). From the ^{1}H NMR (Figure S3.10) comparative integral values of 7H (F8BT) to 1.74H (DFB-SR linker plus one P3HT repeat unit) were found, indicating an approximate maximum grafting efficiency of 58%. By comparing the integral values of signals from F8BT backbone with the terminal proton on the P3HT ($H_{g\text{-}a}$) a similar grafting efficiency of 54% was calculated. The ^{19}F NMR displayed a peak from the resulting unsubstituted fluorine along the F8BT backbone at δ -113.82 ppm and a peak corresponding to the fluorine on the DFB-SH end group at δ -104.31 ppm.

Diffusion ordered spectroscopy (DOSY), shown in Figure S3.2 (P3HT and F8fBT mixture) and S3.3 (F8BT-g-P3HT), was used to confirm the ^{1}H signals of the graft co-polymer were associated with the graft material, not the ungrafted separate polymer chains. F8BT-g-P3HT was found to have a relatively low diffusion coefficient (1.81×10^{-8} cm^2s^{-1}) compared to P3HT and F8fBT mixture (1.05×10^{-6} and 3.10×10^{-7} cm^2s^{-1} respectively). It is well known that with increasing polymer molecular weight, thus an increased hydrodynamic radius, the diffusion coefficient decreases.[195]

Although the maximum grafting efficiency was limited to ca. 58%, this value corresponds to a 73 wt. % of P3HT to F8fBT. Weight percentage (wt.%) was calculated using Equation 3.3 where n was defined as number of moles, M_n as average molecular weight and M_r as relative molecular mass.

$$wt\%\ (P3HT) = \frac{n(P3HT) \times M_n(P3HT)}{[n(P3HT) \times (M_n(P3HT)] + [n(F8BT\ rep.unit) \times M_r(F8BT\ rep.unit)]} \quad (3.3)$$

For this calculation, it was assumed that P3HT had an average molecular weight of 2.6 kDa (determined by MALDI). Previous reports show in blended films of P3HT:F8BT, weight ratios up to 60:40 showed the highest performance in solar cell devices, therefore, a grafting efficiency of ca. 58% was considered sufficient.[196]

3.4 Synthesis of graft co-polymer series

Following the successful demonstration of grafting P3HT-SH side chains onto F8fBT via S_NAr, a graft co-polymer series of F8BT-g-P3HT with varied P3HT content was designed. By controlling the molar equivalence of P3HT-SH added relative to F8fBT, it was possible to synthesise a graft co-polymer series with a high, medium and low P3HT content. To compose the graft co-polymer series, molar ratios of 0.5, 0.2 and 0.1 equivalence of P3HT-SH to 1.0 equivalence of F8fBT were used, corresponding to a 70, 48 and 32 wt.% of P3HT respectively. The graft co-polymers were synthesised and purified using the procedure described above for P3HT-g-F8BT to afford F8BT-g-P3HT-0.1, F8BT-g-P3HT-0.2 and F8BT-g-P3HT-0.5 in a relatively high yield (82 – 85%). Using a grafting onto process and the same batch of starting polymers allowed the direct comparison of the graft co-polymers with increasing P3HT content. The number average molecular weight (M_n) values, summarised in Table 3.2, were determined by GPC. Figure S3.14 shows the unimodal broad GPC traces for the graft co-polymer series. The GPC traces show a small signal at lower molecular weight presumably arises from a trace amount of oxidised P3HT (P3HT-S-S-P3HT), which was not detected by NMR. For F8BT-g-P3HT-0.1, F8BT-g-P3HT-0.2 and F8BT-g-P3HT-0.5 increasing M_n values of 42.7, 72.4 and 74.0 kDa were recorded. The observed M_n for starting polymer F8fBT (59.7 KDa) was found to be slightly higher compared to F8BT-g-P3HT-0.1 (42.7 KDa). The observed decrease could be due to a slight aggregation of F8fBT in chlorobenzene. Once a small quantity of P3HT-SH was

grafted on, for F8BT-g-P3HT-0.1, the aggregation effects were lessened due to the incorporation of more soluble P3HT chains, hence, causing a reduction in the M_n value.

Structures of the graft co-polymers were confirmed by ^1H and ^{19}F NMR, shown in Figures S3.11-S3.13. Upon grafting P3HT onto F8fBT, the ^1H NMR showed a general broadening of the signals from the graft co-polymer structures compared to the starting polymers. The ^1H NMR signals assigned to protons (7H) on the F8BT repeat unit were found at δ 7.58-8.20 ppm. As the content of P3HT side chains was increased, the relative intensity of signals assigned protons on P3HT-SH were amplified with respect to the respective signals from the F8BT repeat unit. Focusing on the aromatic region, comparing the integral values of the signals associated with the protons along the F8BT backbone to those associated with the protons on the linking DFB group, the grafting efficiency could be determined. Approximate grafting efficiencies of 12, 19 and 45% were recorded for F8BT-g-P3HT-0.1, F8BT-g-P3HT-0.2 and F8BT-g-P3HT-0.5 respectively. In the ^{19}F NMR spectra for F8BT-g-P3HT-0.1, F8BT-g-P3HT-0.2 and F8BT-g-P3HT-0.5, two signals assigned to the fluorine on the linking DFB unit (F_{graft}) and the remaining un-displaced fluorine along the F8BT backbone (F_{F8BT}) were observed. As the P3HT content was increased the relative intensity of the F_{graft} signal intensified comparative to F_{F8BT}. Here the successful synthesis and characterisation of F8BT-g-P3HT with varied P3HT content was demonstrated, controlled by quantitative addition of P3HT-SH side chain into the reaction. Utilising the facile grafting onto method, via S_NAr, allowed the synthesis of a highly comparable graft co-polymer series. In the following sections, the polymer properties of the graft co-polymer series are reported as well as the morphology of thin films and finally the solar cell device performance.

Table 3.2. Summary of GPC data of F8fBT, F8BT-g-P3HT 0.5, F8BT-g-P3HT 0.2 and F8BT-g-P3HT 0.1.

Polymer	P3HT wt%[b]	M_n (kDa)	M_w (kDa)	Đ[a]	Yield (%)	Graft efficiency[c]
F8fBT	-	59.7	109.7	1.8	-	-
F8BT-g-P3HT 0.1	32	42.7	81.6	1.9	84	0.12
F8BT-g-P3HT 0.2	48	72.4	123.7	1.7	82	0.19
F8BT-g-P3HT 0.5	70	74.0	144.1	2.0	85	0.45

[a]Polydispersity index M_w/M_n

[b]P3HT weight percentage with respect to F8fBT

[c]Determined by integral values from ^1H NMR

3.5 Optical properties

For the F8BT-g-P3HT graft co-polymer series, solution (chlorobenzene) and film absorption spectra are shown in Figure 3.5. Thin films were prepared by spin-coating onto glass from chlorobenzene solutions. In this section, variation of the absorption spectra upon increasing the molar quantity of P3HT within the graft co-polymer for F8BT-g-P3HT-0.1, F8BT-g-P3HT-0.2 and F8BT-g-P3HT-0.5 was investigated. Identified characteristic peaks and the calculated optical energy band gaps ($E_{g,opt}$) are summarised in Table 3.3.

In solution, the starting polymer F8fBT displays two key absorption bands at high energy (318 nm) and lower energy (446 nm) with λ_{max} at 446 nm. The high energy absorption could be assigned to the π-π* transition and the lower energy absorption to intramolecular charge transfer (ICT).[168] On the other hand, P3HT has a single absorption band and respective λ_{max} at 460 nm which arises from a π-π* transition.[197,198] As P3HT were introduced side chains onto the F8fBT backbone two key observations were made; (a) the high energy absorption at 318 nm decreases in intensity relative to the lower energy absorption and (b) the lower energy absorption at 446 nm was slightly blue-shifted to 442 nm and the peak broadens. Furthermore, when the quantity of P3HT side chains was increased from F8BT-g-P3HT-0.1 to F8BT-g-P3HT-0.2 to F8BT-g-P3HT-0.5 the high energy absorption continues to decrease and the lower energy absorption continues to broaden. These observations are indicative of the superposition of the absorption spectra for pristine F8fBT and P3HT. As the P3HT content increases, the contribution from the P3HT absorption spectra increases, hence, leading to a larger and broader absorption at 442nm.

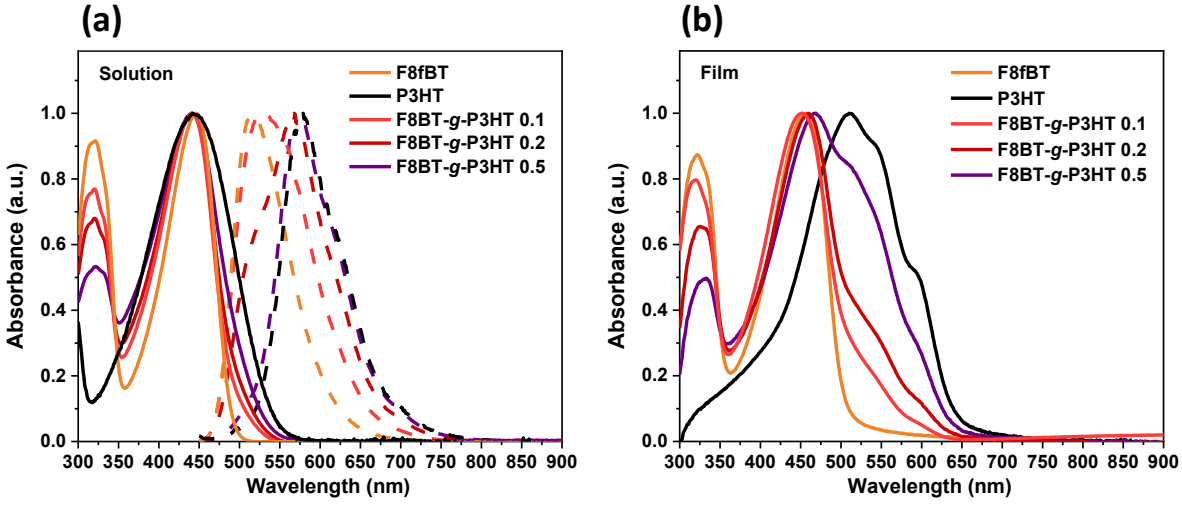


Figure 3.5. UV-Vis absorption and PL emission spectra for F8fBT, F8BT-g-P3HT-0.1, F8BT-g-P3HT-0.2, F8BT-g-P3HT-0.5 and P3HT-SH in chlorobenzene (5 µM) (a) and UV-Vis absorption spectra for all polymers as thin films on glass.

For the collected photoluminescence spectra, solutions of F8fBT and the F8BT-g-P3HT graft co-polymers in chlorobenzene (5 µM) were measured, as shown in the non-normalised emission spectra in Figure S3.15. The observed emission maxima ($\lambda_{em,max}$) and corresponding emission intensity of the signal at $\lambda_{em,max}$ has been summarised in Table S3.1. Upon grafting 10 mol% P3HT sidechains onto the F8fBT backbone, the fluorescence signal from F8fBT was quenched, characterised by the decrease in photoluminescence intensity from >1000 CPS (detector saturated) to 724 CPS. As the density of grafted P3HT chains was further increased to 20 and 50 mol%, the fluorescence signal was further quenched where the maximum photoluminescence intensity was recorded at 539 and 546 CPS respectively. The observed quenched fluorescence provides further confirmation of the covalently bound graft co-polymer structure as well as the indication of Förster resonance energy transfer (FRET) within the graft co-polymer.[199]

In the thin film absorption spectra, a similar reduction in the high energy F8fBT π- π* transition and broadening of the ICT band, upon increased substitution of P3HT onto the F8fBT backbone, was observed. In the solid state, P3HT undergoes a red-shift with the addition of distinctive vibronic peaks at longer wavelength, which are a result of interchain (H-aggregate) and intrachain (J-aggregate) packing effects, and are clear indications of P3HT ordering in the thin-film.[200] These peaks are clearly evident in the graft co-polymers, suggesting that grafting does not inhibit P3HT ordering and aggregation. The observed intensity of the vibronic peaks in the solid-state absorption spectra increases with increasing P3HT content. Whilst this is mostly influenced by the respective P3HT contribution, this may allude to a comparatively increased degree of crystallinity within the graft co-polymer thin films with a higher P3HT

Table 3.3. Summary of optical and electronic properties P3HT, F8fBT, F8BT-g-P3HT 0.5, F8BT-g-P3HT 0.2 and F8BT-g-P3HT 0.1.

	$\lambda_{abs,max}$ (nm)		λ_{onset} (nm)		$E_{g,opt}$[a] (eV)	HOMO[b] (eV)	LUMO[c] (eV)
Polymer	**solution**	**film**	**solution**	**film**	**film**	**-**	**-**
P3HT	460	511	556	641	1.93	-5.11	-3.18
F8fBT	446, 318	456	490	506	2.45	-6.08	-3.63
F8BT-g-P3HT 0.1	442, 318	451	492	520	2.38	-5.18	-2.80
F8BT-g-P3HT 0.2	442, 318	460	500	528	2.35	-5.19	-2.84
F8BT-g-P3HT 0.5	442, 318	468	514	616	2.01	-5.11	-3.10

[a] Estimated from the thin film absorption spectra onset

[b] Estimated from the cyclic voltammetry spectra onset of oxidation

[c] LUMO = HOMO + $E_{g,opt}$

content. Further analysis of the thin film crystallinity was carried out using Grazing-Incidence Wide-Angle X-ray Scattering (GIWAXS) to confirm the trends observed (section 3.8).

The optical energy band gap values for F8BT-g-P3HT-0.1, F8BT-g-P3HT-0.2 and F8BT-g-P3HT-0.5, taken from the onset of absorption, were found to increase upon incorporation of P3HT with $E_{g,opt}$ values of 2.52, 2.48 and 2.41 eV respectively. The observed trend is likely as a result of the broadened absorption at 442 nm as well as the extended conjugation from the P3HT chains.[201]

3.6 Electronic properties

Cyclic voltammetry (CV) was used to determine the HOMO and LUMO energy levels for F8BT-g-P3HT-0.1, F8BT-g-P3HT-0.2 and F8BT-g-P3HT-0.5, in solid state as a thin film. Additionally, the CV experiments were carried out on the starting polymer thin films, F8fBT and P3HT, for comparison. The cyclic voltammograms are displayed in Figure 3.6 and the respective energy levels are recorded in Table 3.3. The polymers were drop cast onto a glassy carbon electrode and measured in a solution of tetrabutylammonium hexafluorophosphate in acetonitrile (0.1 M) with an Ag/AgCl reference electrode. The onset of the first oxidation was used to estimate the HOMO energy levels of the polymers, assuming the ferrocene/ferrocenium (Fc/Fc^+) reference energy level is 4.8 eV below the vacuum level.[202,203] Using the estimated HOMO energy level plus the optical bandgap, measured from the onset of absorption in the thin film absorption spectra, the LUMO energy level was estimated.

Comparing the cyclic voltammograms of the starting polymers (F8fBT and P3HT) with the graft co-polymer series (F8BT-g-P3HT-0.X), a contribution from both starting polymers in the cyclic voltammograms of F8BT-g-P3HT-0.X was observed. The HOMO energy levels for F8fBT and P3HT were found to be -6.08 eV and -5.11 eV respectively, in accordance with reported literature values.[104,173,204] The HOMO energy levels of the graft co-polymers ranged from -5.11 to -5.19 eV, largely determined by the P3HT contribution. As the quantity of grafted P3HT was increased, the optical bandgap values ($E_{g,opt}$) decreased from 2.38 to 2.01 eV, hence, deeper LUMO energy levels were recorded. These results demonstrate the ability to modify the electronic properties of the graft co-polymers by controlling the quantity of P3HT graft onto the polymer backbone.

It should be highlighted that the estimated ionisation potential values from the solid-state cyclic voltammetry measurements were used to obtain approximate values for HOMO energy levels. In this work, LUMO energy levels were calculated by adding the optical band gap to the approximated HOMO energy level. This method of calculating the HOMO and LUMO energy levels does not take into account the exciton binding energy, encompassed in the optical bandgap. This is a well-reported method still currently used to report HOMO and LUMO energy levels, however, values should be considered with discretion. While the CV measurements provide a good insight into the approximate HOMO and LUMO energy levels and observable trends, other techniques should be used to more accurately determine estimated values, such as photoelectron spectroscopy in air (PESA).[205]

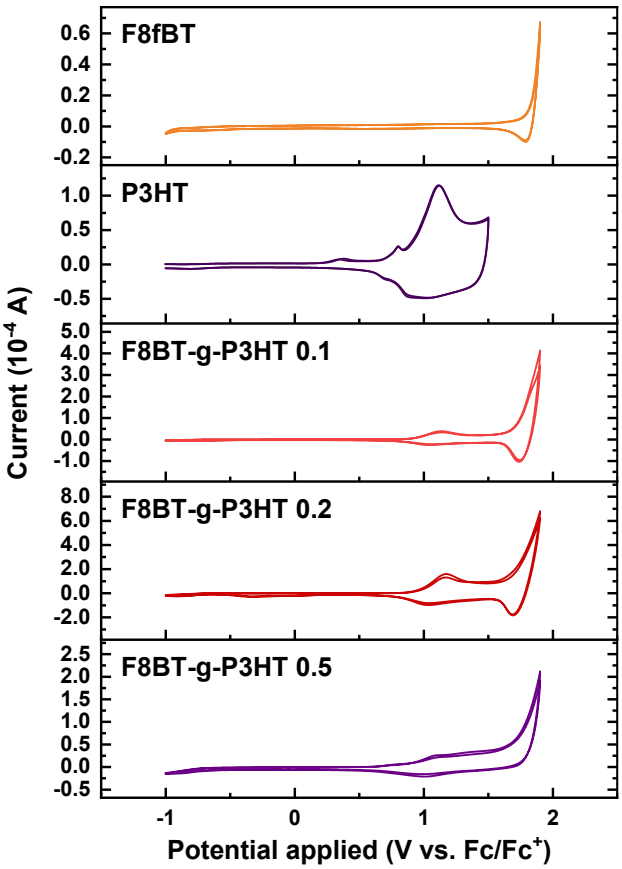


Figure 3.6. CV data for F8fBT, F8BT-g-P3HT-0.1, F8BT-g-P3HT-0.2, F8BT-g-P3HT-0.5 and P3HT-SH showing oxidation cycles in 0.1M acetonitrile-[n-Bu_4N]PF_6 at 100 mVs^{-1}, potentials were measured against an Ag/AgCl reference electrode.

3.7 Thermal properties

Thermogravimetric Analysis (TGA) and Differential Scanning Calorimetry (DSC) techniques were used to investigate the degradation, melt and recrystallisation temperatures for the graft co-polymer series.

Degradation temperature was determined by TGA, shown in Figure 3.7a. Degradation temperatures were determined by (a) 5% mass loss or (b) the onset of mass loss, values are recorded in Table 3.4. All three graft co-polymers, F8BT-g-P3HT-0.1, F8BT-g-P3HT-0.2 and F8BT-g-P3HT-0.5, were found to have high degradation temperatures of 422.6, 416.3 and 412.5 °C respectively at 5% mass loss. Degradation temperatures above 400 °C implies good thermal stability of the graft co-polymer structures. The graft co-polymers showed a similar thermal stability to F8fBT, indicating that the degradation temperature was largely determined by the backbone polymer. Additionally, this observation demonstrates that when the P3HT chains were incorporated in the graft co-polymer structure, a higher resistance to thermal degradation was observed for the side chains compared to the pristine P3HT.

Comparing the DSC traces of the starting polymers with the graft co-polymer series, shown in Figure 3.7b and Figure S3.16, a contribution from both starting polymers was observed in the DSC traces for F8BT-g-P3HT-0.1, F8BT-g-P3HT-0.2 and F8BT-g-P3HT-0.5. P3HT is generally known as a semicrystalline polymer with a melting point around 220 °C.[206,207] Upon heating

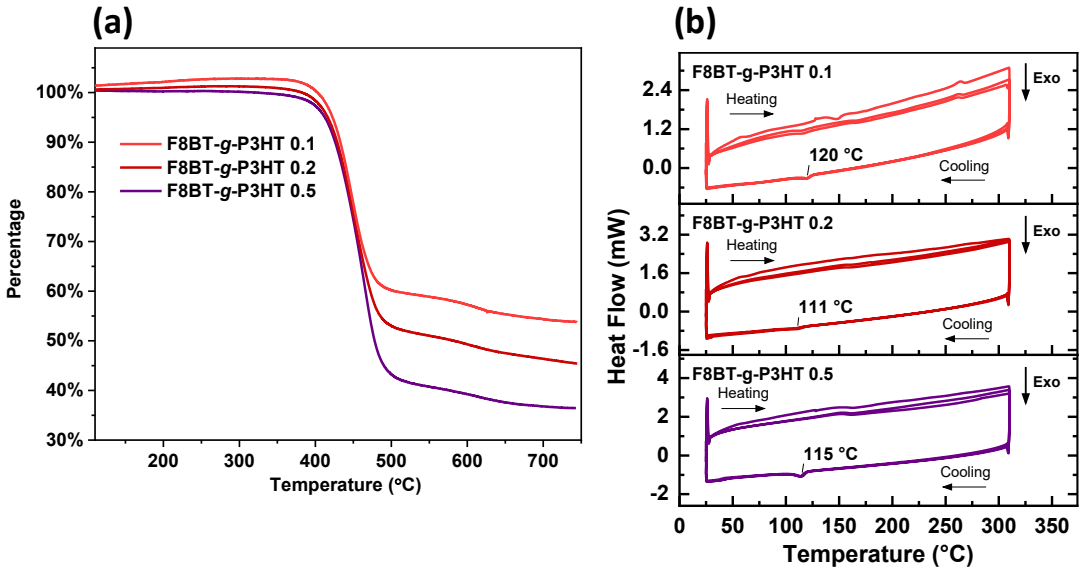


Figure 3.7. (a) TGA data for F8BT-*g*-P3HT-0.1, F8BT-g-P3HT-0.2 and F8BT-g-P3HT-0.5 carried out in a Nitrogen atmosphere at 5 °C min^{-1} (b) DSC data for F8BT-g-P3HT-0.1, F8BT-g-P3HT-0.2 and F8BT-g-P3HT-0.5 carried out in a Nitrogen atmosphere at 10 °C min^{-1}.

the melting point of P3HT shows a poorly defined melting temperature (T_m) at ca. 160 °C, however a clear peak associated with crystallisation temperature (T_c) upon cooling was observed at ca. 137 °C. The relatively low T_m for P3HT can be owed to the low molecular weight (DP≈15), previous reports of low molecular weight P3HT display similar low T_m values.[204,207–209]

Upon cooling, the graft co-polymers displayed a defined T_C at 115, 111 and 120 °C corresponding to the crystallisation of the P3HT side chains. The melting temperature (T_m) of the P3HT chains was observed upon heating between 150 and 158 °C. Previous reports of DSC data for F8fBT show an amorphous substance with no observed transitions in the DSC trace, however, in this work some key transitions were observed in the DSC for F8fBT.[173] Upon heating, an initial glass transition temperature was observed at 75 °C followed by an exothermic cold crystallisation (T_{CC}) at 150 °C (cycle 1) and 125 °C (cycle 2 and 3). Following the cold crystallisation an endothermic crystalline melting transition (T_m) was observed at 253 °C. Transitions associated with F8fBT were also observed in the DSC trace for F8BT-g-P3HT-0.1, where the transitions are related to the F8BT backbone of the graft co-polymer. As the P3HT content was increased, for F8BT-g-P3HT-0.2 and F8BT-g-P3HT-0.5, the transitions associated with F8fBT were not observed. These observations demonstrate the superposition of the DSC traces of pristine F8fBT and P3HT in the traces for the graft co-polymer structures. Similar observations have been recorded for reported block co-polymers and graft co-polymers.[156,210] From the TGA and DSC analysis, annealing temperatures of 120 and 150 °C were selected to investigate the thin film properties of the polymers.

Table 3.4. Summary of thermal properties for F8fBT, F8BT-g-P3HT-0.1, F8BT-g-P3HT-0.2, F8BT-g-P3HT-0.5 and P3HT.

Polymer	T_d (5% mass loss) (°C)	T_d (Onset) (°C)	T_m (°C)	T_c (°C)
P3HT	323.0	-	137	158
F8fBT	411.8	417.6	-	-
F8BT-g-P3HT 0.1	422.6	416.0	120	156
F8BT-g-P3HT 0.2	416.3	413.9	111	152
F8BT-g-P3HT 0.5	412.5	413.7	115	150

3.8 Thin film morphology

It was important determine the degree of crystallinity in the annealed thin films. The crystallinity was determined by Grazing-Incidence Wide-Angle X-ray Scattering (GIWAXS). From previous reports, it was expected that the presence of larger crystalline domains results in improved solar cell device performance.[211,212] It should be noted that the starting polymer F8fBT thin films were found to be largely amorphous as-cast and when annealed after the T_g (100 °C) and cooled. Upon annealing at higher temperatures (200 °C) an increased degree of crystallinity was observed, as shown in the GIWAXS images and diffraction patterns shown in Figure S3.20. Conversely, starting polymer P3HT (low molecular weight) displays crystallinity even in the as-cast thin films.[213] As mentioned in the previous section (Section 3.7), annealing temperatures 120 and 150 °C were chosen after analysis of the TGA and DSC data. At these lower annealing temperatures, it was expected that the P3HT sidechains would contribute the most, if not entirely, to observed crystallinity within the graft co-polymer thin films.

Thin films of the graft co-polymers, F8BT-g-P3HT-0.1, F8BT-g-P3HT-0.2 and F8BT-g-P3HT-0.5, and a P3HT:F8fBT (1:2 molar ratio) blend were prepared. The P3HT:F8fBT (1:2 molar ratio) blend was directly comparable to F8BT-g-P3HT-0.5 with respect to the molar ratio of F8fBT to P3HT. Each of the graft co-polymers and polymer blend were dissolved and spin coated from solution directly onto a silicon wafer. To determine how the thin film morphology changes with different annealing temperatures the films were prepared; as-cast and annealed for 30 minutes at 120 °C and 150 °C. Figure S3.18 and S3.19 shows the 2D GIWAXS images and the diffraction patterns for F8BT-g-P3HT-0.1, F8BT-g-P3HT-0.2 and F8BT-g-P3HT-0.5, and the P3HT:F8fBT blend respectively.

Firstly, considering the P3HT:F8fBT blend film, clear diffraction peaks were observed in the as-cast film. Upon annealing at 120 °C, the diffraction peaks for the P3HT:F8fBT blend film increased in intensity. These films show a distinct ‘edge-on’ alignment, with a progression of diffraction peaks (h00). The observed diffraction peak at 4.1 nm^{-1} assigned to the (100) lamellar peak corresponds to a d-spacing of 1.53 nm, which is consistent with the d-spacing observed for defined oligomers of P3HT.[213] Similarly an in-plane diffraction peak at 16.3 nm^{-1} can be assigned to the (010) π-stacking peak of 0.39 nm.[213] These results clearly show that blending with the amorphous F8fBT does not inhibit the crystallization of the P3HT.

In comparison, the diffraction patterns for as-cast graft co-polymer films showed a lower extent of crystallinity compared to the blended thin film, with a broad (100) lamellar peak apparent in all cases. This suggests that chemically attaching the P3HT to the F8fBT disrupts ability of P3HT to crystallise upon solution casting. Both F8BT-g-P3HT-0.1 and F8BT-g-P3HT-0.2 only show a single (100) lamellar peak, whereas F8BT-g-P3HT-0.5 also shows a weak (200) lamellar peak. Interestingly, for all polymer thin films the crystallinity significantly improved upon annealing at 120 °C, as indicated by an increased in intensity and sharpness of the diffraction peaks, and the appearance of higher order lamellar peaks (up to the third order (300)). However, when the thin films were annealed at 150 °C, close to the melting temperature, the degree of crystallinity was reduced. Therefore, to further study the thin film crystallinity polymer thin films annealed at 120 °C were analysed, where the highest degree of crystallinity was observed. Figure 3.8 shows the complete (combined IP and OOP integrations) diffraction patterns for the thin films annealed at 120 °C.

All thin films exhibit a diffraction peak at (100) with a q value at 4.0, 3.9, 3.9, 4.1 nm^{-1} corresponding to an interlayer d-spacing of 1.57, 1.61, 1.61, 1.53 nm respectively. Observed peaks were predominately orientated in the out-of-plane direction, indicating edge-on orientation in all cases. In addition to the first order lamellar peak (100), the P3HT:F8fBT blend shows a progression up to the third order (300), indicating a high degree of structural order in the edge-on orientation. A higher degree of crystallinity for the blended thin film was observed as the polymer chains were not chemically bound together and have more freedom to rearrange upon annealing. F8BT-g-P3HT-0.2 and F8BT-g-P3HT-0.5 show the same

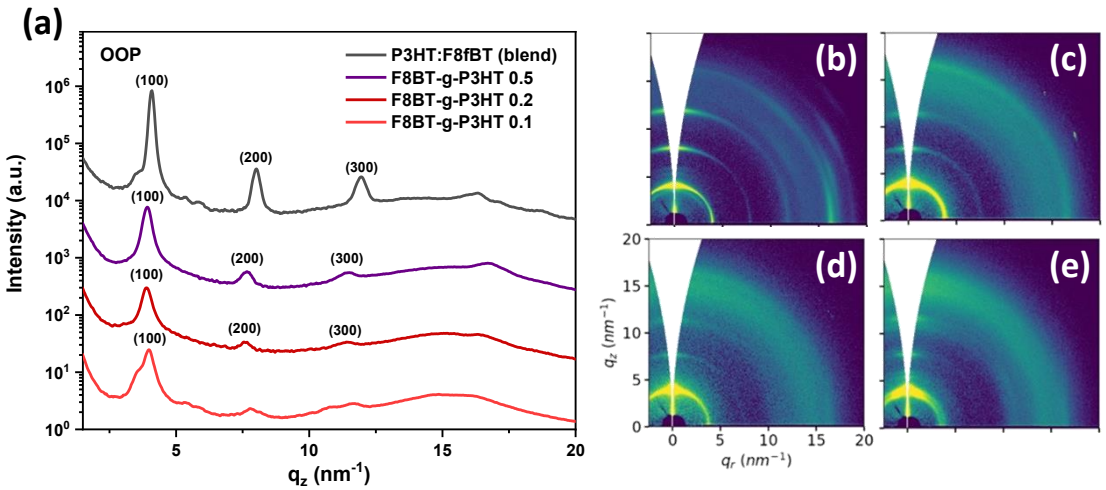


Figure 3.8. (a) GIWAXS diffraction patterns (OOP) for P3HT:F8fBT blend, F8BT-g-P3HT 0.5, F8BT-g-P3HT 0.2 and F8BT-g-P3HT 0.1 films annealed at 120 °C. (b-e) GIWAXS diffraction images for P3HT:F8fBT blend, F8BT-g-P3HT 0.5, F8BT-g-P3HT 0.2 and F8BT-g-P3HT 0.1.

progression of the lamellar peaks to the third order (300). In addition to the advancement up to the third order (300), F8BT-g-P3HT-0.1 displays new peaks that could be associated with the crystallisation of the F8BT backbone.[214,215]

In order to better understand the degree of crystallinity within the thin films, an estimation of the crystallite size was determined using the Scherrer equation (Equation 3.4).[216] In this equation, D is defined as the average size of crystalline domains, λ is x-ray wavelength (0.0957 nm), K is a dimensionless shape factor (0.94 for a homogeneous sample), β is the full width at half maximum (FWHM) of the peak and θ is Bragg's angle.

$$D = \frac{K \times \lambda}{\beta \times \cos\theta} \tag{3.4}$$

Crystallisation of the polymer occurs parallel to the substrate, with a lamellar type structure. A "crystallite" relates to an area of π-stacked conjugated polymer (lamellar stacking) that gives rise to diffraction peaks observed by GIWAXS.[215] A gaussian profile was applied to the (100) diffraction peak to determine the FWHM. Using the Scherrer equation, the average polymer crystallite size was calculated.[217] A summary of the estimated average crystallite size within the polymer blend and graft co-polymer thin films (as-cast, annealed at 120 °C and annealed at 150 °C) are shown in Figure 3.9.

The average crystallite size found within the P3HT:F8fBT blend film (annealed 120 °C) was estimated as 26.4 nm, in line with reported values in the literature for annealed thin films of P3HT.[215,218] From the blend film to the graft co-polymer films (annealed 120 °C) the average crystallite size decreased to 8.5, 12.1 and 13.4 nm for F8BT-g-P3HT-0.1, F8BT-g-P3HT-0.2 and F8BT-g-P3HT-0.5 respectively. A reduction in the average crystallite size indicates a reduced overall degree of crystallinity within the polymer thin film.

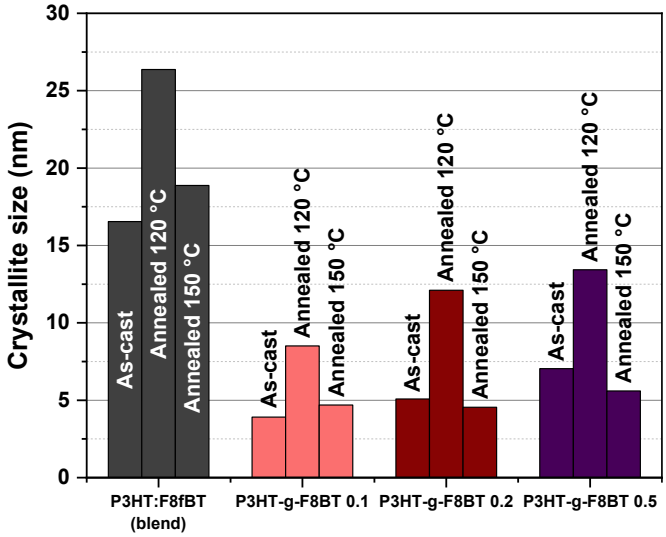


Figure 3.9. Polymer crystallite size determined by the Scherrer equation for P3HT:F8fBT blend, F8BT-g-P3HT 0.1, F8BT-g-P3HT 0.2 and F8BT-g-P3HT 0.5 films: as-cast, annealed at 120 °C and annealed at 150 °C.

Both in-plane (IP) and out-of-plane (OOP) GIWAXS diffraction patterns are shown in Figure S3.21. F8BT-g-P3HT-0.1, F8BT-g-P3HT-0.2 and F8BT-g-P3HT-0.5, showed an isotropic π-π stacking peak observed at 14.7, 15.0 and 15.0 nm^{-1} corresponding to a d-spacing of 4.3, 4.2 and 4.2 Å respectively. This peak in the diffraction pattern is likely associated with the π-π stacking of the F8BT polymer backbone, reported to have a d-spacing of ca. 4.2 Å.[214] Additionally, a second weak peak in the diffraction patterns, also with isotropic orientation, were observed at 16.2, 16.4 and 16.4 nm^{-1} corresponding to a d-spacing of 3.9, 3.8 and 3.8 Å respectively. These peaks could be assigned to the π-π stacking of the P3HT side chains, reported to have a d-spacing of ca. 3.7 Å.[219] In the blended P3HT:F8fBT thin film, the peak orientated in-plane was more clearly resolved at 16.3 nm^{-1} corresponding to a d-spacing of 3.9 Å. This peak corresponds to the π-π stacking of P3HT.[219] With respect to the π-π stacking, a higher degree of crystallinity for the blended thin film compared to the graft co-polymer thin films was observed, determined by the orientation of the peaks. For the blended thin film, the π-π stacking peaks were orientated in-plane where the polymer chains reorganised upon annealing. For the graft co-polymer thin film, the π-π stacking peaks were found to be isotropically ordered, where the polymer chains were more restricted, limiting the ability to reorganise upon annealing.

From the GIWAXS diffraction patterns, it was concluded that the graft co-polymer thin films displayed crystalline domains associated with the backbone polymer (F8BT) and the polymer side chains (P3HT). In the case for graft co-polymer thin films, crystalline domains were

maximised when annealed at 120 °C with a predominantly edge-on configuration of the P3HT side chains determined by the lamellar peaks and isotropic ordering of the F8BT backbone.

Atomic force microscopy (AFM) was used to further understand the surface and topography of the graft co-polymer thin films compared with the blended P3HT:F8fBT thin film, both as-cast and annealed at 120 °C, shown in Figure 3.10. All polymers formed a smooth and continuous thin film (as-cast) from spun polymer solutions in chorobenzene:chloroform (1:1). Furthermore, all thin films appeared to have nanofibrillar polymeric structures in the as-cast and annealed thin films, similar to previously reported pristine F8fBT and P3HT thin films.[173,208] As-cast blended thin film, P3HT:F8fBT, had a surface roughness root-mean-square (RMS) value of 4.5 nm. Comparing the blended thin film with the single component graft co-polymer thin films, the RMS value was reduced considerably to 0.46, 0.56 and 0.55 nm for F8BT-g-P3HT-0.1, F8BT-g-P3HT-0.2 and F8BT-g-P3HT-0.5 respectively. From the GIWAXS data, increased crystalline domains were observed for the blended thin film compared to the more amorphous graft co-polymer thin films. The increased degree of crystallinity contributes to the higher RMS recorded for the blended thin film.

Upon annealing the polymer thin films at 120 °C for 30 minutes, the surface roughness increased with RMS values of 6.3, 2.4, 1.0 and 0.88 nm for P3HT:F8fBT, F8BT-g-P3HT-0.1, F8BT-g-P3HT-0.2 and F8BT-g-P3HT-0.5 respectively. The increase in RMS values corresponds to the increased degree of crystallinity when annealed at 120 °C, which agrees with the previous observations from GIWAXS measurements. Additionally for the graft co-polymer thin films, the AFM images showed spontaneously formed microphase separated structures in the form of small nanometer-sized aggregates. The evenly distributed aggregates were shown clearly in the 10 x 10 µm images shown in Figure S3.22. The average diameter sizes of the aggregates were found to be 58 ± 30 nm (F8BT-g-P3HT-0.1), 94 ± 46 nm (F8BT-g-P3HT-0.2) and 88 ± 43 nm (F8BT-g-P3HT-0.5). The average diameter size of the aggregates was determined by estimating the diameter of between 350 and 400 spherical features in the 10 x 10 µm AFM image, depicted by the histograms in Figure S3.23. Similar nanosized aggregate features have been reported for annealed thin films of non-conjugated graft co-polymers.[119,220,221]

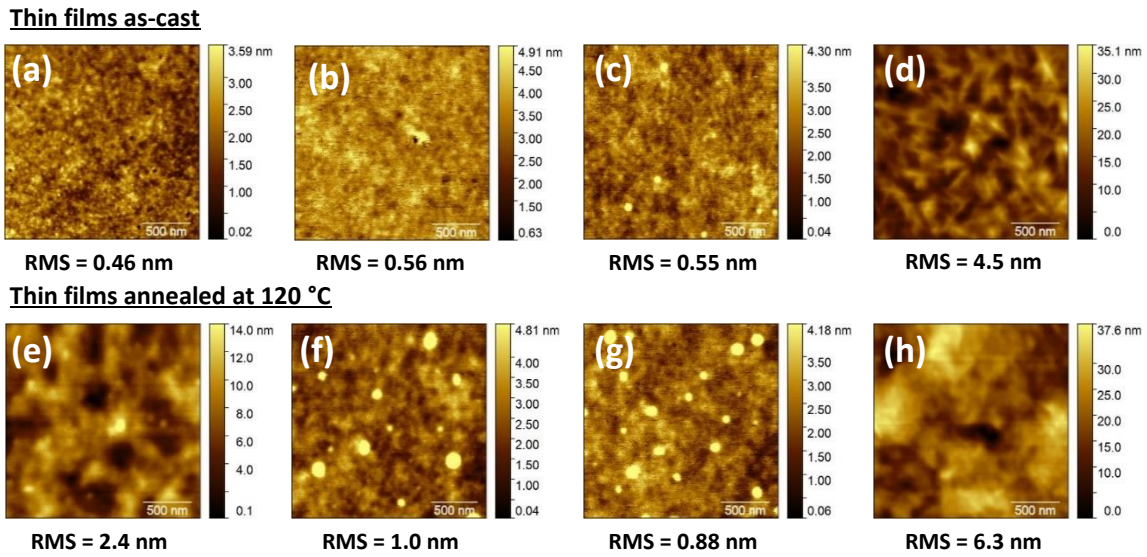


Figure 3.10. AFM images (2x2 µm) of for F8BT-g-P3HT 0.1 (a,e), F8BT-g-P3HT 0.2 (b,f), F8BT-g-P3HT 0.5 (c,g) and P3HT:F8fBT blend (d,h) thin films, from spin casting on Si wafer. The films were imaged as-cast and after thermal annealing (at 120 °C).

3.9 Photovoltaic properties

In this section, the photovoltaic properties of the graft co-polymers and the blended P3HT:F8fBT were evaluated, as an active layer in organic solar cell (OSC) devices. The OSC devices were prepared with an inverted structure: ITO/ZnO/active layer/MoO_x/Ag device architecture, as shown in Figure 3.11. The active layers were prepared from spin coated solutions of F8BT-g-P3HT-0.1, F8BT-g-P3HT-0.2 and F8BT-g-P3HT-0.5, and P3HT:F8fBT annealed at 120 °C for 30 minutes. Figure 3.11 and Table 3.5 show the measured J-V curves under 1 sun illumination (AM1.5G) and corresponding summarised device data for the fabricated OSCs. Whilst the overall efficiency was low, from the J-V curves and the measured power conversion efficiencies (PCE) of 0.013 to 0.017 %, the performance of graft co-polymers reflected that of the blended polymers. Due to the predominantly edge-on configuration of the P3HT, confirmed by GIWAXS (Section 3.8), lower FF and consequently PCE values were expected.[222,223] Further development could focus on achieving a

Table 3.5. Solar cell device performance data for devices containing P3HT:F8fBT blend, F8BT-g-P3HT 0.5, F8BT-g-P3HT 0.2 and F8BT-g-P3HT 0.1 in the active layer.

Active layer	Spin coat speed (rpm)	V_{OC} (V)	J_{SC} (mA cm^{-2})	FF	PCE (%)
P3HT:F8fBT blend	2000	0.73	7.8×10^{-2}	0.29	1.7×10^{-2}
F8BT-g-P3HT 0.1	1500	0.99	6.1×10^{-2}	0.22	1.3×10^{-2}
F8BT-g-P3HT 0.2	3000	0.91	8.4×10^{-2}	0.23	1.7×10^{-2}
F8BT-g-P3HT 0.5	3000	0.79	8.9×10^{-2}	0.23	1.6×10^{-2}

predominantly face-on configuration within the polymer thin films, by optimisation of the device fabrication, with an aim to improve OPV device properties.

Interestingly for F8BT-g-P3HT-0.1, F8BT-g-P3HT-0.2 and F8BT-g-P3HT-0.5, increased V_{oc} values of 0.99, 0.91 and 0.79 V respectively were observed where the open circuit voltage (V_{oc}) for the blended film (P3HT:F8fBT) was found to be 0.73 V. Increased V_{oc} values implies smaller charge transfer (CT) energy loss for the single-component graft co-polymers (intramolecular interfaces) compared to the blend (intermolecular interfaces). Similar observations have been made in the literature for single component organic solar cells verses the corresponding organic solar cells with a blended active layer.[224] It should be noted that the fabricated OSC devices displayed a distinctively low performance respective to current examples of all-polymer solar cells.[58,116] However, the graft co-polymers did display a comparable device performance level as the recorded blended P3HT:F8fBT, where previous literature also reports similar PCE values.[196] Furthermore, these results demonstrate attempts to advance our understanding the photovoltaic properties of not only all-polymer OSCs but of single-component all polymer OSC's. These insights are essential for future development and progression of this class of materials.

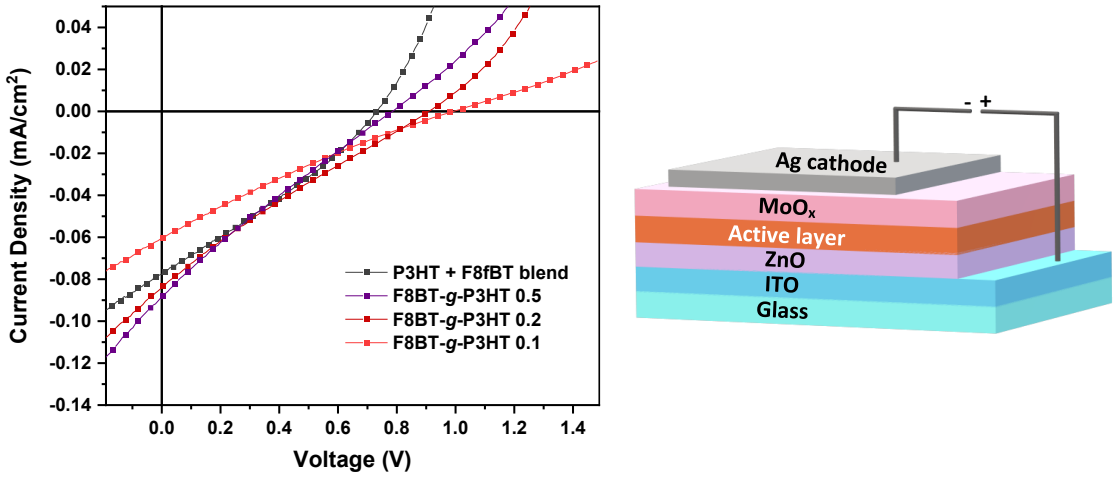


Figure 3.11. Current density vs. voltage data for devices containing P3HT:F8fBT blend, F8BT-g-P3HT 0.5, F8BT-g-P3HT 0.2 and F8BT-g-P3HT 0.1 in the active layer (left). Solar cell device architecture (right).

3.10 Conclusion

In summary, S_NAr was utilised as an effective 'grafting onto' method to synthesise graft co-polymers with a conjugated acceptor polymer backbone and conjugated donor sidechains, designed as a single-component active layer for photovoltaic devices. Synthetic routes towards (a) end-functionalised P3HT side chains (donor) and (b) conjugated F8BT-g-P3HT graft co-polymers, using F8fBT backbone polymer (acceptor), were explored. Thiol terminated P3HT sidechains were synthesised with precise molecular weight (DP=15) and high end-group fidelity, via SCTP followed by S_NAr, confirmed by GPC, MALDI-TOF and NMR. Backbone polymer F8fBT was sythesised via palladium catalysed suzuki coupling reaction. The separately prepared P3HT sidechains were 'grafted onto' the F8fBT backbone using S_NAr to afford the graft co-polymer F8BT-g-P3HT. Successful synthesis and purification of the graft co-polymer structure was confirmed by GPC, UV-Vis, NMR and DOSY. By NMR a maximum grafting efficiency was found to be ca. 58%. Limited grafting efficiencies are generally experienced with 'grafting onto' methods owed to steric hindrance. Although the 'grafting onto' method presents a maximum grafting efficiency, the corresponding P3HT weight percentage of 73% to F8fBT was sufficient for use as an active layer in photovoltaic devices.

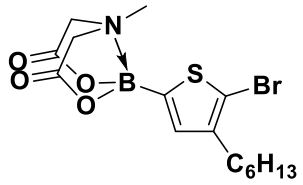
The versatility of the 'grafting onto' method, via S_NAr, was demonstrated by the synthesis of the graft co-polymer series with increasing amounts of P3HT sidechains along the F8BT backbone. Effective control of the grafting efficiency was confirmed by ^1H NMR. Further characterisation by GPC, ^{19}F NMR, UV-Vis supported the successful synthesis of graft co-polymers with increasing P3HT content along the backbone. Graft co-polymers showed good thermal stability with degradation temperatures above 400 °C determined by TGA. Suitable stabilisation of P3HT side chains was demonstrated where a degradation temperature for pristine P3HT was found at 312 °C. GIWAXS and AFM images of the graft co-polymer and blended P3HT:F8fBT thin films highlighted the increased amorphous morphology for the graft co-polymers. Finally, solar cell devices fabricated with single component graft co-polymer and bicomponent blended P3HT:F8fBT active layers showed the graft co-polymers performed comparably to the blended polymer with PCE values up to 0.017%. Most interestingly, single component solar cell devices fabricated with graft co-polymers gave higher V_{oc} values (0.79-0.99 V) than the polymer blend (0.73 V). These preliminary results provide a promising insight into the use of this class of materials for photovoltaic applications. Further developments,

such as a suitably designed acceptor backbone, is essential to obtain competitive photovoltaic devices. Ultimately, using the straightforward ‘grafting onto’ approach it is possible to rapidly broaden the library of graft co-polymers and easily optimise these structures (by ratio of backbone to sidechain) for desired applications.

3.11 Experimental

Synthesis of end-functionalised P3HT-TFB polymer 5-Bromo-2-thiophenylboronic acid MIDA ester (Monomer)

As prepared by collaborator Hyunwoo Park according to previously reported methods.[80,225]

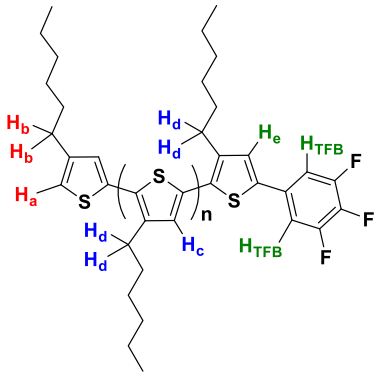


To a round-bottom flask equipped with a magnetic stir bar, 5-bromo-4-hexylthiophen-2-ylboronic acid (0.58 g, 2.0 mmol) and N-methyliminodiacetic acid (0.44 g, 3.0 mmol) were added. To the solid mixture benzene (63 mL) and DMSO (7 mL) were added and the solution was stirred at 100 °C for 16 h. The crude mixture was diluted with diethyl ether, washed with water three times, dried over anhydrous $MgSO_4$, and concentrated under reduced pressure. The crude product was purified by column chromatography on silica gel with hexane and ethyl acetate as the eluent. The solvent was removed under vacuum and the product was dried to obtain the desired product as a white solid (0.72 g, 90% yield).

^{1}H NMR (400 MHz, $CDCl_3$): δ 7.00 (s, 1H), 3.96 (dd, *J* = 16.3 Hz, 2H), 3.79 (dd, *J* = 16.6 Hz, 2H), 2.71 (s, 3H), 2.54 (d, *J* = 7.7 Hz, 2H), 1.55 (m, 2H), 1.30 (m, 6H), 0.89 (t, *J* = 6.9 Hz, 3H) ppm. ^{13}C NMR (100.6 MHz, $CDCl_3$): δ 167.1, 143.9, 134.7, 113.6, 61.5, 47.5, 31.5, 29.7, 29.4, 28.9, 22.6, 14.1 ppm. MS (m/z) $[M\text{-}H^+]^-$ calcd for $C_{15}H_{21}BBrNO_4S^-$: 400.0394, found: 400.0391 (ESI).

Synthesis of end-functionalised P3HT-TFB polymer

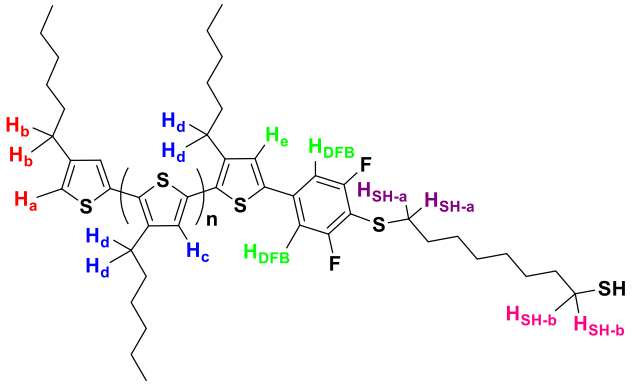
As prepared by collaborator Hyunwoo Park.



To a round-bottom flask equipped with a magnetic stir bar, RuPhos Pd G3 precatalyst (56.0 mg, 0.067 mmol), 1-Bromo-3,4,5-trifluorobenzene (17.5 mg, 0.083 mmol), RuPhos (46.7 mg, 0.10 mmol), and K_3PO_4 (1.27 g, 6 mmol) were added. The flask was evacuated and backfilled with argon three times. To the solid mixture degassed THF (5 mL) and water (1.6 mL) were added. The mixture was heated and stirred at 50 °C for 1 h to prepare externally initiated catalyst. Monomer 5-Bromo-2-thiophenylboronic acid MIDA ester (0.40 g, 1.0 mmol where M/I = 15/1) in degassed THF (43 mL) was added to the flask, and the polymerisation was left to stir at 45 °C for 21 h. The polymerisation was quenched with 6M HCl (5 mL). The crude reaction mixture was diluted with $CHCl_3$, washed with saturated $NaHCO_3$ (aq), dried over anhydrous $MgSO_4$, and concentrated under reduced pressure. The polymer was purified by precipitation into methanol. The precipitate was collected by filtration, washed with methanol, and dried under vacuum. The product obtained was a deep purple solid (140 mg, 88% yield).

^{1}H NMR (400 MHz, $CDCl_3$): δ 7.18 (m(br), 3H, H_e and H_{TFB}), 6.98 (s(br), 14H, H_c), 6.82 (s(br), 1H, H_a), 2.81 (m(br), 30H, H_d), 2.62 (t(br), 2H, H_b), 2.51 (m(br), 2H, $H_{SH\text{-}b}$) 1.80-1.65 (m, 30H, β-CH2), 1.50-1.20 (m, 90H), 1.0-0.8 (m, 45H, CH_3) ppm. ^{19}F NMR (377 MHz, $CDCl_3$): δ -133.9 (d, 2F, $J_{F,F}$ = 20 Hz), -166.8 (t, 1F, $J_{F,F}$ = 24 Hz) ppm. GPC (80 °C, chlorobenzene, vs PS): M_n = 2.1 KDa, M_w = 2.7 KDa, PDI = 1.3.

Synthesis of end-functionalized P3HT-SH polymer

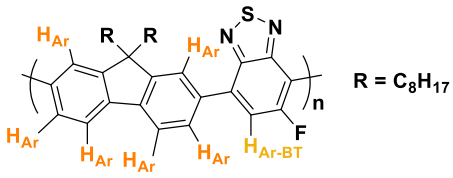


To a 20 mL microwave vial equipped with a stirrer bar, P3HT-TFB (~2500 $gmol^{-1}$ by MALDI-TOF, 130 mg, 0.052 mmol) and K_2CO_3 (108 mg, 0.52 mmol) were added and degassed with nitrogen. To the degassed solids, degassed THF (6.5 mL) was added. The solution was gently heated to dissolve the polymer in THF. To the reaction mixture, a degassed solution of 1,8-octanedithiol (97 uL, 0.78 mmol) in DMF (1.3 mL) was added and heated to 70 °C for 3 hours. A small aliquot (<0.1 mL) was taken every 90 minutes and analysed by MALDI-TOF for the depletion of P3HT-TFB peaks and the emergence of P3HT-SH peaks. Upon the complete consumption of P3HT-TFB, the reaction was cooled to room temperature, precipitated into methanol (50 mL), filtered and washed with excess methanol. The resulting polymer was washed with hot acetone (3 x 20 mL) to remove unreacted 1,8-octanedithiol. The product was further purified by preparative Size Exclusion Chromatography (eluent: chloroform). The product was dissolved in chloroform (<5 mL), purified by preparative GPC, collected, concentrated down, precipitated into methanol, collected in a vial and dried under vacuum. The product obtained was a deep purple solid. (83.4 mg, 64% yield).

^{1}H NMR (400 MHz, $CDCl_3$): δ 7.21 (s(br), 1H, H_e), 7.17 (d(br), 2H, H_{DFB}), 7.00 (s(br), 14H, H_c), 6.93 (s(br), 1H, H_a), 2.81 (m(br), 30H, H_d), 2.62 (t(br), 2H, H_b), 1.80-1.65 (m, 30H, β-CH2), 1.50-1.20 (m, 90H), 1.0-0.8 (m, 45H, CH_3) ppm. ^{19}F NMR (377 MHz, $CDCl_3$): δ -103.1 (s, 2F) ppm. GPC (80 °C, chlorobenzene, vs PS): M_n = 3.3 KDa, M_w = 3.8 KDa, PDI = 1.1.

Synthesis of F8fBT polymer

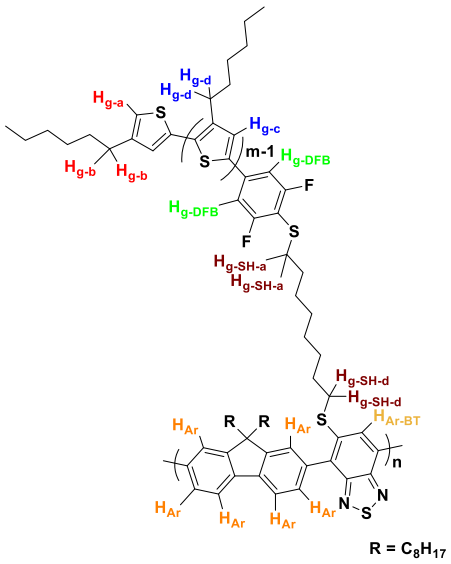
as prepared according to a modified procedure of Adam Creamer et al.[97]



In a dry 100 mL round bottom flask under nitrogen, 9,9-dioctylfluorene-2,7-diboronic acid bis(pinacol) ester (2.39 g, 3.72 mmol), 4,7-dibromo-5-fluoro-2,1,3-benzothiadiazole (1.16 g, 3.72 mmol) and tetrakis(-triphenylphosphine) palladium(0) (86 mg, 0.07 mmol) were added and degassed with nitrogen. To the solid mixture degassed toluene (32 mL) with on drop of aliquot 336 and degassed aqueous 2 M Na_2CO_3 (20 mL) were added before the solution was heated to reflux for 72 h. After the reaction was cooled to room temperature and the mixture was precipitated into methanol. The precipitate was filtered into a Soxhlet thimble and washed (Soxhlet) with methanol, acetone and hexane (in that order) and the final product was extracted into chloroform. After extraction, the solvent was removed using a rotary evaporator. The product was dissolved in the minimum amount of chlorobenzene (approx. 5 mL) and precipitated into methanol (approx. 500 mL). The precipitate was collected by vacuum filtration through a nylon pad (pore size 20 µm), washed with methanol and acetone then dried. The dry product was collected in a vial and further dried under vacuum. The product obtained was a yellow solid (1.41-1.99g, 70–99% yield).

^{1}H NMR (400 MHz, $CDCl_3$): δ 8.20-7.80 (m, 7H, H_{ar}), 2.13(m, 4H, CH2), 1.20–1.15 (m, 20H, CH2), 0.96 (s, 4H, CH2), 0.85–0.75 (m, 6H, CH3) ppm. ^{19}F NMR (377 MHz, $CDCl_3$): δ -114.51 ppm. GPC (80 °C, chlorobenzene, vs PS): M_n = 59.7 kDa, M_w = 109.7 kDa, PDI = 1.8.

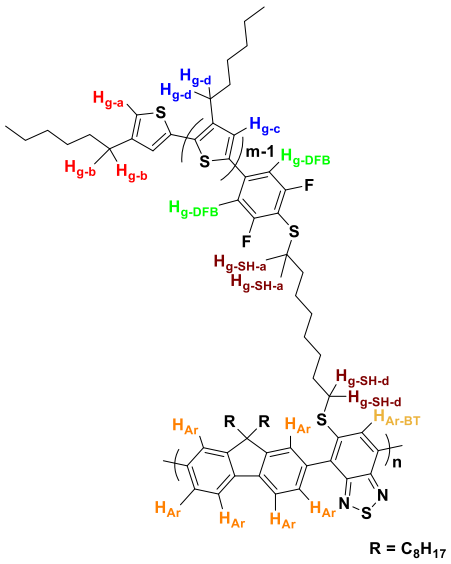
Synthesis of F8BT-g-P3HT



In a dry 20mL microwave vial equipped with a stirrer bar, P3HT-SH (19 mg, 0.019 mmol), F8fBT (4.2 mg, 0.008 mmol) and K_2CO_3 (33 mg, 0.24 mmol) were added and degassed with nitrogen for 20 min. To the solid mixture chlorobenzene (3 mL) and DMF (1 mL) were added and degassed for a further 10 min. The solution was heated in the microwave reactor at 150 °C for 30 minutes. The reaction was cooled to room temperature, precipitated in methanol. The precipitate was collected by vacuum filtration through a nylon pad (pore size 20 µm), washed with excess methanol, followed by hot hexane to remove excess non-grafted P3HT chains and dried. The product obtained was a deep purple fibrous solid (9 mg, 73% yield).

^{1}H NMR (400 MHz, $CDCl_3$): δ 8.35-7.55 (m(br), 7H, H_{Ar}+$H_{Ar\text{-}BT}$), 7.16 (m(br), 3H, $H_{g\text{-}e}$+H_{DFB}), 7.00 (s(br), 6H, $H_{g\text{-}c}$), 6.93 (s(br), 1H, $H_{g\text{-}a}$), 2.95 (m(br), 2H, $H_{g\text{-}SH\text{-}d}$), 2.81 (m(br), 12H, $H_{g\text{-}d}$), 2.61 (t(br), 2H, $H_{g\text{-}b}$), 1.80-1.65 (m, 12H, β-CH2), 1.50-1.25 (m, 80H), 1.25-1.05 (m, 24H), 1.0-0.85 (m, 18H, CH_3), 0.85-0.75 (m, 6H, CH_3) ppm. ^{19}F NMR (377 MHz, $CDCl_3$): δ -104.8 (s, 1F), -114.6 (s, 2F) ppm. GPC (80 °C, chlorobenzene, vs PS): M_n = 68.4 KDa, M_w = 182.2 KDa, PDI = 2.7.

Synthesis of F8BT-g-P3HT-0.5, F8BT-g-P3HT-0.2 and F8BT-g-P3HT-0.1 polymers



In a dry 20mL microwave vial equipped with a stirrer bar, P3HT-SH (0.5: 37.5 mg, 0.015 mmol, 0.2: 25.0 mg, 0.01 mmol, 0.1: 17.9 mg, 0.007 mmol), F8fBT (0.5: 16.2 mg, 0.03mmol, 0.2: 27.0 mg, 0.05 mmol, 0.1: 37.5 mg, 0.07 mmol) and K_2CO_3 (> 42 mg, 0.3 mmol) were added and degassed with nitrogen for 20 min. To the solid mixture chlorobenzene (3.4 mL) and DMF (1.7 mL) were added and degassed for a further 10 min. The solution was heated in the microwave reactor at 150 °C for 30 minutes. The reaction was cooled to room temperature, precipitated in methanol. The precipitate was collected by vacuum filtration through a nylon pad (pore size 20 µm), washed with excess methanol, followed by hot hexane to remove excess non-grafted P3HT chains and dried.

F8BT-g-P3HT 0.5: The product obtained was a deep purple fibrous solid (45.5 mg, 85% yield). ^{1}H NMR (400 MHz, $CDCl_3$): δ 8.35-7.55 (m(br), 7H, H_{Ar}+$H_{Ar\text{-}BT}$), 7.16 (m(br), 1.5H, $H_{g\text{-}e}$+H_{DFB}), 7.00 (s(br), 7H, $H_{g\text{-}c}$), 6.93 (s(br), 0.5H, $H_{g\text{-}a}$), 2.95 (m(br), 1H, $H_{g\text{-}SH\text{-}d}$), 2.81 (m(br), 15H, $H_{g\text{-}d}$), 2.61 (t(br), 1H, $H_{g\text{-}b}$), 1.80-1.65 (m, 15H, β-CH2), 1.50-1.25 (m, 45H), 1.25-1.05 (m, 24H), 1.0-0.85 (m, 24H, CH_3), 0.85-0.75 (m, 6H, CH_3) ppm. ^{19}F NMR (377 MHz, $CDCl_3$): δ -104.3 (s, 1F), -113.9 (s, 0.5F) ppm. GPC (80 °C, chlorobenzene, vs PS): M_n = 74.0 KDa, M_w = 144.1 KDa, PDI = 2.0.

F8BT-g-P3HT 0.2: The product obtained was a deep purple fibrous solid (42.6 mg, 82% yield). ^{1}H NMR (400 MHz, $CDCl_3$): δ 8.35-7.55 (m(br), 7H, H_{Ar}+$H_{Ar\text{-}BT}$), 7.16 (m(br), 0.6H, $H_{g\text{-}e}$+H_{DFB}), 7.00 (s(br), 3H, $H_{g\text{-}c}$), 6.93 (s(br), 0.2H, $H_{g\text{-}a}$), 2.95 (m(br), 0.4H, $H_{g\text{-}SH\text{-}d}$), 2.81 (m(br), 6H, $H_{g\text{-}d}$),

2.61 (t(br), 0.4H, $H_{g\text{-}b}$), 1.80-1.65 (m, 6H, β-CH2), 1.50-1.25 (m, 18H), 1.25-1.05 (m, 24H), 1.0-0.85 (m, 9H, CH_3), 0.85-0.75 (m, 6H, CH_3) ppm. ^{19}F NMR (377 MHz, $CDCl_3$): δ -104.3 (s, 0.4F), -113.9 (s, 0.8F) ppm. GPC (80 °C, chlorobenzene, vs PS): M_n = 72.4 KDa, M_w = 123.7 KDa, PDI = 1.7.

F8BT-g-P3HT 0.1: The product obtained was a deep red fibrous solid (46.5 mg, 84% yield). ^1H NMR (400 MHz, $CDCl_3$): δ 8.35-7.55 (m(br), 7H, H_{Ar}+$H_{Ar\text{-}BT}$), 7.16 (m(br), 0.3H, $H_{g\text{-}e}$+H_{DFB}), 7.00 (s(br), 1.5H, $H_{g\text{-}c}$), 6.93 (s(br), 0.1H, $H_{g\text{-}a}$), 2.95 (m(br), 0.2H, $H_{g\text{-}SH\text{-}d}$), 2.81 (m(br), 3H, $H_{g\text{-}d}$), 2.61 (t(br), 0.2H, $H_{g\text{-}b}$), 1.80-1.65 (m, 3H, β-CH2), 1.50-1.25 (m, 9H), 1.25-1.05 (m, 24H), 1.0-0.85 (m, 5H, CH_3), 0.85-0.75 (m, 6H, CH_3) ppm. ^{19}F NMR (377 MHz, $CDCl_3$): δ -104.3 (s, 0.2F), -113.9 (s, 0.9F) ppm. GPC (80 °C, chlorobenzene, vs PS): M_n = 42.7 KDa, M_w = 81.6 KDa, PDI = 1.9.

3.12 Appendix Chapter 3 - list of figures

All supplementary figures for Chapter 3 are presented in the Appendix (Chapter 8).

Figure S3.1. (a) GPC trace of crude reaction mixture at 30 and 60 minutes and (b) corresponding UV-VIS traces of polymer material eluted at 14 and 16.5 minutes.

Figure S3.2. DOSY NMR of polymer blend P3HT:F8fBT (1:1 molar blend).

Figure S3.3. DOSY NMR of polymer blend F8BT-g-P3HT.

Figure S3.4. ^{1}H NMR (left) and ^{19}F NMR (right) of P3HT-TFB.

Figure S3.5. ^{1}H NMR (left) and ^{19}F NMR (right) of P3HT-SH.

Figure S3.6. GPC trace of P3HT-TFB and P3HT-SH.

Figure S3.7. ^{1}H NMR of F8fBT where α-CH_2 is the methylene group adjacent to the conjugated polymer backbone on the C_8H_{17} sidechain.

Figure S3.8. GPC trace of starting polymers F8fBT and P3HT and graft co-polymer F8BT-g-P3HT pre-purification.

Figure S3.9. UV-Vis absorption spectra for F8fBT, P3HT and F8BT-g-P3HT in chloroform.

Figure S3.10. ^{1}H NMR (top) and ^{19}F NMR (bottom) of F8BT-g-P3HT.

Figure S3.11. ^{1}H NMR (top) and ^{19}F NMR (bottom) of F8BT-g-P3HT-0.5.

Figure S3.12. ^{1}H NMR (top) and ^{19}F NMR (bottom) of F8BT-g-P3HT-0.2.

Figure S3.13. ^{1}H NMR (top) and ^{19}F NMR (bottom) of F8BT-g-P3HT-0.1.

Figure S3.14. GPC trace of F8BT-g-P3HT-0.5, F8BT-g-P3HT-0.2 and F8BT-g-P3HT-0.1 post-purification.

Figure S3.15. PL emission spectra for F8fBT, F8BT-g-P3HT-0.1, F8BT-g-P3HT-0.2 and F8BT-g-P3HT-0.5 in chlorobenzene (5 μM).

Table S3.1. Summary of fluorescence quenching of F8fBT, F8BT-g-P3HT 0.5, F8BT-g-P3HT 0.2 and F8BT-g-P3HT 0.1.

Figure S3.16. DSC traces of F8fBT, P3HT, F8BT-g-P3HT-0.5, F8BT-g-P3HT-0.2 and F8BT-g-P3HT-0.1.

Figure S3.17. TGA curves of F8fBT, P3HT, F8BT-g-P3HT-0.5, F8BT-g-P3HT-0.2 and F8BT-g-P3HT-0.1.

Figure S3.18. GIWAXS images of P3HT:F8fBT (blend), F8BT-g-P3HT-0.5, F8BT-g-P3HT-0.2 and F8BT-g-P3HT-0.1 films as-cast and annealed at 120 °C and 150 °C.

Figure S3.19. GIWAXS diffraction patterns (complete) for P3HT:F8fBT (blend), F8BT-g-P3HT-0.1, F8BT-g-P3HT-0.2 and F8BT-g-P3HT-0.5 films as-cast and annealed at 120 °C and 150 °C.

Figure S3.20. GIWAXS images of F8fBT films as-cast and annealed at 100 °C and 200 °C (left) and GIWAXS diffraction patterns (complete) for F8fBT films as-cast and annealed at 100 °C and 200 °C.

Figure S3.21. GIWAXS diffraction patterns, OOP (left) and IP (right) for P3HT:F8fBT blend, F8BT-g-P3HT 0.5, F8BT-g-P3HT 0.2 and F8BT-g-P3HT 0.1 films annealed at 120 °C.

Figure S3.22. AFM images (10x10 μm) of P3HT:F8fBT blend, F8BT-g-P3HT 0.1, F8BT-g-P3HT 0.2 and F8BT-g-P3HT 0.5 thin films, from spin casting on Si wafer. The films were imaged as-cast and after thermal annealing (at 120 °C).

Figure S3.23. AFM images (10x10 μm) and corresponding nanosized aggregate sizes of F8BT-g-P3HT 0.5, F8BT-g-P3HT 0.2 and F8BT-g-P3HT 0.1 thin film annealed at 120 °C.

4 Chapter 4: Development of N-type Conjugated Polymer Backbones Engineered for Versatile Post-Polymerisation Modification towards Specifically Designed Functionalised Polymers

4.1 Introduction

The development of solution processable conjugated polymers (CPs) has continued to spark the interest of researchers. Interest in these materials stems from the useful semiconducting properties that allow the materials to be considered for a wide range of applications in organic electronic devices.[3,4] Applications include, but are not limited to, organic light emitting diodes (OLEDs)[5–8], organic photovoltaic (OPVs) cells[9–11], organic field effect transistors (OFETs)[12,13], organic thin film transistors (OTFTs)[14–16], organic electrochemical transistors (OECTs)[17], sensors[18–20], supercapacitors[21,22], lithium ion batteries[23–25]. Development of novel materials, designed to maximise charge mobility, have been explored for use in OTFT devices. OTFTs are a well-established principal building block for flexible, reel-to-reel processable electronic devices, displays and sensors.

A typical OTFT device architecture is comprised of an organic semiconductor thin film (active layer), a dielectric film, and three electrodes; the source (S), the drain (D) and the gate (G). Organic semiconductors can be identified by the predominant charge carrier it transports; hole carrier (p-type), electron carrier (n-type) or a balanced hole and electron carrier (ambipolar). It is well known that p-type donor CPs have been more widely explored and researched, leading to faster development comparatively to n-type acceptor CPs. Reasons for relatively slow development are revealed by consideration of the limited examples of highly electron deficient building blocks used to compose the n-type CPs. In recent years there has been a strong driving force in this area of research, not only to develop novel n-type CPs but to explore new design and synthetic techniques to enable advanced progression of n-type CPs with various properties, such as improved solubility, processability, thermal stability, flexibility.

Amongst the electron deficient building blocks, the naphthalene diimide (NDI) based building blocks have been widely investigated, in early examples as well as more recently.[226–229] The

planar conjugated naphthalene core and the electron deficient diimide groups have been shown to improve charge transport and improve chemical and photostability. Furthermore, the imide positions provide the ability to attach a variety of solubilising groups or groups with other functionality.[230,231]

Introducing functional or solubilising sidechains within the polymer chain via modification of the monomer is generally the most common method used to manipulate and tune polymer properties for specific applications. Less explored avenues to modify polymers include utilisation of post-polymerisation techniques to introduce solubilising sidechains or functionalised pendant groups. Direct post-polymerisation modification onto the polymer chain has a key advantage over monomer modification: final polymer products are comparable with respect to chain length and polydispersity. Click reactions are typically used for post-polymerisation modification.[232] Whilst click reactions seem to be an unmatched method to synthesise wide and extensive libraries of new polymer materials, there are limitations that have restricted the development of these techniques for post-polymerisation modification, such as a lack of selectivity or incomplete/partial substitution. Such challenges have meant that there are few reports of polymers synthesised via post-polymerisation modification methods.

Previous research in the group, carried out by Creamer *et.al.,* focused on using nucleophillic aromatic substitution (S_NAr) to modify poly(9,9'-dioctylfluorene-5-fluoro-2,1,3-benzothiadiazole) (F8fBT). The fluoride on 5-fluorobenzo-2,1,3-thiadiazole (fBT) repeat unit was displaced via S_NAr with a range of functionalised thiols, thioacetates and alcohols.[97] Using the easily processable F8fBT polymer, the versatility of the post-polymerisation modification was demonstrated. This work highlights the use of 5-fluorobenzo-2,1,3-thiadiazole (fBT) as an effective building block for synthesising backbone polymers that can be further functionalised via S_NAr. Development of post-polymerisation modification techniques and reports in the literature has seen examples of fully conjugated backbone polymers designed for post-polymerisation modification via S_NAr.[104,129,233] Implementation of such techniques on fully conjugated backbone polymers allows the potential to tune electronic properties, modify the planarity of the backbone, manipulate physical properties (e.g. solubility) and introduce new functionality.

This work looks at the development of n-type polymers designed for post-polymerisation modification in combination. Thus, two n-type polymers were designed, PNDI-TfBTT and PNDIV-TfBTT, to undergo post-polymerisation modification via S_NAr. The polymers were designed with two key building blocks; a strongly electron withdrawing NDI repeat unit and fBT repeat unit (also considered to be an electron withdrawing repeat unit), that can undergo S_NAr. Similar polymers, containing NDI and BT (non-fluorinated or difluorinated) repeat units, have been reported for their high electron mobility, up to 3.1 $cm^2 V^{-1} s^{-1}$, in field effect transistors (FETs) and thin film transistors (TFTs). In addition to the high electron mobility, these polymers were also shown to have low-lying LUMO energy levels in the range of -3.77 to -3.85 eV.[234] n-Type polymers with low-lying LUMO energy levels, similar to PCBM, are desirable for high efficiency in organic electronic devices.

In this chapter, the relative stability of NDI to S_NAr reaction conditions was explored followed by the demonstration of post-polymerisation modification of PNDI-TfBTT and PNDIV-TfBTT via S_NAr with an thioalkyl sidechain. As mentioned previously, performing post-polymerisation modification on the polymer backbone enables the ability to tune the polymer backbone as well as introduce new functionality. Therefore, the versatility of post-polymerisation modification through quantitative polymer substitution was explored. Further developments focused on the substitution with both a low and high quantity of a thiol-containing functional pendant group.

4.2 Synthesis of monomers and polymer backbone structures

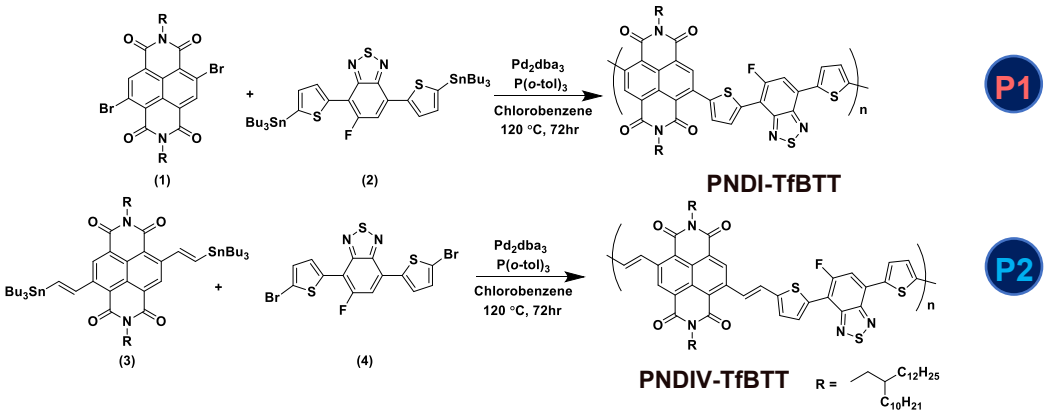
The naphthalene diimide monomers were synthesised from commercially available 2,6-dibromonaphthalene-1,4,5,8-tetracarboxydianhydride (NDA-Br_2). Monomer N,N'-bis(2-decyltetradecyl)-2,6-dibromonaphthalene-1,4,5,8-bis(dicarboximide) (1) was synthesised according to the modified reported procedure.[235] Monomer 2,7-bis(2-octyldodecyl)-4,9-bis((E)-2-(tributylstannyl)vinyl)benzo[lmn][3,8]phenanthr-oline-1,3,6,8(2H,7H)-tetraone (3) was synthesised from a reported palladium-catalysed Stille coupling reaction with trans-1,2-bis(tributylstannyl)ethene and monomer (1).[70]

Backbone polymers PNDI-TfBTT and PNDIV-TfBTT were synthesised using palladium-catalysed Stille polymerisation. Stoichiometric amounts of monomer (1) and commercially available 5-fluoro-4,7-bis(5-(trimethylstannyl)thiophen-2-yl)benzo[c][1,2,5]thiadiazole (2) were reacted

in the presence of a palladium(0) catalyst and phosphine ligand at 120 °C in chlorobenzene in a sealed vial for 3 days (Scheme 4.1). The mixture was precipitated into methanol, filtered and purified by Soxhlet extraction. Purification using Soxhlet extraction removed excess catalyst residues and low molecular weight oligomers. The final polymer PNDI-TfBTT was collected in two main fractions from (a) chlorobenzene extraction and (b) unextracted material removed from the Soxhlet thimble. The polymer product from the two fractions were isolated and dried separately, with combined yield of 87% yield.

As for PNDIV-TfBTT, stoichiometric amounts of monomer (3) and commercially available 4,7-dibromo-5-fluoro-2,1,3-benzothiadiazole (4) were reacted and purified using the same procedure as outlined above for PNDI-TfBTT. The final polymer PNDIV-TfBTT was collected in two main fractions from (a) chlorobenzene extraction and (b) unextracted material removed from the Soxhlet thimble. The polymer product from the two fractions was isolated and dried separately, with combined yield of 82% yield. The majority of PNDIV-TfBTT was not extracted into chlorobenzene therefore the unextracted polymer material was collected.

For PNDI-TfBTT, the more soluble polymer material extracted from chlorobenzene was used for quantitative substitution studies. For both PNDI-TfBTT and PNDIV-TfBTT, the unextracted polymer material was used for complete substitution reactions.

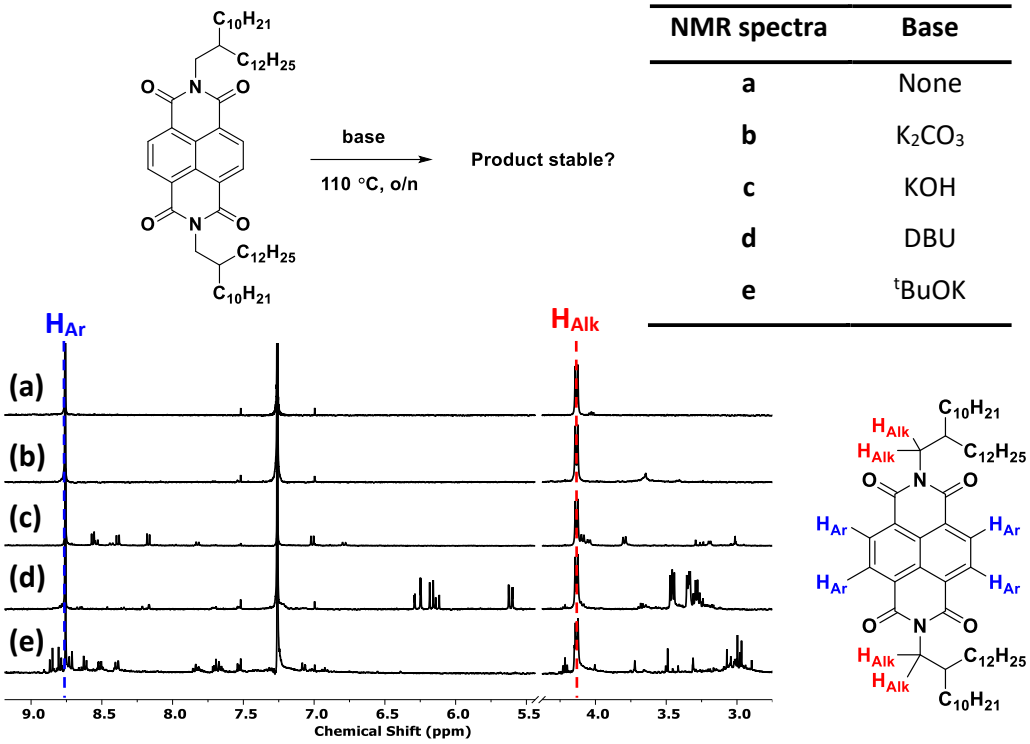


Scheme 4.1. Synthesis of NDI backbone polymers.

4.3 Hydrolysis of NDI core with stronger bases

The post-polymerisation modification (S_NAr) requires a base to deprotonate the thioalkyl sidechain. In this reaction, as the thiol has a relatively high acidity, a weak base such as K_2CO_3 was used. For nucleophiles with comparatively reduced acidity, such as alcohols or amines, a stronger base would be required for deprotonation. Therefore, to explore the versatility of the post-polymerisation modification onto the backbone polymers it was essential to test if the polymer backbones would be subject to hydrolysis in the presence of stronger base under the S_NAr reaction conditions. Previous reports have utilitsed the hydrolysis of naphthalene diimide in the presence of strong bases such as NaOH and KOH.[236,237] However, for these experiments, it was essential to avoid the hydrolysis of naphthalene diimide that could lead to unwanted defects on the polymer backbone that are not possible to isolate or remove.

For the investigation, 2,7-bis(2-decyltetradecyl)benzo[lmn][3,8]phenanthroline-1,3,6,8 (2H,7H)-tetraone (NDI) was dissolved in a chlorobenzene:DMAc (3:1) mixture and heated to 110 °C in the presence of base overnight. These conditions mimic those required for post-polymerisation modification by S_NAr reactions. As there was no nucleophile present, the NDI should not react and should remain intact. The bases tested were potassium carbonate



NMR spectra	Base
a	None
b	K_2CO_3
c	KOH
d	DBU
e	^tBuOK

Figure 4.1. ^1H NMR data of the products from the reaction (a) without base and with (b) K_2CO_3, (c) KOH, (d) DBU, and (e) ^tBuOK under S_NAr post-polymerisation modification conditions.

(K_2CO_3), potassium hydroxide (KOH, strong base, strong nucleophile), 1,8-diazabicyclo[5.4.0]undec-7-ene (DBU, non-nucleophilic base) and potassium tert-butoxide (^tBuOK, strong base, weak nucleophile). Once the reaction time was reached the mixture was precipitated into methanol. If a precipitate formed it was filtered, redissolved into chloroform and washed with water and brine. After washing, the organic phase was dried and the solvent removed to give the final product. If a precipitate did not form, the methanol was removed and the material was redissolved into chloroform and washed with water and brine. After washing, the organic phase was dried and the solvent removed to give the final product. The final products were characterised by ^1H NMR and UV-Vis to confirm if any unwanted side products were produced.

From the ^1H NMR, shown in Figure 4.1 a-e, two characteristic peaks for the NDI were observed: a singlet at δ 8.76 ppm corresponding to the four aromatic protons ($H_{Ar,}$ 4H) and a doublet at δ 4.14 ppm corresponding to the four alkyl protons adjacent to the nitrogen ($H_{Alk,}$ 4H). Any other peaks appearing in the aromatic region indicated unwanted formation of side products. Comparing ^1H NMR spectra of starting material (Figure 4.1a) to the NMR of the resulting products from the base stability experiments, it was possible to determine whether the NDI was altered. When the NDI molecule was reacted under S_NAr post-polymerisation modification conditions in the presence of K_2CO_3 (Figure 4.1b) only the characteristic peaks for NDI were observed. The lack of new peaks in the ^1H NMR suggests the NDI remained unaltered. When the NDI molecule was reacted under S_NAr post-polymerisation modification conditions in the presence of KOH, DBU and ^tBuOK, new peaks in and outside of the aromatic region were observed in ^1H NMR (Figure 4.1 c-e), indicating the formation of unwanted side products.

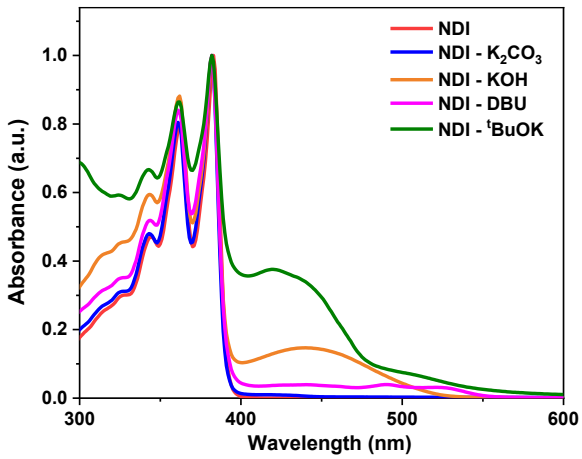


Figure 4.2. UV-Vis absorption spectra of the products from the reaction (a) without base and with (b) K_2CO_3, (c) KOH, (d) DBU, and (e) ^tBuOK under S_NAr post-polymerisation modification conditions.

UV-Vis spectra, shown in Figure 4.2a-e, was used as further confirmation for any stuctural changes to the NDI molecule. No shift or emergence of new peaks was observed after the NDI molecule was reacted in the presence of K_2CO_3. Both the UV-Vis and ^{1}H NMR data confirms the structure of the NDI was unchanged. However, when the NDI molecule was reacted under S_NAr post-polymerisation modification conditions in the presence of KOH, DBU and ^{t}BuOK, a new broad low energy absorption band was revealed. Considering the UV-Vis and NMR data, it was deduced that KOH, DBU and ^{t}BuOK were not suitable bases for S_NAr reactions with NDI containing backbone polymers PNDI-TfBTT and PNDIV-TfBTT. For subsequent S_NAr reactions with NDI based polymer backbones, K_2CO_3 was used as a base to deprotonate nucleophiles terminated with thiol or thioacetate.

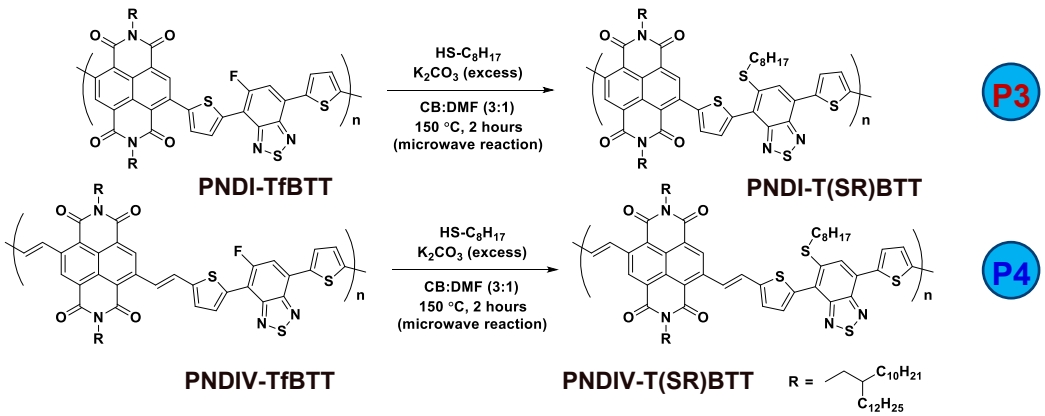
4.4 Synthesis of substituted polymer structures

Post-polymerisation modification directly onto the polymer backbone was investigated via nucleophilic aromatic substitution (S_NAr), where a thiol-terminated sidechain was used to displace the fluoride on the benzothiadiazole unit. Displacement with a thiol-terminated sidechain allows the employment of mild reaction conditions due to the increased nucleophilicity of the thiol compared to alcohols and thioacetate, as discussed in Section 4.3. Backbone polymers PNDI-TfBTT and PNDIV-TfBTT (from the unextracted fraction) were functionalised with commercially available 1-ocatanethiol, in the presence of K_2CO_3, in a chlorobenzene/DMF (3:1) solvent mixture (Scheme 4.2). Complete substitution on the polymer backbone was observed after reacting at 150 °C for 2 hours in a microwave reactor (Biotage Initiator). The mixtures were precipitated into methanol and purified by Soxhlet extraction to remove any excess base and thiol. Finally, the polymers were extracted with chloroform to afford dark blue solids, PNDI-T(SR)BTT and PNDIV-T(SR)BTT, in a yield of 62% and 48% respectively. Both alkyl-functionalized polymers were found to be more soluble with the substitution of solubilising alkyl chains, where the substituted polymers were extracted with chloroform. In comparison, the starting backbone polymers could not be extracted with chloroform or chlorobenzene.

PNDI-TfBTT, PNDIV-TfBTT, PNDI-T(SR)BTT and PNDIV-T(SR)BTT were fully characterised and their structures confirmed by ^{1}H NMR and ^{19}F NMR shown in Figures S4.15-S4.22. For PNDI-TfBTT and PNDIV-TfBTT broad signals in the ^{1}H NMR indicates the polymeric structure of the

material. In addition, for both polymers a signal in the ^{19}F NMR was observed, corresponding to the fluorine on the fBT repeat unit. Due to the increased planarity of the polymer, enabled by the vinylene spacer, PNDIV-TfBTT was found to strongly aggregate resulting in a reduced intensity in NMR signals. Similar aggregation effects were previously reported for conjugated co-polymers containing vinylene flanked NDI repeat units.[70]

Upon complete substitution on the polymer backbone with 1-octanethiol, a characteristic peak appears in the ^{1}H NMR at δ 3.2 ppm corresponding to the two CH_2 protons adjacent to the thiol. For PNDI-T(SR)BTT, by comparing integral values of the peak at δ 3.2 ppm (2H) with the characteristic aromatic peak corresponding to the two aromatic protons on the NDI core repeat unit at δ 8.9 ppm (2H), the complete substitution with 1-octanethiol was confirmed. Complete substitution, and displacement of fluoride, was further confirmed by the absence of a signal in the ^{19}F NMR. For PNDIV-T(SR)BTT, the peak at δ 3.2 ppm (2H) was compared with the broad aromatic peak at δ 9.5-8.0 ppm (6H) corresponding to the two protons on the NDI core and the four protons on the flanking vinylene groups. Comparison of the integral values for the ^{1}H NMR peaks showed complete substitution with 1-octanethiol and the absence of a signal in the ^{19}F NMR confirmed the full displacement of the fluoride.



Scheme 4.2. Post-polymerisation modification of NDI backbone polymers with 1-octanethiol.

Size exclusion chromatography (SEC) using an analytical gel permeation chromatography (GPC) system in chlorobenzene at 80 °C was used to determine the number-average molecular weight (M_n) of the polymers, against polystyrene standards. The backbone polymers PNDI-TfBTT and PNDIV-TfBTT, extracted from chlorobenzene, were found to have M_n values 49 and 83 kDa with polydispersity index (Đ) 3.4 and 2.0 respectively. Due to the planarity of PNDIV-TfBTT the polymer strongly aggregates, therefore, the M_n value for PNDIV-

TfBTT was expected to be an overestimation of the true value. The unextracted polymer fractions could not be analysed by GPC due to the poor solubility in chlorobenzene.

Polymers PNDI-T(SR)BTT and PNDIV-T(SR)BTT were synthesised from the unextracted starting polymers, PNDI-TfBTT and PNDIV-TfBTT respectively. Post alkyl substitution, the polymer was completely soluble in chloroform and chlorobenzene. PNDI-T(SR)BTT and PNDIV-T(SR)BTT were found to have M_n values 53 and 60 kDa with polydispersity index (Đ) 1.6 and 2.2 respectively. Upon substitution onto the polymer backbone, not only have more soluble alkyl chains been introduced, inclusion of the alkyl chains also induces an increased degree of twisting in the polymer backbone, supported by DFT calculations summarised in Table S4.1. This increased degree of twisting disrupts the planarity of the polymer structure, therefore, the potential for the polymer to aggregate was reduced.

Table 4.1. GPC data of PNDI-TfBTT, PNDIV-TfBTT, PNDI-T(SR)BTT and PNDIV-T(SR)BTT.

Polymer	M_n (kDa)	M_w (kDa)	DP_n[a]	DP_w[b]	Đ[c]
PNDI-TfBTT	49	166	39	132	3.4
PNDIV-TfBTT	83	170	64	130	2.0
PNDI-T(SR)BTT	53	86	39	97	1.6
PNDIV-T(SR)BTT	60	129	42	90	2.2

[a]Degree of polymerisation calculated from M_n
[b]Degree of polymerisation calculated from M_w
[c]Polydispersity index M_w/M_n

4.5 Optical properties

For the polymer backbones and corresponding alkyl substituted polymers, the UV-Vis absorption spectra in solution (chlorobenzene) and film are shown in Figure 4.3. Thin films were prepared by spin-coating onto glass from chlorobenzene solutions. In this section, variation in the UV-Vis absorption upon (a) substitution of thioalkyl onto the NDI polymer backbone and (b) the inclusion of the vinylene groups (flanking the NDI unit) was investigated. Characteristic absorption features have been summarised in Table 4.2.

In solution, PNDI-TfBTT and PNDI-T(SR)BTT both show three main absorption bands. Two of the absorption bands were identified as high energy bands, at approximately 300-400 nm and 400-525 nm, assigned to the π-π* transition of the NDI and fBT units respectively.[238] The third key absorption band, observed at a lower in energy in the range of 525-800 nm, can be assigned to intramolecular charge transfer (ICT) from thiophene (electron rich) to NDI/fBT (electron poor) moieties.[239,240] Post thioalkyl substitution, the ICT absorption peak blue-shifts from 710 nm (PNDI-TfBTT) to 575 nm (PNDI-T(SR)BTT), corresponding to 1.75 eV to 2.16 eV respectively, thus a shift of 0.41 eV was observed. In this case, twisting of the backbone was induced by introduction of the large thioether group, with such twisting causing a reduction in the effective conjugation length. This observation is further supported by DFT calculations of the energy minimised oligomeric structures summarised in Table S4.1. Absorption spectra of PNDI-TfBTT and PNDI-T(SR)BTT thin films also showed two characteristic absorption peaks from the π-π* transition (400-550 nm) and the ICT (550-800 nm). Similar to the solution absorption spectra, after thioalkyl substitution the ICT absorption peak for blue-shifts slightly from 695 nm (PNDI-TfBTT) to 650 nm (PNDI-T(SR)BTT), corresponding to 1.78 eV to 1.90 eV

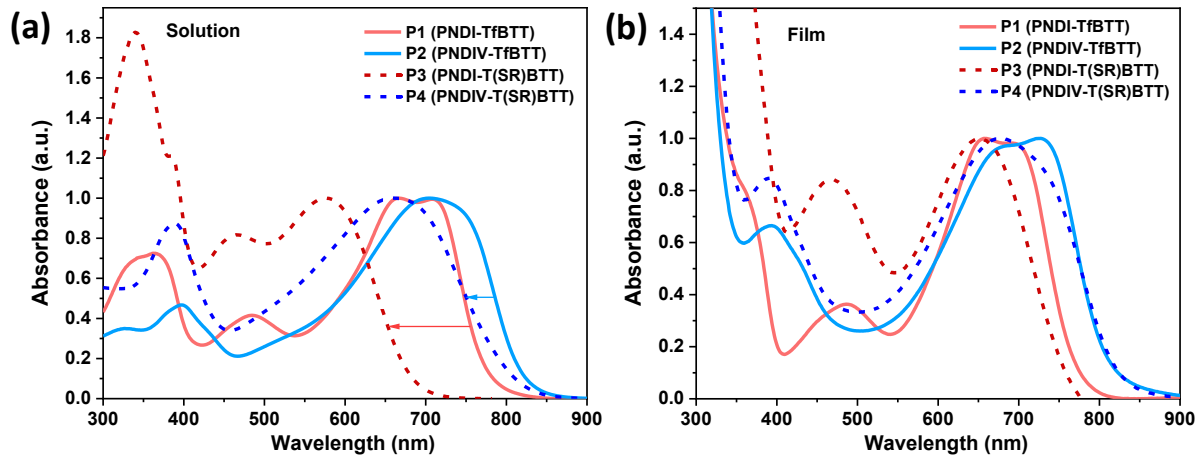


Figure 4.3. UV-Vis absorption spectra for (a) PNDI-TfBTT, PNDIV-TfBTT, PNDI-T(SR)BTT and PNDIV-T(SR)BTT in chlorobenzene (dilute) and (b) as a spun-cast thin film onto glass.

respectively, thus a shift of 0.12 eV was observed. The observed blue shift could be owed to the reduced conjugation along the PNDI-T(SR)BTT backbone. The reduced degree of blue-shift in the absorption spectra, likely due to a less pronounced backbone twist, of the thin film compared to the solution suggests the electronic properties of PNDI-TfBTT and PNDI-T(SR)BTT thin films may only differ slightly.

For the vinylene based polymer in solution, PNDIV-TfBTT and PNDIV-T(SR)BTT, two main absorption bands were observed, attributed to the π-π* transition (350-450 nm) and ICT (550-850 nm), as described previously. Post thioalkyl substitution, the ICT absorption peak blue-from 710 nm (PNDIV-TfBTT) to 665 nm (PNDIV-T(SR)BTT), corresponding to 1.75 eV to 1.86 eV respectively, thus a shift of 0.11 eV was observed, less than that observed for the non-vinylene containing polymer. Additionally, the thin film absorption spectra for PNDIV-TfBTT and PNDIV-T(SR)BTT shows a blue-shift of the ICT absorption peak from 724 nm (PNDIV-TfBTT) to 680nm (PNDIV-T(SR)BTT), corresponding to 1.71 eV to 1.82 eV respectively, thus a shift of 0.11 eV was observed. No change to the onset of absorption, post thioalkyl substitution onto PNDIV-TfBTT, was recorded.

In both solution and thin film spectra, for vinylene and non-vinylene containing polymers, a blue shift was observed after the thioalkyl sidechain had been substituted onto the polymer backbone, associated with a reduced level in conjugation along the backbone. The reduction of conjugation in the backbone was found to be less prominent for the vinylene containing polymer compared to the non-vinylene containing polymer.

From solution to thin film, polymers generally exhibit a red-shift in the absorption spectra due to solid-state packing effects. For the backbone polymers, PNDI-TfBTT and PNDIV-TfBTT, the spectra were not red-shifted. For the alkyl substituted polymers, PNDI-T(SR)BTT and PNDIV-T(SR)BTT the spectra were red-shifted, the onset of absorption wavelength increased by 85 and 13 nm corresponding to 0.19 and 0.02 eV respectively. The degree of red-shift for the polymers can be attributed to the level of planarisation of the polymer backbone, where the larger shift corresponds to increased planarisation.

In the solid-state UV-Vis absorption spectra, the onset of absorption for PNDI-TfBTT, PNDI-T(SR)BTT, PNDIV-TfBTT and PNDIV-T(SR)BTT were found to be 773, 770, 812, 822 nm with the respective measured bandgap values of 1.60, 1.63, 1.53, 1.50 eV. A large shift in the onset of

absorption was not observed, hence, the corresponding similarity of the optical bad gap measured, for the backbone polymer and respective alkyl substituted polymer.

Table 4.2. Optical and electronic properties for PNDI-TfBTT, PNDIV-TfBTT, PNDI-T(SR)BTT and PNDIV-T(SR)BTT.

Polymer	$\lambda_{abs,max}$ (nm), solution	$\lambda_{abs,max}$ (nm), film	λ_{onset} (nm), solution	λ_{onset} (nm), film	$E_{g,opt}$[a] (eV)
PNDI-TfBTT	365, 485, 666, 710	485, 660, 695	773	773	1.60
PNDIV-TfBTT	325, 400, 710	392, 680, 724	819	812	1.53
PNDI-T(SR)BTT	340, 385, 460, 575	468, 650	685	770	1.61
PNDIV-T(SR)BTT	390, 665	390, 680	809	822	1.50

[a]Estimated from the onset of absorption from the measured thim film UV-Vis absorption spectra where E = hc/λ

4.6 Electronic properties

In this section, the HOMO and LUMO energy levels of the polymer thin films measured by photoelectron spectroscopy in air (PESA) were evaluated (see Table 4.3 for corresponding data). Furthermore, the experimental data was evaluated against computational data from density functional theory (DFT). In our investigation, the effects of (a) the inclusion of the vinylene groups (flanking the NDI unit) and (b) substitution of thioalkyl onto the NDI polymer backbone on the measured energy levels are discussed.

PESA measurements for PNDI-TfBTT, PNDI-T(SR)BTT, PNDIV-TfBTT and PNDIV-T(SR)BTT are shown in Figure S4.1. The ionisation potential (IP) of the polymer thin films were measured by PESA and the highest occupied molecular orbital (HOMO) energy levels were approximated as the negative of the ionisation potential. The lowest unoccupied molecular orbital (LUMO) energy levels were estimated from the HOMO energy values plus the optical band gap ($E_{g,opt}$). The HOMO energy levels were estimated as -5.67, -5.53, -5.47 and -5.35 eV respectively. The lowest unoccupied molecular orbital (LUMO) energy levels were estimated as -4.07, -3.92, -3.94 and -3.85 eV respectively.

Firstly, the effect on the measured energy levels after inclusion of the vinylene group into the polymer backbone were evaluated. Based on literature reports, it would be sensible to predict that the reduced level of twisting in the backbone and greater co-planar crystallinity from the added vinylene moiety would lead to a slight increase HOMO and LUMO energy.[241,242] As predicted, a small increase in the HOMO and LUMO energy levels of ~0.2 eV and ~0.1 eV respectively was observed.

Secondly, the effect on the energy levels after thioalkyl substitution onto the polymer was evaluated. From PNDI-TfBTT and PNDIV-TfBTT to PNDI-T(SR)BTT and PNDIV-T(SR)BTT respectively, a slight increase in both the HOMO and LUMO energy levels by approximately 0.1-0.15 eV was noted. Following displacement of the fluoride on the backbone polymer, the frontier molecular orbital levels increase, as the PESA measurements show, where the accuracy of the measurement is ±0.05 eV.[63,173]

DFT calculations were performed on the oligomers shown in Figure S4.3-S4.6 (B3LYP level of theory and a basis set of 6-31G). From the DFT calculations the HOMO and LUMO energy levels of the polymers were estimated, shown in Table 4.3. The estimated frontier orbital levels from DFT broadly agree with the observed trends from the PESA measurements for both (a) the inclusion of the vinylene group and (b) the inclusion of a thioalkyl substituent.

Table 4.3. Electronic properties for PNDI-TfBTT, PNDIV-TfBTT, PNDI-T(SR)BTT and PNDIV-T(SR)BTT.

Polymer	HOMO[a] (eV) PESA	LUMO[b] (eV) PESA	$E_{g,opt}$[c] (eV)	HOMO[d] (eV) DFT	LUMO[d] (eV) DFT
PNDI-TfBTT	-5.67	-4.07	1.60	-5.55	-3.51
PNDIV-TfBTT	-5.47	-3.94	1.53	-5.40	-3.51
PNDI-T(SR)BTT	-5.53	-3.92	1.61	-5.54	-3.45
PNDIV-T(SR)BTT	-5.35	-3.85	1.50	-5.41	-3.43

[a]Estimated from the ionisation potential from the measured PESA spectra

[b]LUMO = HOMO + $E_{g,opt}$

[c]Estimated from the onset of absorption from the measured UV-VIS spectra where E = hc/λ

[d]Calculated with DFT (B3LYP level of theory and a basis set of 6-31G)

4.7 Thermal properties

Thermogravimetric Analysis (TGA) and Differential Scanning Calorimetry (DSC) techniques were used to investigate the degradation, melt and recrystallisation temperatures for PNDI-TfBTT, PNDI-T(SR)BTT, PNDIV-TfBTT and PNDIV-T(SR)BTT, shown in Figure 4.4.

The degradation temperature was determined from the TGA curve, the polymer was heated from 25 to 750 °C at 5 °C min^{-1} under nitrogen. The TGA curve indicated for all four polymers, PNDI-TfBTT, PNDIV-TfBTT, PNDI-T(SR)BTT, and PNDIV-T(SR)BTT, exhibits a reasonable thermal stability with recorded degradation temperatures of 441, 413, 346 and 393 °C respectively, where 5% weight loss was observed. Comparatively, the unsubstituted backbone polymers show a higher thermal stability than the thioalkyl substituted polymers.

Melt and recrystallisation temperatures were determined from the DSC curves. DSC analysis was carried out from 40 °C up to a temperature below the degradation temperature observed from the TGA, the upper temperature limit varied for each polymer. PNDI-TfBTT showed a distinct melt and recrystallisation peak with an onset of 347 and 322 °C respectively. Post thioalkyl substitution no defined phase transitions were observed, potentially due to restricted upper temperature limit of 300 °C. The DSC curve for PNDIV-TfBTT revealed an energetically less intense melt and recrystallisation transition compared to PNDI-TfBTT, with an onset of 141 and 112 °C. Post thioalkyl substitution, PNDIV-T(SR)BTT showed a clear melt and recrystallisation transition with an onset of 324 and 315 °C. From the TGA and DSC analysis, an annealing temperature range between 120 °C and 250 °C was selected to investigate the electrical properties of the polymers within OTFT devices.

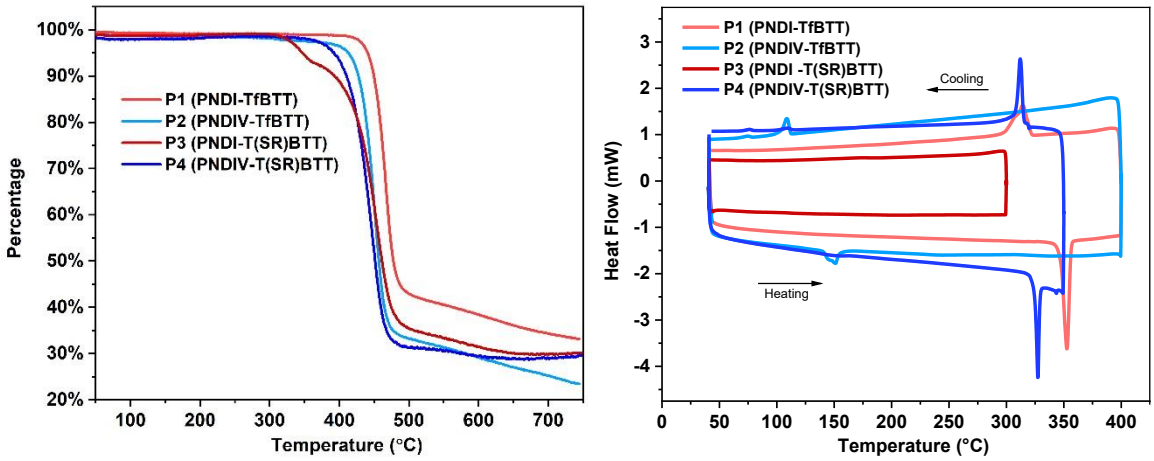


Figure 4.4. (a) TGA data for PNDI-TfBTT, PNDIV-TfBTT, PNDI-T(SR)BTT and PNDIV-T(SR)BTT carried out in a nitrogen atmosphere at 5 °C min^{-1} (b) DSC data for PNDI-TfBTT, PNDIV-TfBTT, PNDI-T(SR)BTT and PNDIV-T(SR)BTT carried out in a nitrogen atmosphere at 10 °C min^{-1}.

4.8 Thin film morphology

Analysis of the charge transport properties in OTFT devices required the polymers to be deposited as thin films. It was important to consider the thin film morphology as it is known to impact the device performance. From previous reports, the presence of larger crystalline domains suggests higher charge transport mobility within semiconductor materials.[243–245] Therefore, it was important to determine the degree of crystallinity of the thin films annealed at different temperatures. The crystallinity was determined by Grazing-Incidence Wide-Angle X-ray Scattering (GIWAXS).

All polymers, PNDI-TfBTT, PNDI-T(SR)BTT, PNDIV-TfBTT and PNDIV-T(SR)BTT, were dissolved in chlorobenzene (5 mg/mL) and spun directly onto silicon wafer substrates. To determine how the thin film morphology changes with different annealing temperatures the films were analysed as-cast and annealed for 30 minutes at 100 °C and 200 °C. The GIWAXS patterns are presented in Figure 4.5 and S4.7. Complete (combined in-plane (IP) and out-of-plane (OOP)) diffraction curves for all polymers after annealing at 200 °C (Figure 4.5) show a distinct diffraction peak (100), with q value at 2.55, 2.40, 2.61 and 2.40 nm^{-1} corresponding to an interlayer d-spacing of 24.6, 26.2, 24.1 and 26.2 Å respectively. The diffraction peak (100) signifies lamellar-type packing of the conjugated polymer strands. Introduction of the vinylene spacer into the backbone decreases the lamellar spacing, suggesting that the polymer chains are more densely packed together. Introduction of the thioalkyl chain encourages the polymer chains to pack less densely and the observed lamellar spacing increases. In addition to the first order lamellar peak (100), PNDI-TfBTT shows a further advancement up to the fifth order (500), hence, an increased degree of structural order in the edge-on orientation. For PNDIV-TfBTT and PNDI-T(SR)BTT, lamellar peaks up to the second order (200) were measured, thus, comparatively reduced degree of structural order. The lowest degree of structural order was observed for PNDIV-T(SR)BTT with solely the first order lamellar peak (100).

For the backbone polymers PNDI-TfBTT and PNDIV-TfBTT, π-π stacking was prominently oriented in-plane, with diffraction peaks at 16.5 and 17.7 nm^{-1} and a corresponding d-spacing of 3.8 and 3.5 Å. The d-spacing for PNDIV-TfBTT at 3.5 Å is amongst the shortest observed for NDI based polymers. From previous reports, it was found that the vinylene spacer generally

reduces the torsion in the conjugated polymer backbone, facilitating more efficient polymer packing.[70] From the diffraction patterns, a pronounced edge-on orientation can be assigned to the polymer packing in thin films of PNDI-TfBTT and PNDIV-TfBTT. The π-π stacking orientation was altered for PNDI-T(SR)BTT and PNDIV-T(SR)BTT, the polymer chains in the thin film orient prominently in the OOP directions with diffraction peaks at 16.4 and 17.5 nm^{-1} and a corresponding d-spacing of 3.8 and 3.6 Å. Upon inclusion of the thioalkyl sidechain the d-spacing is marginally increased, despite the difference in orientation. A bimodal face-on and edge-on orientation was assigned to PNDI-T(SR)BTT and PNDIV-T(SR)BTT. GIWAXS patterns of PNDI-T(SR)BTT and PNDIV-T(SR)BTT confirm the thin films have a reduced degree of crystallinity, evidenced by the weaker (100) and (010) diffraction peaks orientated in-plane (IP) and out-of-plane (OOP).

The GIWAXS data shows the crystalline domains were maximised when annealed at 200 °C, therefore, increased mobility should be observed for all four polymer thin films when annealed at 200 °C or above.

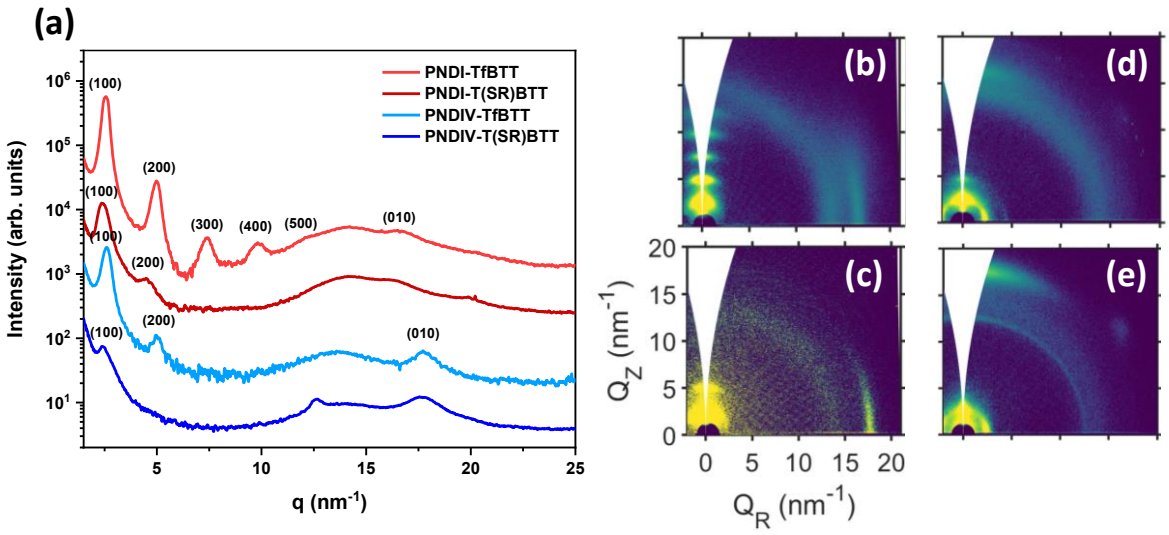


Figure 4.5. (a) GIWAXS diffraction patterns, combined IP and OOP, for PNDI-TfBTT, PNDIV-TfBTT, PNDI-T(SR)BTT and PNDIV-T(SR)BTT films annealed at 200 °C. GIWAXS diffraction images for (b) PNDI-TfBTT, (c) PNDIV-TfBTT, (d) PNDI-T(SR)BTT and (e) PNDIV-T(SR)BTT thin films annealed at 200 °C.

4.9 OTFT charge transport properties

All polymer OTFT devices were fabricated with a top-gate bottom-contact (TG/BC) configuration, containing gold source and drain electrodes, a poly(methylmethacrylate) (PMMA) dielectric and an aluminium gate electrode, as shown in Figure 4.6b. Polymers were deposited from dichlorobenzene solutions (5 mg/mL) via spin coating. The thin films were then dried and annealed at a range of temperatures, from 120 to 250 °C, for 30 minutes before PMMA (gate insulator) was spun and annealed at 95 °C for 2 hours. Finally, the Al gate electrode was deposited by thermal evaporation. The fabricated devices were used to determine the electron charge carrier mobility for each polymer. The optimum annealing temperature was identified by measuring the electron mobility (μ_e) after annealing at 120, 150, 180, 200, 220 and 250 °C. The maximum electron mobility was recorded for all four polymers after annealing at 200 °C or above, shown in Table 4.4, and is in agreement with observations from the GIWAXS data where crystalline domains are maximised after annealing at 200 °C or above.

The transfer characteristics for PNDI-TfBTT, PNDI-T(SR)BTT, PNDIV-TfBTT and PNDIV-T(SR)BTT are shown in Figure 4.6 and Figures S4.9 to S4.13 under a positive gate bias. From the measurements, PNDI-TfBTT was shown to have the highest electron mobility of 0.16 $cm^2 V^{-1} s^{-1}$. It was projected that a higher degree of microstructural order within the deposited and annealed thin films, could result in an increased ability for the semiconducting material to transport electrons.[243–245] From previous reports in the literature, the polymer containing the vinylene spacer could be expected to have an improved electron mobility due to the polymers ability to pack more densely (d-spacing 3.5 Å from the GIWAXS analysis).[246] In the case for PNDIV-TfBTT, there was no improvement in electron mobility compared to the non-vinylene analogue. Instead, the electron mobility reduces by more than two-thirds to 0.047 $cm^2 V^{-1} s^{-1}$, compared to PNDI-TfBTT. The reduced mobility for the vinylene containing polymer is

Table 4.4. Summary of OTFT data for PNDI-TfBTT, PNDIV-TfBTT, PNDI-T(SR)BTT and PNDIV-T(SR)BTT with a (TG/BG) configuration.

Polymer	$\mu_{e,av}$ ($cm^2V^{-1}s^{-1}$)	$\mu_{e,max}$ ($cm^2V^{-1}s^{-1}$)	Temperature annealed (°C)	Optimum annealing temperature (°C)
PNDI-TfBTT	1.4×10^{-1}	1.6×10^{-1}	200	180 - 200
PNDIV-TfBTT	3.7×10^{-2}	4.7×10^{-2}	220	220
PNDI-T(SR)BTT	1.3×10^{-2}	1.5×10^{-2}	250	250
PNDIV-T(SR)BTT	1.4×10^{-2}	1.4×10^{-2}	220	220

consistent with the thin film morphology, where comparatively lower overall crystallinity was observed for PNDIV-TfBTT by GIWAXS. Previous reports in literature have confirmed a similar reduction in thin film crystallinity upon incorporation of a vinylene linker within the polymer backbone with a corresponding reduction in charge carrier mobility when compared with their non-vinylene containing analogue.[247,248]

Post-substitution with the thioalkyl, the induced twisting in the backbone was expected to reduce the electron mobility.[249] A reduction in electron mobility was indeed observed for both PNDI-T(SR)BTT and PNDIV-T(SR)BTT compared to the unsubstituted backbone polymer. For PNDI-T(SR)BTT a reduction by one order of magnitude from 0.16 $cm^2 V^{-1} s^{-1}$ (PNDI-TfBTT) to 0.015 $cm^2 V^{-1} s^{-1}$ (PNDI-T(SR)BTT) and for PNDIV-T(SR)BTT a reduction from 0.047 $cm^2 V^{-1} s^{-1}$ (PNDIV-TfBTT) to 0.014 $cm^2 V^{-1} s^{-1}$ (PNDIV-T(SR)BTT) was observed. The reduction in electron mobility for the thioalkyl substituted polymers correlates with the reduced degree of crystallinity shown in the thin film morphology measured by GIWAXS.

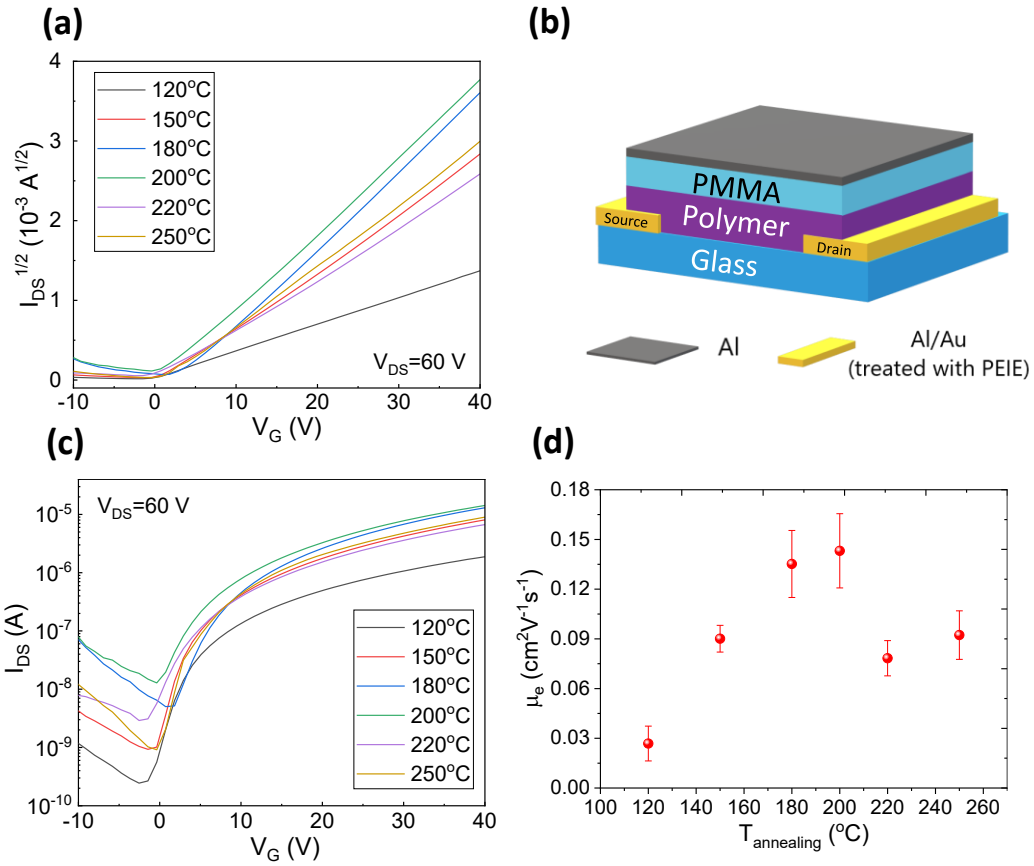


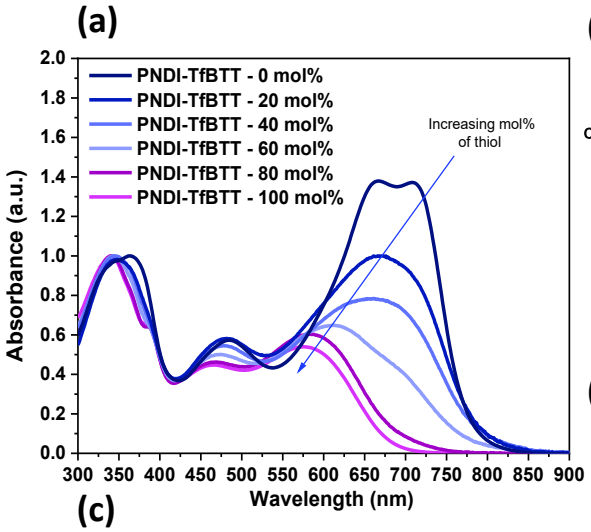
Figure 4.6. Transfer (a,c) characteristics of PNDI-TfBTT OTFT device. (b) OTFT device architecture. (d) Electron mobility vs. annealing temperature of polymer thin film.

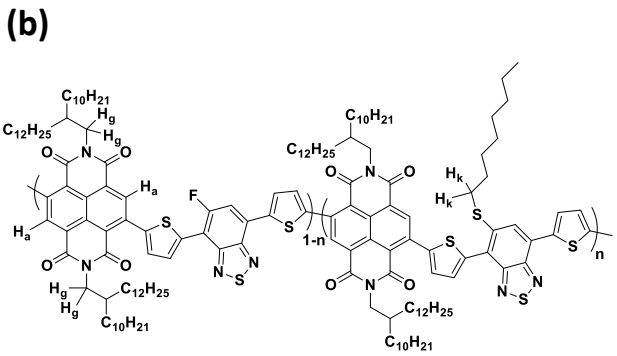
4.10 Quantitative post-polymerisation substitution on PNDI-TBTT

Quantitative substitution of thioalkyl sidechains onto a polymer backbone, via S_NAr onto the fluorinated benzothiadiazole unit, has been previously demonstrated for F8fBT.[97] In this section, quantitative substitution of the thioalkyl reagent was explored, in a similar way, by controlling the molar quantity of sidechain added. Displacement of fluoride by the thioalkyl sidechain was confirmed by ^{1}H NMR. Integration values for the signal at δ 3.21 ppm, corresponding to the -CH_2- adjacent to the thioether (XH), and the signal at δ 8.98 ppm, corresponding to the aromatic protons on the NDI unit (2H), were compared. As the quantity of thiol added was increased, the integrated signal at δ 3.21 ppm increased relative to the 2H at δ 8.98 ppm, hence, the degree of substitution along the polymer backbone increased. Whilst the integrated values confirm a controlled degree of substitution, the expected integrated value did not perfectly match with the measured integrated values. Deviation of the measured values from the expected values in ^{1}H NMR could be related to aggregation of the polymer in solution. ^{1}H NMR spectra were measured at high temperature (393K), due to the low solubility of the polymer, but even at high temperature aromatic and aliphatic signals could be affected by aggregation of the polymer.

Further analysis of the quantitative substitution onto the polymer backbone looked at the absorption spectra for each polymer, shown in Figure 4.7a. Upon substitution onto the polymer backbone, a distinct blue shift was observed and the absorption band edge was shifted to shorter wavelengths. The band edge does not shift significantly up to 40 mol% substitution, but further substitution (60 mol% or greater) does result in a significant blue shift. The observed blue-shift in the spectra indicates an increased degree of twisting in the polymer backbone, resulting in reduced conjugation along the polymer backbone. The relative intensity of the low energy ICT absorption (525-825 nm) and low energy π-π* transition (400-525nm) gradually decreases with increasing sidechain substitution along the backbone, comparatively to the high energy π-π* transition at 300-400 nm. The high energy π-π* transition starts to shift slightly, revealing a shoulder at ~385 nm. Emergence of the shoulder at ~385 nm could be associated with the attachment of the thioalkyl substituent. Previous reports show a new absorption peak at ~370 nm after thioalkyl inclusion onto F8fBT.[97]

The ability to quantitatively incorporate thiol/thioacetate terminated substituents enables quantitative substitution of functionality along the polymer backbone. Quantitative substitution onto the polymer backbone opens up the opportunity to tune a variety of polymer properties, including optical, electronic, thermal properties.





(c)

mol% of thiol added	X H_k (expected)	X H_k (measured)
0.00	0.00	0.11
0.20	0.40	0.62
0.40	0.80	0.87
0.60	1.20	1.22
0.80	1.60	1.86
1.00	2.00	2.18

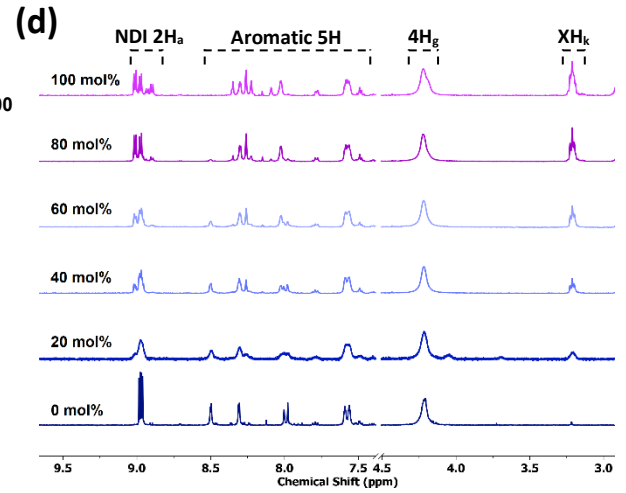
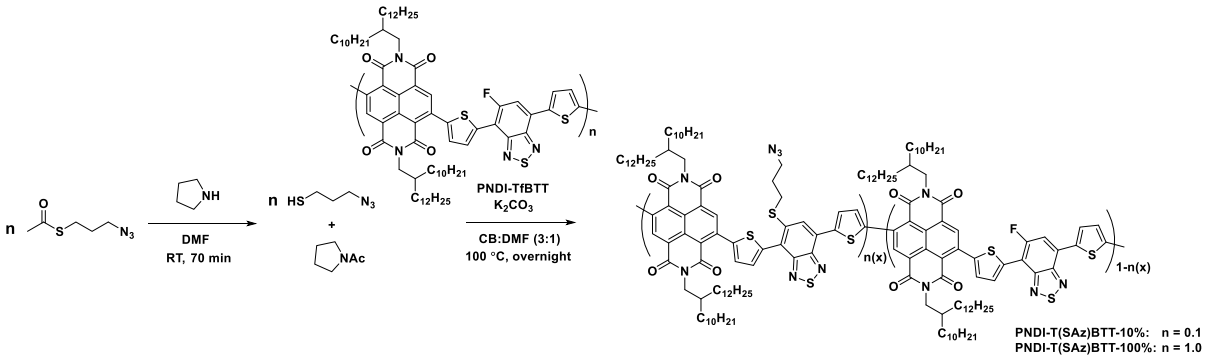


Figure 4.7. Quantitative substitution of octanethiol onto PNDI-TfBTT backbone (a) UV-Vis absorption spectra (normalised to the peak at 350-370nm) for the unsubstituted (0 mol%), partially substituted (20, 40, 60, 80 mol%) and fully substituted (100 mol%) polymers, (b) structure of the PNDI-TfBTT based polymers, (c) table of expected and measured integration values for H_k vs H_a by NMR, (d) ^{1}H NMR spectra for increasing substitution along the PNDI-TfBTT backbone where the aromatic peaks for H_a were set to an integral of 2H and directly compared with XH_k.

4.11 Inclusion of azide functionality on PNDI-TfBTT

Thus far, PNDI-TfBTT has been as an ideal backbone polymer for post-polymerisation modification via S_NAr, where a thiol was used to displace the fluoride on the fBT repeat unit. Additionally, quantitative substitution onto the polymer backbone was demonstrated by controlling the mol% of thioalkyl added. In this section, the inclusion of an azide ($-N_3$) functional group at the end of a short alkyl chain was investigated. Azide terminated pendant groups are interesting for various processes including their ability to crosslink both thermally and photochemically. Therefore, two polymers were synthesised using post-polymerisation modification via S_NAr: PNDI-T(SAz)BTT – 10% (low azide content) and PNDI-T(SAz)BTT – 100% (high azide content). Low and high azide content polymers were chosen to investigate thermal and photochemical crosslinking, and the effects on thin film morphology and OTFT charge transport properties.



Scheme 4.3. Post-polymerisation modification of NDI backbone polymers with 3-azidopropane-1-thiol.

The backbone polymer PNDI-TfBTT was reacted with 3-azidopropane-1-thiol in the presence K_2CO_3 in a chlorobenzene/DMF (3:1) solvent mixture. The reactant 3-azidopropane-1-thiol was not commercially available and was therefore synthesised and reacted in situ. To synthesise 3-azidopropane-1-thiol, commercially available S-(3-azidopropyl)thioacetate was reacted with pyrrolidine in DMF at room temperature for approximately 70 minutes. The resulting mixture was added to a solution of PNDI-TfBTT and K_2CO_3 in chlorobenzene/DMF (3:1) and reacted at 100 °C overnight in an oil bath. For (a) PNDI-T(SAz)BTT – 10% (low azide content): 0.1 mol% 3-azidopropane-1-thiol was reacted relative to the polymer repeat unit and (b) PNDI-T(SAz)BTT – 100% (high azide content): 1.0 mol% 3-azidopropane-1-thiol was reacted relative to the polymer repeat unit. The mixtures were precipitated into methanol and purified by Soxhlet extraction to remove the acetylpyrrolidine (formed in the synthesis of 3-azidopropane-1-thiol), excess base and unreacted 3-azidopropane-1-thiol. In the final

Soxhlet extraction step, the polymers PNDI-T(SAz)BTT – 10% and PNDI-T(SAz)BTT – 100% were treated with chloroform. PNDI-T(SAz)BTT – 100% was mostly dissolved with chloroform to afford a dark blue solid after evaporation of the solvent (69% yield). The partially substituted polymer PNDI-T(SAz)BTT – 10% could not be dissolved in chloroform. This polymer was collected from the Soxhlet thimble and dried to give a dark blue solid (85% yield). Substitution of S-(3-azidopropyl)thioacetate directly onto the polymer backbone can be achieved using a strong base, such as KOH, as demonstrated by Creamer *et. al*.[97] However, in order to avoid the hydrolysis of naphthalene diimide, it was important to consider a synthetic route that formed 3-azidopropane-1-thiol to enable effective deprotonation with a weaker base (K_2CO_3).

The successful reaction of 3-azidopropane-1-thiol and introduction of the azide groups along the polymer backbone was confirmed initially by infrared (IR) spectroscopy (Figure 4.8a). The IR spectra for both PNDI-T(SAz)BTT – 10% and PNDI-T(SAz)BTT – 100% show an absorption peak at 2100 cm^{-1} corresponding to the N=N=N azide stretch. For PNDI-T(SAz)BTT – 10% the

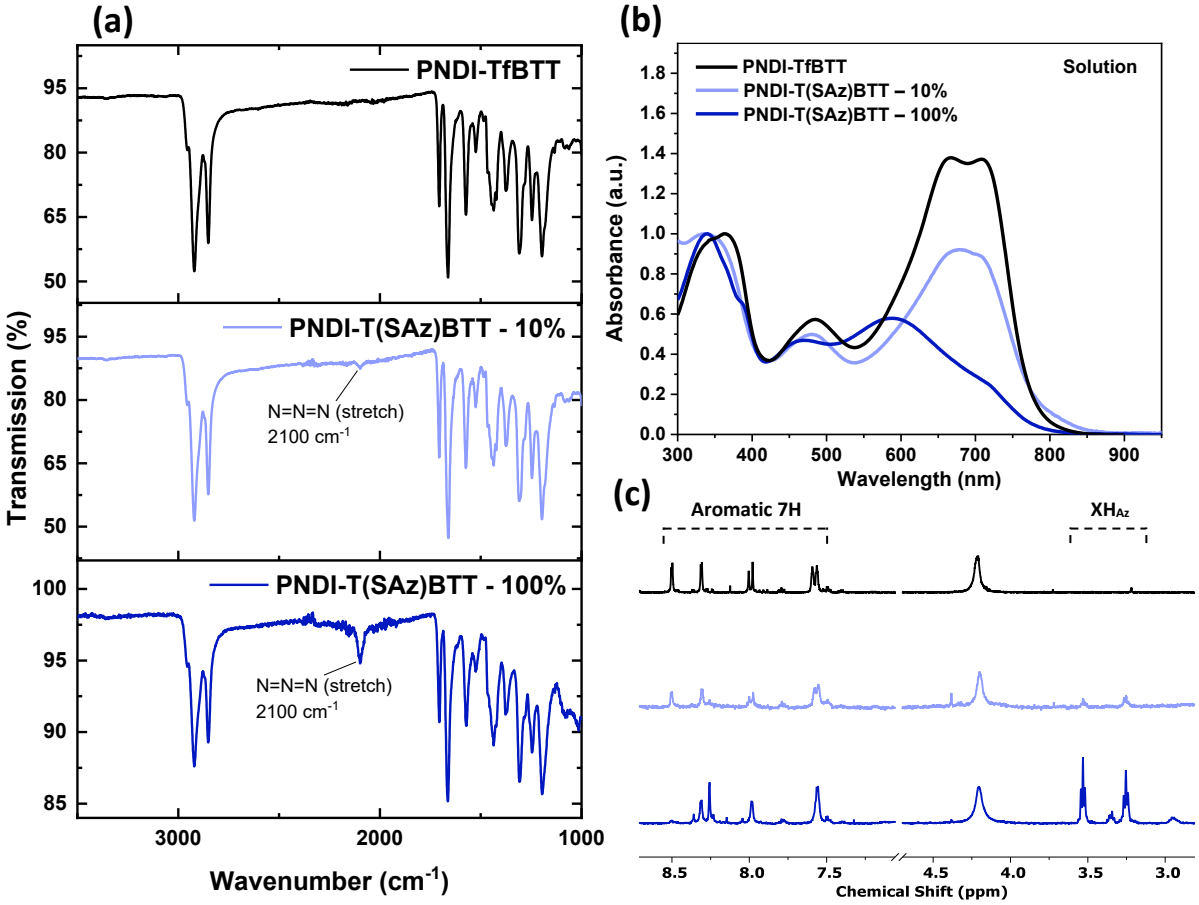


Figure 4.8. Substitution of 3-azidopropane-1-thiol onto the PNDI-TfBTT backbone with a low (10 mol%) and high (100 mol%) degree of substitution: (a) IR, (b) UV-Vis, and (c) ^{1}H NMR spectra for increasing substitution along the PNDI-TfBTT backbone where the aromatic peaks from the aromatic protons were set to an integral value of 7H and directly compared with XH_{Az}.

absorption peak from the azide stretch is relatively weaker compared to PNDI-T(SAz)BTT – 100%. The distinct absorption peak suggests that the attached azide group remains intact after the S_NAr reaction.

Further validation that 3-azidopropane-1-thiol had been successfully substituted onto the polymer backbone was shown by ^1H NMR (Figure 4.8c). Displacement of the fluoride on the fBT with the azide containing substituent was confirmed by appearance of two new triplet peaks at δ 3.53 ppm and δ 3.25 ppm, corresponding to the $-CH_2-N_3$ and $-S-CH_2-$ protons from the substituted pendant group. The intensity of the new ^1H NMR peaks was relatively lower for PNDI-T(SAz)BTT – 10% compared to PNDI-T(SAz)BTT – 100%.

UV-Vis absorption spectra (Figure 4.8b) was comparable to the quantitative substitution of thioalkyl onto PNDI-TfBTT, the respective absorption shifts as the quantity of azide containing substituent was increased. The absorption band edge for PNDI-T(SAz)BTT – 10% does not show a blue shift compared with the starting polymer PNDI-TfBTT. Conversely for PNDI-T(SAz)BTT – 100%, the absorption band edge showed a considerable band shift compared with PNDI-TfBTT. For both substituted polymers the relative intensity of the low energy ICT absorption and low energy π-π* transition, at 525-825 nm and 400-525 nm respectively, gradually decreases with increasing displacement of fluoride along the backbone, comparatively to the high energy π-π* transition at 300-400 nm. For the PNDI-T(SAz)BTT – 100%, the high energy π-π* transition was blue shifted, revealing a shoulder at ~385 nm that could be associated with the substitution of a thiol-based substituent.

4.12 Crosslinking via the azide functionality on PNDI-TfBTT

4.12.1 Thermal crosslink

Azide containing polymer thin films can be intramolecularly thermally crosslinked by simply annealing the thin film in an inert atmosphere.[250,251] Here the thermal crosslinking of azide containing polymers PNDI-T(SAz)BTT – 10% and PNDI-T(SAz)BTT – 100% is reported. Thermal gravimetric analysis (TGA) and differential scanning calorimetry (DSC) measurements were used to determine the thermal crosslink temperature range, shown in Figure S4.29. From the TGA trace, both polymers were shown to thermally degrade at 400 °C or above. At 230 to 300 °C a very small reduction in the mass of the sample was measured, corresponding to loss of nitrogen (N_2) from the azide group, leaving behind a reactive nitrene radical ($N^{\bullet -}$). The reactive nitrene radical goes on to initiate multiple crosslinking mechanisms. The mass loss was more prominent for PNDI-T(SAz)BTT – 100% than PNDI-T(SAz)BTT – 10%, where the theoretical mass loss of N_2 was calculated to be 2.0% and 0.2% respectively. From the DSC curve, an exothermic peak within the range of 230 to 285 °C and 210 to 295 °C for PNDI-T(SAz)BTT – 10% and PNDI-T(SAz)BTT – 100% respectively was observed. Both the TGA and DSC data show the liberation of N_2 within the same temperature range. Therefore, it was possible to predict thermal crosslinking of the thin film occurs between 250 and 300 °C.

Polymer solutions, PNDI-T(SAz)BTT – 10% and PNDI-T(SAz)BTT – 100%, in chlorobenzene (10 mg/mL) were drop cast onto a glass substrate before they were transferred to a glovebox with a nitrogen atmosphere. In the glovebox, the drop cast samples were annealed at four different temperatures: 150, 200, 250 and 300 °C. The annealed drop cast films were immersed in chlorobenzene and the solubility of the films was recorded. This process for thermal crosslinking of PNDI-T(SAz)BTT – 10% and PNDI-T(SAz)BTT – 100% is depicted in Figure 4.9a. When the polymer was thermally crosslinked, a very high molecular weight polymer network was expected to form, resulting in an insoluble polymer thin film. Therefore, when the polymer was immersed in the chlorobenzene the polymer thin film should remain insoluble. As the starting polymer required heat to dissolve, the solution was heated to dissolve any un-crosslinked material. The chlorobenzene solution was analysed by UV-Vis (Figure 4.9c-e) to identify if any un-crosslinked material redissolved. Additionally, this process

was carried out with the starting polymer, PNDI-TfBTT, to ensure that the crosslinking and subsequent insolubility in chlorobenzene was a result of the crosslinked azide groups.

Firstly for the control polymer PNDI-TfBTT, after annealing the drop cast sample at 150, 200, 250 and 300 °C, all four samples redissolved in the hot chlorobenzene. The UV-Vis spectra shows clear absorption traces for all four chlorobenzene solutions. Therefore, it was confirmed that simply annealing the sample up to 300 °C does not alter the solubility of the thin film in chlorobenzene. PNDI-T(SAz)BTT – 10% drop cast samples annealed at 150, 200 and 250 °C, redissolved in hot chlorobenzene and the corresponding UV-Vis spectra for these solutions shows clear absorption traces, confirming the presence of un-crosslinked polymer in solution. When the PNDI-T(SAz)BTT – 10% drop cast sample was annealed at 250 °C, the polymer was only partially soluble in hot chlorobenzene and the resulting thin film

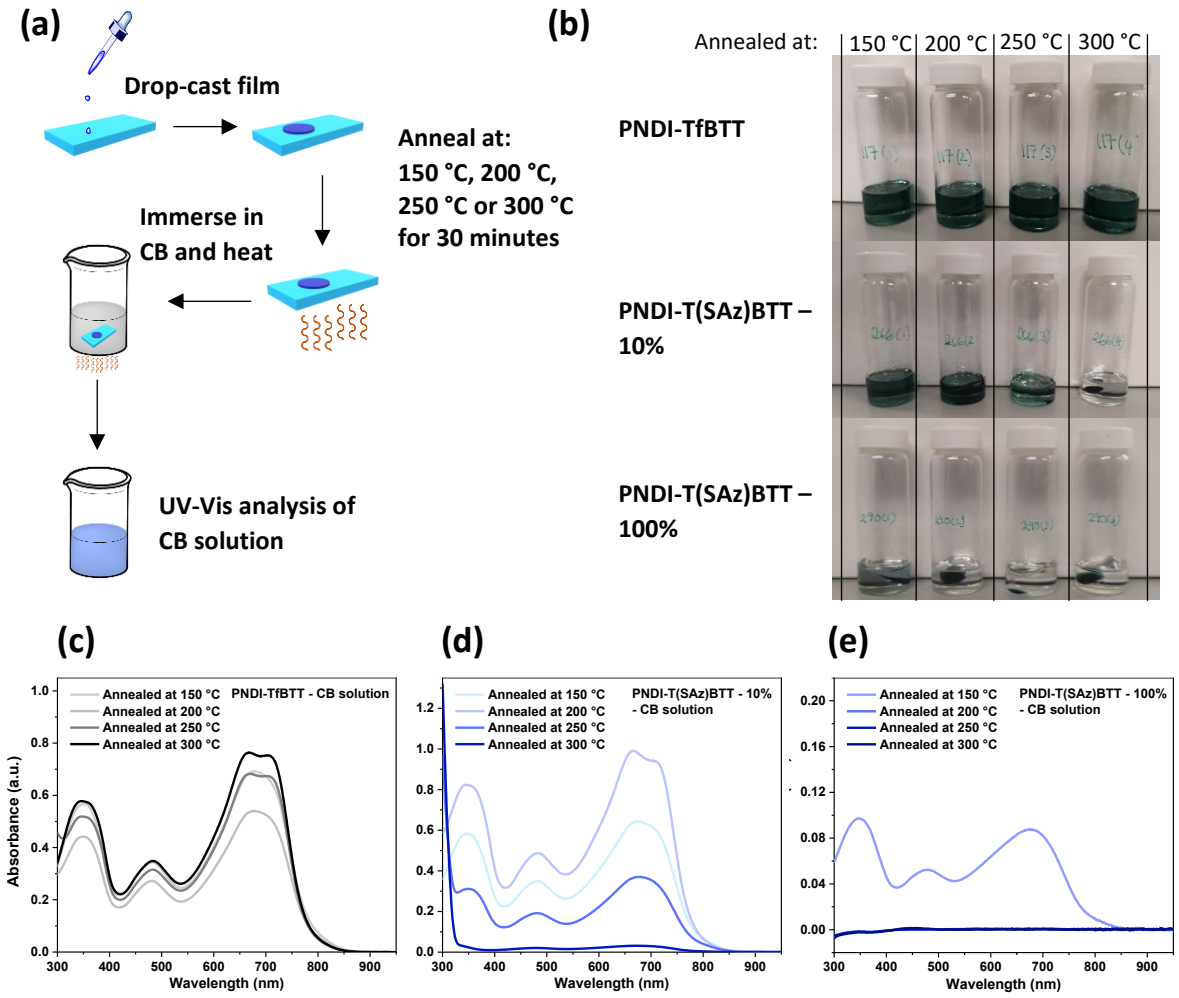


Figure 4.9. Thermal crosslink studies of PNDI-TfBTT, PNDI-T(SAz)BTT – 10% and PNDI-T(SAz)BTT – 100%. Drop-cast films were annealed at 150, 200, 250 and 300 °C for 30 minutes under N_2 before immersing in chlorobenzene where the resulting solution was analysed by UV-Vis. (a) Depiction of thermal crosslink experiment (b) Solutions after thermal anneal and hot chlorobenzene wash. (c-e) UV-Vis absorption spectra for solutions of each polymer.

delaminated from the glass slide. The partial solubility of the thin film suggests the polymer thin film begins to crosslink at 250 °C. When the PNDI-T(SAz)BTT – 10% drop cast sample was annealed at 300 °C the polymer thin film did not redissolve in hot chlorobenzene and the polymer thin film did not delaminate from the glass substrate, demonstrating some degree of crosslinking. PNDI-T(SAz)BTT – 100% drop cast samples annealed at 200, 250 and 300 °C did not redissolve in hot chlorobenzene and the insoluble thin films did not delaminate from the glass. When the PNDI-T(SAz)BTT – 100% drop cast sample was annealed at 150 °C, the thin film was partially soluble in hot chlorobenzene and the remaining thin film did not delaminate from the glass substrate.

In summary, thin films of PNDI-T(SAz)BTT – 100% were thermally immobilised (via thermal crosslinking) at a lower annealing temperature (200 °C and above) compared to PNDI-T(SAz)BTT – 10% (~300 °C).

4.12.2 Photo-crosslink

In order to further explore the crosslinking functionality of the azide containing polymers, the ability for the polymer thin films to crosslink upon exposure to UV light was tested, shown in Figure 4.10. As for the thermal crosslinking, exposing the azide containing polymer to UV light liberates N_2, leaving behind a reactive nitrene radical that initiates multiple crosslinking mechanisms. For the photo-crosslink experiments, polymers were dissolved in chlorobenzene (10 mg/mL), the solutions were spin coated onto glass substrates before they were transferred to a glovebox with a nitrogen atmosphere. Under inert atmosphere, the samples were irradiated with UV light (254 nm) for 60 minutes through a patterned mask. The samples were then immersed in chlorobenzene (and heated if required) and the solubility of the thin films were recorded. If the polymer had successfully crosslinked in the presence of UV light the polymer material would remain on the glass substrate in the pattern of the mask used.

For PNDI-T(SAz)BTT – 10%, the resulting patterned material did not remain intact on the glass substrate after immersion in chlorobenzene. Upon inspection of the sample, it was possible to see a slight retention of the polymer on the glass slide, indicating that the polymer may have partially crosslinked. However, most of the polymer thin film remained uncrosslinked and was washed away. This observation suggested a higher azide content along the polymer backbone was needed to crosslink the polymer thin film photochemically. For PNDI-T(SAz)BTT

– 100%, the resulting patterned material did remain intact on the glass substrate after immersion in chlorobenzene. The final sample clearly shows the transferred pattern from the mask used, where the non-exposed un-crosslinked polymer was washed away with the chlorobenzene wash.

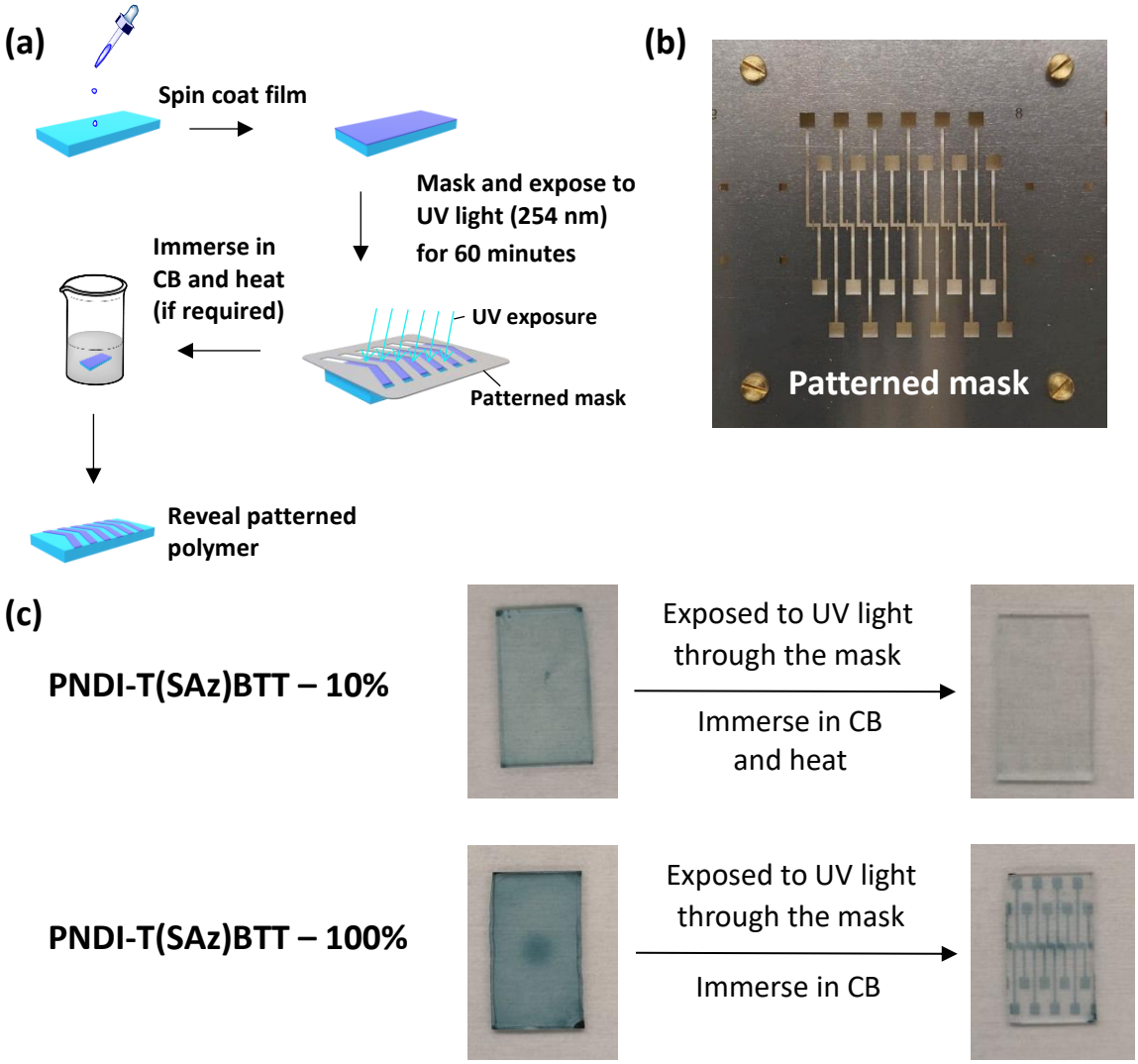


Figure 4.10. Photo-crosslink studies of PNDI-TfBTT, PNDI-T(SAz)BTT – 10% and PNDI-T(SAz)BTT – 100%. Spin coated films were exposed to UV light (254 nm) for 60 minutes under N_2 before immersing in chlorobenzene: (a) depiction of thermal crosslink experiment, (b) mask used to pattern the thin film by restricting UV light exposure to specific areas and (c) thin films after UV light exposure (254 nm) and chlorobenzene wash.

4.12.3 Crosslinking summary

To summarise, the ability of both low and high azide content polymers (PNDI-T(SAz)BTT – 10% and PNDI-T(SAz)BTT – 100%) to crosslink thermally and photochemically was investigated. Both low and high azide containing polymer thin films were thermally immobilised, via thermal crosslinking, when heated to 200 °C and 300 °C respectively. After thermal crosslinking the thin films were no longer soluble in organic solvents. In addition, lithographic techniques were shown to photo-crosslink PNDI-T(SAz)BTT – 100%, where the crosslinked patterned film exhibited considerably reduced solubility in organic solvents. The reduced solubility of the polymer thin film in organic solvents allows the potential to fabricate solution-processable multi-layer devices. When the azide content was reduced, for PNDI-T(SAz)BTT – 10%, it was not possible to photo-crosslink the polymer thin film sufficiently for photopatterning, indicating that a higher quantity of azide containing pendant groups along the polymer backbone would be required to photo-pattern the thin film. In the final sections, the effects of thermally and photochemically crosslinking the polymer thin films on the thin film morphology and OTFT charge transport properties are discussed.

4.13 Thin film morphology post crosslinking

To determine how the thin film morphology changes with different annealing temperatures, thin films of PNDI-T(SAz)BTT – 10% and PNDI-T(SAz)BTT – 100% were prepared as-cast and annealed (in an inert atmosphere) for 30 minutes at 200 °C and 300 °C. Additionally, the effect on thin film morphology after PNDI-T(SAz)BTT – 10% and PNDI-T(SAz)BTT – 100% thin films were exposed to UV light (254 nm) for 60 minutes was explored. Finally, the effect on thin film morphology after thermally annealing thin films of PNDI-T(SAz)BTT – 10% and PNDI-T(SAz)BTT – 100%, for 30 minutes at 200 °C and 300 °C, that had been previously exposed to UV light was investigated. A combination of GIWAXS and AFM techniques were used to assess the effects of thin film morphology. All GIWAXS images and diffraction patterns are presented in Figures S4.30 to S4.33. Polymers PNDI-T(SAz)BTT – 10% and PNDI-T(SAz)BTT – 100% were dissolved in chlorobenzene (10 mg/mL) and spin coated directly onto a silicon wafer before they were transferred to a glovebox and thermally annealed or exposed to UV light or both.

All thin films of PNDI-T(SAz)BTT – 10% (as-cast, annealed at 200 °C and 300 °C) exhibit lamellar-type packing with a diffraction peak (100) in the out-of-plane orientation at 2.56, 2.57 and 2.59 nm^{-1} corresponding to an interlayer d-spacing of 24.5, 24.4, and 24.3 Å respectively (Figure 4.11). The as-cast thin film shows a relatively reduced degree of order within the film where lamellar peaks up to the second order (200) were observed. Thermally annealed thin films become more ordered with a further advancement up to the fourth (400) and fifth order (500) in the lamellar peaks when annealed at 200 °C and 300 °C respectively.

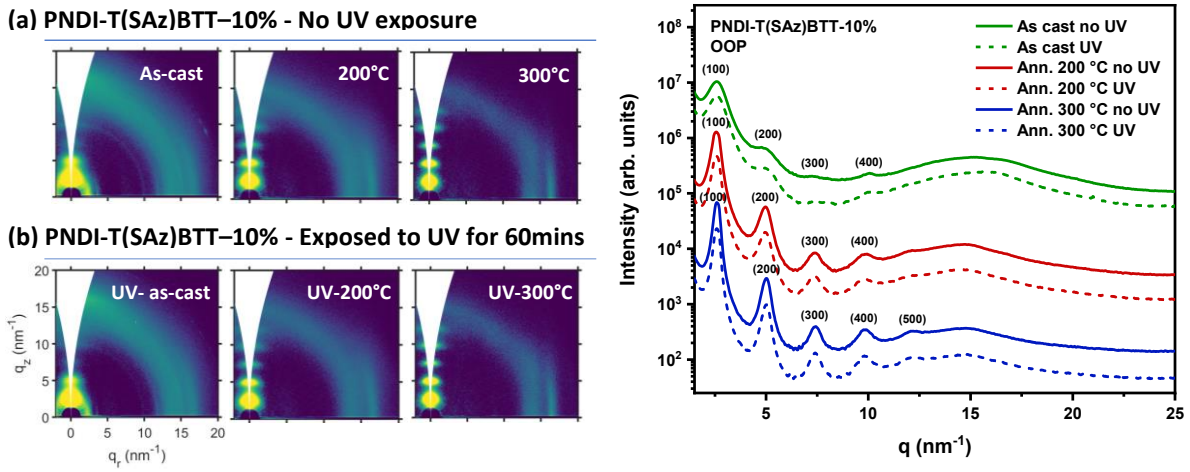


Figure 4.11. GIWAXS images (left) and GIWAXS diffraction patterns (out-of-plane) (right) of PNDI-T(SAz)BTT-10% films (a) as-cast (no thermal anneal) and annealed at 200 °C and 300 °C and (b) exposed to UV light (254 nm) for 60 minutes before no thermal anneal (UV only) and annealed at 200 °C and 300 °C.

When the thin films of PNDI-T(SAz)BTT – 10% were thermally annealed, the π-π stacking diffraction peak (prominently oriented in the in-plane) becomes more prominent indicating a higher degree of order. The π-π stacking peak found at 16.5 to 16.7 nm^{-1} corresponds to a d-spacing of 3.8 Å (Figure S4.31). The diffraction patterns for PNDI-T(SAz)BTT – 10% compared with the diffraction patterns for starting polymer PNDI-TfBTT were notably similar. These observations confirm that thermally crosslinking PNDI-T(SAz)BTT – 10% leads to a higher degree of crystallinity in the film, similar to the unsubstituted starting polymer PNDI-TfBTT. Furthermore, the GIWAXS patterns show that exposing the thin film to UV-light does not alter the structure or orientation of the thin film. This finding was expected, as there was not sufficient azide present in PNDI-T(SAz)BTT – 10% to effectively photo-crosslink the polymer thin film, as discussed in Section 4.12.2.

As observed previously, substitution onto the polymer backbone results in a reduced degree of order in the thin film, where the diffraction patterns for PNDI-TfBTT and PNDI-T(SR)BTT were compared (Section 4.8). A similar reduction in the order of the thin film was observed from PNDI-T(SAz)BTT – 10% to PNDI-T(SAz)BTT – 100%. All thin films of PNDI-T(SAz)BTT – 100% (as-cast, annealed at 200 °C and 300 °C) show lamellar-type packing with a diffraction peak (100) in the out-of-plane orientation at 2.63, 2.56 and 2.55 nm^{-1} corresponding to an interlayer d-spacing of 23.9, 24.5, and 24.6 Å respectively (Figure 4.12). For the as-cast thin film, first order lamellar peaks (100) were observed. When the thin films were annealed at 200 °C and 300 °C, lamellar peaks up to the second (200) and third order (300) were observed respectively. From the GIWAXS data, it was possible to conclude that thermally crosslinking

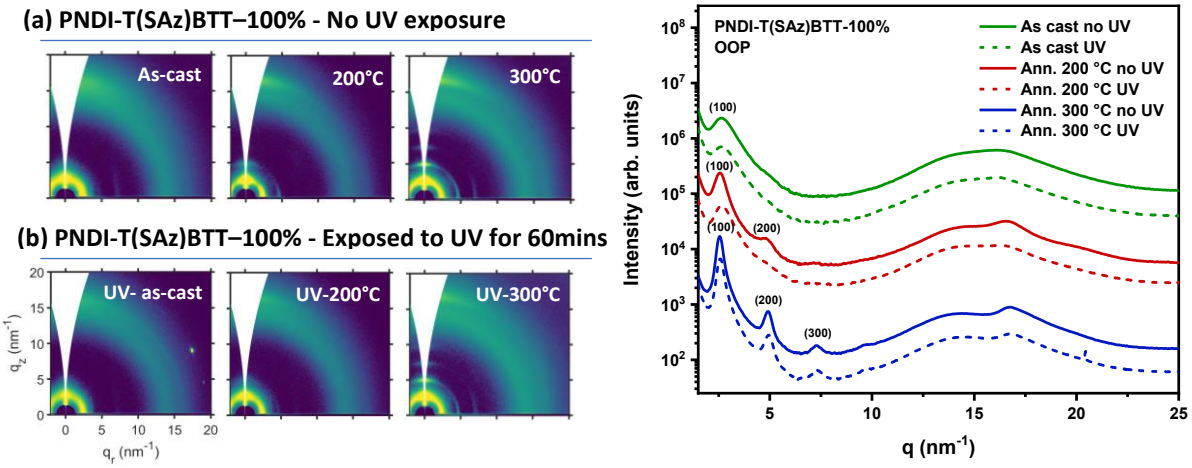


Figure 4.12. GIWAXS images (left) and GIWAXS diffraction patterns (out-of-plane) (right) of PNDI-T(SAz)BTT-100% films (a) as-cast (no thermal anneal) and annealed at 200 °C and 300 °C and (b) exposed to UV light (254 nm) for 60 minutes before no thermal anneal (UV only) and annealed at 200 °C and 300 °C.

PNDI-T(SAz)BTT – 100% also leads to a higher degree of crystallinity in the film. Previously, exposing the thin film of PNDI-T(SAz)BTT – 100% to UV light was shown to effectively crosslink the polymer thin film, hence, the thin film was photo-patterned. When the thin film was exposed to UV light, a new isotropic reflection (prominently oriented in the in-plane) appeared at 16.2 nm^{-1} (d-spacing 3.9 Å), as shown in Figure S4.33. The isotropic reflection indicates order in all directions of the thin film, hence, a reduced degree of crystallinity within the thin film. When the thin film was exposed to UV light and annealed at 200 or 300 °C, the isotropic reflection at 16.2 nm^{-1} disappears suggesting the film becomes more crystalline.

In summary, both PNDI-T(SAz)BTT – 10% to PNDI-T(SAz)BTT – 100% thin films showed a higher degree of crystallinity after thermally annealing at 200 and 300 °C. PNDI-T(SAz)BTT – 10% exhibits a higher crystallinity comparatively to PNDI-T(SAz)BTT – 100%. Upon exposure to UV light, the crystallinity of the PNDI-T(SAz)BTT – 100% thin film was shown to decrease, due to the photochemical crosslinking within the film. The crystallinity of the UV exposed thin film was improved after it was thermally annealed.

To further characterise the thin films of NDI-T(SAz)BTT – 10% and PNDI-T(SAz)BTT – 100%, they were imaged using atomic force microscopy (AFM), as shown in Figure 4.13. The thin films were prepared via the method described previously for GIWAXS samples. Thin films were analysed by AFM (a) as-cast, (b) annealed at 200 °C for 30 minutes, (c) exposed to UV light (254 nm) for 60 minutes and (d) exposed to UV light (254 nm) for 60 minutes followed by thermal anneal at 200 °C for 30 minutes.

Both polymers as-cast, PNDI-T(SAz)BTT – 10% and PNDI-T(SAz)BTT – 100%, formed a continuous-smooth thin film (as-cast) with a surface roughness root-mean-square (RMS) value of 0.60 and 0.80 nm respectively. Upon thermal annealing some reorganisation in the thin films for both PNDI-T(SAz)BTT – 10% and PNDI-T(SAz)BTT – 100% was observed. The AFM images show that more order was introduced after the thin films were thermally annealed, as the GIWAXS data also highlights. When the thin films were exposed to UV light, the AFM images displayed no or little change to the thin film morphology. As demonstrated previously, PNDI-T(SAz)BTT – 100% was shown to crosslink under UV light exposure. Whilst the AFM images do not highlight any morphological changes in the thin film, the GIWAXS data did show an increasingly amorphous film. Finally, the AFM images show the PNDI-T(SAz)BTT – 100%

thin film becomes more ordered when exposed to UV light and thermally annealed at 200 °C. This observation was also reflected in the GIWAXS data.

Overall, the AFM images show a higher degree of crystallinity for PNDI-T(SAz)BTT – 10% than for PNDI-T(SAz)BTT – 100%. As seen previously, the more crystalline thin films tend to show a higher electron mobility in OTFT devices, therefore, the thermally annealed PNDI-T(SAz)BTT – 10% was expected to provide a relatively higher electron mobility. Furthermore, the UV exposed thin films were expected to show a reduction in electron mobility, where the electron mobility could be improved by thermally annealing the UV exposed thin film.

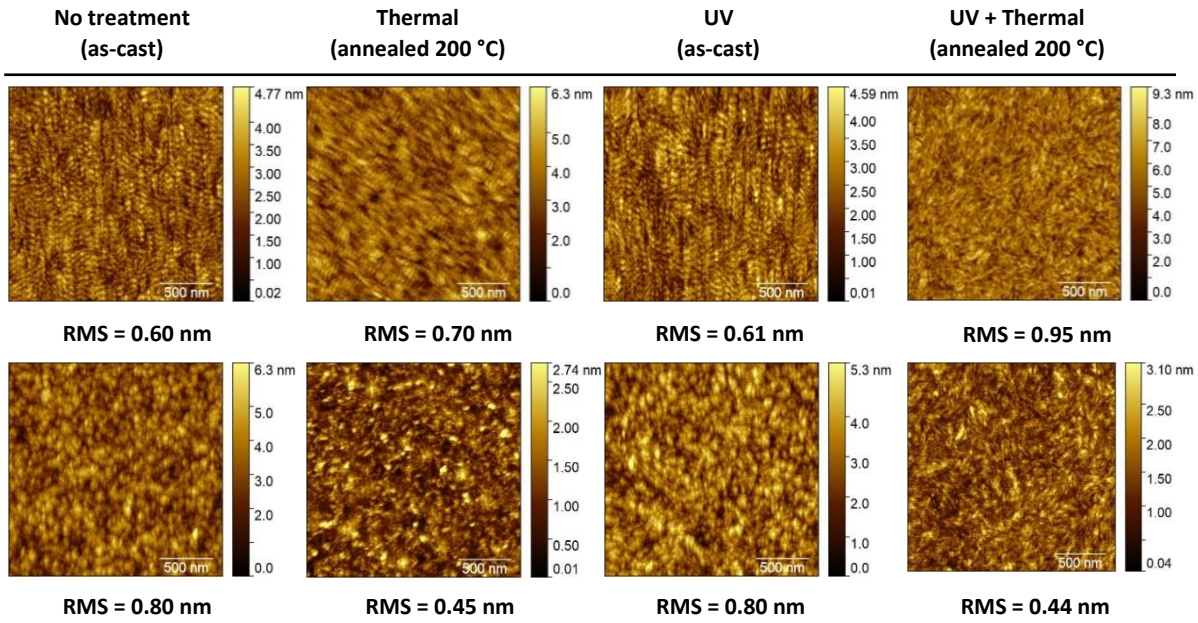


Figure 4.13. AFM images of PNDI-T(SAz)BTT-10% (top) and PNDI-T(SAz)BTT-100% (bottom) thin films, from spin casting on Si wafer. The films were imaged as-cast, after thermal annealing (at 200 °C), after UV light exposure (254 nm) and after both UV exposure (254 nm) followed by thermal annealing (at 200 °C).

4.14 OTFT charge transport properties post crosslinking

OTFT devices were fabricated with a top-gate bottom-contact (TG/BC) configuration. PNDI-T(SAz)BTT – 10% and PNDI-T(SAz)BTT – 100% polymers were dissolved in dichlorobenzene (5 mg/mL) and deposited onto glass via spin coating. The thin films were then dried and (a) thermally annealed at 200 or 300 °C for 30 minutes or (b) exposed to UV-light (254 nm) for 60 minutes or (c) both exposed to UV-light (254 nm) for 60 minutes and thermally annealed at 200 or 300 °C for 30 minutes. Finally, the PMMA (gate insulator) was spun and annealed at 95 °C for 2 hours before the Al gate electrode was deposited by thermal evaporation. The fabricated devices were used to determine the electron mobility (μ_e) within the polymer thin

films. The effects on electron mobility after thermal annealing, UV exposure and UV exposure followed by thermal annealing were evaluated and the data summarised in Table 4.5. The transfer characteristics for PNDI-T(SAz)BTT – 10% and PNDI-T(SAz)BTT – 100%, shown in Figures S4.34-S4.37, under a positive gate bias.

4.14.1 Thermally annealed active layer

For PNDI-T(SAz)BTT – 10%, the average electron mobility increases from 1.4 x 10^{-2} (film as-cast) to 7.7 x 10^{-2} $cm^2V^{-1}s^{-1}$ (film annealed at 300 °C) with increasing annealing temperature. The increase in the average electron mobility demonstrates little or no sacrifice in charge mobility when the polymer thin films were thermally crosslinked, where shown previously that the PNDI-T(SAz)BTT – 10% polymer thin film crosslinks at 300 °C. Conversely, for PNDI-T(SAz)BTT – 100%, the average electron mobility does not drastically change with increasing annealing temperature. A slight variation in average electron mobility was recorded with values of 8.1 x 10^{-3} (film as-cast), 1.3 x 10^{-2} (film annealed at 200 °C) and 7.4 x 10^{-3} $cm^2V^{-1}s^{-1}$ (film annealed at 300 °C). Upon thermal annealing, the polymer thin film of PNDI-T(SAz)BTT – 100% was shown to thermally crosslink at 200 °C. It was therefore concluded that the mobility was not greatly affected after thermally crosslinking PNDI-T(SAz)BTT – 100%.

4.14.2 UV exposed active layer

From photo-crosslinking experiments, PNDI-T(SAz)BTT – 10% did not sufficiently crosslink when exposed to UV light (254 nm), where the thin film remained soluble in organic solvents. Consequently, no change to the average mobility was observed when tested in an OTFT device, from the as-cast thin film (1.4 x 10^{-2} $cm^2V^{-1}s^{-1}$) to the UV exposed as-cast thin film (1.5 x 10^{-2} $cm^2V^{-1}s^{-1}$). On the other hand, PNDI-T(SAz)BTT – 100% was shown to crosslink when exposed to UV light. The corresponding average electron mobility values from the OTFT device showed a distinct decrease by an order of magnitude from the as-cast thin film (8.1 x 10^{-3} $cm^2V^{-1}s^{-1}$) to the UV exposed as-cast thin film (2.1 x 10^{-4} $cm^2V^{-1}s^{-1}$). The reduction in electron mobility was likely due to the thin film morphology, where the GIWAXS data showed a reduction in crystallinity of the polymer thin film upon exposure to UV light. Interestingly, further annealing the UV exposed samples improved the average mobility from 2.1 x 10^{-4} $cm^2V^{-1}s^{-1}$ (as-cast UV exposed film) to 1.5 x 10^{-3} $cm^2V^{-1}s^{-1}$ (annealed at 200 °C) and 1.3 x 10^{-3} $cm^2V^{-1}s^{-1}$ (annealed at 300 °C). Furthermore, the GIWAXS and AFM data showed an increase

in crystallinity of the polymer thin film after the UV exposed thin films were thermally annealed.

Summarising the data from the OTFT devices, the highest mobility was achieved with PNDI-T(SAz)BTT – 10% thermally annealed at 300 °C, compared to thin films annealed and a lower temperature and compared to the OTFT devices fabricated with PNDI-T(SAz)BTT – 100%. For PNDI-T(SAz)BTT – 100%, the electron mobility was not largely altered for thermally crosslinked thin films. For photo-crosslinked thin films of PNDI-T(SAz)BTT – 100%, the respective average electron mobility dropped by one order of magnitude after UV exposure. When the UV exposed thin films were annealed at 200 °C or above the average mobility did increase again. Therefore, thermal annealing can be used after photo-patterning to improve charge carrier mobility by increasing the crystallinity of the thin film. It should be noted that there was a reduction in average electron mobility for the as-cast thin film of PNDI-T(SAz)BTT – 10% to PNDI-T(SAz)BTT – 100%. The reduced electron mobility can be attributed to the increased degree of twisting in the backbone from increased substitution along the polymer backbone.

Table 4.5. Summary of OTFT data for PNDI-T(SAz)BTT – 10% and PNDI-T(SAz)BTT – 100% with a (TG/BG) configuration. (a) Summarises the effects of thermal crosslinking and (b) summarises the effects of photo-crosslinking and combined photo-crosslinking followed by thermal crosslinking.

(a)	**No treatment (as-cast)**		**Thermal (annealed 200 °C)**		**Thermal (annealed 300 °C)**	
Polymer	μ_{avg} ($cm^2V^{-1}s^{-1}$)	μ_{max} ($cm^2V^{-1}s^{-1}$)	μ_{avg} ($cm^2V^{-1}s^{-1}$)	μ_{max} ($cm^2V^{-1}s^{-1}$)	μ_{avg} ($cm^2V^{-1}s^{-1}$)	μ_{max} ($cm^2V^{-1}s^{-1}$)
PNDI-T(SAz)BTT – 10%	1.4×10^{-2}	1.6×10^{-2}	4.0×10^{-2}	5.0×10^{-2}	7.7×10^{-2}	9.8×10^{-2}
PNDI-T(SAz)BTT – 100%	8.1×10^{-3}	1.0×10^{-2}	1.3×10^{-2}	1.6×10^{-2}	7.4×10^{-3}	9.6×10^{-3}
(b)	**UV (as-cast)**		**UV + Thermal (annealed 200 °C)**		**UV + Thermal (annealed 300 °C)**	
Polymer	μ_{avg} ($cm^2V^{-1}s^{-1}$)	μ_{max} ($cm^2V^{-1}s^{-1}$)	μ_{avg} ($cm^2V^{-1}s^{-1}$)	μ_{max} ($cm^2V^{-1}s^{-1}$)	μ_{avg} ($cm^2V^{-1}s^{-1}$)	μ_{max} ($cm^2V^{-1}s^{-1}$)
PNDI-T(SAz)BTT – 10%	1.5×10^{-2}	2.2×10^{-2}	-	-	-	-
PNDI-T(SAz)BTT – 100%	2.1×10^{-4}	3.0×10^{-4}	1.5×10^{-3}	1.8×10^{-3}	1.3×10^{-3}	1.7×10^{-3}

4.15 Conclusion

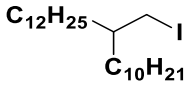
In conclusion, two new backbone polymers were designed, synthesised and shown to undergo post-polymerisation modification, by S_NAr, directly onto the polymer backbone. The polymers were designed with electron withdrawing NDI and fBT repeat units, where the fluoride on the fBT repeat unit could be displaced with a thiol or thioacetate terminated substituent in an S_NAr reaction. Backbone polymers were designed (a) without a vinylene spacer and (b) with a vinylene spacer. The ability to directly functionalise these polymers along the polymer backbone with a thiol terminated alkyl chain (1-octanethiol) was demonstrated. The effects of thioalkyl substitution on the optical, electronic and thin film properties were evaluated. Substitution along the polymer backbone did have a distinct effect on the solubility, which was advantageous for the processability of the polymer. With respect to the electronic properties, substitution along the polymer backbone induced an increased degree of twisting. Therefore, the UV-Vis absorption was blue shifted and a slight increase in the HOMO and LUMO energy levels was observed. In the polymer thin film, a reduced degree of crystallinity after substitution onto the polymer backbone was observed. The resulting electron mobilities in OTFT devices showed a lower electron mobility for the polymers after substitution. The highest mobility of 0.16 $cm^2V^{-1}s^{-1}$ was achieved with the PNDI-TfBTT backbone. The introduction of the vinylene spacers did not improve the overall crystallinity of the polymer thin films, thus, leading to a lower overall electron mobility for vinylene containing polymers.

From these findings, further investigations went on to demonstrate the potential to substitute 1-octanethiol quantitatively along the PNDI-TfBTT polymer backbone, highlighting the versatility of post-polymerisation modification via S_NAr. The final investigation looked at the substitution of S-(3-Azidopropyl)thioacetate onto the PNDI-TfBTT with a low (10%) and high (100%) azide content with the aim to crosslink the polymer (thermally or photochemically) towards an immobilised active layer. The polymer functionalised with a low % of azide was shown to thermally crosslink at 300 °C and did display the highest electron mobility of 0.098 $cm^2V^{-1}s^{-1}$ respectively. From the low to high % azide containing polymer, the increased degree of substitution led to a lower electron mobility. When further functionalised, the high % azide containing polymer was shown to thermally crosslink at 200 °C and the respective electron mobility was maintained. Additionally, the high % azide

polymer could be photo-chemically crosslinked and patterned, however, at a cost to the electron mobility, which was reduced by two orders of magnitude. The final key observation saw the mobility of thin films of high % azide containing polymers increase by an order of magnitude after thermally annealing UV exposed polymer thin films. These polymers could be good candidates for multicomponent active layers in electronic devices where the thin film morphologies can be immobilised using the thermal and photochemical crosslinking mechanisms. Furthermore, the backbone polymers PNDI-TfBTT and PNDIV-TfBTT can be further explored for their ability to undergo S_NAr with a wider range of thiols and thioacetates.

4.16 Experimental

Synthesis of 1-iodo-2-decyltetradecane
as prepared according to a modified procedure of Antonio Facchetti et al.[252]

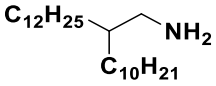


In a dry 250 mL two neck round bottom flask under nitrogen a solution of 2-decyl-1-tetradecanol (12.05 g, 34.0 mmol), triphenylphosphine (10.60 g, 40.4 mmol), imidazole (2.80 g, 41.1 mmol) in toluene (100 mL) was cooled to 0 °C. To the cooled solution iodine (9.90 g, 39.0 mmol) was added and stirred at 0 °C for 15 minutes before the mixture was brought up to room temperature. The reaction mixture was stirred for 2 hours at room temperature followed by addition of sat. Na_2SO_3(aq) (10 mL). The organic solvent was concentrated using a rotary evaporator. The residue was taken up in petroleum ether (250 mL) and washed with water (3 x 200 mL) and brine (180 mL). The organic phase was dried over $MgSO_4$ and concentrated under reduced pressure. The residue was purified by column chromatography over silica (eluent: petroleum ether) to give 1-iodo-2-decyltetradecane as a colourless oil. (14.2 g, 90% yield)

^{1}H NMR (400 MHz, $CDCl_3$): δ 3.26 (d, *J* = 4.56 Hz, 2H), 1.40-1.20 (m, 40H), 1.11 (m, 1H) 0.89 (t, *J* = 6.6 Hz, 6H) ppm. ^{13}C NMR (101 MHz, $CDCl_3$): δ 38.8 (CH, 1C), 34.6 (CH_2, 2C), 32.1 (CH_2, 2C), 29.9 (CH_2, 2C), 29.8 (CH_2, 8C), 29.5 (CH_2, 2C), 26.7 (CH_2, 2C), 22.9 (CH_2, 2C), 17.0 (CH_2-I, 1C), 14.3 (CH_3, 2C) ppm. MS (*m/z)* $[M]^+$ calcd for $C_{24}H_{49}I$: 463.2795, found: 463.2794 (APCI)

Synthesis of 2-decyltetradecylamine

as prepared according to a modified procedure of Antonio Facchetti et al. and Watson et al.[227,252]

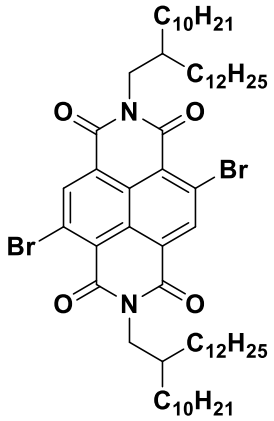


In a dry 100 mL two neck round bottom flask under nitrogen a solution of 1-iodo-2-decyltetradecane (10.05 g, 21.6 mmol) and phthalimide (4.44 g, 30.2 mmol) in DMF (50 mL) was stirred vigorously for 72 hours at 25 °C. The DMF was then removed using a rotary evaporator and the resultant oil was dissolved in petroleum ether (400 mL) and with water (3 x 300 mL) and once with brine (250 mL). The organic phase was dried over $MgSO_4$, concentrated under reduced pressure and passed through a silica plug (eluent: petroleum ether/chloroform 9:1) The resulting oil was dissolved in ethanol (300 mL), in a dry 500 mL two neck round bottom flask filled with nitrogen. To the solution hydrazine hydrate (10 mL) was added dropwise and the mixture was refluxed overnight. The mixture was cooled to room temperature, ethanol was removed under reduced pressure and the remaining crude mixture was diluted with dichloromethane (200 mL). The organic phase was washed with 10% KOH (2 x 100 mL), the resulting aqueous phase was extracted with DCM and the combined organic phases were washed with water (3 x 100 mL) followed by brine (80 mL). The organic phase was dried over $MgSO_4$ and concentrated by rotary evaporator to give 2-decyltetradecylamine as a yellow oil (1.32g, 17% yield)

^{1}H NMR (400 MHz, $CDCl_3$): δ 4.44 (br, 2H), 2.61 (d, *J* = 4 Hz, 2H), 1.42 (m, 1H), 1.28 (br, 40H), 0.90 (t, *J* = 8 Hz, 6H) ppm. ^{13}C NMR (101 MHz, $CDCl_3$): δ 45.2 (CH_2-NH_2, 1C), 40.7 (CH, 1C), 32.1 (CH_2, 2C), 31.6 (CH_2, 2C), 30.2 (CH_2, 2C), 29.8 (CH_2, 8C), 29.5 (CH_2, 2C), 26.9 (CH_2, 2C), 22.9 (CH_2, 2C), 14.3 (CH_3, 2C) ppm. MS (*m/z)* $[M]^+$ calcd for $C_{24}H_{52}N$: 354.4100, found: 354.4105 (ESI).

Synthesis of N,N'-bis(2-decyltetradecyl)-2,6-dibromonaphthalene-1,4,5,8-bis(dicarboximide) (NDI-Br_2) monomer

as prepared according to a modified procedure of Antonio Facchetti et al.[235]

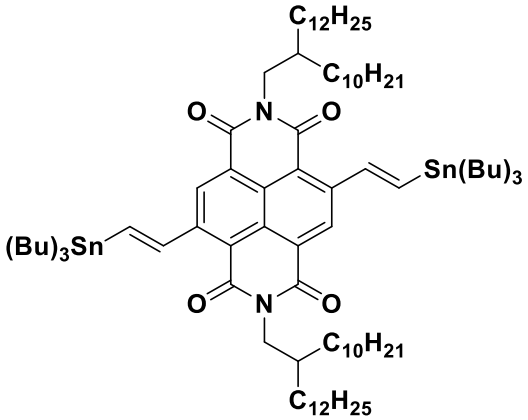


To a 20 mL 2-neck round bottom flask under nitrogen, 2,6-dibromonaphthalene-1,4,5,8-tetracarboxydianhydride (NDA-Br_2) (1.00 g, 2.36 mmol), 2-decyltetradecylamine (2.08 g, 5.88 mmol) in *o*-xylene (8 mL) and propanoic acid (2.6 mL) were added and stirred at 140 °C for 2 hours. The reaction was monitored by TLC. The mixture was cooled to room temperature before direct purification by column chromatography over silica (eluent: hexane/chloroform 1:2). The solvent was removed under reduced pressure before the product was further purified by recrystallisation with ethyl acetate. The recrystallized product was collected by vacuum filtration through a nylon pad (pore size 20 µm), washed with cold ethyl acetate and left to dry. The dry product was collected in a vial and dried under vacuum. The product obtained was a yellow solid. (1.38 g, 55% yield)

^{1}H NMR (400 MHz, $CDCl_3$): δ 9.00 (s, 2H), 4.14 (d, *J* = 8 Hz, 4H), 1.98 (m, 2H), 1.15-1.40 (m, 80H), 0.83-0.92 (m, 12H) ppm. ^{13}C NMR (101 MHz, $CDCl_3$): δ 161.3 (N-C=O, 2C), 161.2 (N-C=O, 2C), 139.3 (C(Ar), 2C), 128.5 (C(Ar), 2C), 127.9 (C(Ar), 2C), 125.4 (C-Br, 2C), 124.2 (C(Ar) , 2C), 45.6 (CH_2, 2C), 36.6 (CH, 2C), 32.1 (CH_2, 4C), 31.7 (CH_2, 4C), 30.2 (CH_2, 4C), 29.8 (CH_2, 16C), 29.5 (CH_2, 4C), 26.47 (CH_2, 4C), 22.8 (CH_2, 4C), 14.3 (CH_3, 4C) ppm. MS (*m/z)* $[M]^+$ calcd for $C_{62}H_{100}Br_2N_2O_4$: 1093.60, found: 1095.6 (MALDI)

Synthesis of 2,7-bis(2-octyldodecyl)-4,9-bis((E)-2-(tributylstannyl)vinyl)benzo[lmn][3,8]-phenanthr-oline-1,3,6,8(2H,7H)-tetraone monomer

as prepared according to a modified procedure of Zhuping Fei et al.[70]

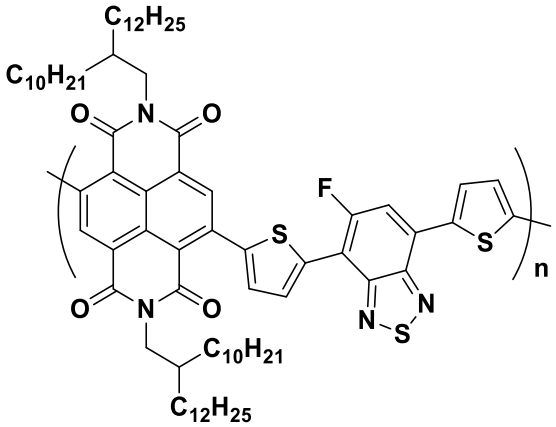


To a 100 mL two-neck round bottom flask under nitrogen, NDI-Br_2 (500 mg, 0.46 mmol), trans-1,2-bis(tributylstannyl)ethene (1.13 g, 1.9 mmol), tris(dibenzylideneacetone)dipalladium(0) ($Pd_2(dba)_3$) (24.3 mg, 0.024 mmol), and tri(o-tolyl)phosphine (P(o-tol)3) (33 mg, 0.036 mmol) were added and degassed thoroughly. To the solid mixture, degassed anhydrous toluene (40 mL) was added and degassed for a further 10 minutes. The solution was heated to 90 °C and stirred at this temperature overnight. The mixture was allowed to cool to room temperature and passed through silica/potassium fluoride (4:1 w:w, eluent: dichloromethane). The solvent was removed under reduced pressure, and the residue was purified by chromatography over silica (eluent: dichloromethane/hexane 1:2). The fractions containing the product were collected, the solvent removed under reduced pressure, the product dissolved in a minimum amount of hexane and further purified by preparative GPC (eluent: hexane). The fractions were collected and the solvent removed to give the product as a yellow oil (277 mg, 38% yield).

^{1}H NMR (400 MHz, $CDCl_3$): δ 8.93 (s, 2H), 8.39 (d, *J* = 19.2 Hz, 2H), 7.36 (d, *J* = 19.2 Hz, 2H), 4.12 (d, *J* = 7.6 Hz, 4H), 2.04−1.93 (m, 2H), 1.68−1.58 (m, 12H), 1.43−1.17 (m, 92H), 1.08 (m, 12H), 0.93 (t, *J* = 7.2 Hz, 18H), 0.88−0.83 (m, 12H) ppm.

Synthesis of PNDI-TfBTT polymer

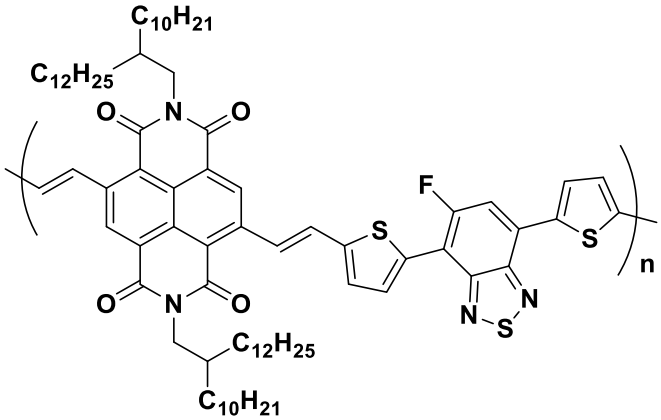
as prepared according to a modified procedure of Huajie Chen and Yunqi Liu et al.[234]



To a 20 mL microwave vial under nitrogen, 5-fluoro-4,7-bis(5-(trimethylstannyl)thiophen-2-yl)benzo[c][1,2,5]thiadiazole (450 mg, 0.70 mmol), NDI-Br_2 (750 mg, 0.70 mmol), $Pd_2(dba)_3$ (22 mg, 0.024 mmol) and P(*o*-tol)$_3$ (35 mg, 0.115 mmol) was added and degassed thoroughly before chlorobenzene (12 mL) was added and degassed for a further 10 minutes. The mixture was heated to 120 °C and stirred at this temperature for 72 hours. The mixture was brought to room temperature, precipitated in methanol and filtered into a Soxhlet thimble. The product was washed (Soxhlet) with methanol, acetone and hexane. The final product was obtained in three fractions: (1) extracted from chloroform (2) extracted from chlorobenzene and (3) unextracted material removed from the thimble. After extraction, the solvent was removed using a rotary evaporator. The product was dissolved in the minimum amount of chlorobenzene (approx. 10 mL) and precipitated into methanol (approx. 500 mL). The precipitate was collected by vacuum filtration through a nylon pad (pore size 20 µm), washed with methanol and left to dry. The dry product was collected in a vial and further dried under vacuum. The product obtained was a dark blue solid (768 mg, 87% yield).

^{1}H NMR (500 MHz, 393K, TCE): δ 9.00-8.95 (m, 2H), 8.50 (d, *J* = 2.8 Hz, 1H), 8.30 (d, *J* = 3.2 Hz, 1H), 8.00 (d, *J* = 10 Hz, 1H), 7.60 (m, 1H) , 7.56 (m, 1H), 4.22 (br, 4H), 2.14 (br, 2H), 1.30-1.50 (m, 80H), 0.90-0.97 (m, 12H) ppm. ^{19}F NMR (471 MHz, 393K, TCE): δ 106.3 (s, 1F) ppm. GPC (80 °C, chlorobenzene, vs PS): M_n = 48.7 kDa, M_w = 166.0 kDa, PDI = 3.4.

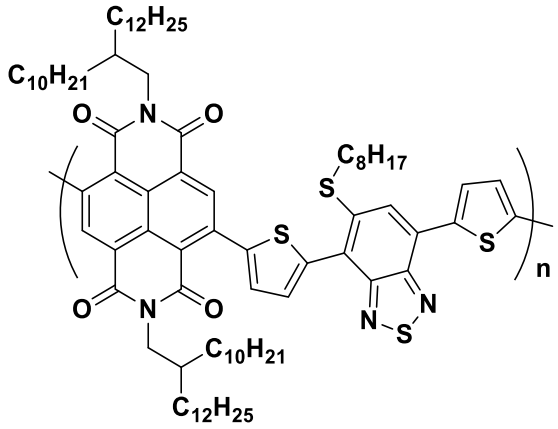
Synthesis of PNDIV-TfBTT polymer



To a 20 mL microwave vial under nitrogen, 4,7-bis(5-bromothiophen-2-yl)-5-fluorobenzo[c][1,2,5]thia-diazole (44.2 mg, 0.093 mmol), 2,7-bis(2-octyldodecyl)-4,9-bis((E)-2-(tributylstannyl)vinyl)benzo[lmn]-[3,8]phenanthroline-1,3,6,8(2H,7H)-tetraone (145.8 mg, 0.093 mmol), $Pd_2(dba)_3$ (2.9 mg, 0.003 mmol) and P(*o*-tol)$_3$ (4.6 mg, 0.015 mmol) was added and degassed thoroughly before toluene (4 mL) was added and degassed for a further 10 minutes. The mixture was heated to 120 °C and stirred at this temperature overnight. The mixture was brought to room temperature, precipitated in methanol and filtered into a Soxhlet thimble. The product was washed (Soxhlet) with methanol, acetone and hexane. The final product was obtained in three fractions: (1) extracted from chloroform (2) extracted from chlorobenzene and (3) unextracted material removed from the thimble. After extraction, the solvent was removed using a rotary evaporator. The product was dissolved in the minimum amount of chlorobenzene (approx. 2 mL) and precipitated into methanol (approx. 100 mL). The precipitate was collected by vacuum filtration through a nylon pad (pore size 20 µm), washed with methanol and left to dry. The dry product was collected in a vial and further dried under vacuum. The product obtained was a dark blue solid (99 mg, 81% yield).

^{1}H NMR (500 MHz, 393K, TCE): δ 9.06-7.48 (br, 7H), 7.22-6.33 (br, 4H), 4.30 (br, 4H), 2.02 (br, 2H), 1.10-1.40 (m, 92H), 0.90-1.00 (br, 15H) ppm. ^{19}F NMR (471 MHz, 393K, TCE): δ 106.0 (br, 1F) ppm. GPC (80 °C, chlorobenzene, vs PS): M_n = 83.2 kDa, M_w = 170.0 kDa, PDI = 2.0.

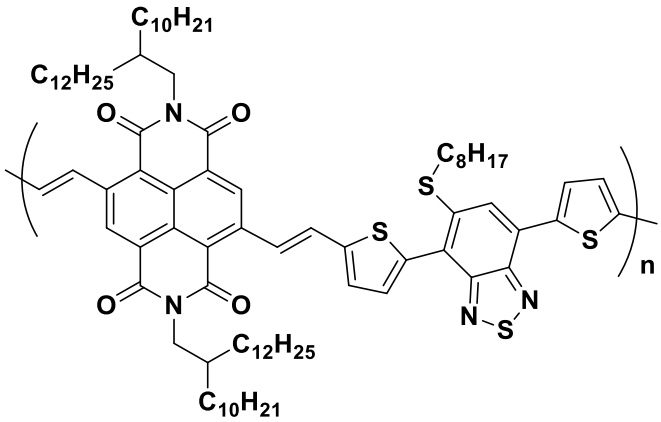
Synthesis of PNDI-T(SR)BTT polymer



To a 2 mL microwave vial under nitrogen, PNDI-TfBTT (10 mg, 0.008 mmol) and an excess of K_2CO_3 (13.8 mg, 0.10 mmol) were added. The vial was sealed with a septum and degassed with nitrogen, before anhydrous chlorobenzene (1.5 mL) and DMF (0.5 mL) (concentration of 5 mg/mL of polymer) were added. Excess 1-ocatanethiol (4 mg, 0.027 mmol) was then added and the solution was degassed with nitrogen. The solution was heated in a microwave reactor at 120 °C for 30 min. After cooling, the solution was precipitated into methanol (10:1 v:v of methanol:solution), stirred for 30 min and filtered through a Soxhlet thimble. Unreacted thiol was removed by washing (Soxhlet) with acetone and the polymer was extracted with $CHCl_3$. The $CHCl_3$ fraction was concentrated to 1 mL, precipitated into MeOH (10:1 v:v of methanol:solution) and filtered to isolate the polymer. The product obtained was a dark blue solid (6.94 mg, 62% yield).

^{1}H NMR (500 MHz, 393K, TCE): δ 9.00-8.85 (br, 2H), 8.32-7.78 (m, 3H), 7.58-7.39 (br, 2H), 4.13 (br, 4H), 3.13 (br, 2H), 1.22-1.40 (m, 80H), 0.90-1.00 (br, 12H) ppm. ^{19}F NMR (471 MHz, 393K, TCE): No signal observed. GPC (80 °C, chlorobenzene, vs PS): M_n = 52.8 kDa, M_w = 86.4 kDa, PDI = 1.6.

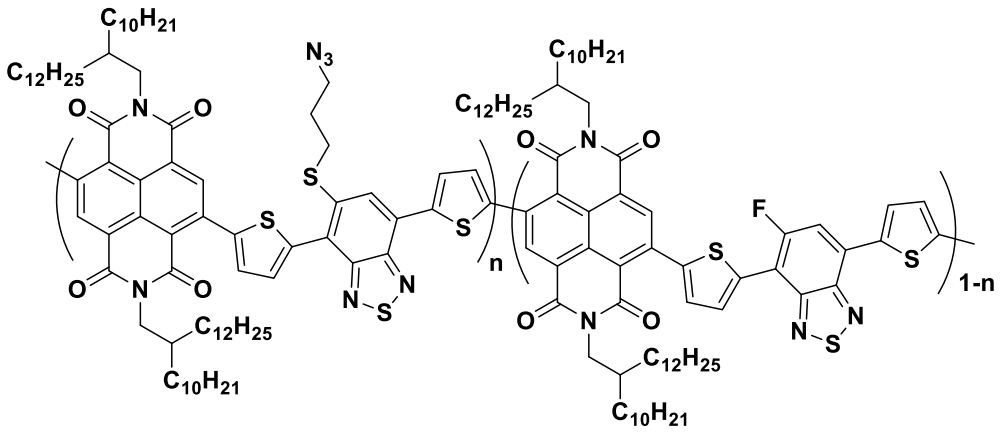
Synthesis of PNDIV-T(SR)BTT polymer



To a 2 mL microwave vial under nitrogen, PNDIV-TfBTT (10 mg, 0.008 mmol) and an excess of K_2CO_3 (13.8 mg, 0.10 mmol) were added. The vial was sealed with a septum and degassed with nitrogen, before anhydrous chlorobenzene (1.5 mL) and DMF (0.5 mL) (concentration of 5 mg/mL of polymer) were added. Excess 1-ocatanethiol (4 mg, 0.027 mmol) was then added and the solution was degassed with nitrogen. The solution was heated in a microwave reactor at 120 °C for 30 min. After cooling, the solution was precipitated into methanol (10:1 v:v of methanol:solution), stirred for 30 min and filtered through a Soxhlet thimble. Unreacted thiol was removed by washing (Soxhlet) with acetone and the polymer was extracted with $CHCl_3$. The $CHCl_3$ fraction was concentrated to 1 mL, precipitated into MeOH (10:1 v:v of methanol:solution) and filtered to isolate the polymer. The product obtained was a dark blue solid (5.49 mg, 48% yield).

^{1}H NMR (500 MHz, 393K, TCE): δ 9.23-7.40 (br, 7H), 7.25-6.35 (br, 4H), 4.29 (br, 4H), 3.18 (br, 2H), 1.40-1.22 (m, 92H), 0.90-1.00 (br, 15H) ppm. ^{19}F NMR (471 MHz, 393K, TCE): No signal observed. GPC (80 °C, chlorobenzene, vs PS): M_n = 60.0 kDa, M_w = 129.2 kDa, PDI = 2.2.

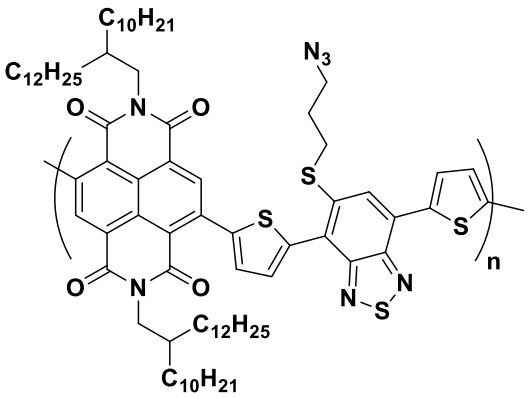
Synthesis of PNDI-T(SAz)BTT – 10% polymer



To a 2mL microwave vial under nitrogen pyrrolidine (16.04 µL, 0.114 mmol) was added to a solution of S-(3-azidopropyl)thioacetate (8.10 µL, 0.096 mmol) in DMF (10 mL) and stirred at room temperature for 70 minutes to obtain 3-azidopropane-1-thiol in situ. To a separate 20 mL microwave vial under nitrogen, PNDI-TfBTT (60 mg, 0.048 mmol) and an excess of K_2CO_3 (33 mg, 0.24 mmol) were added. The vial was sealed with a septum and degassed with nitrogen, before anhydrous chlorobenzene (4.5 mL) and DMF (1.0 mL) (concentration of 5 mg/mL of polymer) were added. The mixture containing 3-azidopropane-1-thiol (0.50 mL, 0.0057 mmol) was then added and the solution was degassed with nitrogen. The solution was heated in an oil bath at 120 °C for 12 hrs. After cooling, the solution was precipitated into methanol (10:1 v:v of methanol:solution), stirred for 30 min and filtered through a Soxhlet thimble. Unreacted thiol was removed by washing (Soxhlet) with methanol and the polymer was extracted with $CHCl_3$. The $CHCl_3$ fraction was concentrated to 1 mL, precipitated into MeOH (10:1 v:v of methanol:solution) and filtered to isolate the polymer. The product obtained was a dark blue solid (52 mg, 85% yield).

^{1}H NMR (500 MHz, 393K, TCE): δ 9.00-8.90 (m, 2H), 8.50 (s, 1H), 8.30 (s, 1H), 8.05-7.75 (m, 1H), 7.61-7.47 (br, 2H), 4.35-4.00 (br, 4H), 3.60-3.45 (br, 0.2H) , 3.30-3.20 (br, 0.2H), 1.40-1.22 (m, 80H), 0.90-1.00 (br, 12H) ppm. ^{19}F NMR (471 MHz, 393K, TCE): δ 106.3 (br, 1F) ppm. GPC (80 °C, chlorobenzene, vs PS): M_n = 194.6 kDa, M_w = 315.2 kDa, PDI = 1.6.

Synthesis of PNDI-T(SAz)BTT – 100% polymer



To a 2mL microwave vial under nitrogen pyrrolidine (161 µL, 1.16 mmol) was added to a solution of S-(3-azidopropyl)thioacetate (81.2 µL, 0.96 mmol) in DMF (10 mL) and stirred at room temperature for 70 minutes to obtain 3-azidopropane-1-thiol in situ. To a separate 20 mL microwave vial under nitrogen, PNDI-TfBTT (60 mg, 0.048 mmol) and an excess of K_2CO_3 (33 mg, 0.24 mmol) were added. The vial was sealed with a septum and degassed with nitrogen, before anhydrous chlorobenzene (4.5 mL) and DMF (1.0 mL) (concentration of 5 mg/mL of polymer) were added. The mixture containing 3-azidopropane-1-thiol (0.50 mL, 0.057 mmol) was then added and the solution was degassed with nitrogen. The solution was heated in an oil bath at 120 °C for 12 hrs. After cooling, the solution was precipitated into methanol (10:1 v:v of methanol:solution), stirred for 30 min and filtered through a Soxhlet thimble. Unreacted thiol was removed by washing (Soxhlet) with methanol and the polymer was extracted with $CHCl_3$. The $CHCl_3$ fraction was concentrated to 1 mL, precipitated into MeOH (10:1 v:v of methanol:solution) and filtered to isolate the polymer. The product obtained was a dark blue solid (45 mg, 69% yield).

^{1}H NMR (500 MHz, 393K, TCE): δ 9.05-8.85 (br, 2H), 8.40-7.75 (m, 3H), 7.65-7.45 (br, 2H), 4.40-4.00 (br, 4H), 3.60-3.45 (br, 2H), 3.32-3.20 (br, 2H), 1.40-1.22 (m, 82H), 1.00-0.85 (br, 12H) ppm. ^{19}F NMR (471 MHz, 393K, TCE): No signal observed. GPC (80 °C, chlorobenzene, vs PS): M_n = 28.9 kDa, M_w = 78.9 kDa, PDI = 2.7.

4.17 Appendix Chapter 4 - list of figures

All supplementary figures for Chapter 4 are presented in the Appendix Chapter 8).

Figure S4.1. PESA measurements for PNDI-TfBTT, PNDIV-TfBTT, PNDI-T(SR)BTT and PNDIV-T(SR)BTT.

Figure S4.2. UV-Vis absorption and PL emission for PNDI-TfBTT, PNDIV-TfBTT, PNDI-T(SR)BTT and PNDIV-T(SR)BTT.

Table S4.1. Summary of HOMO and LUMO energy levels and dihedral angles within energy minimised structures of PNDI-TfBTT, PNDIV-TfBTT, PNDI-T(SR)BTT and PNDIV-T(SR)BTT calculated using DFT at the B3LYP/6.31G* level.

Figure S4.3. (a) Molecular model used for DFT calculations. DFT optimisation of a model of PNDI-TfBTT at the B3LYP/6-31G(d,p) level showing (b) overall backbone geometry (c) HOMO distribution along backbone (d) LUMO distribution along backbone.

Figure S4.4. (a) Molecular model used for DFT calculations. DFT optimisation of a model of PNDI-T(SR)BTT at the B3LYP/6-31G(d,p) level showing (b) overall backbone geometry (c) HOMO distribution along backbone (d) LUMO distribution along backbone.

Figure S4.5. (a) Molecular model used for DFT calculations. DFT optimisation of a model of PNDIV-TfBTT at the B3LYP/6-31G(d,p) level showing (b) overall backbone geometry (c) HOMO distribution along backbone (d) LUMO distribution along backbone.

Figure S4.6. (a) Molecular model used for DFT calculations. DFT optimisation of a model of PNDIV-T(SR)BTT at the B3LYP/6-31G(d,p) level showing (b) overall backbone geometry (c) HOMO distribution along backbone (d) LUMO distribution along backbone.

Figure S4.7. GIWAXS images of PNDI-TfBTT, PNDIV-TfBTT, PNDI-T(SR)BTT and PNDIV-T(SR)BTT films as-cast and annealed at 100 °C and 200 °C.

Figure S4.8. GIWAXS diffraction patterns for PNDI-TfBTT, PNDIV-TfBTT, PNDI-T(SR)BTT and PNDIV-T(SR)BTT films as-cast and annealed at 100 °C and 200 °C.

Figure S4.9. Transfer (a,b) characteristics of PNDI-TfBTT OTFT device. (c) Electron mobility vs. annealing temperature of polymer thin film.

Figure S4.10. Transfer (a,b) and output (c) characteristics of PNDI-TfBTT OTFT device annealed at 200 °C.

Figure S4.11. Transfer (a,b) characteristics of PNDI-T(SR)BTT OTFT device. (c) Electron mobility vs. annealing temperature of polymer thin film.

Figure S4.12. Transfer (a,b) characteristics of PNDIV-TfBTT OTFT device. (c) Electron mobility vs. annealing temperature of polymer thin film.

Figure S4.13. Transfer (a,b) characteristics of PNDIV-T(SR)BTT OTFT device. (c) Electron mobility vs. annealing temperature of polymer thin film.

Figure S4.14. ^{1}H NMR of 2,7-bis(2-decyltetradecyl)benzo[lmn][3,8]phenanthroline-1,3,6,8(2H,7H)-tetraone (NDI-2DT), where peaks assigned to NDI are highlighted in red. (a) NDI before exposure to S_NAr reaction conditions. (b-e) NDI after exposure to S_NAr reaaction conditions with K_2CO_3, KOH, DBU, ^{t}BuOK respectively.

Figure S4.15. ^{1}H NMR of PNDI-TfBTT.

Figure S4.16. ^{1}H NMR of PNDIV-TfBTT.

Figure S4.17. ^{1}H NMR of PNDI-T(SR)BTT.

Figure S4.18. ^{1}H NMR of PNDIV-T(SR)BTT.

Figure S4.19. ^{19}F NMR of PNDI-TfBTT.

Figure S4.20. ^{19}F NMR of PNDIV-TfBTT.

Figure S4.21. ^{19}F NMR of PNDI-T(SR)BTT.

Figure S4.22. ^{19}F NMR of PNDIV-T(SR)BTT.

Figure S4.23. ^{1}H NMR of PNDI-T(SAz)BTT-10%.

Figure S4.24. ^{19}F NMR of PNDI-T(SAz)BTT-10%.

Figure S4.25. ^{1}H NMR of PNDI-T(SAz)BTT-100%.

Figure S4.26. ^{19}F NMR of PNDI-T(SAz)BTT-100%.

Figure S4.27. ^{1}H NMR spectra for increasing substitution along the PNDI-TfBTT backbone.

Figure S4.28. ^{19}F NMR spectra for increasing substitution along the PNDI-TfBTT backbone.

Figure S4.29. (a) TGA data for PNDI-TfBTT, PNDI-T(SAz)BTT-10% and PNDI-T(SAz)BTT-100% carried out in a Nitrogen atmosphere at 5 °C min^{-1} (b,c) DSC data for PNDI-TfBTT, PNDI-T(SAz)BTT-10% and PNDI-T(SAz)BTT-100% carried out in a Nitrogen atmosphere at 10 °C min^{-1}.

Figure S4.30. GIWAXS images of PNDI-T(SAz)BTT-10% films (a) as-cast (no thermal anneal) and annealed at 200 °C and 300 °C and (b) exposed to UV light (254 nm) for 60 minutes before no thermal anneal (UV only) and annealed at 200 °C and 300 °C.

Figure S4.31. GIWAXS diffraction patterns for PNDI-T(SAz)BTT-10% films as-cast and annealed at 200 °C and 300 °C, with and without UV exposure (254 nm) prior to annealing.

Figure S4.32. GIWAXS images of PNDI-T(SAz)BTT-100% films (a) as-cast (no thermal anneal) and annealed at 200 °C and 300 °C and (b) exposed to UV light (254 nm) for 60 minutes before no thermal anneal (UV only) and annealed at 200 °C and 300 °C.

Figure S4.33. GIWAXS diffraction patterns for PNDI-T(SAz)BTT-10% films as-cast and annealed at 200 °C and 300 °C, with and without UV exposure (254 nm) prior to annealing.

Figure S4.34. Transfer and output characteristics of PNDI-T(SAz)BTT-10% OTFT device.

Figure S4.35. Transfer and output characteristics of PNDI-T(SAz)BTT-100% OTFT device.

Figure S4.36. Transfer characteristics of PNDI-T(SAz)BTT-10% OTFT device, where thin films have been exposed to UV light.

Figure S4.37. Transfer characteristics of PNDI-T(SAz)BTT-100% OTFT device, where thin films have been exposed to UV light.

5 Chapter 5: Design and progression of Anionic Conjugated Polyelectrolytes as interfacial layers

5.1 Introduction

Conjugated polyelectrolytes (CPEs) are organic semiconducting materials comprising of a conjugated polymer backbone with ionic pendant groups. These materials display interesting physical and optoelectronic properties, making them perfect candidates for use in organic electronic devices such as OLEDs, OFETS and OSCs.[253–256] In these devices, CPEs are used as an interfacial layer between the active material and the electrode; to modify the work function (WF) of the electrode by formation of permanent molecular dipole moments.[257–259] Ionic pendant groups within the CPE also alter the solubility of the polymer, compared to the non-ionic analogues, where polar solvents are used to dissolve the polymers. The solubility of CPEs is orthogonal to that of non-ionic conjugated polymers used in the active layers of an organic device. Orthogonal solubility enables the deposition of multiple layers within a device without interlayer mixing, thus, multilayer devices can be fabricated.

Seo *et.al.* reported the electronic properties of cationic, neutral and anionic CPEs with identical polymer backbones. Using ultraviolet photoelectron spectroscopy (UPS) measurements the interfacial dipole moment was determined. For cationic CPEs, a negative interfacial dipole was formed, conversely, for the neutral and anionic CPEs a positive interfacial dipole was formed. Figure 5.1 illustrates the absence and presence of negative and positive dipole moments and the respective effect on the measured work function of the electrode.[260] Lee *et.al.* demonstrated the oxidation of n-type CPEs to self-doped p-type CPEs and reported the respective effect on the modified work function of ITO. N-type CPEs with anionic groups presented a negative interfacial dipole, whereas, p-type CPEs presented a positive interfacial dipole.[258,261] From the reported literature, it is understood that both the conjugated polymer backbone and the ionic side chains can influence the interfacial dipole present at the CPE-electrode interface, hence, modifying the work function of the electrode.[125,262]

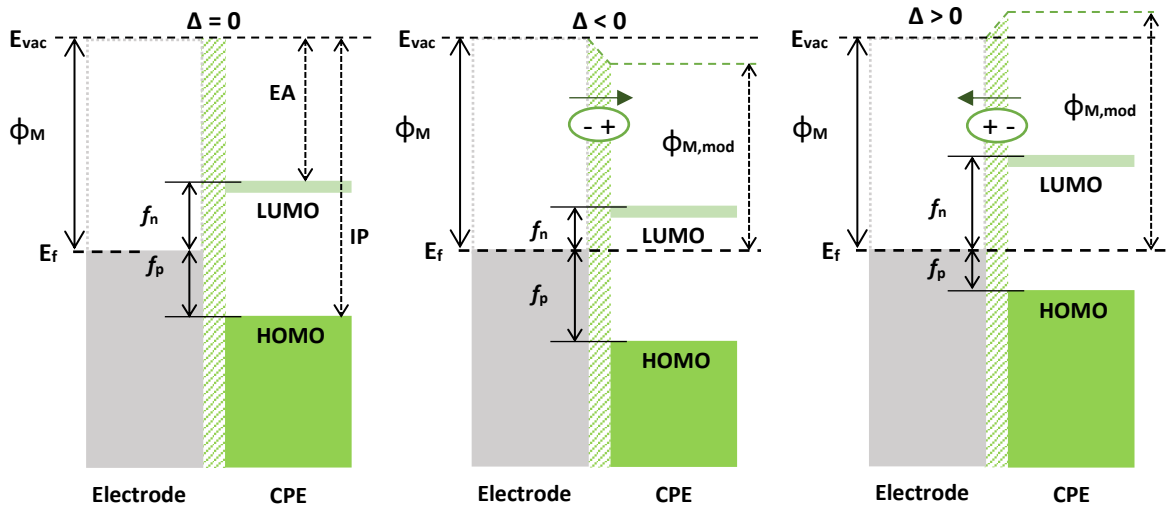


Figure 5.1. General energy level diagram of Au/CPE interface in the absence and presence of interfacial dipoles. E_{vac} represents the vacuum level, ϕ_M and $\phi_{M,mod}$ represent the work function of the ITO (pristine) and ITO modified by a CPE interlayer electrodes respectively, f_p and f_n represent the hole and injection barriers respectively, EA is the electron affinity, IP is the ionisation potential and Δ represents the interfacial dipole.[260,262]

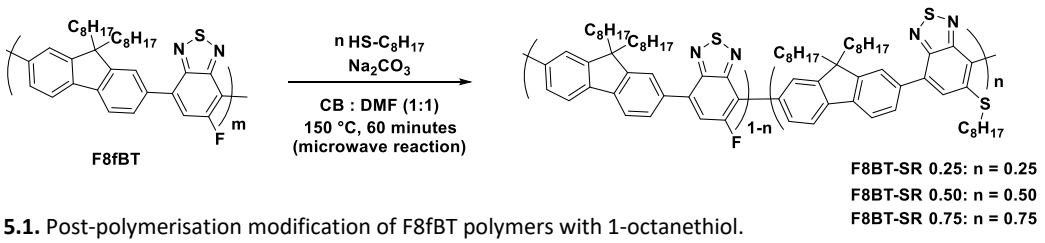
Further developments, reported by Lee *et. al.*, highlighted the effects of increasing the ionic density within CPEs. With increasing the ionic density, the modified work function of the electrode was shown to decrease and the respective interfacial dipole increased.[261] CPEs with wide-ranging ionic densities were synthesised from polymerisation techniques where the monomers had varied ionic densities. However few examples in the literature of CPEs with varied ionic density within the polymer have been reported, which could be owed to the complex synthetic procedures required to afford such polymers.[263,264]

Post-polymerisation techniques could provide a straight-forward alternative to synthesising conjugated polymers with varied ionic density. Post-polymerisation modifications were identified early on as an ideal synthetic method towards CPEs.[265–267] However the use of post-polymerisation techniques to modulate the ionic density has hardly been explored, to the best of my knowledge. In this final chapter, post-polymerisation modification, via S_NAr, to afford anionic n-type CPEs with varied ionic densities is reported. The effect of increasing anionic pendant groups along the polymer backbone on physical and optoelectronic properties was evaluated. Furthermore, the corresponding modified work function of ITO electrode was reported, alluding to how the materials might behave as a hole transport interlayer within an electronic device.

5.2 Synthesis of anionic polymers

Adam Creamer *et.al.* demonstrated by varying the molar percentage of thioalkyl added in an S_NAr reaction (via PPM) with F8fBT, the percentage of thiol substituted along the backbone could be directly controlled. Partial substitution along the backbone was demonstrated on a small scale (ca. 5 mg).[97] In this work, a modified procedure was used to partially substitute 1-octanethiol onto F8fBT on a larger scale (ca. 50-100mg). F8fBT polymers partially substituted with 1-octanethiol (F8BT-SR 0.X) were further functionalised with 3-mercapto-1-propanesulfonic acid sodium salt affording the anionic CPEs (F8BT-SAn X.X); with varied densities of anionic group incorporated along the polymer backbone. Using this method, it was possible to eliminate the presence of fluorine, by substitution with a non-ionic thioalkyl group that should not influence the optoelectronic properties of the material.

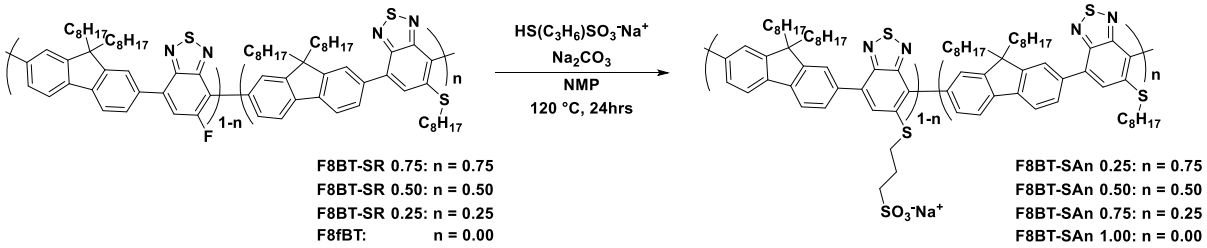
Starting polymer, F8fBT, was synthesised via a Suzuki coupling reaction from previously reported reaction conditions.[97] Utilisation of PPM methods directly enabled the synthesis of a highly comparable polymer series with identical average polymer chain lengths and polydispersties. The M_n of F8fBT was found to be 43 kDa, determined by SEC, hence, polymers synthesised from this batch of F8fBT were expected to have a comparable average molecular weight. F8fBT was partially functionalised with commercially available 1-octanethiol in the presence of Na_2CO_3 in a chlorobenzene/DMF (1:1) solvent mixture, shown in Scheme 5.1. A modification to the original method was made here, to increase the DMF content from a chlorobenzene/DMF 3:1 mixture to a 1:1 mixture. By increasing the content of the polar aprotic solvent (DMF) the ionic transition states are stabilised, therefore, a clean and complete reaction proceeded within 60 minutes at 150 °C in a microwave reactor (Biotage Initiator).[268] The mixtures were precipitated into methanol and purified by Soxhlet extraction to remove any excess base and thiol terminated reactant. Finally, the polymers were extracted from chloroform to afford a fibrous yellow solid in a yield of 77 to 90%. Molar equivalences, 0.25, 0.50 and 0.75, of 1-octanthiol were used to give three polymers (F8BT-SR



Scheme 5.1. Post-polymerisation modification of F8fBT polymers with 1-octanethiol.

0.25, F8BT-SR 0.50 and F8BT-SR 0.75) with 25, 50 and 75% substitution along the polymer backbone respectively.

Unsubstituted, F8fBT, and partially substituted polymers, F8BT-SR 0.25, F8BT-SR 0.50 and F8BT-SR 0.75 were further reacted with 3-mercapto-1-propanesulfonic acid sodium salt in the presence of Na_2CO_3 in N-methyl-2-pyrrolidone (NMP) at 120 °C (hot-plate) for 24 hours, shown in Scheme 5.2. As the anionic polymer products are more soluble in polar solvents, NMP was selected to solubilise both the starting and product polymers. The reaction mixtures were precipitated into ethyl acetate and purified by sequential Soxhlet extraction with ethyl acetate, acetone and chloroform to remove any excess base, thiol terminated reactant and residual starting polymer. Finally, the polymers were removed from the Soxhlet thimble, dissolved in a chlorobenzene:DMF mixture (1:1) and re-precipitated from ethyl acetate to afford a non-fibrous yellow solid in a yield of 69 to 98%. Anionic polymer products, F8BT-SAn 0.50 and F8BT-SAn 0.75 and F8BT-SAn 1.00, with both the alkylchain and anionic functionality, were insoluble in weakly polar aprotic solvents (e.g. chlorobenzene or chloroform), however, were soluble in polar aprotic solvents (e.g. DMF or DMSO). F8BT-SAn 0.25, showed partial solubility in weakly polar aprotic chlorobenzene or polar aprotic DMF. When a mixture of the solvents chlorobenzene:DMF (1:1) was used F8BT-SAn 0.25 was completely soluble. All anionic polymers were found to be soluble in a chlorobenzene:DMF (1:1) mixture.



Scheme 5.2. Post-polymerisation modification of F8fBT, F8BT-SR 0.25, F8BT-SR 0.50 and F8BT-SR 0.75 with 3-mercapto-1-propanesulfonic acid sodium salt to afford anionic polymers.

Using the synthetic method, reported above, the anionic CPEs were synthesised with increasing anionic content along the polymer backbone. Furthermore, by displacement of fluorine with non-ionic 1-octanethiol, no fluorine was present along the backbone of the CPEs. Fluorine present along the polymer backbone is known to influence the electronic properties of the polymer.[97,269] To understand the effect of increasing anionic density solely, it was important to displace the residual fluorine with a non-ionic substituent that would not influence the overall electronic properties of the polymer.

5.2.1 Confirmation of polymer structures by NMR

Structures of the partially substituted polymers (F8BT-SR 0.X) and anionic polymers (F8BT-SAn X.X) were confirmed by a combination of ^{1}H and ^{19}F NMR. Unsubstituted and partially substituted polymer samples were investigated in deuterated chloroform at room temperature. Firstly, the starting polymer, F8fBT, showed a multiplet at δ 7.70 – 8.20 ppm corresponding to the aromatic protons (7H) along the polymer backbone in the ^{1}H NMR spectra, shown in Figure S5.1. A series of peaks corresponding to the alkyl sidechains (34H) were observed in the aliphatic region. After substitution of 1-octanethiol onto the F8fBT backbone, aromatic and aliphatic peaks from the F8BT backbone were observed. Additionally, new peaks in the NMR spectra were observed at δ 0.86, 1.25, 1.42, 1.69 and 2.97 ppm corresponding to the substituted octanethiol sidechain, shown in Figures S5.2 to S5.4,. The peak at δ 2.97 ppm (2H) corresponds to the methylene group (-CH_2-) adjacent to the thiol linker. Integral values of the aromatic peaks (7H) and the methylene group (XH_a) were compared to quantitatively determine the degree of substitution along the polymer backbone, expected and measured values from the ^{1}H NMR spectra are summarised in Table 5.1. For F8BT-SR 0.25, F8BT-SR 0.50 and F8BT-SR 0.75 the methylene group integral values were 0.47, 1.13 and 1.54, indicating approximately 25, 50 and 75% substitution respectively.

Unsubstituted and partially substituted polymers were used to synthesise anionic polymers. Anionic polymer samples were run in deuterated DMSO at 393K as the solubility was low, at high temperature the signals were well resolved. After substitution of 3-mercapto-1-propanesulfonic acid sodium salt onto the polymers, aromatic and aliphatic peaks from the

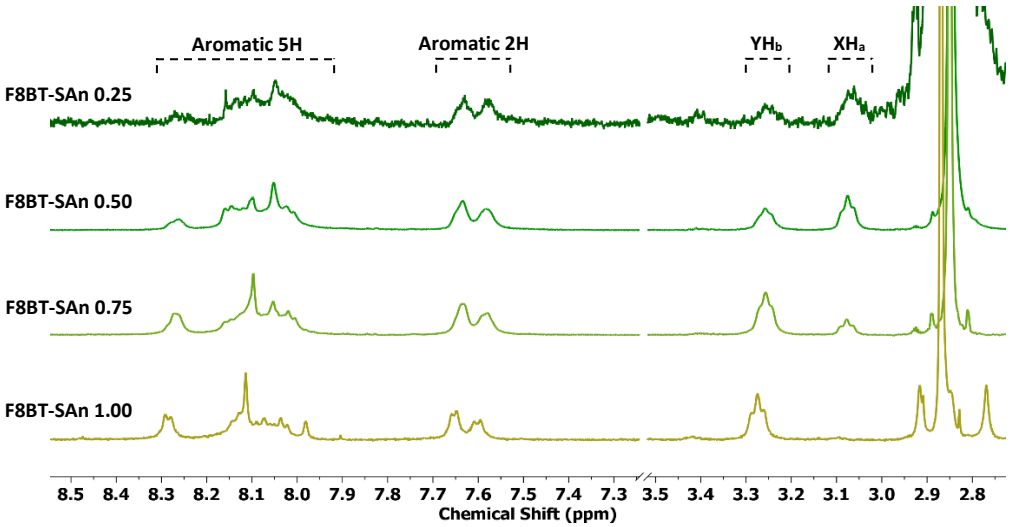


Figure 5.2. ^{1}H NMR spectra for increasing anionic content along the F8fBT backbone where the aromatic peaks were integrated (5H and 2H) and directly compared with XH_a and YH_b.

respective starting polymer backbones were observed in the ^{1}H NMR. New peaks in the ^{1}H NMR spectra appear at δ 2.04, 2.61 and 3.27 ppm corresponding to the substituted 3-mercapto-1-propanesulfonic acid sodium salt sidechain, shown in Figure S5.9 to S5.12. The peak at δ 3.27 ppm (2H) corresponds to the methylene group (-CH_2-) adjacent to the thiol linker. Integral values of the aromatic peak (7H) and the methylene group (YH_b) were compared to quantitatively determine the degree of substitution, expected and measured values are also summarised in Table 5.1. For F8BT-SAn 0.25, F8BT-SAn 0.50, F8BT-SAn 0.75 and F8BT-SAn 1.00 the methylene group integral values were 0.70, 0.91, 1.60 and 2.00 indicating approximately 25, 50, 75 and 100% substitution respectively. Due to the low solubility and high temperatures (393K) required to measure the samples, a lower degree of accuracy in NMR integration values should be expected, hence, some deviation from the expected values was anticipated.

Table 5.1. Table of expected and measured integration values for H_a and H_b vs aromatic H by NMR.

Polymer	mol% of thioalkyl chain added	XH_a (expected)	XH_a (measured)	YH_b (expected)	YH_b (measured)
F8fBT	0.00	-	**-**	-	**-**
F8BT-SR 0.25	0.2 5	0.50	**0.47**	-	**-**
F8BT-SR 0.50	0.50	1.00	**1.13**	-	**-**
F8BT-SR 0.75	0.75	1.50	**1.54**	-	**-**
F8BT-SAn 0.25	0.75	1.50	**1.47**	0.50	**0.70**
F8BT-SAn 0.50	0.50	1.00	**1.16**	1.00	**0.91**
F8BT-SAn 0.75	0.25	0.50	**0.47**	1.50	**1.60**
F8BT-SAn 1.00	0.00	-	**-**	2.00	**2.00**

In the ^{19}F NMR spectra for the unsubstituted (F8fBT) and partially substituted (F8BT-SR 0.25, F8BT-SR 0.50 and F8BT-SR 0.75) polymers, shown in Figures S5.5 to S5.8, a clear single fluorine peak at ca. δ 114.5 ppm was observed. Post functionalisation with 3-mercapto-1-propanesulfonic acid sodium salt to afford the anionic polymers (F8BT-SAn 0.25, F8BT-SAn 0.50, F8BT-SAn 0.75 and F8BT-SAn 1.00) saw the fluorine signal completely disappear, as shown in Figures S5.13 to S5.16.

5.2.2 Confirmation of polymer structures by FTIR

Fourier-transform infrared spectroscopy (FTIR) was used to further characterise the polymers, as shown in Figure 5.3. The absorption band in the range 1450 to 1460 cm^{-1}, relates to the C=C stretch from the aromatic backbone. The bands at 2920 cm^{-1} and 2845 to 2850 cm^{-1} relate to the asymmetric and symmetric stretching of the sp^3 hybridised C-H bonds in the alkyl sidechains. These absorption bands are observed in the IR spectra for all of the polymers. For the anionic polymers two additional absorption bands were identified at 1020 to 1070 cm^{-1} and 1080 to 1285 cm^{-1} associated with the asymmetric and symmetric stretches from the sulfonate group ($-SO_3^-Na^+$).[270] FTIR results confirm the presence of the sulfonate group on the anionic polymers. It should be noted that F8BT-SAn 1.00 also displays a broad absorption at ca. 3430 cm^{-1} which may result from the presence of water in the more hydrophilic polymer.

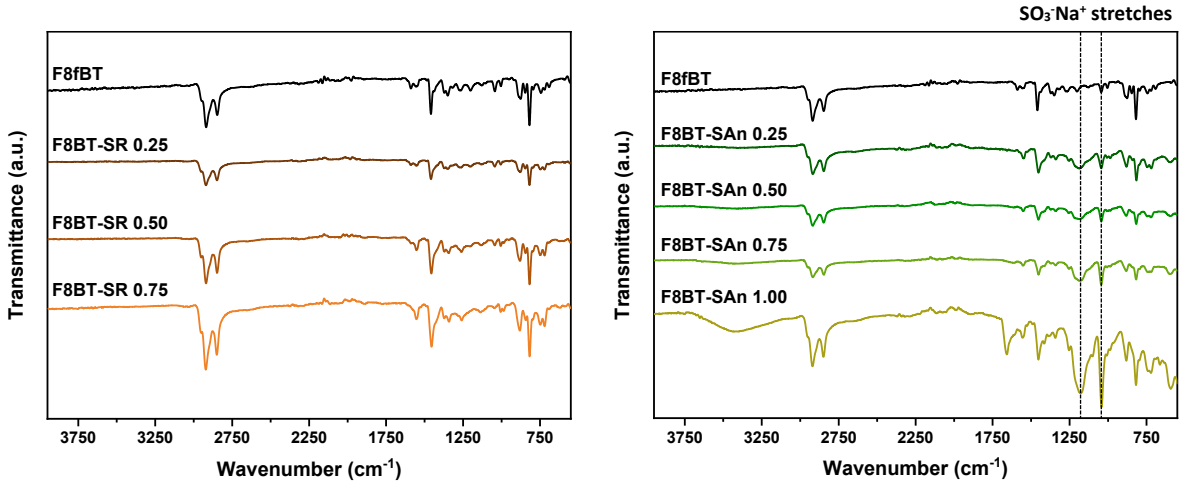


Figure 5.3. FTIR spectra for unsubstituted polymer (F8fBT), partially substituted polymers (F8BT-SR 0.25, F8BT-SR 0.50 and F8BT-SR 0.75) and anionic polymers (F8BT-SAn 0.25, F8BT-SAn 0.50, F8BT-SAn 0.75 and F8BT-SAn 1.00).

5.2.3 Polymer composition by XPS

X-ray photoelectron spectroscopy (XPS) was used to quantitatively analyse the polymer compositions, XPS survey spectra are shown in Figures S5.17 to S5.23. As an example, and for direct reference, XPS survey for F8BT-SR 0.25 and the corresponding anionic polymer F8BT-SAn 0.75 are shown below in Figure 5.4. From the XPS survey of the partially substituted polymers, four key photoelectron peaks were measured with a binding energy of 688, 400, 284 and 185 eV that relate to the emitted photoelectrons from the F_{1s}, N_{1s}, C_{1s} and S_{2p} orbitals respectively. Once the remaining fluorine was displaced with 3-mercapto-1-propanesulfonic acid sodium salt, to afford the anionic polymers, the photoelectron peak at 688 eV (F_{1s})

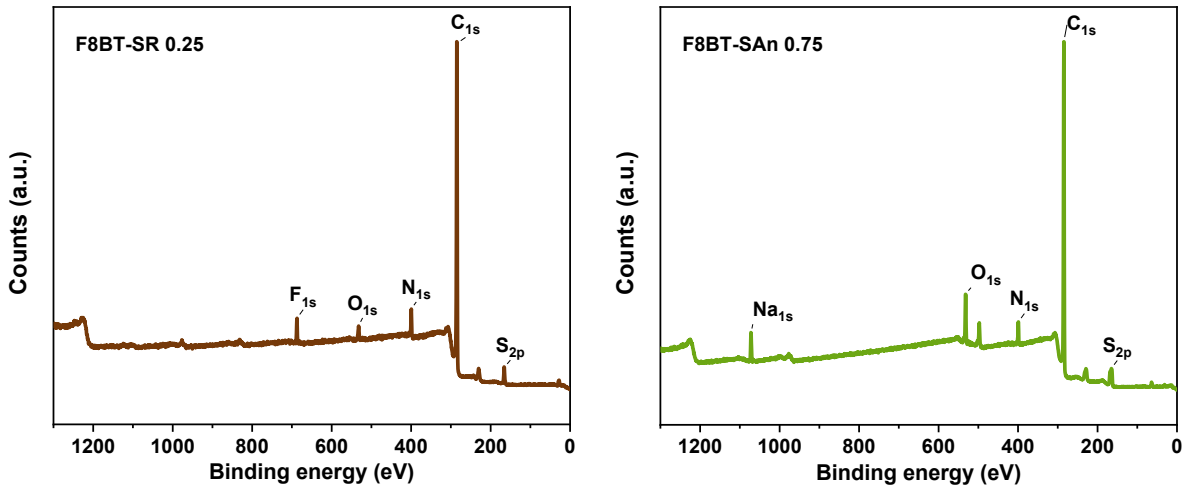


Figure 5.4. XPS survey for partially substituted polymer F8BT-SR 0.25 (left) and for anionic polymer F8BT-SAn 0.75 (right).

disappears. Furthermore, two peaks at 1070 and 534 eV were observed in the XPS spectra for all anionic polymers related to emitted photoelectrons from Na_{1s} and O_{1s} orbitals respectively.

The elemental composition of each polymer was evaluated from the acquired XPS spectra, where the theoretical composition and the measured composition for each polymer are outlined in Table 5.2. As an example, and for direct reference, composition data for F8BT-SR 0.25 shows little deviation from the theoretical ($C_{37.0}N_{2.0}O_{0.0}F_{0.75}S_{1.25}$) to the measured ($C_{36.67}N_{1.91}O_{0.43}F_{0.76}S_{1.23}$) composition. A similar lack of deviation was observed for the corresponding anionic polymer F8BT-SAn 0.75 from the theoretical ($C_{39.25}N_{2.0}Na_{0.75}O_{2.25}S_{2.75}$) to the measured ($C_{37.99}N_{1.94}Na_{0.96}O_{3.27}S_{2.84}$) composition. Variation in oxygen content was likely due to absorbed water in the polymer fibers. All polymers showed a good agreement of theoretical elemental composition to measured elemental composition, confirming the polymer structures were successfully synthesised with a high degree of purity.

Table 5.2. Polymer composition for unsubstituted, partially substituted and anionic polymers by XPS analysis.

Polymer	Theoretical composition	Measured composition
F8fBT	$C_{35.0}N_{2.0}O_{0.0}F_{1.0}S_{1.0}$	$C_{33.22}N_{1.49}O_{2.31}F_{1.35}S_{0.63}$
F8BT-SR 0.25	$C_{37.0}N_{2.0}O_{0.0}F_{0.75}S_{1.25}$	$C_{36.67}N_{1.91}O_{0.43}F_{0.76}S_{1.23}$
F8BT-SR 0.50	$C_{39.0}N_{2.0}O_{0.0}F_{0.5}S_{1.50}$	$C_{38.86}N_{1.92}O_{0.29}F_{0.40}S_{1.53}$
F8BT-SR 0.75	$C_{41.0}N_{2.0}O_{0.0}F_{0.25}S_{1.75}$	$C_{40.57}N_{1.94}O_{0.50}F_{0.20}S_{1.79}$
F8BT-SAn 0.25	$C_{41.75}N_{2.0}Na_{0.25}O_{0.75}S_{2.25}$	$C_{40.33}N_{3.06}Na_{0.25}O_{1.91}S_{1.45}$
F8BT-SAn 0.50	$C_{40.5}N_{2.0}Na_{0.5}O_{1.5}S_{2.5}$	$C_{40.52}N_{2.54}Na_{0.47}O_{2.36}S_{1.11}$
F8BT-SAn 0.75	$C_{39.25}N_{2.0}Na_{0.75}O_{2.25}S_{2.75}$	$C_{37.99}N_{1.94}Na_{0.96}O_{3.27}S_{2.84}$
F8BT-SAn 1.00	$C_{38.0}N_{2.0}Na_{1.0}O_{3.0}S_{3.0}$	$C_{37.39}N_{1.95}Na_{1.04}O_{3.66}S_{2.96}$

5.3 Optical properties

Absorption spectra for; (a) unsubstituted (F8fBT) and partially substituted (F8BT-SR 0.25, F8BT-SR 0.50 and F8BT-SR 0.75) polymers and (b) anionic polymers (F8BT-SAn 0.25, F8BT-SAn 0.50, F8BT-SAn 0.75 and F8BT-SAn 1.00), both in solution and film, are shown in Figures 5.5 and 5.6. Thin films were prepared by spin-coating onto glass from either chlorobenzene solutions (unsubstituted and partially substituted polymers) or chlorobenzene:DMSO 1:1 solutions (anionic polymers). Variation in the absorption spectra, with increasing anionic density along the polymer backbone was investigated. Characteristic peaks were identified and the calculated optical energy band gaps ($E_{g,opt}$) are summarised in Table 5.3.

As reported in Chapter 1 and 2, the starting polymer F8fBT in solution displays two key absorption bands at high energy (318 nm) and lower energy (446 nm) with λ_{max} at 446nm. The high energy absorption was assigned to the π-π* transition and the lower energy absorption to intramolecular charge transfer (ICT).[168] Both solution and film absorption spectra for F8fBT, F8BT-SR 0.25, F8BT-SR 0.50 and F8BT-SR 0.75 shows that with increasing octanethiol content, the low energy ICT absorption band decreases in intensity relatively. Additionally, a new absorption peak appears at ca. 370 nm on thioalkyl substitution, which grew in intensity as the percentage of thioalkyl sidechain was increased (both in solution and film absorption spectra). These peaks arise after the substitution of a thiol-terminated nucleophile, due to n_{sulfur}-π* transition, where the peak increases in intensity with increasing thiol substitution.[270]

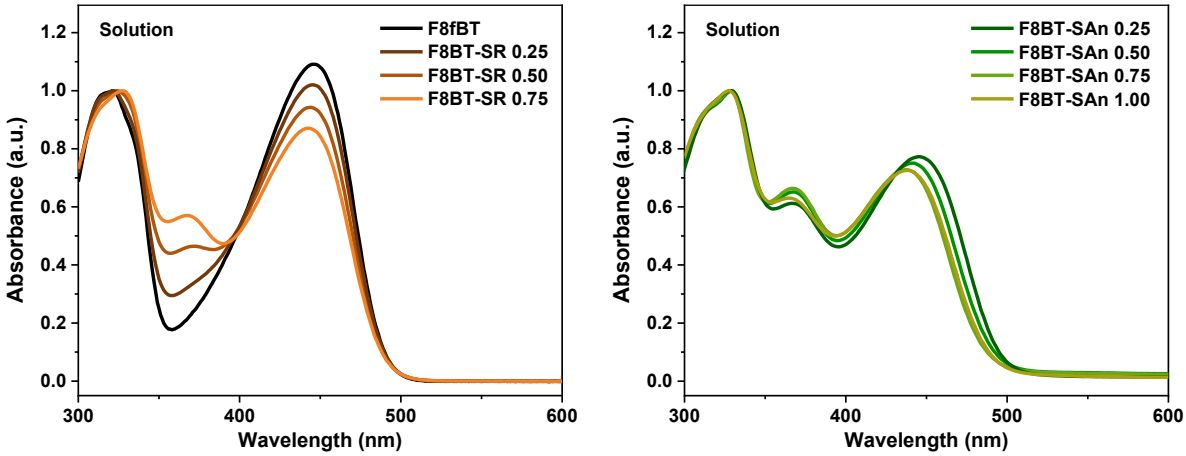


Figure 5.5. UV-Vis absorption spectra for F8fBT, F8BT-SR 0.25, F8BT-SR 0.50 and F8BT-SR 0.75 in chlorobenzene (left) and F8BT-SAn 0.25, F8BT-SAn 0.50, F8BT-SAn 0.75 and F8BT-SAn 1.00 in chlorobenzene:DMSO (1:1) (right).

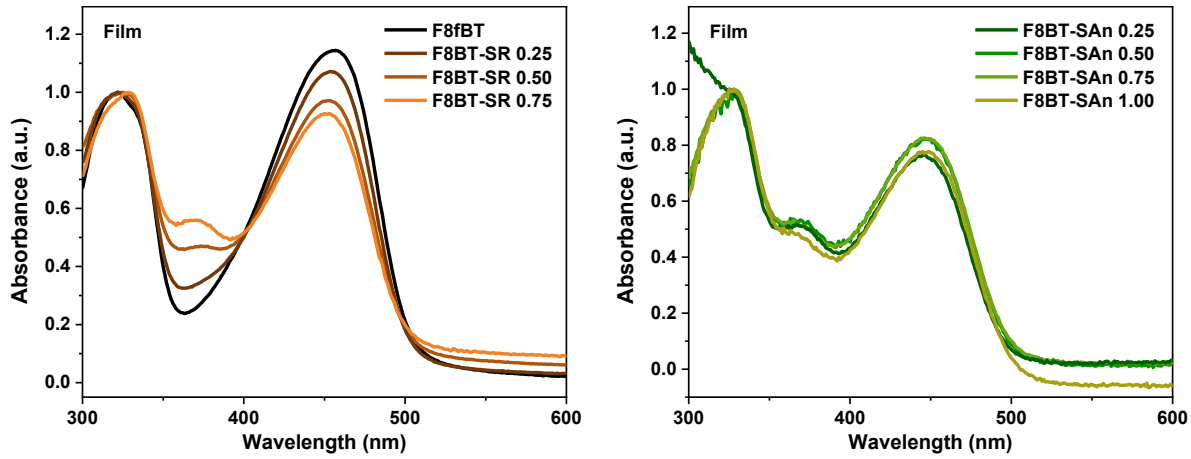


Figure 5.6. UV-Vis absorption spectra for F8fBT, F8BT-SR 0.25, F8BT-SR 0.50 and F8BT-SR 0.75 as a spun-cast thin film onto glass (left) and F8BT-SAn 0.25, F8BT-SAn 0.50, F8BT-SAn 0.75 and F8BT-SAn 1.00 as a spun-cast thin film onto glass. (right)

Anionic polymers, F8BT-SAn 0.25, F8BT-SAn 0.50, F8BT-SAn 0.75 and F8BT-SAn 1.00, showed a further decrease in the ICT absorption band intensity both in solution (ca. 440 nm) and film (ca. 446 nm). Additionally, the peak corresponding to the n_{sulfur}-π* transition was observed for all four anionic polymers in solution (ca. 367 nm) and film (ca. 367 nm). Interestingly, absorption spectra for the anionic polymers are almost indistinguishable, both in solution and film, where the ICT band intensity reduced in intensity compared to unsubstituted and partially substituted polymers. The similarity in the spectra was expected as previous reports of CPE polymers highlight the optical and electronic properties of CPEs are largely determined by the conjugated polymer backbone and not the charged pendant groups.[125] For the anionic polymers, the conjugated backbone remains the same, only the density of anionic side chains was varied.

Table 5.3. Optical properties for unsubstituted, partially substituted and anionic polymers.

Polymer	$\lambda_{abs,max}$ (nm), solution	$\lambda_{abs,max}$ (nm), film	λ_{onset} (nm), solution	λ_{onset} (nm), film	$E_{g,opt}$[a] (eV)
F8fBT	320, 445	322, 456	487	502	2.47
F8BT-SR 0.25	322, 445	322, 454	489	504	2.46
F8BT-SR 0.50	324, 370, 444	325, 373, 452	488	506	2.45
F8BT-SR 0.75	327, 368, 443	328, 371, 452	488	502	2.47
F8BT-SAn 0.25	328, 369, 446	328, 371	496	498	2.49
F8BT-SAn 0.50	328, 368, 442	328, 371	491	501	2.47
F8BT-SAn 0.75	328, 368, 438	328, 371	485	500	2.48
F8BT-SAn 1.00	328, 367, 438	328, 371	488	498	2.49

[a]Estimated from the onset of absorption from the measured UV-VIS spectra where E = hc/λ

From solution to film, a red-shift due to the solid-state packing was indicated by a slight shift (2-18 nm) to lower energy of the onset of absorption. The onset of absorption for all polymers, in the thin film state, was found between 498 and 506 nm giving an optical band gap ($E_{g,opt}$) of 2.49 to 2.45 eV. There was very little variation in the optical bandgap (0.04 eV) after: (a) inclusion of C_8 alkyl sidechains and (b) inclusion of anionic sodium sulfonate containing sidechains.

5.4 Electronic properties

Electronic properties for (a) unsubstituted (F8fBT) and partially substituted (F8BT-SR 0.25, F8BT-SR 0.50 and F8BT-SR 0.75) polymers and (b) anionic polymers (F8BT-SAn 0.25, F8BT-SAn 0.50, F8BT-SAn 0.75 and F8BT-SAn 1.00), were investigated by CV, shown in Figure 5.7. The polymers were drop cast onto a glassy carbon electrode and measured in a solution of tetrabutylammonium hexafluorophosphate in acetonitrile (0.1 M) with an Ag/AgCl reference electrode. The onset of the first oxidation was used to estimate the HOMO energy levels of the polymers, assuming the ferrocene/ferrocenium (Fc/Fc^+) reference energy level is 4.8 eV below the vacuum level.[202,203] Using the estimated HOMO energy level plus the optical bandgap, measured from the onset of absorption in the thin film absorption spectra, the LUMO energy level was estimated. A summary of the oxidation onset, optical bandgap and respective HOMO and LUMO energy levels are detailed in Table 5.4.

Firstly, the effect of decreasing the fluorine content along the polymer backbone was investigated, by evaluating the CV spectra of unsubstituted and partially substituted polymers. For F8fBT, F8BT-SR 0.25, F8BT-SR 0.50 and F8BT-SR 0.75 the onsets of oxidation

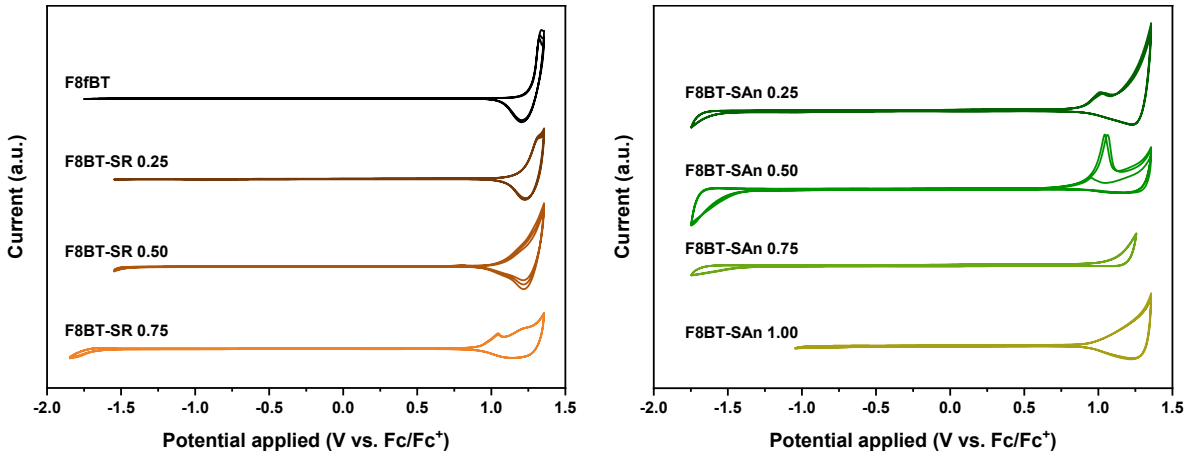


Figure 5.7. CV spectra for unsubstituted and partially substituted polymers (left) and anionic polymers (right) showing oxidation cycles in 0.1M acetonitrile-[n-Bu_4N]PF_6 at 100 mVs^{-1}, potentials were measured against an Ag/AgCl reference electrode.

were found to be 1.28, 1.22, 1.16 and 0.93 V and HOMO energy levels were -6.08, -6.02, -5.96 and -5.73 eV respectively. The data indicates that with decreasing fluorine along the polymer backbone the HOMO energy level decreases. Measured optical energy bandgaps for each polymer were found to be very similar at 2.45 to 2.47 eV, therefore, the same trend was observed from the calculated LUMO energy levels. As the fluorine content was reduced along the polymer backbone, the LUMO energy also decreased for F8fBT, F8BT-SR 0.25, F8BT-SR 0.50 and F8BT-SR 0.75 with values of -3.61, -3.56, -3.51 and -3.26 eV respectively.

The effect of increasing the sodium sulfonate content along the polymer backbone was investigated, by evaluating the spectra of anionic polymers. For F8BT-SAn 0.25, F8BT-SAn 0.50, F8BT-SAn 0.75 and F8BT-SAn 1.00 the onsets of oxidation were found to be 0.89, 0.98, 1.14 and 1.17 V and HOMO energy levels were -5.69, -5.78, -5.94 and -5.97 eV respectively. The recorded HOMO energy levels decrease in energy, slightly, with increasing sodium sulfonate content. Furthermore, the energy bandgap for each material did not differ greatly, within the range of 2.47 to 2.49 eV, hence, the calculated LUMO values also showed a similar trend. Increasing the anionic content along the polymer backbone reduces the LUMO energy level slightly for F8BT-SAn 0.25, F8BT-SAn 0.50, F8BT-SAn 0.75 and F8BT-SAn 1.00 with values of -3.20, -3.31, -3.46 and -3.48 eV. Whilst slight trends were observed from the electrochemical spectra, the estimated HOMO and LUMO energy levels from CV should be considered with discretion as CV measurements can have associated errors of ±0.1 eV. Particularly in cases where thin films of the polymer material were drop-cast, from solutions, directly onto the working electrode.[271]

Table 5.4. Electronic properties for unsubstituted, partially substituted and anionic polymers.

Polymer	Oxidation onset (V)	HOMO[a] (eV)	$E_{g,opt}$[c] (eV)	LUMO[b] (eV)
F8fBT	1.28	-6.08	2.47	-3.61
F8BT-SR 0.25	1.22	-6.02	2.46	-3.56
F8BT-SR 0.50	1.16	-5.96	2.45	-3.51
F8BT-SR 0.75	0.93	-5.73	2.47	-3.26
F8BT-SAn 0.25	0.89	-5.69	2.49	-3.20
F8BT-SAn 0.50	0.98	-5.78	2.47	-3.31
F8BT-SAn 0.75	1.14	-5.94	2.48	-3.46
F8BT-SAn 1.00	1.17	-5.97	2.49	-3.48

[a]Determined by CV referenced to ferrocene at 4.8 eV

[b]LUMO = HOMO + $E_{g,opt}$

[c]Estimated from the onset of absorption from the measured UV-VIS spectra where E = hc/λ

As mentioned in Chapter 3, solid-state CV measurements provide a good insight into the approximate HOMO and LUMO energy levels and observable trends. Other techniques to more accurately determine estimated values, such as photoelectron spectroscopy in air (PESA), should be considered.[205]

5.5 X-ray photoelectron spectroscopy (XPS) analysis

To determine the work function for the anionic polymer CPEs, X-ray photoelectron spectroscopy (XPS) was used. F8BT-SAn 0.25, F8BT-SAn 0.50, F8BT-SAn 0.75 and F8BT-SAn 1.00 were spin-coated onto ITO substrates from chlorobenzene:DMSO solutions (2mg/mL), the films were dried and annealed at 80 °C for 10 minutes. Prepared CPE thin films on ITO substrates were then analysed by XPS to estimate the vacuum level shifts. The modified work function was determined from the energy difference between the secondary electron cut-off (Figure S5.24) and the Fermi energy.[272–274]

All ITO coated substrates with deposited CPE thin films, F8BT-SAn 0.25, F8BT-SAn 0.50, F8BT-SAn 0.75 and F8BT-SAn 1.00, showed average work function values compared to pristine ITO (4.47 eV) of 4.12, 4.41, 4.00 and 4.07 eV respectively, where the plotted data points are shown in Figure 5.8. With increasing anionic content, a further reduction in the work function and corresponding increase in the interfacial dipole would be expected.[275] Anionic CPEs (F8BT-SAn 0.X) showed no distinct trend in the measured work function with increasing anionic groups along the polymer backbone. Anionic CPEs were designed with a non-ionic alkyl chain (C_8) in the place of the fluorine atom, as the fluorine can influence the work function of the

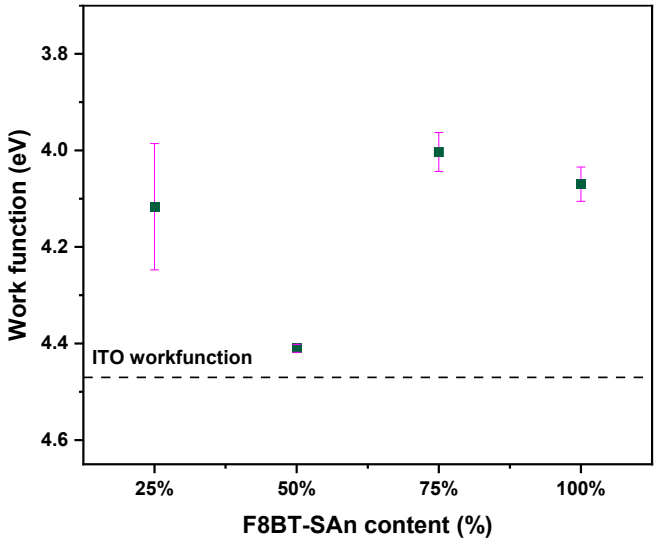


Figure 5.8. Estimated work-function for anionic CPEs as obtained from XPS measurements.

electrode (as well as the anionic groups).[97,269] Whilst the alkyl chain is non-ionic, the octyl chain may still influence the orientation of the anionic groups on the ITO surface, hence, altering the work function. Previous reports in the literature highlight the importance of the orientation or binding of the thin film to the ITO electrode.[275,276] Although these anionic CPEs may not be suitable to fine tune the work function of the ITO electrode, they did show an overall reduction in the work function which could be advantageous to improve charge extraction at the active layer-electrode interface of OLED or OPV devices for example. It should be noted that these values were estimated from XPS measurements where features at low binding energies, at less than 30 eV, can be resolved due to the ejection of valance electrons.[277,278] While the XPS measurements provide a good insight into the modified work function, other techniques to confirm the trends in work function, such as ultraviolet photoelectron spectroscopy (UPS) should be considered.[279] UPS is a high-resolution technique that operates the same as XPS, however, the ultraviolet source has a lower energy and can selectively irradiate the valance electrons with lower binding energies.[278]

5.6 Conclusion

In summary, this chapter highlights the straight-forward and versatile methods towards synthesising polymers with increasing anionic functionality. Multiple substitutions were made onto the polymer backbone, thioalkyl followed by sulfonated thioalkane, via S_NAr in two simple synthetic steps. Once the reactions were optimised, it was possible to synthesise the polymers with varying anionic content in quick succession. Anionic polymer structures were confirmed by NMR, IR and XPS analysis. Polymer products were found to show orthogonal solubility in polar solvents, such as DMF or DMSO, compared to the starting polymer, where orthogonal solubility would facilitate the facile fabrication of multilayer organic devices.

Furthermore, all anionic polymers showed little variation in both solution and thin film absorption spectra, indicating the electronic properties were largely determined by the backbone of the polymer and not the sidechains. Therefore, measured optical bandgap values for anionic polymers were very similar at 2.47 to 2.49 eV. HOMO and LUMO energy levels determined by CV and absorption spectra showed some, but very little variation, with energy levels ranging from -5.69 to -5.97 eV (HOMO) and -3.20 to -3.48 eV (LUMO).

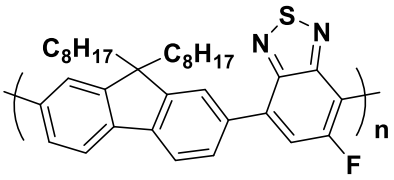
CPEs were shown to modify the work function of the ITO electrode, reducing by up to 0.5 eV for F8BT-SAn 0.75. No definitive trend was observed for the work function of the material with increasing anionic content along the polymer backbone. The lack of trend could be due to interactions from long non-ionic alkyl chains at the ITO-CPE interface, which decrease in content as the anionic groups increase. Whilst these materials were not perfectly designed for fine tuning of the work function, future designs may look at the displacement of F with a shorter non-ionic alkyl chain that is less likely to interfere with the orientation of the anionic group at the ITO-CPE interface.

In this work, the developed synthetic techniques provide a simple route access to a wide range of ionic CPEs, where ionic content can be easily varied by controlling the molar content added. Using the developed synthetic method, future investigations of polymers with increasing ionic density can be easily facilitated.

5.7 Experimental

Synthesis of F8fBT polymer

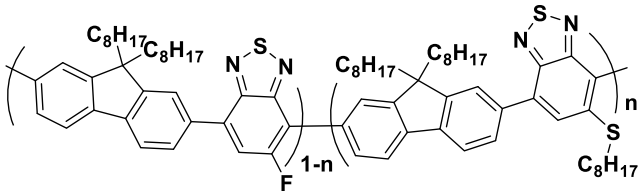
as prepared according to a modified procedure of Adam Creamer et al.[97]



In a dry 100 mL round bottom flask under nitrogen 9,9-dioctylfluorene-2,7-diboronic acid bis(pinacol) ester (2.39 g, 3.72 mmol), 4,7-dibromo-5-fluoro-2,1,3-benzothiadiazole (1.16 g, 3.72 mmol) and tetrakis(-triphenylphosphine) palladium(0) (86 mg, 0.07 mmol) were added and degassed with nitrogen. To the solid mixture degassed toluene (32 mL) with on drop of aliquot 336 and degassed aqueous 2 M Na_2CO_3 (20 mL) were added before the solution was heated to reflux for 72 h. After the reaction was cooled to room temperature and the mixture was precipitated into methanol. The precipitate was filtered into a Soxhlet thimble and washed (Soxhlet) with methanol, acetone and hexane (in that order) and the final product was extracted into chloroform. After extraction, the solvent was removed using a rotary evaporator. The product was dissolved in the minimum amount of chlorobenzene (approx. 5 mL) and precipitated into methanol (approx. 500 mL). The precipitate was collected by vacuum filtration through a nylon pad (pore size 20 µm), washed with methanol and acetone then dried. The dry product was collected in a vial and further dried under vacuum. The product obtained was a yellow solid (1.41-1.99g, 70–99% yield).

^{1}H NMR (400 MHz, $CDCl_3$): δ 8.20-7.80 (m, 7H, H_{ar}), 2.13(m, 4H, CH2), 1.20–1.15 (m, 20H, CH2), 0.96 (s, 4H, CH2), 0.85–0.75 (m, 6H, CH3) ppm. ^{19}F NMR (377 MHz, $CDCl_3$): δ -114.51 ppm. GPC (80 °C, chlorobenzene, vs PS): M_n = 56.9 kDa, M_w = 126 kDa, PDI = 2.2.

Synthesis of F8BT-SR 0.X polymer



F8BT-SR 0.25: n = 0.25
F8BT-SR 0.50: n = 0.50
F8BT-SR 0.75: n = 0.75

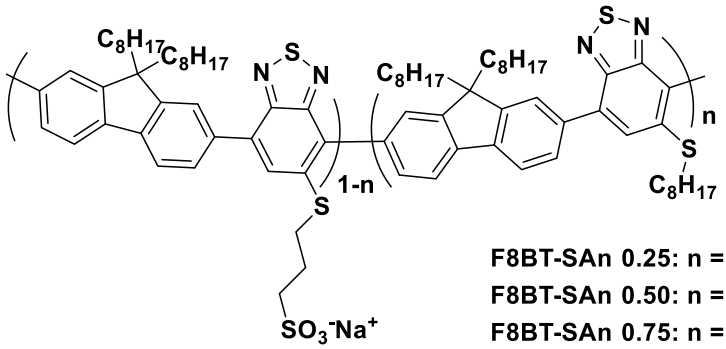
To a 20 mL microwave vial under nitrogen, F8fBT (50 mg, 0.092 mmol) and an excess of K_2CO_3 (500 mg, 3.62 mmol) were added. The vial was sealed with a septum and degassed with nitrogen before anhydrous chlorobenzene (5 mL) and DMF (5 mL) (concentration of 5 mg/mL of polymer) were added. Various molar quantities of 1-octanethiol were added depending on the degree of partial substitution (detailed below) and the solution was degassed with nitrogen for a further 10 minutes. The solution was heated in a microwave reactor at 150 °C for 60 min. After, the reaction was cooled to room temperature and the solution was precipitated into methanol (10:1 v:v of methanol:solvent), stirred for 30 min and filtered through a Soxhlet thimble. Excess base was removed by washing with water (3 x 20 mL) through the thimble. Unreacted thiol was removed by washing (Soxhlet) with methanol and the final product was extracted into chloroform. After extraction, the solvent was removed using a rotary evaporator and precipitated into methanol. The precipitate was collected by vacuum filtration through a nylon pad (pore size 20 µm), washed with methanol and acetone then dried. and further dried under vacuum This synthesis was repeated and the dry product was collected in a vial and further dried under vacuum to give final products detailed below:

F8BT-SR 0.25: 1-octanethiol (4.01 µL, 0.023 mmol): The product was obtained as a yellow fibrous solid (76.7 mg, 77% yield). ^{1}H NMR (400 MHz, $CHCl_3$): δ 8.26-7.52 (m, 7H, H_{ar}), 2.97 (m(br), 0.5H, CH_2), 2.11 (m, 4H, CH_2), 1.32–0.90 (m, 27H, CH_2),0.89–0.72 (m, 6.75H, CH_3) ppm. ^{19}F NMR (377 MHz, $CDCl_3$): δ -114.50 ppm.

F8BT-SR 0.50: 1-octanethiol (8.02 µL, 0.046 mmol): The product was obtained as a yellow fibrous solid (83.8 mg, 84% yield). ^{1}H NMR (400 MHz, $CHCl_3$): δ 8.26-7.52 (m, 7H, H_{ar}), 2.97 (m(br), 0.5H, CH_2), 2.11 (m, 4H, CH_2), 1.32–0.90 (m, 30H, CH_2),0.89–0.72 (m, 7.5H, CH_3) ppm. ^{19}F NMR (377 MHz, $CDCl_3$): δ -114.46 ppm.

F8BT-SR 0.75: 1-octanethiol (12.03 µL, 0.069 mmol): The product was obtained as a yellow fibrous solid (89.8 mg, 90% yield). ^{1}H NMR (400 MHz, $CHCl_3$): δ 8.26-7.52 (m, 7H, H_{ar}), 2.97 (m(br), 0.5H, CH_2), 2.11 (m, 4H, CH_2), 1.32–0.90 (m, 33H, CH_2),0.89–0.72 (m, 8.25H, CH_3) ppm. ^{19}F NMR (377 MHz, $CDCl_3$): δ -114.49 ppm.

Synthesis of F8BT-SAn X.X polymer



F8BT-SAn 0.25: n = 0.75
F8BT-SAn 0.50: n = 0.50
F8BT-SAn 0.75: n = 0.25
F8BT-SAn 1.00: n = 0.00

To a 20 mL microwave vial under nitrogen, starting polymer F8BT-SR 0.X (20 mg, 0.037 mmol) and an excess of Na_2CO_3 (150 mg, 1.42 mmol) were added. The vial was sealed with a septum and degassed with nitrogen before anhydrous N-methyl-2-pyrrolidone (10 mL) (concentration of 2 mg/mL of polymer) was added. An excess of 3-mercapto-1-propanesulfonic acid sodium salt (19.8 mg, 0.11 mmol) was added and the solution was degassed with nitrogen for a further 10 minutes. The solution was heated on the hot plate at 120 °C for 12 hours. After, the reaction was cooled to room temperature and the solution was precipitated into ethyl acetate (10:1 v:v of ethyl acetate:solvent), stirred for 30 min and filtered through a Soxhlet thimble. Excess base was removed by washing with water (3 x 20 mL) through the thimble. Unreacted thiol terminated sidechain was removed by washing (Soxhlet) with ethyl acetate, acetone and chloroform. The final product was removed from the thimble and dried. The dry product was collected in a vial and further dried under vacuum to give final products detailed below:

F8BT-SAn 0.25: Starting polymer F8BT-SR 0.75 (20 mg, 0.037 mmol) was used. The product was obtained as a yellow solid (19.2 mg, 76.8% yield). ^{1}H NMR (500 MHz, 393K, DMSO-d_6): δ 8.34-7.86 (m, 5H, $H_{ar,1}$), 7.78-7.40 (m, 2H, $H_{ar,2}$), 3.24 (m(br), 0.5H, CH_2), 3.06 (m(br), 1.5H, CH_2), 2.61 (m(br), 0.5H, CH_2), 2.16 (m, 4H, CH_2), 2.03 (m(br), 0.5H, CH_2), 1.63 (m(br), 1.5H, CH_2), 1.43 (m(br), 1.5H, CH_2), 1.34–0.92 (m, 33.5H, CH_2), 0.91–0.70 (m, 8.25H, CH_3) ppm. ^{19}F NMR (471 MHz, 393K, DMSO-d_6): No signal observed.

F8BT-SAn 0.50: Starting polymer F8BT-SR 0.50 (20 mg, 0.037 mmol) was used. The product was obtained as a yellow fibrous solid (17.8 mg, 70.5% yield). ^{1}H NMR (500 MHz, 393K, DMSO-d_6): δ 8.40-7.88 (m, 5H, $H_{ar,1}$), 7.72-7.50 (m, 2H, $H_{ar,2}$), 3.25 (m(br), 1H, CH_2), 3.08 (m(br), 1H, CH_2), 2.58 (m(br), 1H, CH_2), 2.16 (m, 4H, CH_2), 2.03 (m(br), 1H, CH_2), 1.66 (m(br), 1H, CH_2), 1.43 (m(br), 1H, CH_2), 1.34–0.88 (m, 31H, CH_2), 0.87–0.70 (m, 7.5H, CH_3) ppm. ^{19}F NMR (471 MHz, 393K, DMSO-d_6): No signal observed.

F8BT-SAn 0.75: Starting polymer F8BT-SR 0.25 (20 mg, 0.037 mmol) was used. The product was obtained as a yellow fibrous solid (17.7 mg, 69.2% yield). ^{1}H NMR (500 MHz, 393K, DMSO-d_6): δ 8.40-7.88 (m, 5H, $H_{ar,1}$), 7.72-7.50 (m, 2H, $H_{ar,2}$), 3.27 (m(br), 1.5H, CH_2), 3.10 (m(br), 0.5H, CH_2), 2.60 (m(br), 1.5H, CH_2), 2.16 (m, 4H, CH_2), 2.04 (m(br), 1.5H, CH_2), 1.68 (m(br), 0.5H, CH_2), 1.43 (m(br), 0.5H, CH_2), 1.34–0.88 (m, 28.5H, CH_2), 0.87–0.70 (m, 6.75H, CH_3) ppm. ^{19}F NMR (471 MHz, 393K, DMSO-d_6): No signal observed.

F8BT-SAn 1.00: Starting polymer F8fBT (20 mg, 0.037 mmol) was used. The product was obtained as a yellow fibrous solid (24.6 mg, 97.8% yield). ^{1}H NMR (500 MHz, 393K, DMSO-d_6): δ 8.34-7.74 (m, 5H, $H_{ar,1}$), 7.71-7.52 (m, 2H, $H_{ar,2}$), 3.27 (m(br), 2H, CH_2), 2.61 (m(br), 2H, CH_2), 2.16 (m, 4H, CH_2), 2.04 (m(br), 2H, CH_2), 1.63 (m(br), 1.75H, CH_2), 1.43 (m(br), 1.75H, CH_2), 1.26–0.88 (m, 24H, CH_2), 0.87–0.70 (m, 6H, CH_3) ppm. ^{19}F NMR (471 MHz, 393K, DMSO-d_6): No signal observed.

5.8 Appendix Chapter 5 - list of figures

All supplementary figures for Chapter 5 are presented in the Appendix (Chapter 8).

Figure S5.1. ^{1}H NMR of F8fBT.

Figure S5.2. ^{1}H NMR of F8BT-SR 0.25.

Figure S5.3. ^{1}H NMR of F8BT-SR 0.5.

Figure S5.4. ^{1}H NMR of F8BT-SR 0.75.

Figure S5.5. ^{19}F NMR of F8fBT.

Figure S5.6. ^{19}F NMR of F8BT-SR 0.25.

Figure S5.7. ^{19}F NMR of F8BT-SR 0.5.

Figure S5.8. ^{19}F NMR of F8BT-SR 0.75.

Figure S5.9. ^{1}H NMR of F8BT-SAn 0.25.

Figure S5.10. ^{1}H NMR of F8BT-SAn 0.50.

Figure S5.11. ^{1}H NMR of F8BT-SAn 0.75.

Figure S5.12. ^{1}H NMR of F8BT-SAn 1.00.

Figure S5.13. ^{19}F NMR of F8BT-SAn 0.25.

Figure S5.14. ^{19}F NMR of F8BT-SAn 0.50.

Figure S5.15. ^{19}F NMR of F8BT-SAn 0.75.

Figure S5.16. ^{19}F NMR of F8BT-SAn 1.00.

Figure S5.17. XPS survey for F8BT-SR 0.25.

Figure S5.18. XPS survey for F8BT-SR 0.50.

Figure S5.19. XPS survey for F8BT-SR 0.75.

Figure S5.20. XPS survey for F8BT-SAn 0.25.

Figure S5.21. XPS survey for F8BT-SAn 0.50.

Figure S5.22. XPS survey for F8BT-SAn 0.75.

Figure S5.23. XPS survey for F8BT-SAn 1.00.

Figure S5.24. Secondary electron cut-off region from XPS measurements of ITO, F8BT-SAn 0.25, F8BT-SAn 0.50, F8BT-SAn 0.75, F8BT-SAn 1.00.

Figure S5.25. Fermi edge region from XPS measurements of gold.

6 General experimental

All chemicals were used as received, purchased from major commercial suppliers: Sigma-Aldrich, Merk, Fluorochem, VWR, Alfa Aesar, Organtecsolar Materials Inc. and Tokyo Chemical Industry Co.. Synthetic reactions were carried out in an inert nitrogen atmosphere using standard Schlenk line techniques, unless otherwise stated. All analysis and characterisation were carried out in air at room temperature unless otherwise stated.

Microwave-assisted reactions were processed in Teflon capped glass vials using the Biotage Initiator+ reactor. All nuclear magnetic resonance (NMR) spectra were recorded on either an AV-400 (400 MHz) or AV-500 (500 MHz) Bruker Spectrometer, chemical shift (δ) is reported in parts per million (ppm). MALDI-TOF spectra was recorded on Micromass MALDI-ToF. Matrix used was terthiophene in THF with a concentration of 10 mg mL^{-1}. Purification of monomers and polymers by preparative GPC were carried out on Shimadzu GPC system running in hexane at 40 °C with an agilent PLgel 10 µm mixed-d column, DGU-20A3 Degasser, LC-20A Pump, CTO-20A Column Oven and SPD-20A UV Detector. Purification of graft co-polymers (Chapter 2) by recycling GPC from Japan Analytical Industry Co, Ltd; in chloroform at room temperature. The high-pressure liquid chromatography apparatus (JAI LaboACE LC 5060 series) was equipped with a pump (P-LA60, flow rate 10 $mlmin^{-1}$), a UV detector (UV-VIS4ch LA, λ = 254, 360, 450 and 540 nm) and two columns (Jaigel 2HR and 2.5HR, 20 mm × 600 mm). Photoelectron spectroscopy in air (PESA) measurements were recorded on a Riken Keiki PESA spectrometer (Model AC-2) using a 10 nW power setting and a power number of 0.3. Fourier transform infrared (FTIR) spectra were recorded on Cary 630 FTIR spectrometer. UV-Vis data was collected from either Agilent Cary 60 UV-Vis spectrometer or Shimadzu UV-1800 UV-Vis spectrometer. Photoluminescence (PL) was collected from an Agilent Cary Eclipse fluorescence spectrometer. Solid state (thin film) cyclic voltammetry (CV) experiments were carried out with Metrohm Autolab PGSTAT101 Electrochemical Analyser where spectra were collected on NOVA software. Number-average (M_n) and weight-average (M_w) molecular weight were determined by analytical GPC on the Agilent Technologies 1200 series GPC equipped with a RI and UV detector. The GPC system, running in chlorobenzene at 80 °C, was set up with two PL mixed-B columns in series and narrow polydispersity polystyrene standards

were used for calibration. Dynamic scanning calorimetry (DSC) was performed on either a Mettler Toledo DSC1 or TA instruments model Q10 DSC at a scan rate of 10 °C/min. Thermogravimetric analysis (TGA) was carried out using a Mettler Toledo TGA/DSC1, heating from 25 to 750 °C at 5 °C/min under N_2. Atomic force microscope (AFM) images were collected from a Picoscan PicoSPM LE scanning probe in tapping mode. Density function theory (DFT) calculations were modeled using Gaussian at the B3LYP/6-31G* level. X-ray photoelectron spectroscopy (XPS) studies were performed on a high-throughput ThermoFisher Scientific K-Alpha+ photoelectron spectrometer using a monochromated Al Kα (1,486.6 eV) X-ray source operating at 2×10^{-9} mbar base pressure. The X-ray source used a 6mA emission current and -30 eV anode bias, giving an X-ray spot size of up to 400 μm^2. A pass energy of 200 eV was used for survey spectra and 20 eV for core levels. Avantage software was used for quantitative analysis and binding energy values were corrected by setting the C 1s peak to 284.5 eV.

Chapter 2 materials: 9,9-Dioctyl-2,7-dibromofluorene (Sigma Aldrich, 96%), 4,7-dibromo-5-fluoro-2,1,3-benzothiadiazole (Sigma Aldrich, 96%), 2,5-dibromo-3-hexylthiophene (Sigma Aldrich, 97%), 4-hydroxyphenylboronic acid pinacol ester (Fluorochem, 97%), 4-Mercaptophenylboronic acid (Sigma Aldrich, 90%), tetrakis(triphenylphosphine)palladium(0) (Sigma Aldrich, 99%), [1,3-bis(diphenylphosphino) propane]dichloronickel(II) (Sigma Aldrich, 95%), Butylmagnesium chloride solution in diethyl ether (Sigma Aldrich, 2.0M), thiophenol (Sigma Aldrich, 97%), phenol (Sigma Aldrich, 99%)

Chapter 3 materials: RuPhos Pd G3 (Sigma Aldrich, 98%), RuPhos (Sigma Aldrich, 98%), 5-Bromo-1,2,3-trifluorobenzene (Sigma Aldrich, 99%), 9,9-Dioctyl-2,7-dibromofluorene (Sigma Aldrich, 96%), 4,7-dibromo-5-fluoro-2,1,3-benzothiadiazole (Sigma Aldrich, 96%), tetrakis(triphenylphosphine)palladium(0) (Sigma Aldrich, 99%).

Chapter 4 materials: 2-decyl-1-tetradecanol (Sigma Aldrich, 97%), 2,6-dibromonaphthalene-1,4,5,8-tetracarboxydianhydride (NDA-Br_2) (Tokyo Chemical Industry Co., 98%), Triphenylphosphine (Sigma Aldrich 99%), Imidazole (Sigma Aldrich, 99%), Phthalimide (Sigma Aldrich, 99%), trans-1,2-bis(tributylstannyl)ethene (Sigma Aldrich, 97%), tris(dibenzylideneacetone)dipalladium(0) (Sigma Aldrich, 97%), Tri(o-tolyl)phosphine (Sigma Aldrich, 97%), 5-Fluoro-4,7-bis(5-(trimethylstannyl)thiophen-2-yl)benzo[c][1,2,5]thiadiazole (Organtecsolar Materials Inc.), 4,7-dibromo-5-fluoro-2,1,3-benzothiadiazole (Organtecsolar

Materials Inc.), 1-ocatanethiol (Sigma Aldrich, 98.5%), S-(3-Azidopropyl)thioacetate (Sigma Aldrich, 95%)

Chapter 5 materials: 9,9-Dioctyl-2,7-dibromofluorene (Sigma Aldrich, 96%), 4,7-dibromo-5-fluoro-2,1,3-benzothiadiazole (Sigma Aldrich, 96%), tetrakis(triphenylphosphine)palladium(0) (Sigma Aldrich, 99%), Aliquat® 336 (Sigma Aldrich), 1-octanethiol (Sigma Aldrich, 98.5%), 3-mercapto-1-propanesulfonic acid sodium salt (Sigma Aldrich, 90%).

7 References

1 The Nobel Prize in Chemistry 2000, https://www.nobelprize.org/prizes/chemistry/2000/summary/, (accessed 23 November 2021).

2 C. K. Chiang, C. R. Fincher, Y. W. Park, A. J. Heeger, H. Shirakawa, E. J. Louis, S. C. Gau and A. G. MacDiarmid, *Phys. Rev. Lett.*, 1977, **39**, 1098–1101.

3 D. Khokhar, S. Jadoun, R. Arif and S. Jabin, *Polym. Technol. Mater.*, 2021, **60**, 463–485.

4 R. M. Pankow and B. C. Thompson, *Polymer (Guildf).*, 2020, **207**, 122874.

5 D. Han, J. Li, Q. Zhang, Z. He, Z. Wu, J. Chu and Y. Lu, *Polymers (Basel).*, 2021, **13**, 254.

6 Y. Wu, J. Guo, W. Wang, Z. Chen, Z. Chen, R. Sun, Q. Wu, T. Wang, X. Hao, H. Zhu and J. Min, *Joule*, 2021, **5**, 1800–1815.

7 G. L. Ong, Q. Zhang, T. S. Ong, R. Kek, C. H. Nee, T. Y. Tou, D. J. Liaw, S. L. Yap and S. S. Yap, *Synth. Met.*, 2021, **272**, 116658.

8 Y. Liu, Y. Wang, C. Li, Z. Ren, D. Ma and S. Yan, *Macromolecules*, 2018, **51**, 4615–4623.

9 M. Saito, H. Ohkita and I. Osaka, *J. Mater. Chem. A*, 2020, **8**, 20213–20237.

10 S. H. Park, N. Y. Kwon, H. J. Kim, E. Cho, H. Kang, A. K. Harit, H. Y. Woo, H. J. Yoon, M. J. Cho and D. H. Choi, *ACS Appl. Mater. Interfaces*, 2021, **13**, 13487–13498.

11 T. Jia, J. Zhang, W. Zhong, Y. Liang, K. Zhang, S. Dong, L. Ying, F. Liu, X. Wang, F. Huang and Y. Cao, *Nano Energy*, 2020, **72**, 104718.

12 W. Yang, M. Sun, Y. Wang, H. Yan, G. Zhang and Q. Zhang, *Polym. Chem.*, 2021, **12**, 2317–2324.

13 Y. Pan, J. Huang, D. Gao, Z. Chen, W. Zhang and G. Yu, *Polym. Chem.*, 2021, **12**, 2471–2480.

14 K. Feng, H. Guo, J. Wang, Y. Shi, Z. Wu, M. Su, X. Zhang, J. H. Son, H. Y. Woo and X. Guo, *J. Am. Chem. Soc.*, 2021, **143**, 1539–1552.

15 M. Comí, M. U. Ocheje, S. Attar, A. U. Mu, B. K. Philips, A. J. Kalin, K. E. Kakosimos, L. Fang, S. Rondeau-Gagné and M. Al-Hashimi, *Macromolecules*, 2020, **54**, 665–672.

16 J. Liu, J. Wang, Z. Zhang, F. Molina-Lopez, G. J. N. Wang, B. C. Schroeder, X. Yan, Y. Zeng, O. Zhao, H. Tran, T. Lei, Y. Lu, Y. X. Wang, J. B. H. Tok, R. Dauskardt, J. W. Chung, Y. Yun and Z. Bao, *Nat. Commun.*, 2020, **11**, 3362.

17 B. Ding, G. Kim, Y. Kim, F. D. Eisner, E. Gutiérrez-Fernández, J. Martín, M.-H. Yoon and M. Heeney, *Angew. Chemie Int. Ed.*, 2021, **60**, 19679–19684.

18 A. Jebnouni, N. Leclerc, S. Teka, D. Mansour and N. S. Jaballah, *J. Mol. Struct.*, 2021, **1244**, 130994.

19 Y. Kang, D. H. Kwak, J. E. Kwon, B.-G. Kim and W. H. Lee, *ACS Appl. Mater. Interfaces*, 2021, **13**, 31910–31918.

20 L. Cui, J. Zhou, C. Li, S. Deng, W. Gao, X. Zhang, X. Luo, X. Wang and C. Zhang, *ACS Appl. Mater. Interfaces*, 2021, **13**, 28782–28789.

21 M. M. Samy, M. G. Mohamed, A. F. M. El-Mahdy, T. H. Mansoure, K. C. W. Wu and S. W. Kuo, *ACS Appl. Mater. Interfaces*, 2021, **13**, 51906–51916.

22 M. B. Miltenburg, S. Y. An, N. K. Obhi, E. Grignon, B. T. McAllister and D. S. Seferos, *ACS Appl. Polym. Mater.*, 2020, **2**, 5574–5580.

23 X. Guo, Q. Yuan, C. Li, H. Du, J. Zhao, L. Liu, Y. Li, Y. Xie and V. Vaidya, *RSC Adv.*, 2021, **11**, 15044–15053.

24 K. Amin, N. Ashraf, L. Mao, C. F. J. Faul and Z. Wei, *Nano Energy*, 2021, **85**, 105958.

25 B. T. McAllister, E. Grignon, T. B. Schon, S. Y. An, C.-H. Yim, Y. Abu-Lebdeh and D. S. Seferos, *ACS Appl. Energy Mater.*, 2021, **4**, 6659–6666.

26 M. Xiong, X. Yan, J. T. Li, S. Zhang, Z. Cao, N. Prine, Y. Lu, J. Y. Wang, X. Gu and T. Lei, *Angew. Chemie Int. Ed.*, 2021, **60**, 8189–8197.

27 X. Guo, M. Baumgarten and K. Müllen, *Prog. Polym. Sci.*, 2013, **38**, 1832–1908.

28 D. Corzo, K. Almasabi, E. Bihar, S. Macphee, D. Rosas-Villalva, N. Gasparini, S. Inal and D. Baran, *Adv. Mater. Technol.*, 2019, **4**, 1900040.

29 X. Gu, Y. Zhou, K. Gu, T. Kurosawa, Y. Guo, Y. Li, H. Lin, B. C. Schroeder, H. Yan, F. Molina-Lopez, C. J. Tassone, C. Wang, S. C. B. Mannsfeld, H. Yan, D. Zhao, M. F. Toney and Z. Bao, *Adv. Energy Mater.*, 2017, **7**, 1602742.

30 J. Yang, Y. Lin, W. Zheng, A. Liu, W. Cai, X. Yu, F. Zhang, Q. Liang, H. Wu, D. Qin and L. Hou, *ACS Appl. Mater. Interfaces*, 2018, **10**, 22485–22494.

31 R. Søndergaard, M. Hösel, D. Angmo, T. T. Larsen-Olsen and F. C. Krebs, *Mater. Today*, 2012, **15**, 36–49.

32 F. C. Krebs, T. Tromholt and M. Jørgensen, *Nanoscale*, 2010, **2**, 873–886.

33 H. Meier, U. Stalmach and H. Kolshorn, *Acta Polym.*, 1997, **48**, 379–384.

34 M. J. Mirshojaeian Hosseini and R. A. Nawrocki, *Micromachines*, 2021, **12**, 655.

35 S. R. Thomas, P. Pattanasattayavong and T. D. Anthopoulos, *Chem. Soc. Rev.*, 2013, **42**, 6910–6923.

36 M. T. Greiner and Z. H. Lu, *NPG Asia Mater. 2013 57*, 2013, **5**, 55.

37 A. Tsumura, H. Koezuka and T. Ando, *Appl. Phys. Lett.*, 1986, **49**, 1210–1212.

38 A. Assadi, C. Svensson and M. Willander, *Appl. Phys. Lett*, 1988, **53**, 195–197.

39 S. Nagamatsu, M. Ishida, S. Miyajima and S. S. Pandey, *Materials (Basel).*, 2019, **12**, 3643.

40 L. Janasz, D. Chlebosz, M. Gradzka, W. Zajaczkowski, T. Marszalek, K. Müllen, J.

Ulanski, A. Kiersnowski and W. Pisula, *J. Mater. Chem. C*, 2016, **4**, 11488–11498.

41 H. Lee, B. Moon, S. Y. Son, T. Park, B. Kang and K. Cho, *ACS Appl. Mater. Interfaces*, 2021, **13**, 16722–16731.

42 R. D. McCullough, R. D. Lowe, M. Jayaraman and D. L. Anderson, *J. Org. Chem.*, 1993, **58**, 904–912.

43 H. Sirringhaus, P. J. Brown, R. H. Friend, M. M. Nielsen, K. Bechgaard, B. M. W. Langeveld-Voss, A. J. H. Spiering, R. A. J. Janssen, E. W. Meijer, P. Herwig and D. M. De Leeuw, *Nature*, 1999, **401**, 685–688.

44 R. J. Kline, M. D. McGehee, E. N. Kadnikova, J. Liu, J. M. J. Fréchet and M. F. Toney, *Macromolecules*, 2005, **38**, 3312–3319.

45 C. Luo, A. K. K. Kyaw, L. A. Perez, S. Patel, M. Wang, B. Grimm, G. C. Bazan, E. J. Kramer and A. J. Heeger, *Nano Lett.*, 2014, **14**, 2764–2771.

46 Z. Wang, X. Song, Y. Jiang, J. Zhang, X. Yu, Y. Deng, Y. Han, W. Hu and Y. Geng, *Adv. Sci.*, 2019, **6**, 1902412.

47 A. F. Paterson, S. Singh, K. J. Fallon, T. Hodsden, Y. Han, B. C. Schroeder, H. Bronstein, M. Heeney, I. McCulloch and T. D. Anthopoulos, *Adv. Mater.*, 2018, **30**, 1801079.

48 H. Sun, X. Guo and A. Facchetti, *Chem*, 2020, **6**, 1310–1326.

49 D. M. De Leeuw, M. M. J. Simenon, A. R. Brown and R. E. F. Einerhand, *Synth. Met.*, 1997, **87**, 53–59.

50 T. D. Anthopoulos, F. B. Kooistra, H. J. Wondergem, D. Kronholm, J. C. Hummelen and D. M. De Leeuw, *Adv. Mater.*, 2006, **18**, 1679–1684.

51 W. Xu, Z. Hu, H. Liu, L. Lan, J. Peng, J. Wang and Y. Cao, *Sci. Rep.*, 2016, **6**, 29055.

52 X. Guo, Y. Xu, S. Ogier, T. N. Ng, M. Caironi, A. Perinot, L. Li, J. Zhao, W. Tang, R. A. Sporea, A. Nejim, J. Carrabina, P. Cain and F. Yan, *IEEE Trans. Electron Devices*, 2017, **64**, 1906–1921.

53 L. Hong, H. Yao, Y. Cui, Z. Ge and J. Hou, *APL Mater.*, 2020, **8**, 120901.

54 F. T. A. Wibowo, N. V. Krishna, S. Sinaga, S. Lee, W. T. Hadmojo, Y. R. Do and S.-Y. Jang, *Cell Reports Phys. Sci.*, 2021, **2**, 100517.

55 Q. Liu, Y. Jiang, K. Jin, J. Qin, J. Xu, W. Li, J. Xiong, J. Liu, Z. Xiao, K. Sun, S. Yang, X. Zhang and L. Ding, *Sci. Bull.*, 2020, **65**, 272–275.

56 T. Jia, J. Zhang, K. Zhang, H. Tang, S. Dong, C. H. Tan, X. Wang and F. Huang, *J. Mater. Chem. A*, 2021, **9**, 8975–8983.

57 J. Zhang, T. Jia, C. H. Tan, K. Zhang, M. Ren, S. Dong, Q. Xu, F. Huang and Y. Cao, *Sol. RRL*, 2021, **5**, 2100076.

58 H. Fu, Y. Li, J. Yu, Z. Wu, Q. Fan, F. Lin, H. Y. Woo, F. Gao, Z. Zhu and A. K. Y. Jen, *J. Am. Chem. Soc.*, 2021, **143**, 2665–2670.

59 Y. Lin, Y. Jin, S. Dong, W. Zheng, J. Yang, A. Liu, F. Liu, Y. Jiang, T. P. Russell, F. Zhang, F.

Huang and L. Hou, *Adv. Energy Mater.*, 2018, **8**, 1701942.

60 L. Zhang, F. Yang, X. Meng, S. Yang, L. Ke, C. Zhou, H. Yan, X. Hu, S. Zhang, W. Ma and Y. Yuan, *Org. Electron.*, 2021, **89**, 106027.

61 B. Ray, M. R. Khan, C. Black and M. A. Alam, *IEEE J. Photovoltaics*, 2013, **3**, 318–329.

62 C. Wang, X. Xu, W. Zhang, J. Bergqvist, Y. Xia, X. Meng, K. Bini, W. Ma, A. Yartsev, K. Vandewal, M. R. Andersson, O. Inganäs, M. Fahlman and E. Wang, *Adv. Energy Mater.*, 2016, **6**, 1600148.

63 K. Feng, J. Yuan, Z. Bi, W. Ma, X. Xu, G. Zhang and Q. Peng, *iScience*, 2019, **12**, 1–12.

64 V. Causin, C. Marega, A. Marigo, L. Valentini and J. M. Kenny, *Macromolecules*, 2005, **38**, 409–415.

65 S. Savagatrup, A. S. Makaram, D. J. Burke and D. J. Lipomi, *Adv. Funct. Mater.*, 2014, **24**, 1169–1181.

66 T. Muntasir and S. Chaudhary, *J. Appl. Phys.*, 2015, **118**, 205504.

67 A. Facchetti, *Mater. Today*, 2013, **16**, 123–132.

68 R. S. Kularatne, H. D. Magurudeniya, P. Sista, M. C. Biewer and M. C. Stefan, *J. Polym. Sci. Part A Polym. Chem.*, 2013, **51**, 743–768.

69 P. Cheng and Y. Yang, *Acc. Chem. Res.*, 2020, **53**, 1218–1228.

70 Z. Fei, Y. Han, J. Martin, F. H. Scholes, M. Al-Hashimi, S. Y. Alqaradawi, N. Stingelin, T. D. Anthopoulos and M. Heeney, *Macromolecules*, 2016, **49**, 6384–6393.

71 T. L. Choi, K. M. Han, J. Il Park, D. H. Kim, J. M. Park and S. Lee, *Macromolecules*, 2010, **43**, 6045–6049.

72 J. M. Park, S. K. Park, W. S. Yoon, J. H. Kim, D. W. Kim, T. L. Choi and S. Y. Park, *Macromolecules*, 2016, **49**, 2985–2992.

73 A. K. Leone, E. A. Mueller and A. J. McNeil, *J. Am. Chem. Soc.*, 2018, **140**, 15126–15139.

74 Q. Fan, Q. An, Y. Lin, Y. Xia, Q. Li, M. Zhang, W. Su, W. Peng, C. Zhang, F. Liu, L. Hou, W. Zhu, D. Yu, M. Xiao, E. Moons, F. Zhang, T. D. Anthopoulos, O. Inganäs and E. Wang, *Energy Environ. Sci.*, 2020, **13**, 5017–5027.

75 A. K. Leone, P. K. Goldberg and A. J. McNeil, *J. Am. Chem. Soc.*, 2018, **140**, 7846–7850.

76 K. Mikami, M. Nojima, Y. Masumoto, Y. Mizukoshi, R. Takita, T. Yokozawa and M. Uchiyama, *Polym. Chem.*, 2017, **8**, 1708–1713.

77 R. D. McCullough and R. D. Lowe, *J. Chem. Soc. Chem. Commun.*, 1992, **1**, 70–72.

78 A. Yokoyama, R. Miyakoshi and T. Yokozawa, *Macromolecules*, 2004, **37**, 1169–1171.

79 E. E. Sheina, J. Liu, M. C. Lovu, D. W. Laird and R. D. McCullough, *Macromolecules*, 2004, **37**, 3526–3528.

80 K.-B. Seo, I.-H. Lee, J. Lee, I. Choi and T.-L. Choi, *J. Am. Chem. Soc.*, 2018, **140**, 4335–

4343.

81 A. K. Leone and A. J. McNeil, *Acc. Chem. Res.*, 2016, **49**, 2822–2831.

82 J. Lee, H. Kim, H. Park, T. Kim, S. H. Hwang, D. Seo, T. D. Chung and T. L. Choi, *J. Am. Chem. Soc.*, 2021, **143**, 11180–11190.

83 J. U. Izunobi and C. L. Higginbotham, *J. Chem. Educ.*, 2011, **88**, 1098–1104.

84 S. Qu, C. Ming, Q. Yao, W. Lu, K. Zeng, W. Shi, X. Shi, C. Uher and L. Chen, *Polymers (Basel).*, 2018, **10**, 815.

85 K. Gu, J. Onorato, S. S. Xiao, C. K. Luscombe and Y. L. Loo, *Chem. Mater.*, 2018, **30**, 570–576.

86 M. A. Gauthier, M. I. Gibson and H. A. Klok, *Angew. Chemie Int. Ed.*, 2009, **48**, 48–58.

87 H. Staudinger and J. Fritschi, *Helv. Chim. Acta*, 1922, **5**, 785–806.

88 H. Staudinger, E. Geiger and E. Huber, *Berichte der Dtsch. Chem. Gesellschaft*, 1929, **62**, 263–267.

89 H. Staudinger, *Rubber Chem. Technol.*, 1939, **12**, 117–118.

90 K. A. Günay, P. Theato and H. A. Klok, *J. Polym. Sci. Part A Polym. Chem.*, 2013, **51**, 1–28.

91 E. M. Muzammil, A. Khan and M. C. Stuparu, *RSC Adv.*, 2017, **7**, 55874–55884.

92 I. Van Severen, F. Motmans, L. Lutsen, T. J. Cleij and D. Vanderzande, *Polymer (Guildf).*, 2005, **46**, 5466–5475.

93 M. Lanzi, P. Costa-Bizzarri, L. Paganin and G. Cesari, *React. Funct. Polym.*, 2007, **67**, 329–340.

94 H. B. Bu, G. Götz, E. Reinold, A. Vogt, S. Schmid, R. Blanco, J. L. Segura and P. Bäuerle, *Chem. Commun.*, 2008, **11**, 1320–1322.

95 T. L. Benanti, A. Kalaydjian and D. Venkataraman, *Macromolecules*, 2008, **41**, 8312–8315.

96 J. Duchateau, L. Lutsen, W. Guedens, T. J. Cleij and D. Vanderzande, *Polym. Chem.*, 2010, **1**, 1313–1322.

97 A. Creamer, C. S. Wood, P. D. Howes, A. Casey, S. Cong, A. V. Marsh, R. Godin, J. Panidi, T. D. Anthopoulos, C. H. Burgess, T. Wu, Z. Fei, I. Hamilton, M. A. McLachlan, M. M. Stevens and M. Heeney, *Nat. Commun.*, 2018, **9**, 3237.

98 N. K. Devaraj and M. G. Finn, *Chem. Rev.*, 2021, **121**, 6697–6698.

99 N. Z. Fantoni, A. H. El-Sagheer and T. Brown, *Chem. Rev.*, 2021, **121**, 7122–7154.

100 M. Urien, H. Erothu, E. Cloutet, R. C. Hiorns, L. Vignau and H. Cramail, *Macromolecules*, 2008, **41**, 7033–7040.

101 S. Vertommen, O. Deschaume, C. Bartic, J. De Winter, P. Gerbaux, T. Verbiest and G. Koeckelberghs, *Polymer (Guildf).*, 2021, **222**, 123630.

102 A. Bolognesi, F. Galeotti, W. Mróz, V. Gancheva and L. Terlemezyan, *Macromol. Chem. Phys.*, 2010, **211**, 1488–1495.

103 V. Kardelis, K. Li, I. Nierengarten, M. Holler, J. F. Nierengarten and A. Adronov, *Macromolecules*, 2017, **50**, 9144–9150.

104 S. Cong, A. Creamer, Z. Fei, S. A. J. Hillman, C. Rapley, J. Nelson and M. Heeney, *Macromol. Biosci.*, 2020, **20**, 2000087.

105 N. Shida, K. Ninomiya, N. Takigawa, K. Imato, Y. Ooyama, I. Tomita and S. Inagi, *Macromolecules*, 2021, **54**, 725–735.

106 R. C. Chadwick, V. Kardelis, S. Liogier and A. Adronov, *Macromolecules*, 2013, **46**, 9593–9598.

107 V. Kardelis, R. C. Chadwick and A. Adronov, *Angew. Chemie*, 2016, **128**, 957–961.

108 T. Michinobu, *Chem. Soc. Rev.*, 2011, **40**, 2306–2316.

109 D. Burmeister, L. Ahrens, A. Opitz, G. Ligorio, F. Hermerschmidt, D. Jänsch, J. Freudenberg, U. H. F. Bunz, K. Müllen and E. J. W. List-Kratochvil, *J. Mater. Chem. C*, 2020, **8**, 3302–3307.

110 V. Kardelis, M. M. Denk and A. Adronov, *Angew. Chemie Int. Ed.*, 2021, **60**, 2980–2986.

111 P. Xu, X. Han, B. Zhang, Y. Du and H. L. Wang, *Chem. Soc. Rev.*, 2014, **43**, 1349–1360.

112 S. Wei, J. Xia, E. J. Dell, Y. Jiang, R. Song, H. Lee, P. Rodenbough, A. L. Briseno and L. M. Campos, *Angew. Chemie Int. Ed.*, 2014, **53**, 1832–1836.

113 E. Reichsöllner, A. Creamer, S. Cong, A. Casey, S. Eder, M. Heeney and F. Glöcklhofer, *Front. Chem.*, 2019, **7**, 123.

114 M. Rimmele, K. Ableidinger, A. V. Marsh, N. J. Cheetham, M. J. Taublaender, A. Buchner, J. Prinz, J. Fröhlich, M. M. Unterlass, M. Heeney and F. Glöcklhofer, *Polym. Chem.*, 2019, **10**, 738–750.

115 H. Bildirir, I. Osken, T. Ozturk and A. Thomas, *Chem. Eur. J.*, 2015, **21**, 9306–9311.

116 C. Dong, B. Meng, J. Liu and L. Wang, *ACS Appl. Mater. Interfaces*, 2020, **12**, 10428–10433.

117 Y. Wang, S. Zhang, L. Wang, W. Zhang, N. Zhou, Z. Zhang and X. Zhu, *Polym. Chem.*, 2015, **6**, 4669–4677.

118 S. Hayashi, Y. Togawa, Y. Kojima and T. Koizumi, *Polym. Chem.*, 2016, **7**, 5671–5686.

119 P. Alagi, G. Zapsas, N. Hadjichristidis, S. C. Hong, Y. Gnanou and X. Feng, *Macromolecules*, 2021, **54**, 6144–6152.

120 P. Boufflet, A. Casey, Y. Xia, P. N. Stavrinou and M. Heeney, *Chem. Sci.*, 2017, **8**, 2215–2225.

121 H. S. Lee, A. Roy, O. Lane, S. Dunn and J. E. McGrath, *Polymer (Guildf).*, 2008, **49**, 715–723.

172

122 Z. Shao, H. Nederstedt and P. Jannasch, *ACS Appl. Energy Mater.*, 2021, **4**, 2570–2577.

123 T. Kubo, C. A. Figg, J. L. Swartz, W. L. A. Brooks and B. S. Sumerlin, *Macromolecules*, 2016, **49**, 2077–2084.

124 J. H. Seo, A. Gutacker, B. Walker, S. Cho, A. Garcia, R. Yang, T. Q. Nguyen, A. J. Heeger and G. C. Bazan, *J. Am. Chem. Soc.*, 2009, **131**, 18220–18221.

125 W. Lee, J. H. Seo and H. Y. Woo, *Polymer (Guildf).*, 2013, **54**, 5104–5121.

126 M. Y. Wong, *J. Electron. Mater.*, 2017, **46**, 6246–6281.

127 L. A. Lozano-Hernández, J. L. Maldonado, O. Hernández-Cruz, J. Nicasio-Collazo, M. Rodríguez, O. Barbosa-García, G. Ramos-Ortíz, M. G. Zolotukhin and U. Scherf, *Dye. Pigment.*, 2020, **173**, 107989.

128 Q. Wei, Z. Ge and B. Voit, *Macromol. Rapid Commun.*, 2019, **40**, 1800570.

129 Y. Sui, Y. Deng, T. Du, Y. Shi and Y. Geng, *Mater. Chem. Front.*, 2019, **3**, 1932–1951.

130 L. An, Y. Huang, X. Wang, Z. Liang, J. Li and J. Tong, *Polymers (Basel).*, 2020, **12**, 504.

131 S. Holliday, Y. Li and C. K. Luscombe, *Prog. Polym. Sci.*, 2017, **70**, 34–51.

132 A. Leventis, T. N. Chmovzh, E. A. Knyazeva, Y. Han, M. Heeney, O. A. Rakitin and H. Bronstein, *Polym. Chem.*, 2020, **11**, 581–585.

133 N. S. Sariciftci, L. Smilowitz, A. J. Heeger and F. Wudl, *Science*, 1992, **258**, 1474–6.

134 H. Spanggaard and F. C. Krebs, *Sol. Energy Mater. Sol. Cells*, 2004, **83**, 125–146.

135 R. P. Xu, Y. Q. Li and J. X. Tang, *J. Mater. Chem. C*, 2016, **4**, 9116–9142.

136 S. R. Forrest, *Nature*, 2004, **428**, 911–918.

137 G. Li, W. H. Chang and Y. Yang, *Nat. Rev. Mater.*, 2017, **2**, 17043.

138 M. Wang, P. Baek, A. Akbarinejad, D. Barker and J. Travas-Sejdic, *J. Mater. Chem. C*, 2019, **7**, 5534–5552.

139 X. Liu, X. Li, N. Zheng, C. Gu, L. Wang, J. Fang and C. Yang, *ACS Appl. Mater. Interfaces*, 2019, **11**, 43433–43440.

140 Y. Huang, E. J. Kramer, A. J. Heeger and G. C. Bazan, *Chem. Rev.*, 2014, **114**, 7006–7043.

141 S. Rafique, S. M. Abdullah, K. Sulaiman and M. Iwamoto, *Renew. Sustain. Energy Rev.*, 2018, **84**, 43–53.

142 S. Nepurek and J. Sworakowski, *J. Appl. Phys.*, 1980, **51**, 2098–2102.

143 N. Wang, X. Long, Z. Ding, J. Feng, B. Lin, W. Ma, C. Dou, J. Liu and L. Wang, *Macromolecules*, 2019, **52**, 2402–2410.

144 C. Zhang and S. Holdcroft, *J. Mater. Res.*, 2018, **33**, 1879–1890.

145 T. Kim, J. Choi, H. J. Kim, W. Lee and B. J. Kim, *Macromolecules*, 2017, **50**, 6861–6871.

146 Z. Hu, B. Shao, G. T. Geberth and D. A. Vanden Bout, *Chem. Sci.*, 2018, **9**, 1101–1111.

147 S. Wang, X. Jin, B. Yao, X. Du, L. Dong, X. Wang and W. Huang, *Synth. Met.*, 2019, **253**, 20–25.

148 M. P. Aplan, C. Grieco, Y. Lee, J. M. Munro, W. Lee, J. L. Gray, Z. D. Seibers, B. Kuei, J. H. Litofsky, S. M. Kilbey, Q. Wang, I. Dabo, J. B. Asbury and E. D. Gomez, *Adv. Funct. Mater.*, 2019, **29**, 1804858.

149 R. Sarvari, S. Agbolaghi, B. Massoumi and N. Sorkhishams, *Polym. Int.*, 2020, **69**, 397–403.

150 S. H. Kim, H. S. Lee, M. S. Lee and W. H. Jo, *Macromol. Chem. Phys.*, 2002, **203**, 2188–2195.

151 G. M. Fanta, P. Jarka, U. Szeluga, T. Tański and J. Y. Kim, *Polymers (Basel).*, 2020, **12**, 1726.

152 I. Botiz and S. B. Darling, *Mater. Today*, 2010, **13**, 42–51.

153 C. Guo, Y. H. Lin, M. D. Witman, K. A. Smith, C. Wang, A. Hexemer, J. Strzalka, E. D. Gomez and R. Verduzco, *Nano Lett.*, 2013, **13**, 2957–2963.

154 T. Jarosz, K. Gebka and A. Stolarczyk, *Molecules*, 2019, **24**, 3019.

155 C. D. Heinrich and M. Thelakkat, *J. Mater. Chem. C*, 2016, **4**, 5370–5378.

156 J. Wang, C. Lu, T. Mizobe, M. Ueda, W. C. Chen and T. Higashihara, *Macromolecules*, 2013, **46**, 1783–1793.

157 J. Wang, C. Lu, T. Higashihara and W. C. Chen, *Microsyst. Technol.*, 2017, **23**, 1183–1189.

158 M. Jeffries-El, G. Sauvé and R. D. McCullough, *Macromolecules*, 2005, **38**, 10346–10352.

159 F. Monnaie, W. Brullot, T. Verbiest, J. De Winter, P. Gerbaux, A. Smeets and G. Koeckelberghs, *Macromolecules*, 2013, **46**, 8500–8508.

160 R. Miyakoshi, A. Yokoyama and T. Yokozawa, *J. Am. Chem. Soc.*, 2005, **127**, 17542–17547.

161 R. H. Lohwasser and M. Thelakkat, *Macromolecules*, 2011, **44**, 3388–3397.

162 A. Krasovskiy and P. Knochel, *Synthesis (Stuttg).*, 2006, **5**, 890–891.

163 C. M. Chen, T. H. Jen and S. A. Chen, *ACS Appl. Mater. Interfaces*, 2015, **7**, 20548–20555.

164 T. Itoh and T. Mase, *J. Org. Chem.*, 2006, **71**, 2203–2206.

165 N. V. Tsarevsky, S. A. Bencherif and K. Matyjaszewski, *Macromolecules*, 2007, **40**, 4439–4445.

166 Q. Fu, W. Lin and J. Huang, *Macromolecules*, 2008, **41**, 2381–2387.

167 F. Sun, G. Lu, C. Feng, Y. Li and X. Huang, *Polym. Chem.*, 2017, **8**, 431–440.

168 Y. Zhu, R. D. Champion and S. A. Jenekhe, *Macromolecules*, 2006, **39**, 8712–8719.

169 J. Clark, J. F. Chang, F. C. Spano, R. H. Friend and C. Silva, *Appl. Phys. Lett.*, 2009, **94**, 163306.

170 M. Chang, D. Choi, G. Wang, N. Kleinhenz, N. Persson, B. Park and E. Reichmanis, *ACS Appl. Mater. Interfaces*, 2015, **7**, 14095–14103.

171 R. Xie, Y. Lee, M. P. Aplan, N. J. Caggiano, C. Müller, R. H. Colby and E. D. Gomez, *Macromolecules*, 2017, **50**, 5146–5154.

172 F. P. V. Koch, J. Rivnay, S. Foster, C. Müller, J. M. Downing, E. Buchaca-Domingo, P. Westacott, L. Yu, M. Yuan, M. Baklar, Z. Fei, C. Luscombe, M. A. McLachlan, M. Heeney, G. Rumbles, C. Silva, A. Salleo, J. Nelson, P. Smith and N. Stingelin, *Prog. Polym. Sci.*, 2013, **38**, 1978–1989.

173 W. Zhong, J. Liang, S. Hu, X. F. Jiang, L. Ying, F. Huang, W. Yang and Y. Cao, *Macromolecules*, 2016, **49**, 5806–5816.

174 Y. Wei, X. Lin, al -, F. Wang, K. Zhang, B. Yang, Y. Zhang and W. Fang, *J. Semicond.*, 2021, **42**, 080301.

175 I. Burgués-Ceballos, M. Stella, P. Lacharmoise and E. Martínez-Ferrero, *J. Mater. Chem. A*, 2014, **2**, 17711–17722.

176 D. Koo, S. Jung, J. Seo, G. Jeong, Y. Choi, J. Lee, S. M. Lee, Y. Cho, M. Jeong, J. Lee, J. Oh, C. Yang and H. Park, *Joule*, 2020, **4**, 1021–1034.

177 J. Du, K. Hu, J. Zhang, L. Meng, J. Yue, I. Angunawela, H. Yan, S. Qin, X. Kong, Z. Zhang, B. Guan, H. Ade and Y. Li, *Nat. Commun. 2021 121*, 2021, **12**, 1–10.

178 J. Miao, H. Li, T. Wang, Y. Han, J. Liu and L. Wang, *J. Mater. Chem. A*, 2020, **8**, 20998–21006.

179 D. van As, J. Subbiah, D. J. Jones and W. W. H. Wong, *Macromol. Chem. Phys.*, 2016, **217**, 403–413.

180 D. Schiefer, R. Hanselmann and M. Sommer, *Polym. Chem.*, 2017, **8**, 4368–4377.

181 Y. He, T. Heumüller, W. Lai, G. Feng, A. Classen, X. Du, C. Liu, W. Li, N. Li and C. J. Brabec, *Adv. Energy Mater.*, 2019, **9**, 1900409.

182 D. F. Zeigler, K. A. Mazzio and C. K. Luscombe, *Macromolecules*, 2014, **47**, 5019–5028.

183 J. F. Chang, B. Sun, D. W. Breiby, M. M. Nielsen, T. I. Sölling, M. Giles, I. McCulloch and H. Sirringhaus, *Chem. Mater.*, 2004, **16**, 4772–4776.

184 M. T. Dang, L. Hirsch and G. Wantz, *Adv. Mater.*, 2011, **23**, 3597–3602.

185 A. Rodrigues, M. C. R. Castro, A. S. F. Farinha, M. Oliveira, J. P. C. Tomé, A. V. Machado, M. M. M. Raposo, L. Hilliou and G. Bernardo, *Polym. Test.*, 2013, **32**, 1192–1201.

186 S. Hotta, S. D. D. V. Rughooputh, A. J. Heeger and F. Wudl, *Macromolecules*, 2002, **20**, 212–215.

187 K. Khawas, S. Daripa, P. Kumari, M. K. Bera, S. Malik and B. K. Kuila, *J. Polym. Sci. Part A Polym. Chem.*, 2019, **57**, 945–951.

188 J. Lee, H. Park, S.-H. Hwang, I.-H. Lee and T.-L. Choi, *Macromolecules*, 2020, **53**, 3306–3314.

189 N. V. Handa, A. V. Serrano, M. J. Robb and C. J. Hawker, *J. Polym. Sci. Part A Polym. Chem.*, 2015, **53**, 831–841.

190 A. Bousquet, H. Awada, R. C. Hiorns, C. Dagron-Lartigau and L. Billon, *Prog. Polym. Sci.*, 2014, **39**, 1847–1877.

191 N. K. Obhi, D. M. Peda, E. L. Kynaston and D. S. Seferos, *Macromolecules*, 2018, **51**, 2969–2978.

192 J. Steverlynck, J. De Winter, P. Gerbaux, R. Lazzaroni, P. Leclère and G. Koeckelberghs, *Macromolecules*, 2015, **48**, 8789–8796.

193 G. M. Brooke, *J. Fluor. Chem.*, 1997, **86**, 1–76.

194 M. E. Payne and S. M. Grayson, *J. Vis. Exp.*, 2018, **136**, 57174.

195 P. Groves, *Polym. Chem.*, 2017, **8**, 6700–6708.

196 Y. Kim, S. Cook, S. A. Choulis, J. Nelson, J. R. Durrant and D. D. C. Bradley, 2004, **16**, 4812–4818.

197 P. J. Brown, D. S. Thomas, A. Köhler, J. S. Wilson, J.-S. Kim, C. M. Ramsdale, H. Sirringhaus and R. H. Friend, *Phys. Rev. B*, 2003, **67**, 064203.

198 M. Urien, L. Bailly, L. Vignau, E. Cloutet, A. de Cuendias, G. Wantz, H. Cramail, L. Hirsch and J. P. Parneix, *Polym. Int.*, 2008, **57**, 764–769.

199 L. Wu, S. Casado, B. Romero, J. M. Otón, J. Morgado, C. Müller, R. Xia and J. Cabanillas-Gonzalez, *Macromolecules*, 2015, **48**, 8765–8772.

200 F. C. Spano and C. Silva, *Annu. Rev. Phys. Chem*, 2014, **65**, 477–500.

201 D. Khlaifia, C. P. Ewels, F. Massuyeau, M. Chemek, E. Faulques, J. L. Duvail and K. Alimi, *RSC Adv.*, 2016, **6**, 56174–56182.

202 H. -M. Koepp, H. Wendt and H. Stkehlow, *Zeitschrift für Elektrochemie, Berichte der Bunsengesellschaft für Phys. Chemie*, 1960, **64**, 483–491.

203 R. R. Gagne, C. A. Koval and G. C. Lisensky, *Inorg. Chem.*, 1980, **19**, 2854–2855.

204 N. Yaghoobi Nia, M. Bonomo, M. Zendehdel, E. Lamanna, M. M. H. Desoky, B. Paci, F. Zurlo, A. Generosi, C. Barolo, G. Viscardi, P. Quagliotto and A. Di Carlo, *ACS Sustain. Chem. Eng.*, 2021, **9**, 5061–5073.

205 J. L. Bredas, *Mater. Horizons*, 2013, **1**, 17–19.

206 T.-A. Chen, X. Wu and R. D. Rieke, *J. Am. Chem. Soc*, 1995, **117**, 233–244.

207 D. Chirvase, J. Parisi, J. C. Hummelen and V. Dyakonov, *Nanotechnology*, 2004, **15**, 1317.

208 A. Zen, M. Saphiannikova, D. Neher, J. Grenzer, S. Grigorian, U. Pietsch, U. Asawapirom, S. Janietz, U. Scherf, I. Lieberwirth and G. Wegner, *Macromolecules*, 2006, **39**, 2162–2171.

209 M. Chevrier, S. Richeter, O. Coulembier, M. Surin, A. Mehdi, R. Lazzaroni, R. C. Evans, P. Dubois and S. Clément, *Chem. Commun.*, 2015, **52**, 171–174.

210 S. Y. Ku, M. A. Brady, N. D. Treat, J. E. Cochran, M. J. Robb, E. J. Kramer, M. L. Chabinyc and C. J. Hawker, *J. Am. Chem. Soc.*, 2012, **134**, 16040–16046.

211 A. J. Heeger, *Adv. Mater.*, 2014, **26**, 10–28.

212 D. Qiu, M. A. Adil, K. Lu and Z. Wei, *Front. Chem.*, 2020, **8**, 603134.

213 F. P. V. Koch, M. Heeney and P. Smith, *J. Am. Chem. Soc.*, 2013, **135**, 13699–13709.

214 C. L. Donley, J. Zaumseil, J. W. Andreasen, M. M. Nielsen, H. Sirringhaus, R. H. Friend and J. S. Kim, *J. Am. Chem. Soc.*, 2005, **127**, 12890–12899.

215 A. Ashraf, D. M. N. M. Dissanayake and M. D. Eisaman, *Phys. Chem. Chem. Phys.*, 2015, **17**, 23326–23331.

216 A. L. Patterson, *Phys. Rev.*, 1939, **56**, 978–981.

217 D. M. Smilgies, *J. Appl. Crystallogr.*, 2009, **42**, 1030–1034.

218 X. Jiao, M. Statz, L. Lai, S. Schott, C. Jellett, I. McCulloch, H. Sirringhaus and C. R. McNeill, *J. Phys. Chem. B*, 2020, **124**, 10529–10538.

219 F. A. Larrain, C. Fuentes-Hernandez, W. F. Chou, V. A. Rodriguez-Toro, T. Y. Huang, M. F. Toney and B. Kippelen, *Energy Environ. Sci.*, 2018, **11**, 2216–2224.

220 N. Liu, B. Liu, C. Yao and D. Cui, *Polymers (Basel).*, 2016, **8**, 17.

221 S. Honda and H. Sugimoto, *Macromolecules*, 2016, **49**, 6810–6816.

222 J. R. Tumbleston, B. A. Collins, L. Yang, A. C. Stuart, E. Gann, W. Ma, W. You and H. Ade, *Nat. Photonics*, 2014, **8**, 385–391.

223 Y. W. Su, Y. C. Lin and K. H. Wei, *J. Mater. Chem. A*, 2017, **5**, 24051–24075.

224 T. Luan Nguyen, T. Ho Lee, B. Gautam, S. Yi Park, K. Gundogdu, J. Young Kim and H. Young Woo, *Adv. Funct. Mater.*, 2017, **27**, 1702474.

225 J. A. Carrillo, M. J. Ingleson and M. L. Turner, *Macromolecules*, 2015, **48**, 979–986.

226 N. Zhou and A. Facchetti, *Mater. Today*, 2018, **21**, 377–390.

227 X. Guo and M. D. Watson, *Org. Lett.*, 2008, **10**, 5333–5336.

228 S. Shi, P. Chen, H. Wang, C. W. Koh, M. A. Uddin, B. Liu, Q. Liao, K. Feng, Y. Woo, G. Xiao and X. Guo, *Macromol. Rapid Commun.*, 2020, **41**, 2000144.

229 G. Zhang, H. Yu, Y. Sun, W. Wang, Y. Zhao, L. Wang, L. Qiu and Y. Ding, *J. Mater. Chem. C*, 2021, **9**, 633–639.

230 H. You, D. Kim, H. H. Cho, C. Lee, S. Chong, N. Y. Ahn, M. Seo, J. Kim, F. S. Kim and B. J.

Kim, *Adv. Funct. Mater.*, 2018, **28**, 1803613.

231 A. Giovannitti, I. P. Maria, D. Hanifi, M. J. Donahue, D. Bryant, K. J. Barth, B. E. Makdah, A. Savva, D. Moia, M. Zetek, P. R. F. Barnes, O. G. Reid, S. Inal, G. Rumbles, G. G. Malliaras, J. Nelson, J. Rivnay and I. McCulloch, *Chem. Mater.*, 2018, **30**, 2945–2953.

232 R. M. Arnold, N. E. Huddleston and J. Locklin, *J. Mater. Chem.*, 2012, **22**, 19357–19365.

233 K. Ninomiya, N. Shida, T. Nishikawa, T. Ishihara, H. Nishiyama, I. Tomita and S. Inagi, *ACS Macro Lett.*, 2020, **9**, 284–289.

234 Z. Zhao, Z. Yin, H. Chen, L. Zheng, C. Zhu, L. Zhang, S. Tan, H. Wang, Y. Guo, Q. Tang and Y. Liu, *Adv. Mater.*, 2017, **29**, 1602410.

235 Z. Chen, Y. Zheng, H. Yan and A. Facchetti, *J. Am. Chem. Soc.*, 2009, **131**, 8–9.

236 M. B. Kim and D. W. Dixon, *J. Phys. Org. Chem.*, 2008, **21**, 731–737.

237 Z. Yuan, J. Li, Y. Xiao, Z. Li and X. Qian, *J. Org. Chem.*, 2010, **75**, 3007–3016.

238 Z. Li, J. Lu, S. C. Tse, J. Zhou, X. Du, Y. Tao and J. Ding, *J. Mater. Chem.*, 2011, **21**, 3226–3233.

239 H. Bronstein, J. M. Frost, A. Hadipour, Y. Kim, C. B. Nielsen, R. S. Ashraf, B. P. Rand, S. Watkins and I. McCulloch, *Chem. Mater.*, 2013, **25**, 277–285.

240 N. Wang, Z. Chen, W. Wei and Z. Jiang, *J. Am. Chem. Soc.*, 2013, **135**, 17060–17068.

241 J. Li, M. Yan, Y. Xie and Q. Qiao, *Energy Environ. Sci.*, 2011, **4**, 4276–4283.

242 W. Sun, Y. Chen, X. Liang, L. Tan, Z. Liu, Z. Cai, L. Dong and L. Wang, *New J. Chem*, 2018, **42**, 15372–15378.

243 B. J. Kim, H. S. Lee, J. S. Lee, S. Cho, H. Kim, H. J. Son, H. Kim, M. J. Ko, S. Park, M. S. Kang, S. Y. Oh, B. Kim and J. H. Cho, *J. Phys. Chem. C*, 2013, **117**, 11479–11486.

244 S. Griggs, A. Marks, H. Bristow and I. McCulloch, *J. Mater. Chem. C*, 2021, **9**, 8099–8128.

245 R. Steyrleuthner, R. Di Pietro, B. A. Collins, F. Polzer, S. Himmelberger, M. Schubert, Z. Chen, S. Zhang, A. Salleo, H. Ade, A. Facchetti and D. Neher, *J. Am. Chem. Soc.*, 2014, **136**, 4245–4256.

246 H. Chen, Y. Guo, Z. Mao, G. Yu, J. Huang, Y. Zhao and Y. Liu, *Chem. Mater.*, 2013, **25**, 3589–3596.

247 B. Fu, J. Baltazar, Z. Hu, A.-T. Chien, S. Kumar, C. L. Henderson, D. M. Collard and E. Reichmanis, *Chem. Mater.*, 2012, **24**, 4123–4133.

248 C. B. Nielsen, M. Turbiez and I. McCulloch, *Adv. Mater.*, 2013, **25**, 1859–1880.

249 Z. Fei, P. Pattanasattayavong, Y. Han, B. C. Schroeder, F. Yan, R. J. Kline, T. D. Anthopoulos and M. Heeney, *J. Am. Chem. Soc.*, 2014, **136**, 15154–15157.

250 J. M. Spruell, M. Wolffs, F. A. Leibfarth, B. C. Stahl, J. Heo, L. A. Connal, J. Hu and C. J. Hawker, *J. Am. Chem. Soc.*, 2011, **133**, 16698–16706.

251 S. Neumann, G. Bengtson, D. Meis and V. Filiz, *Polymers (Basel).*, 2019, **11**, 1241.

252 J. A. Letizia, M. R. Salata, C. M. Tribout, A. Facchetti, M. A. Ratner and T. J. Marks, *J. Am. Chem. Soc.*, 2008, **130**, 9679–9694.

253 B. M. Squeo, W. Mróz, U. Giovanella and M. Pasini, *Chem. Proc.*, 2021, **3**, 18.

254 Q. Li, J. Wu, R. Wu, Y. Liu, H. Chen, F. Huang and H. Li, *Sci. China Chem.*, 2017, **60**, 490–496.

255 R. Xia, D.-S. Leem, T. Kirchartz, S. Spencer, C. Murphy, Z. He, H. Wu, S. Su, Y. Cao, J. Seon Kim, J. C. DeMello, D. D. Bradley and J. Nelson, *Adv. Energy Mater.*, 2013, **3**, 718–723.

256 Z. Chen, Z. Hu, Z. Wu, X. Liu, Y. Jin, M. Xiao, F. Huang and Y. Cao, *J. Mater. Chem. A*, 2017, **5**, 19447–19455.

257 D. X. Long, K. J. Baeg, Y. Xu, S. J. Kang, M. G. Kim, G. W. Lee and Y. Y. Noh, *Adv. Funct. Mater.*, 2014, **24**, 6484–6491.

258 J.-H. Lee, B. Hoon Lee, S. Yi Jeong, S. Byeol Park, G. Kim, S. Ho Lee, K. Lee, J. Lee, B. H. Lee, S. Y. Jeong, S. B. Park, G. Kim, S. H. Lee and K. Lee, *Adv. Energy Mater.*, 2015, **5**, 1501292.

259 E. J. Lee, M. H. Choi, Y. W. Han and D. K. Moon, *ACS Appl. Mater. Interfaces*, 2017, **9**, 44060–44069.

260 H. S. Jung and T. Q. Nguyen, *J. Am. Chem. Soc.*, 2008, **130**, 10042–10043.

261 B. Hoon Lee, J.-H. Lee, S. Yi Jeong, S. Byeol Park, S. Ho Lee, K. Lee, B. H. Lee, J. Lee, S. Y. Jeong, S. B. Park, S. H. Lee and K. Lee, *Adv. Energy Mater.*, 2015, **5**, 1401653.

262 R. Kang, S. H. Oh and D. Y. Kim, *ACS Appl. Mater. Interfaces*, 2014, **6**, 6227–6236.

263 C. K. Mai, T. Arai, X. Liu, S. L. Fronk, G. M. Su, R. A. Segalman, M. L. Chabinyc and G. C. Bazan, *Chem. Commun.*, 2015, **51**, 17607–17610.

264 E. Dae Jung, A. Kumar Harit, D. Hui Kim, C. Hyeon Jang, J. Hyun Park, S. Cho, M. Hoon Song and H. Young Woo, *Adv. Mater.*, 2020, **32**, 2002333.

265 R. Rulkens, M. Schulze and G. Wegner, *Macromol. Rapid Commun.*, 1994, **15**, 669–676.

266 M. Wittemann, *Chem. Commun.*, 1998, **5**, 623–624.

267 P. B. Balanda, M. B. Ramey and J. R. Reynolds, *Macromolecules*, 1999, **32**, 3970–3978.

268 O. Banjoko and C. Ezeani, *J. Chem. Soc. Perkin Trans. 2*, 1986, **2**, 531–536.

269 X. Jin, Y. Wang, X. Cheng, H. Zhou, L. Hu, Y. Zhou, L. Chen and Y. Chen, *J. Mater. Chem. A*, 2018, **6**, 423–433.

270 L. Sheng, T. Higashihara, S. Nakazawa and M. Ueda, *Polym. Chem.*, 2012, **3**, 3289–

3295.

271 C. M. Cardona, W. Li, A. E. Kaifer, D. Stockdale and G. C. Bazan, *Adv. Mater.*, 2011, **23**, 2367–2371.

272 J. W. Kim and A. Kim, *Curr. Appl. Phys.*, 2021, **31**, 52–59.

273 J. Sitte, *Chem. Phys. Lett.*, 1976, **42**, 131–132.

274 S. Evans, *Chem. Phys. Lett.*, 1973, **23**, 134–138.

275 B. H. Lee, I. H. Jung, H. Y. Woo, H. K. Shim, G. Kim and K. Lee, *Adv. Funct. Mater.*, 2014, **24**, 1100–1108.

276 M. K. Jeong, J. Kang, D. Park, S. Yim and I. H. Jung, *J. Mater. Chem. C*, 2020, **8**, 2542–2550.

277 M. Demeter, M. Neumann and W. Reichelt, *Surf. Sci.*, 2000, **454**–**456**, 41–44.

278 F. A. Stevie and C. L. Donley, *J. Vac. Sci. Technol. A*, 2020, **38**, 063204.

279 M. G. Helander, M. T. Greiner, Z. B. Wang and Z. H. Lu, *Appl. Surf. Sci.*, 2010, **256**, 2602–2605.

8 Appendix

Chapter 2 appendix……182

Chapter 3 appendix……193

Chapter 4 appendix……205

Chapter 5 appendix……228

2 Chapter 2 Appendix:

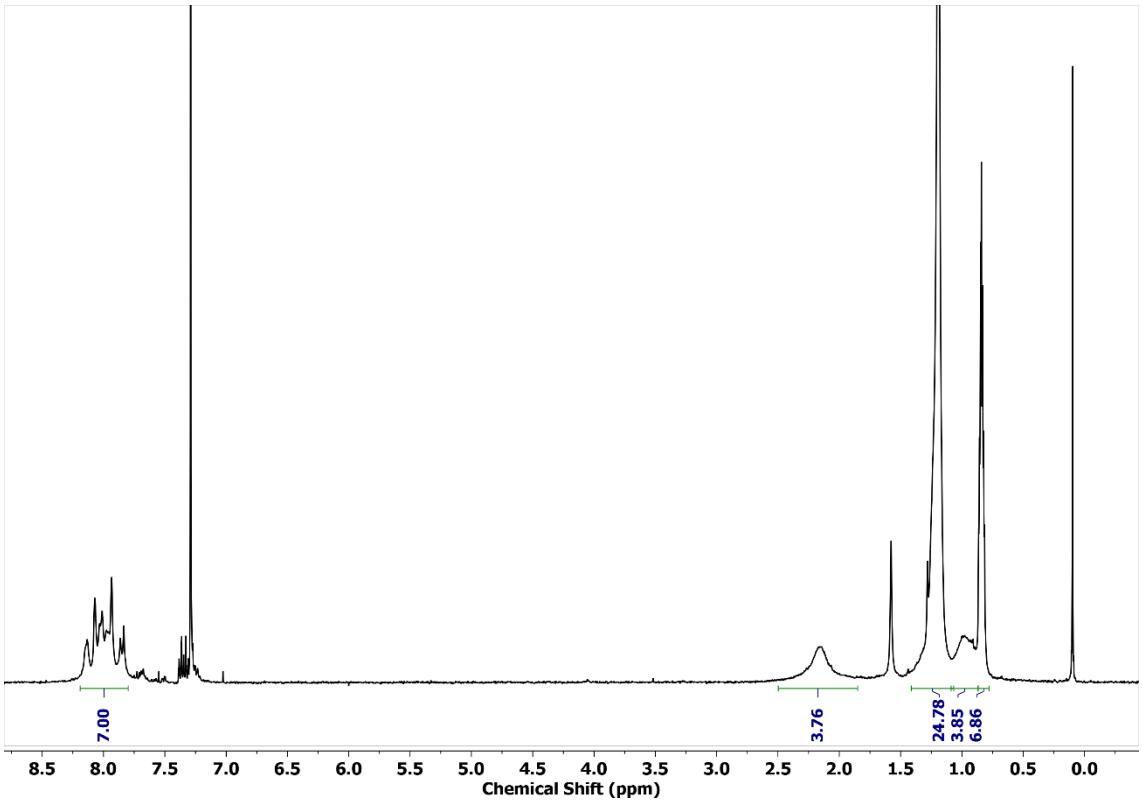


Figure S2.1. ^{1}H NMR of F8fBT.

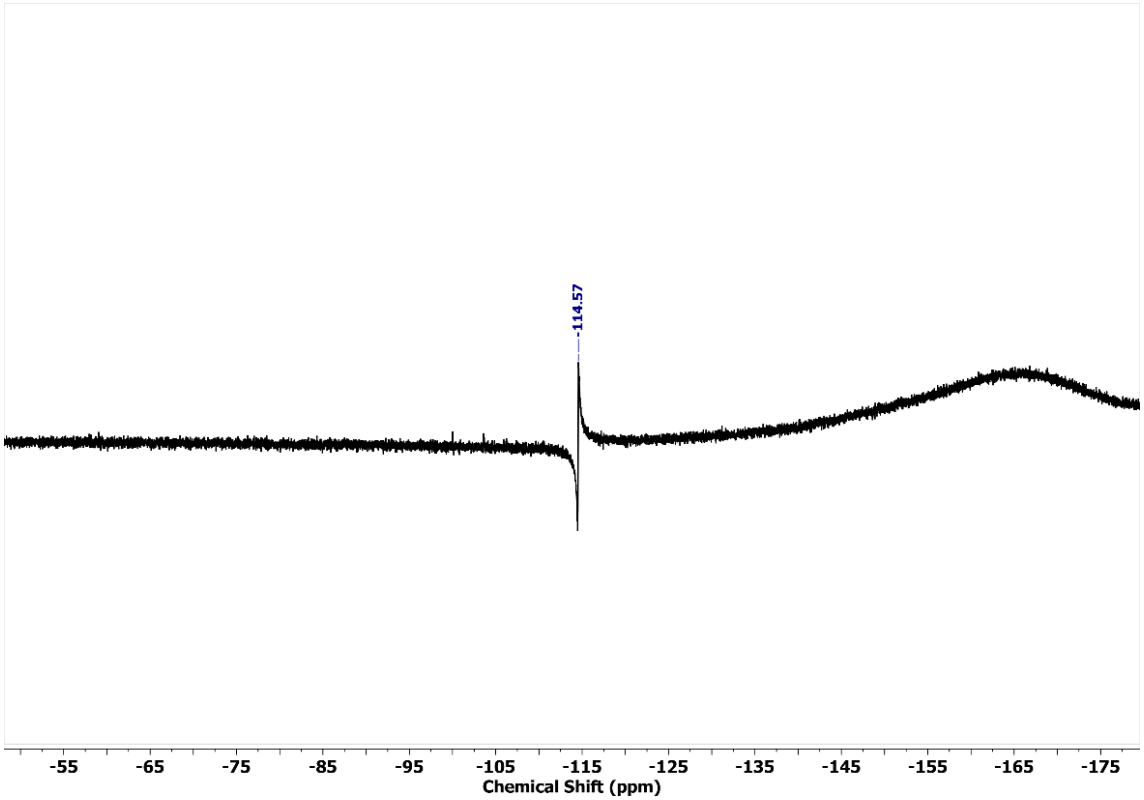


Figure S2.2. ^{19}F NMR of F8fBT.

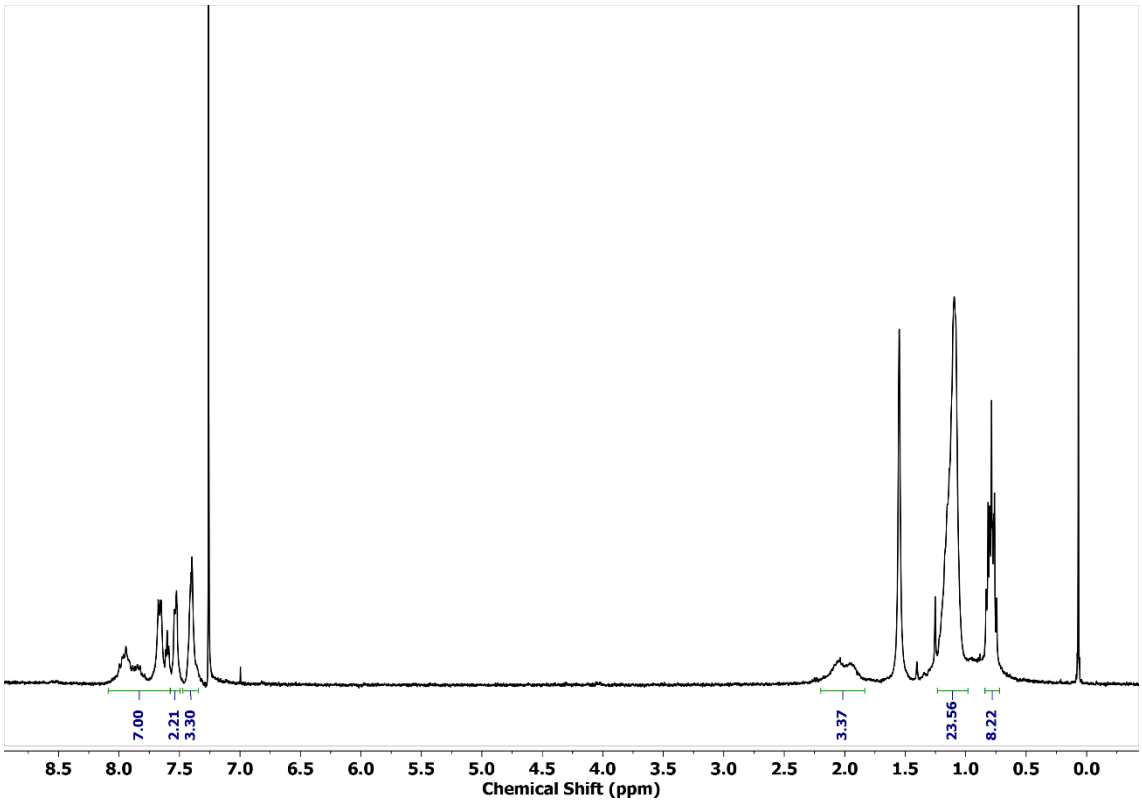


Figure S2.3. ^{1}H NMR of F8BT-SPh.

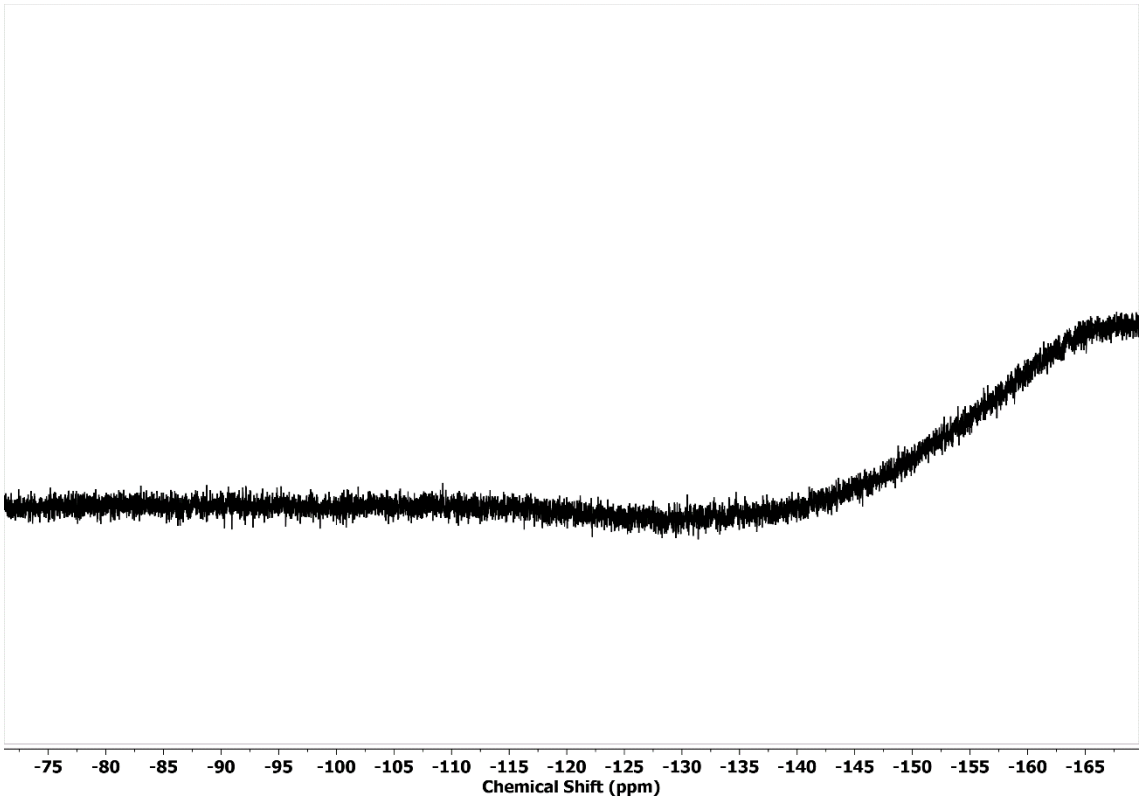


Figure S2.4. ^{19}F NMR of F8BT-SPh.

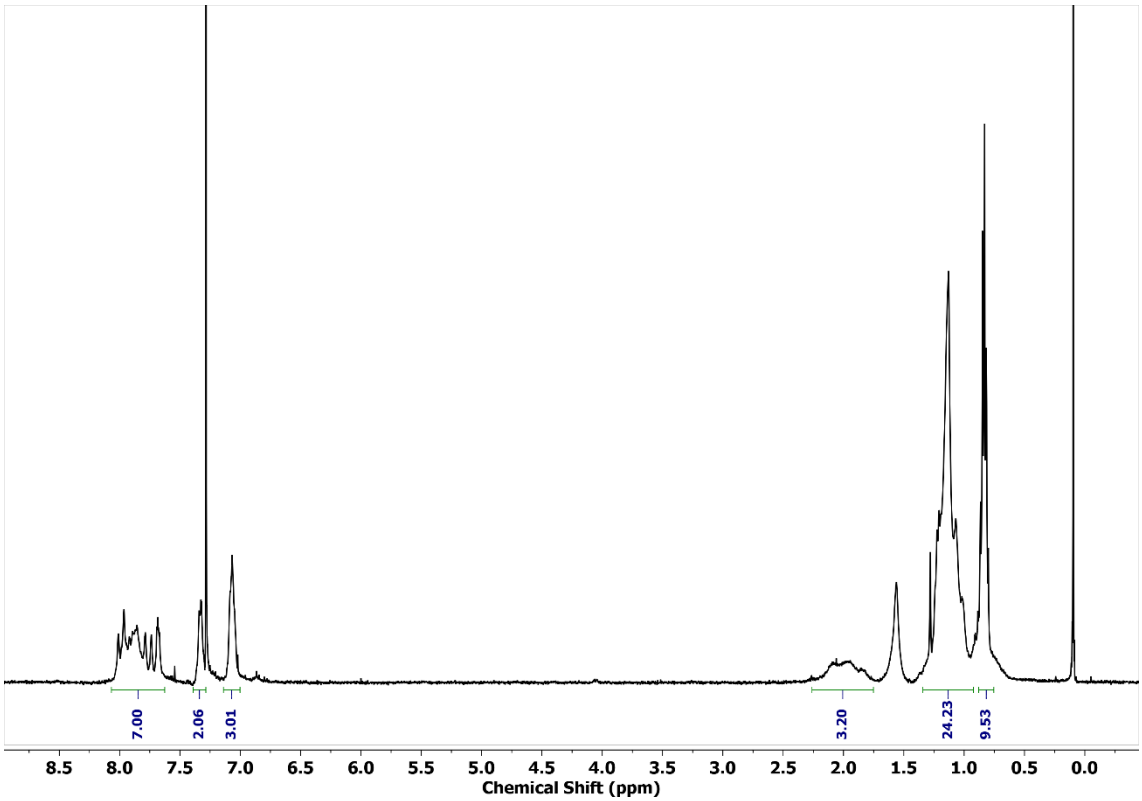


Figure S2.5. ^{1}H NMR of F8BT-OPh.

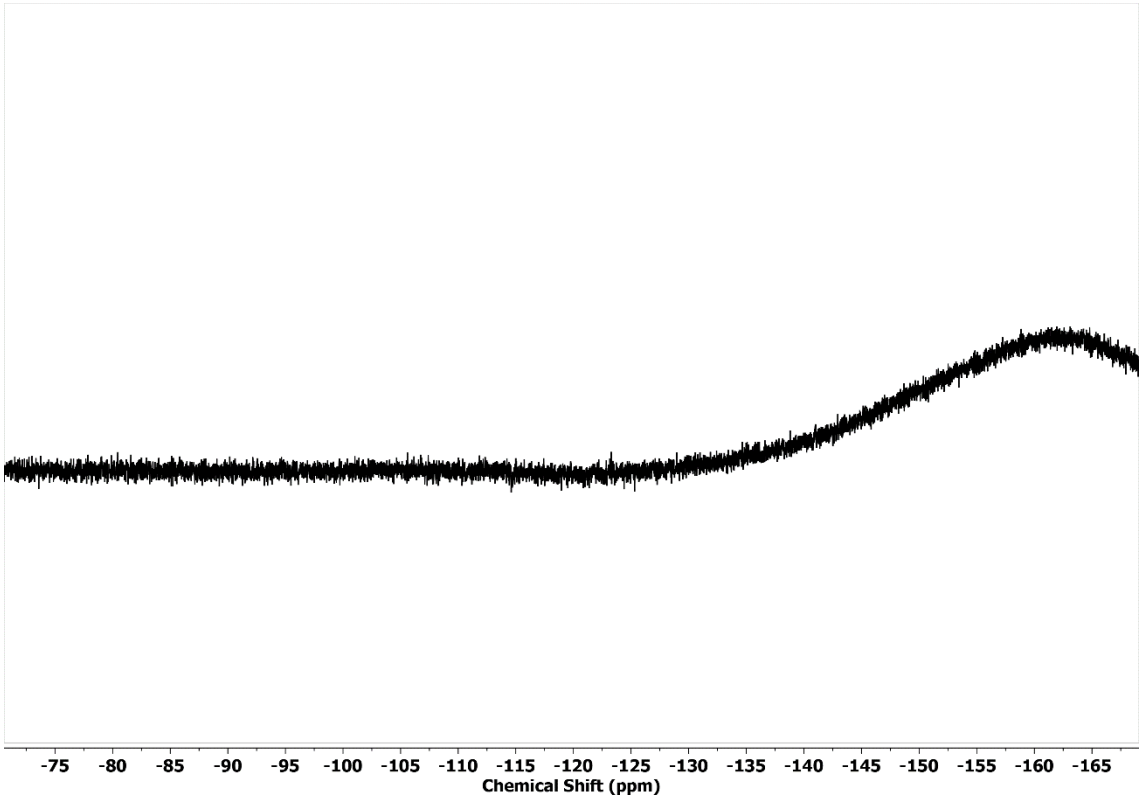


Figure S2.6. ^{19}F NMR of F8BT-OPh.

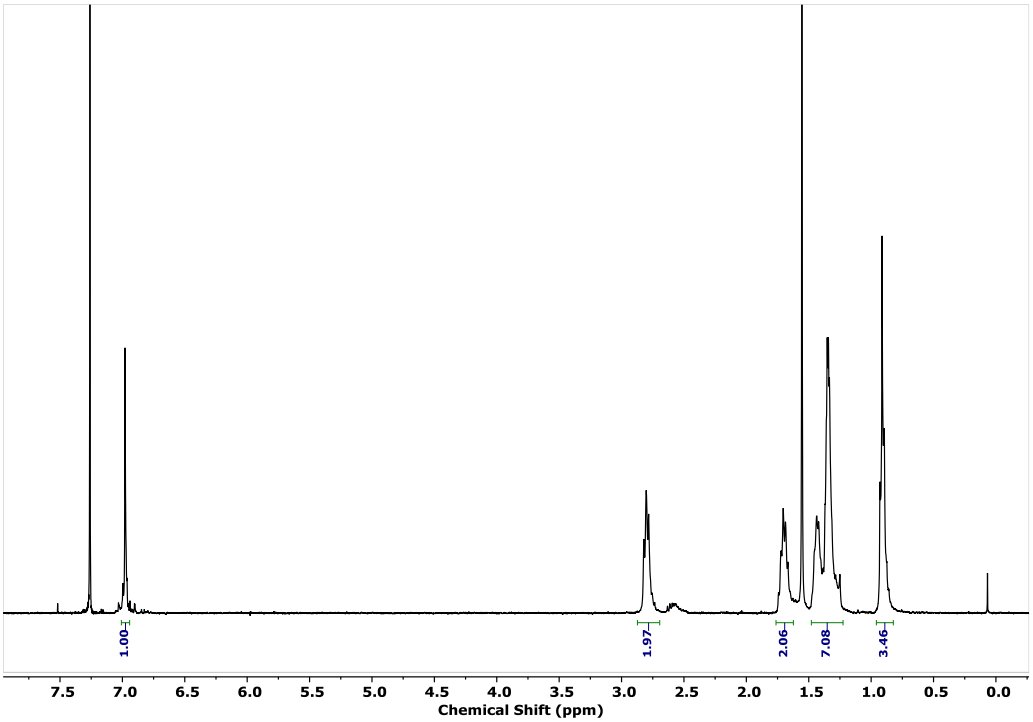


Figure S2.7. ^{1}H NMR of P3HT-Br.

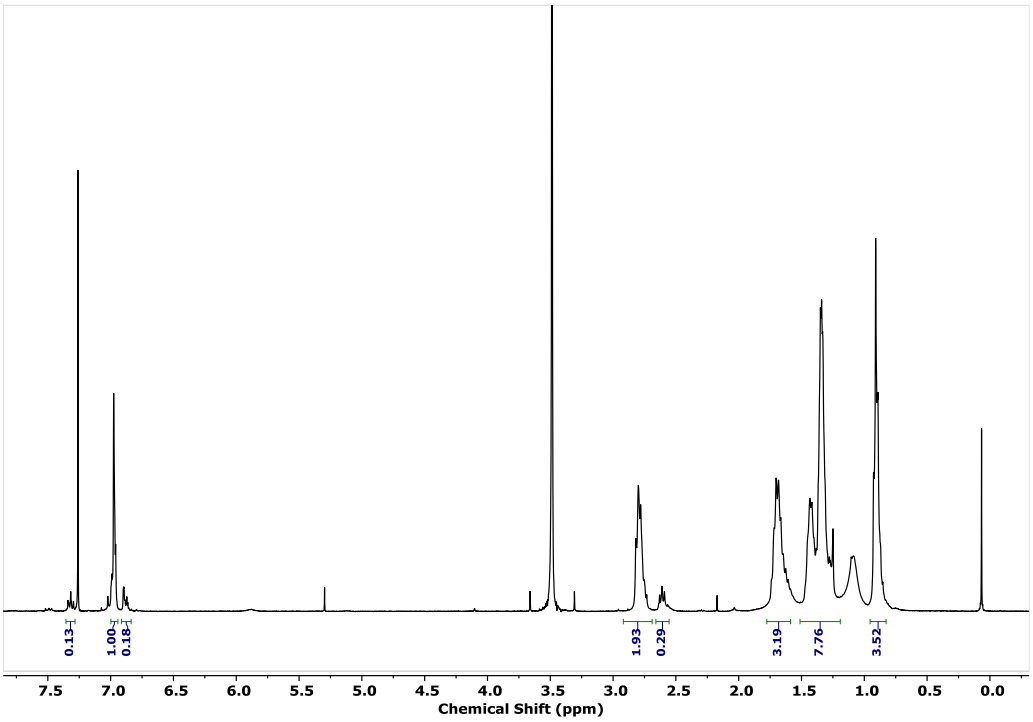


Figure S2.8. ^{1}H NMR of P3HT-PhOH.

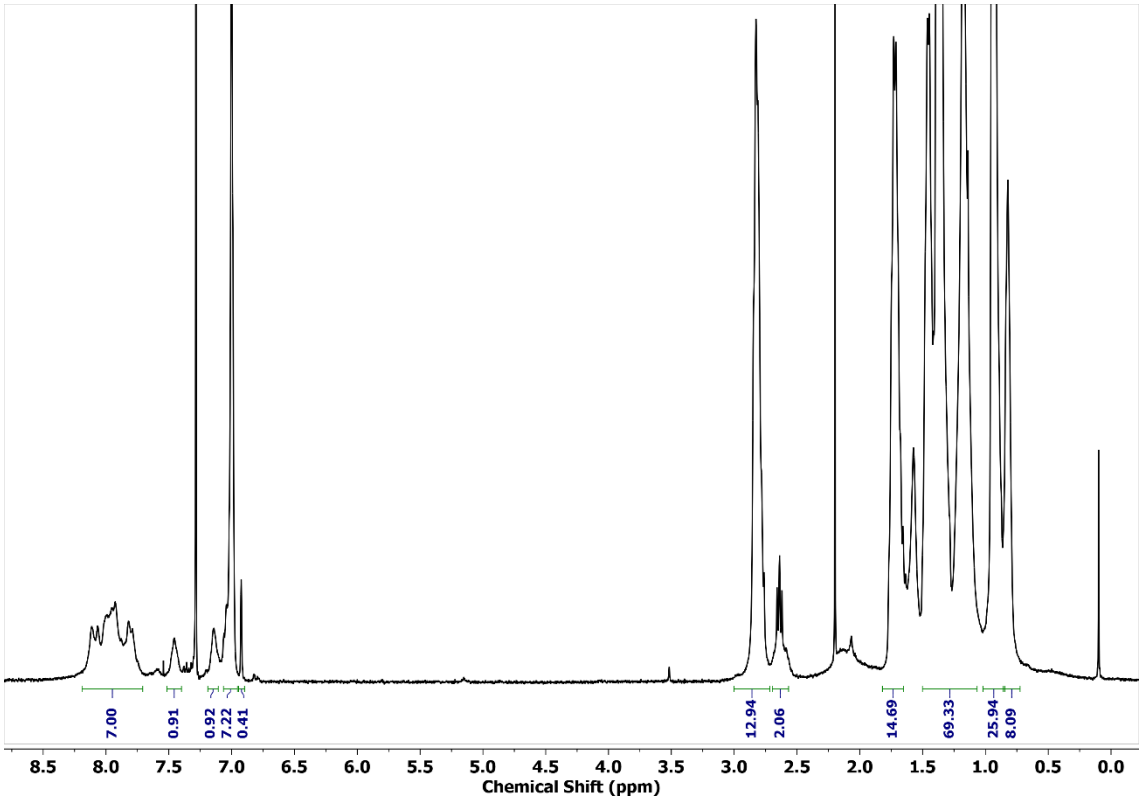


Figure S2.9. ^{1}H NMR of F8BT-g-P3HT(OPh).

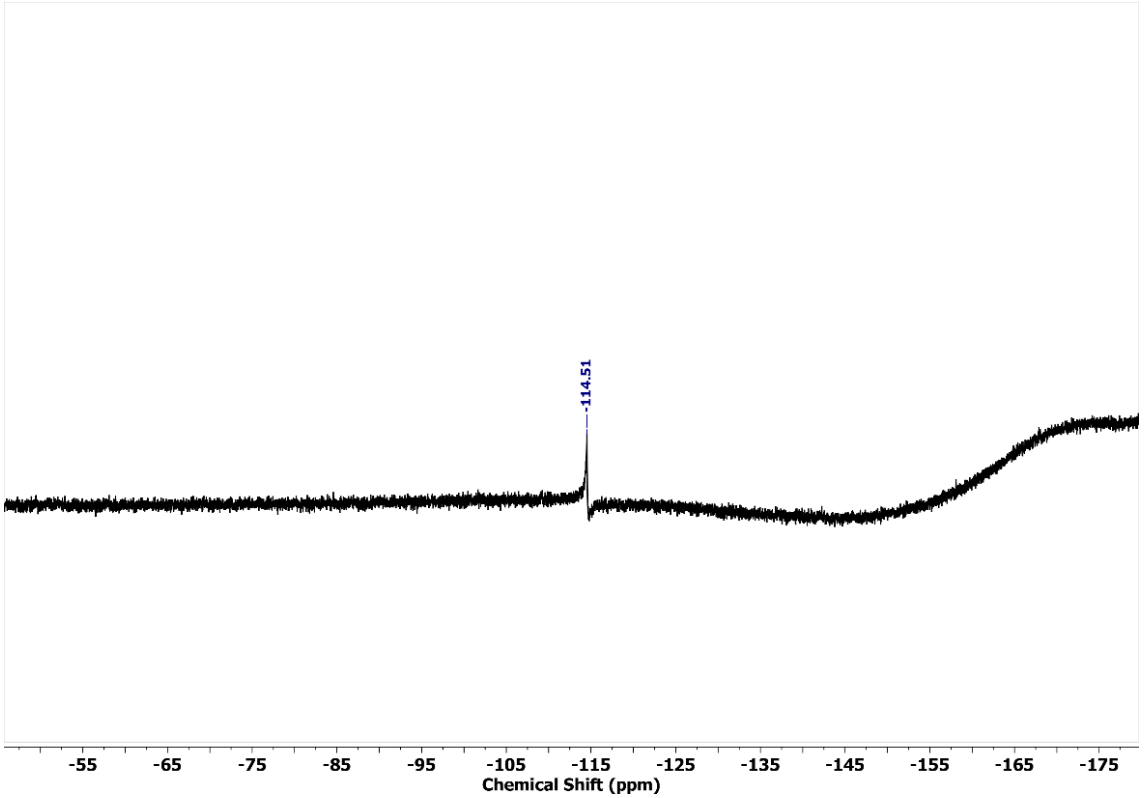


Figure S2.10. ^{19}F NMR of F8BT-g-P3HT(OPh).

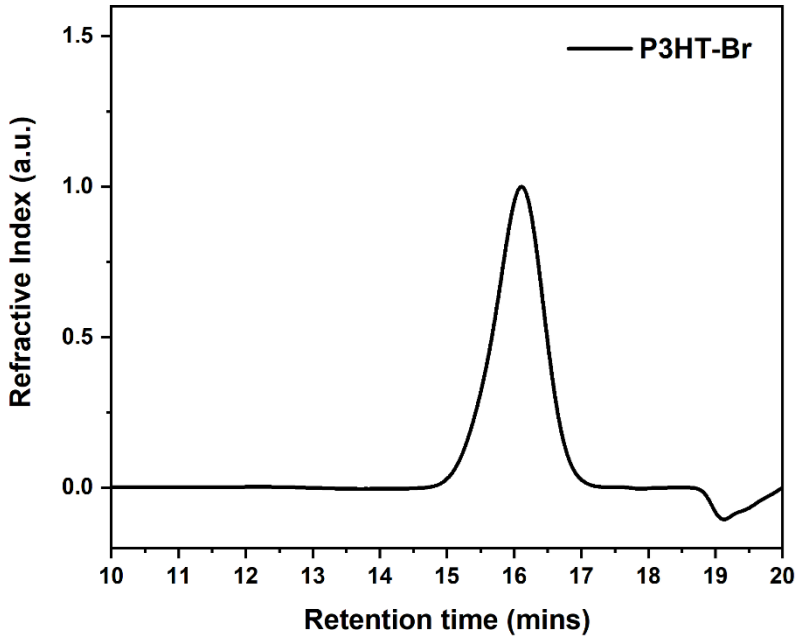


Figure S2.11. GPC trace of P3HT-Br.

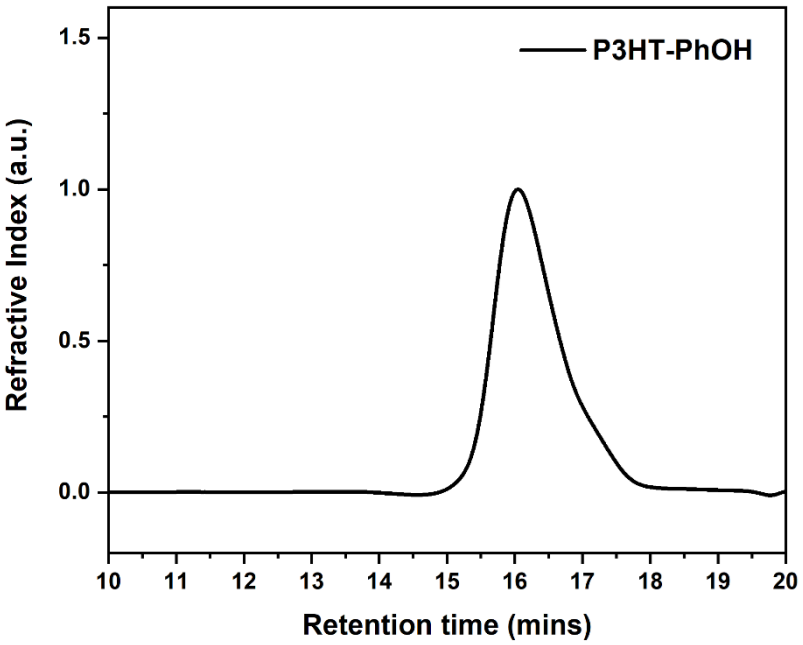


Figure S2.12. GPC trace of P3HT-PhOH.

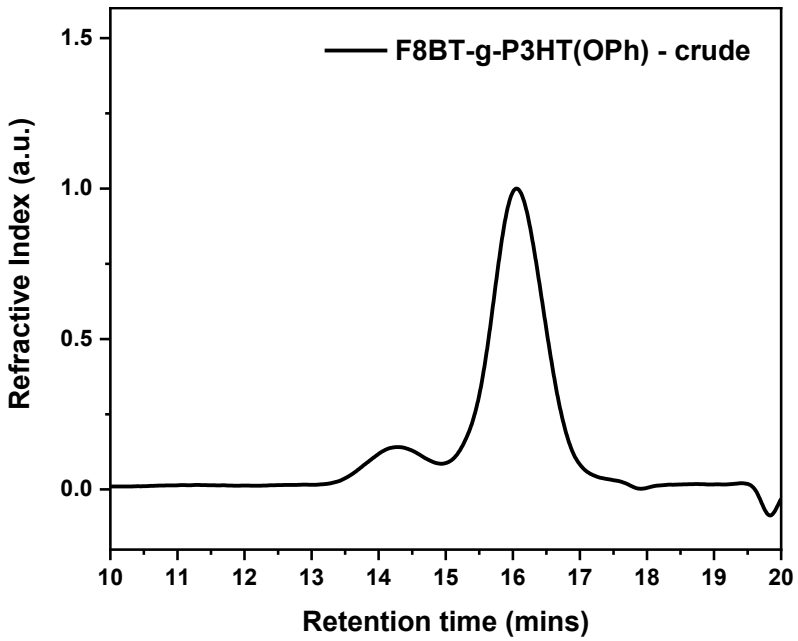


Figure S2.13. GPC trace of F8BT-g-P3HT(OPh) crude.

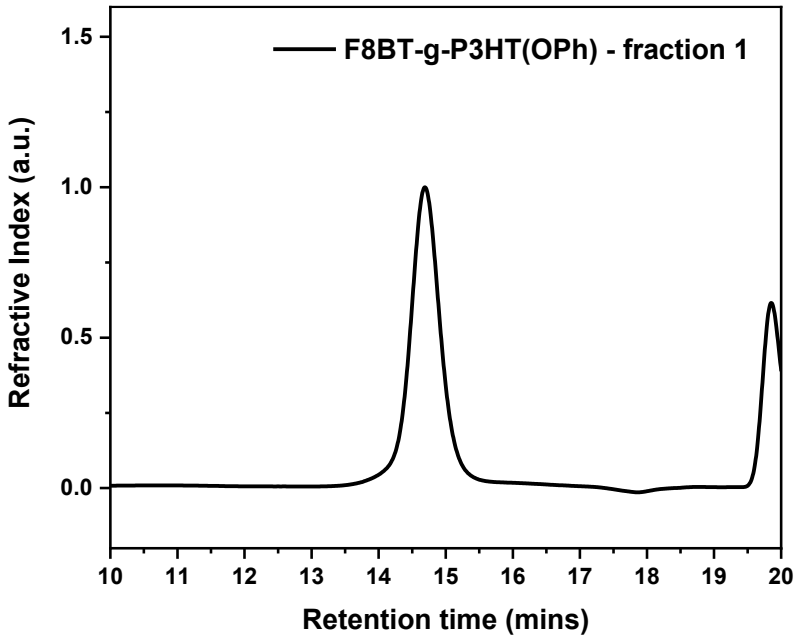


Figure S2.14. GPC trace of F8BT-g-P3HT(OPh) fraction 1, post-purification.

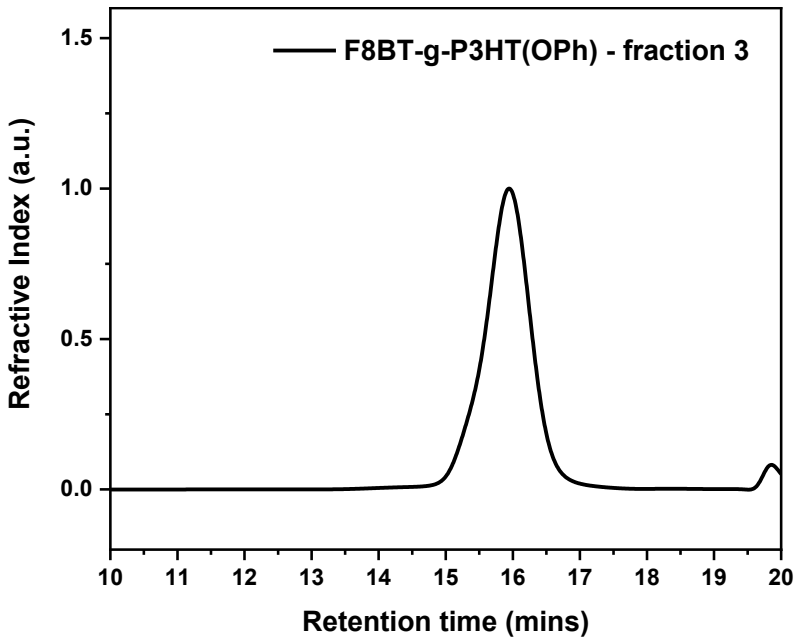


Figure S2.15. GPC trace of F8BT-g-P3HT(OPh) fraction 3, post-purification.

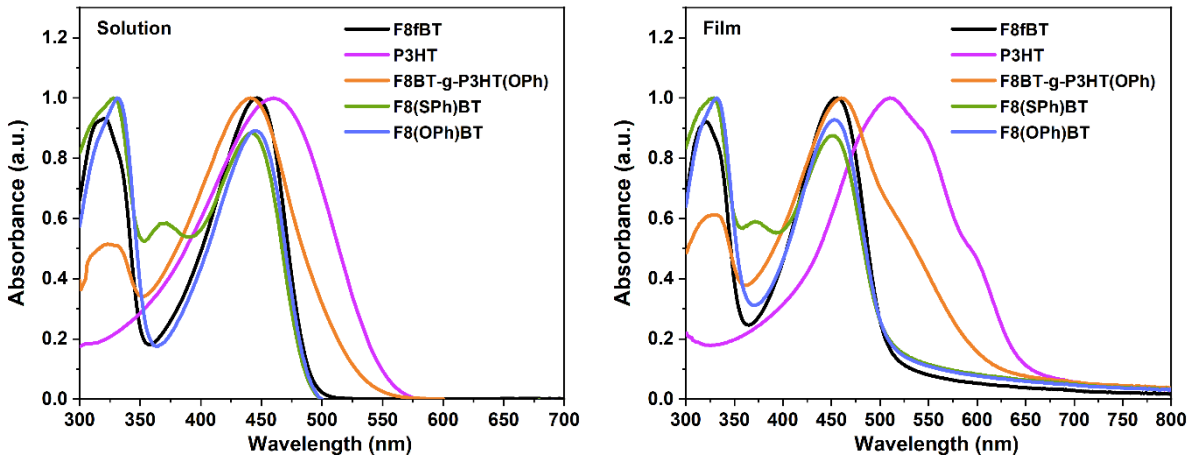


Figure S2.16. UV-Vis absorption spectra for F8fBT, F8BT-SPh, F8BT-OPh, P3HT and F8BT-g-P3HT(OPh) in solution (left) and thin film (right)

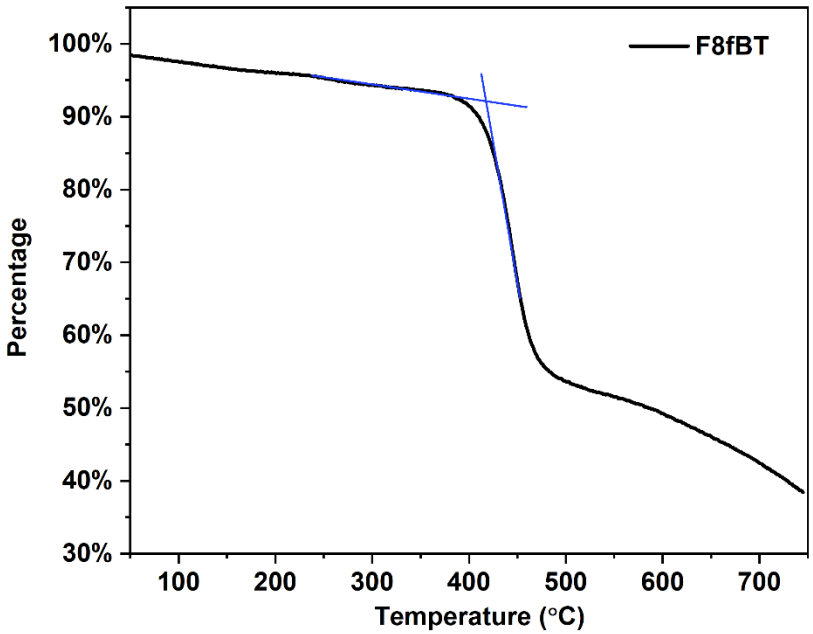


Figure S2.17. TGA curve of F8fBT.

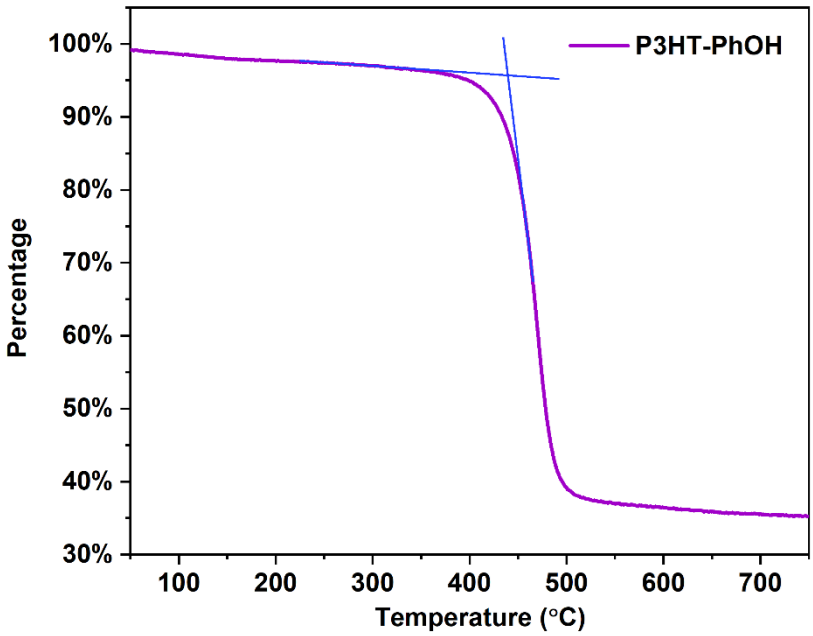


Figure S2.18. TGA curve of P3HT-PhOH.

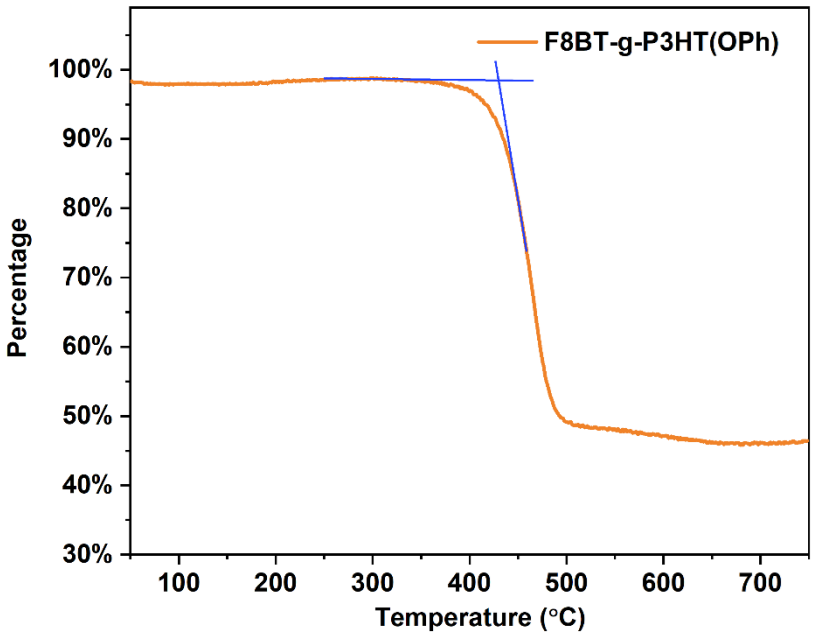


Figure S2.19. TGA curve of F8BT-g-P3HT(OPh).

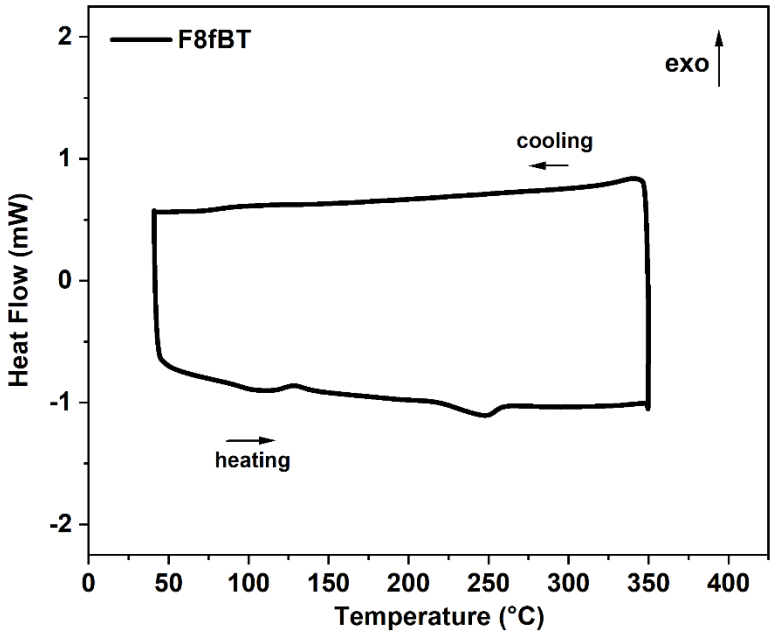


Figure S2.20. DSC curve of F8fBT.

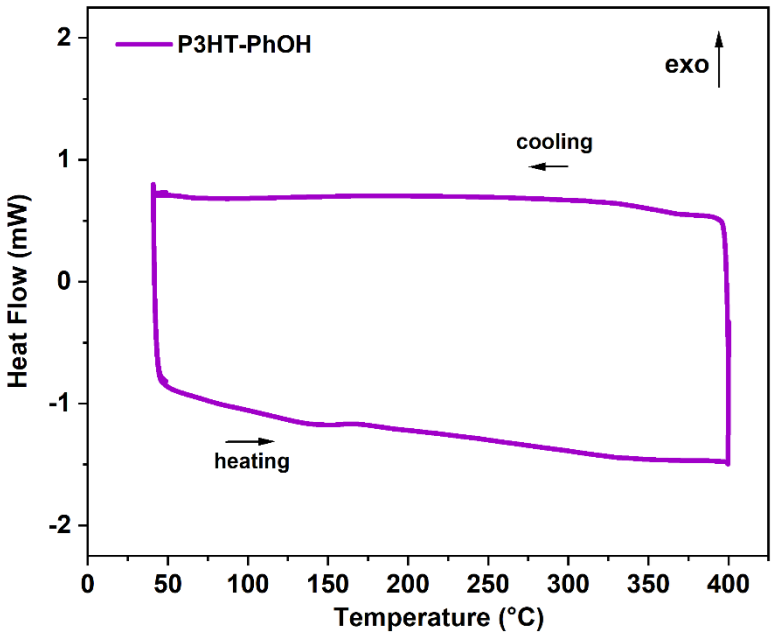


Figure S2.21. DSC curve of P3HT-PhOH.

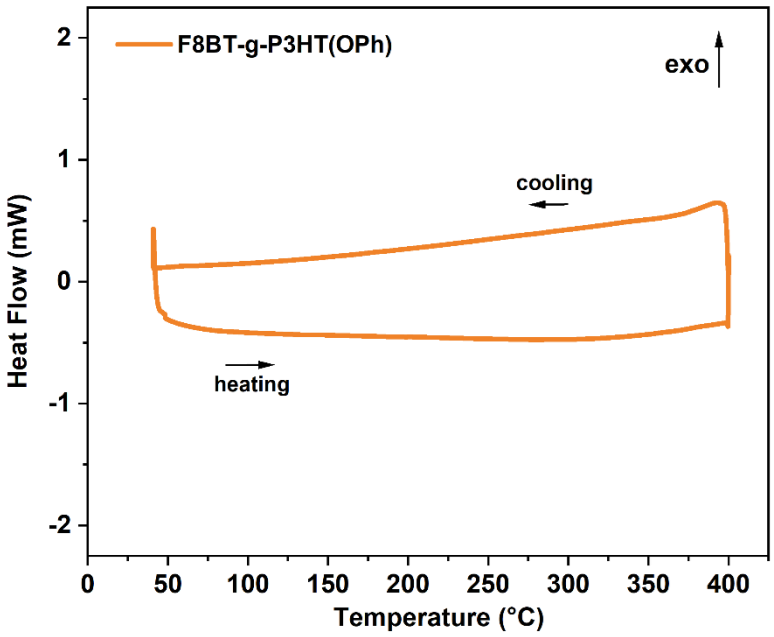


Figure S2.22. DSC curve of F8BT-g-P3HT(OPh).

3 Chapter 3 Appendix:

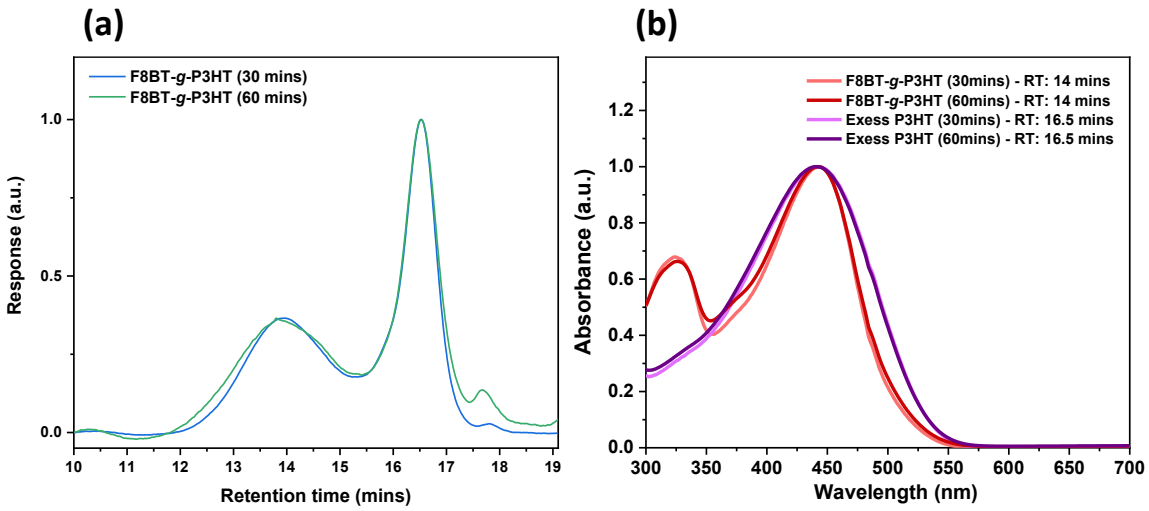


Figure S3.1. (a) GPC trace of crude reaction mixture at 30 and 60 minutes and (b) corresponding UV-VIS traces of polymer material eluted at 14 and 16.5 minutes.

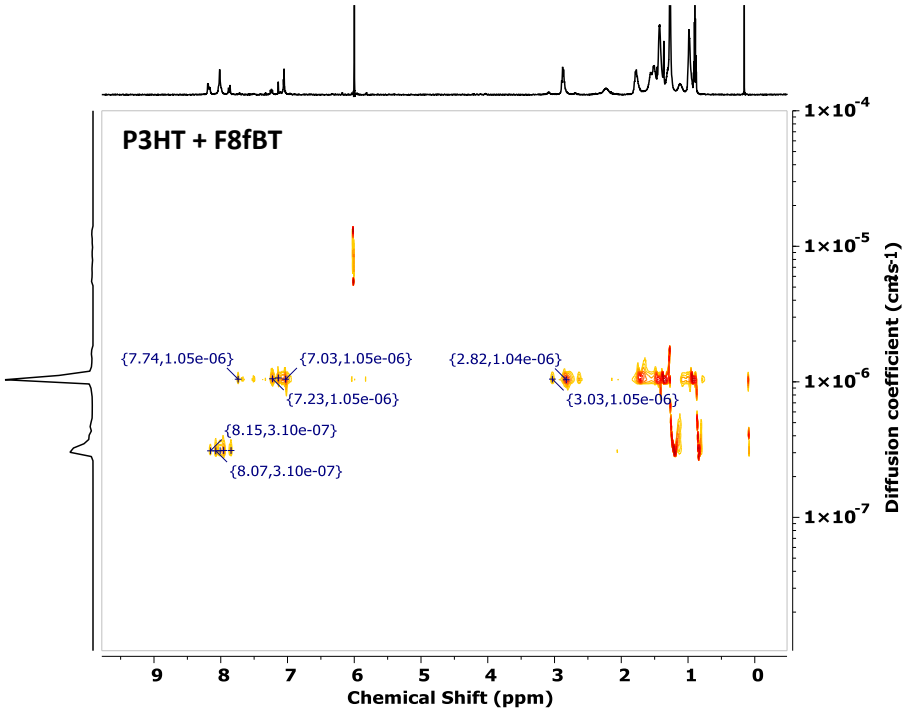


Figure S3.2. DOSY NMR of polymer blend P3HT:F8fBT (1:1 molar blend).

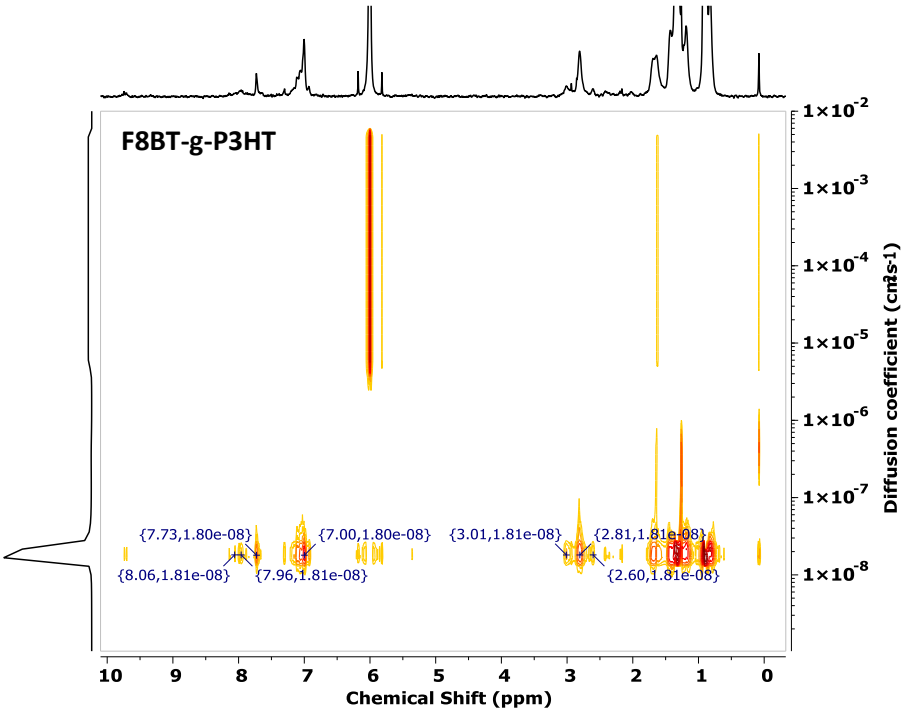


Figure S3.3. DOSY NMR of polymer blend F8BT-g-P3HT.

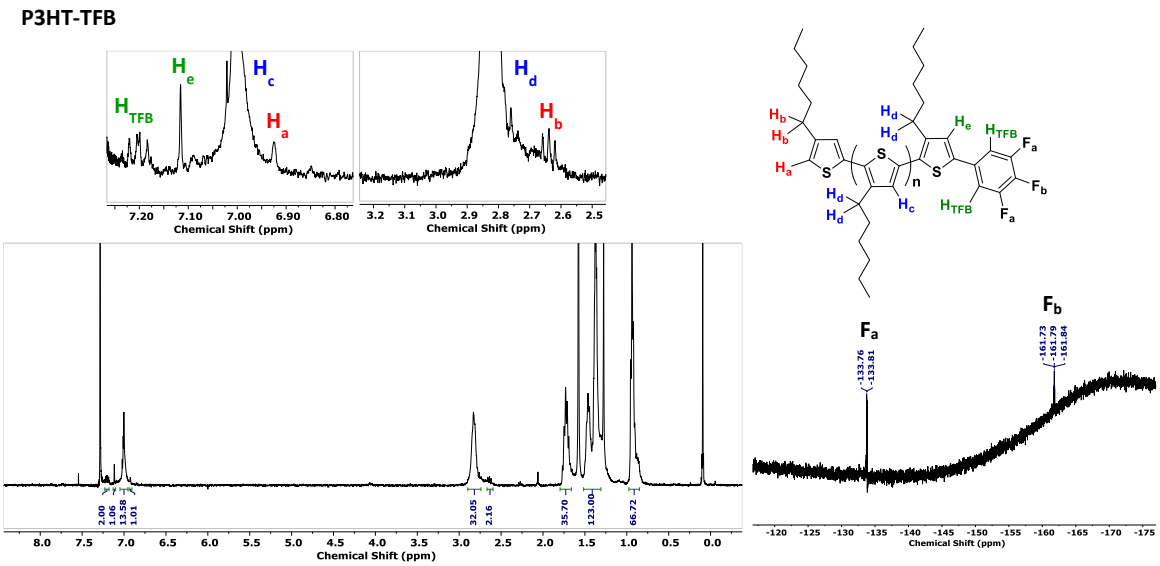


Figure S3.4. ^{1}H NMR (left) and ^{19}F NMR (right) of P3HT-TFB.

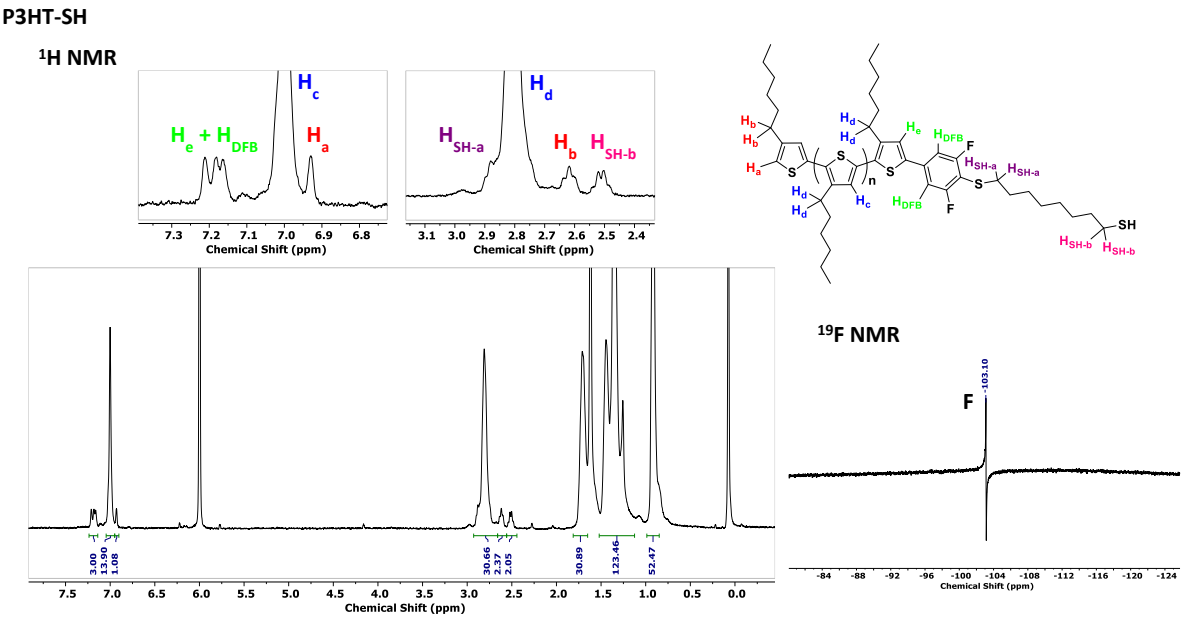


Figure S3.5. ^{1}H NMR (left) and ^{19}F NMR (right) of P3HT-SH.

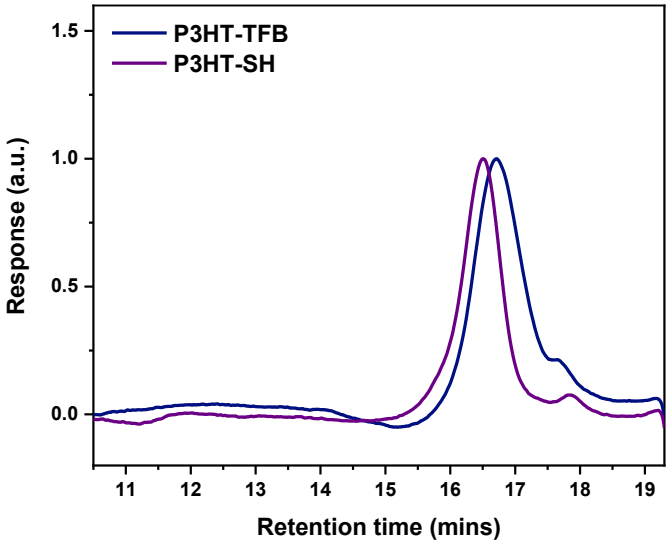


Figure S3.6. GPC trace of P3HT-TFB and P3HT-SH.

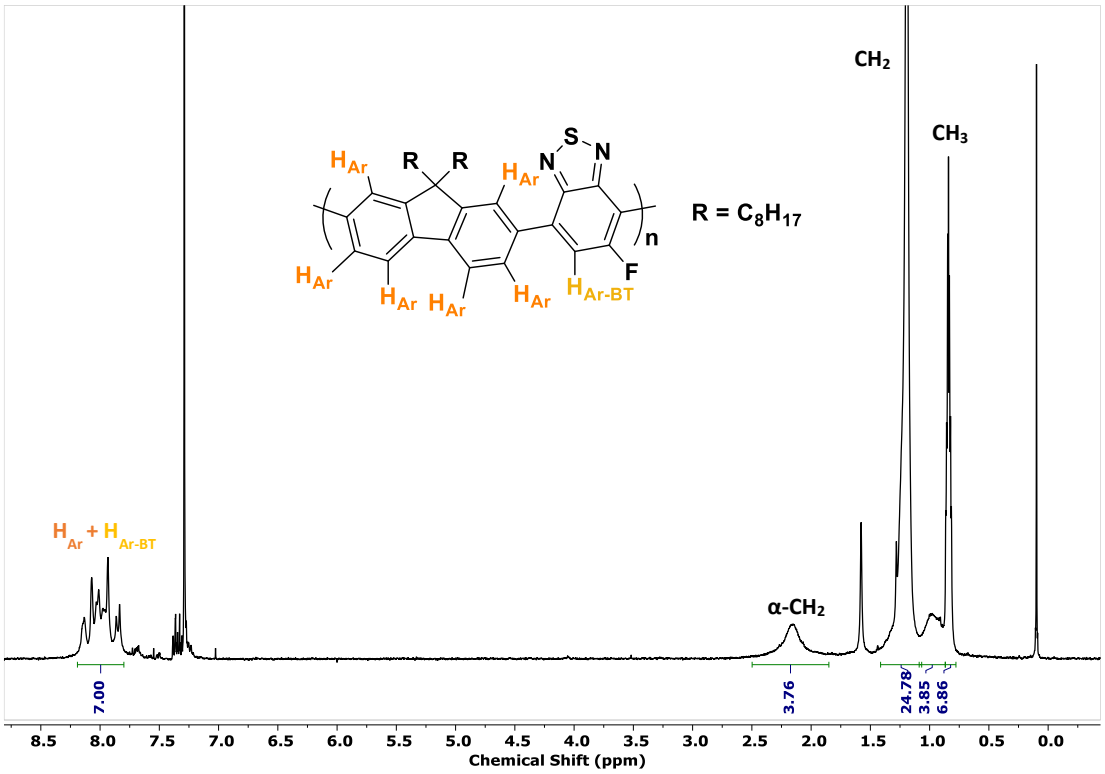


Figure S3.7. ^{1}H NMR of F8fBT where α-CH_2 is the methylene group adjacent to the conjugated polymer backbone on the C_8H_{17} sidechain.

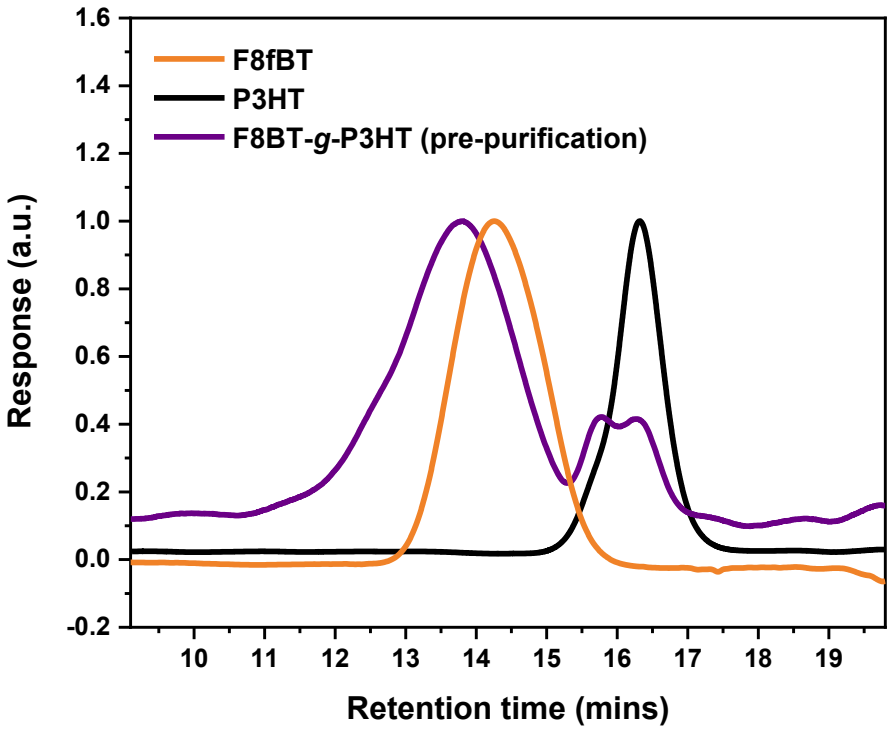


Figure S3.8. GPC trace of starting polymers F8fBT and P3HT and graft co-polymer F8BT-g-P3HT pre-purification.

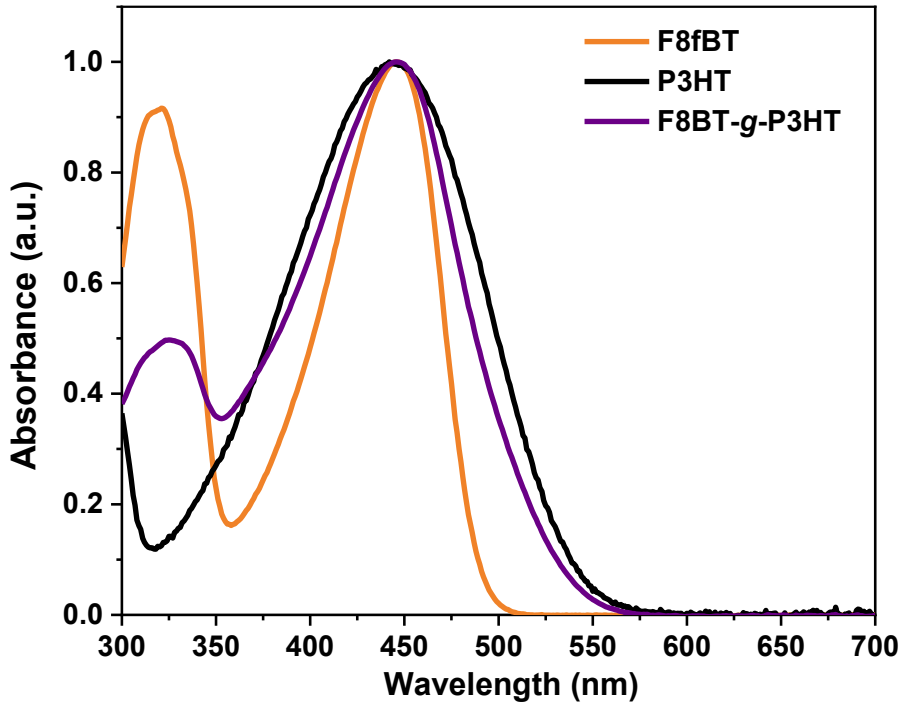
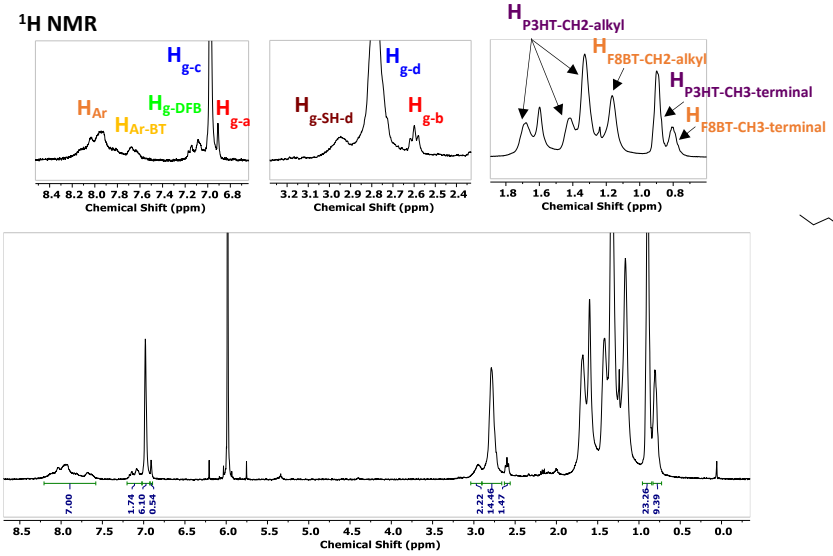
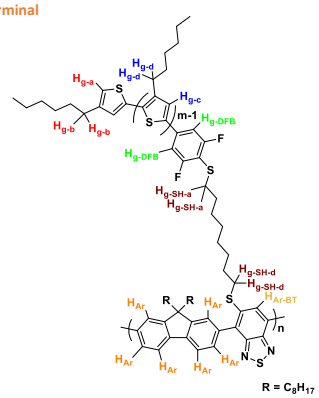


Figure S3.9. UV-Vis absorption spectra for F8fBT, P3HT and F8BT-g-P3HT in chloroform.

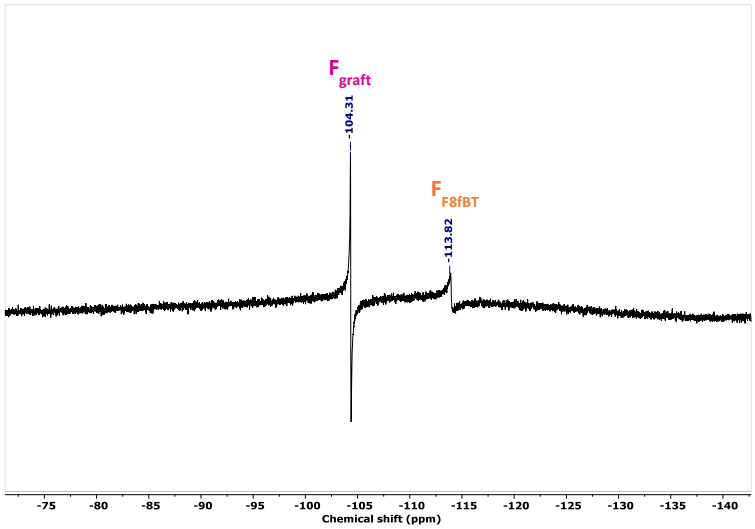
F8BT-g-P3HT

^{1}H NMR





^{19}F NMR



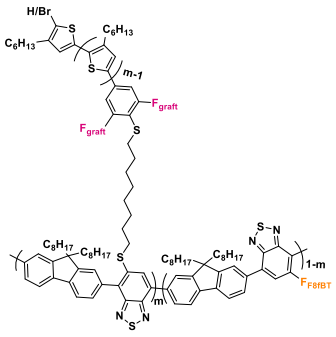


Figure S3.10. ^{1}H NMR (top) and ^{19}F NMR (bottom) of F8BT-g-P3HT.

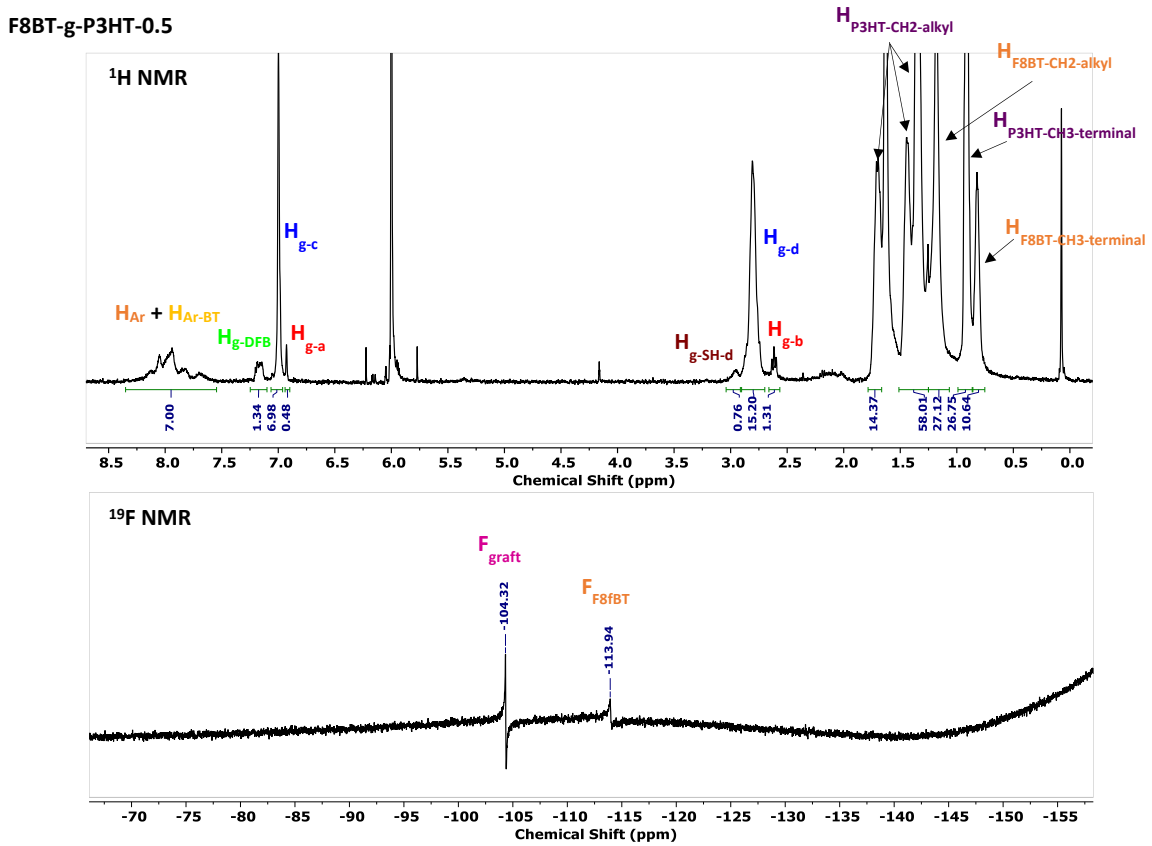


Figure S3.11. ^{1}H NMR (top) and ^{19}F NMR (bottom) of F8BT-g-P3HT-0.5.

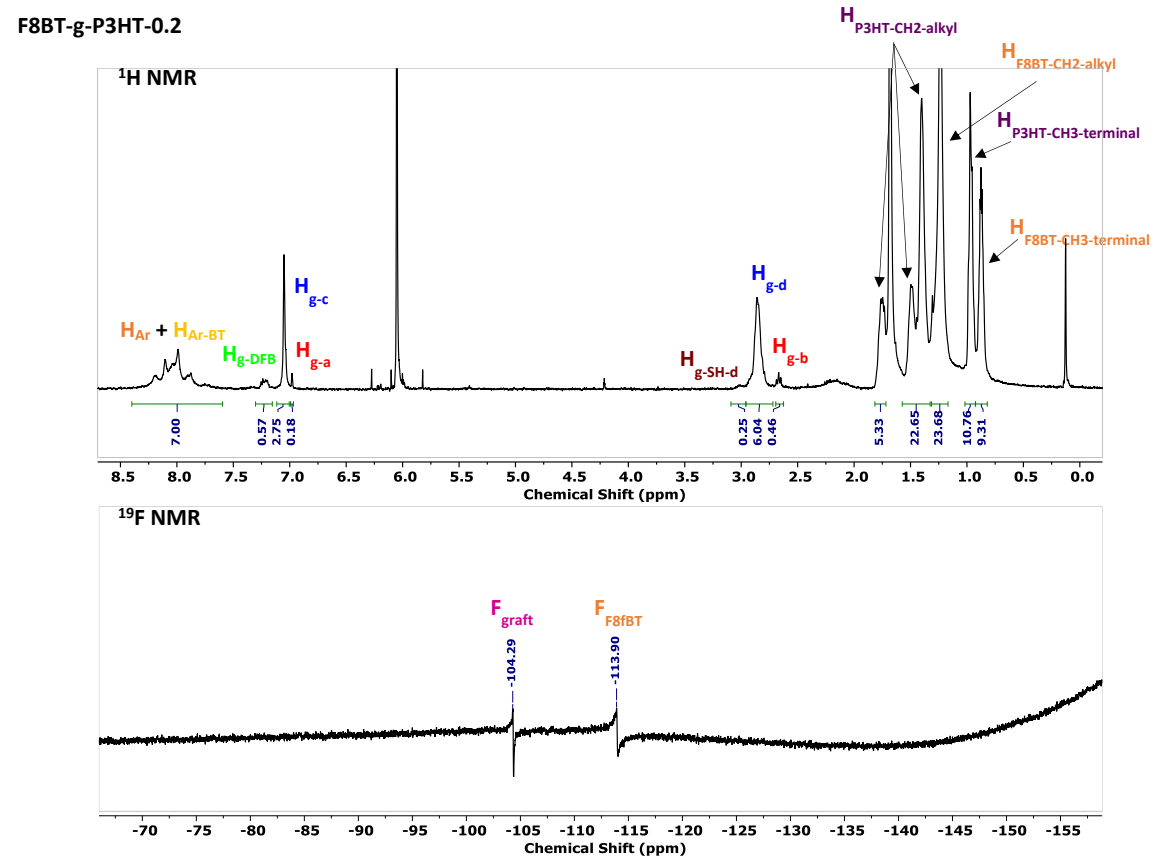


Figure S3.12. ^{1}H NMR (top) and ^{19}F NMR (bottom) of F8BT-g-P3HT-0.2.

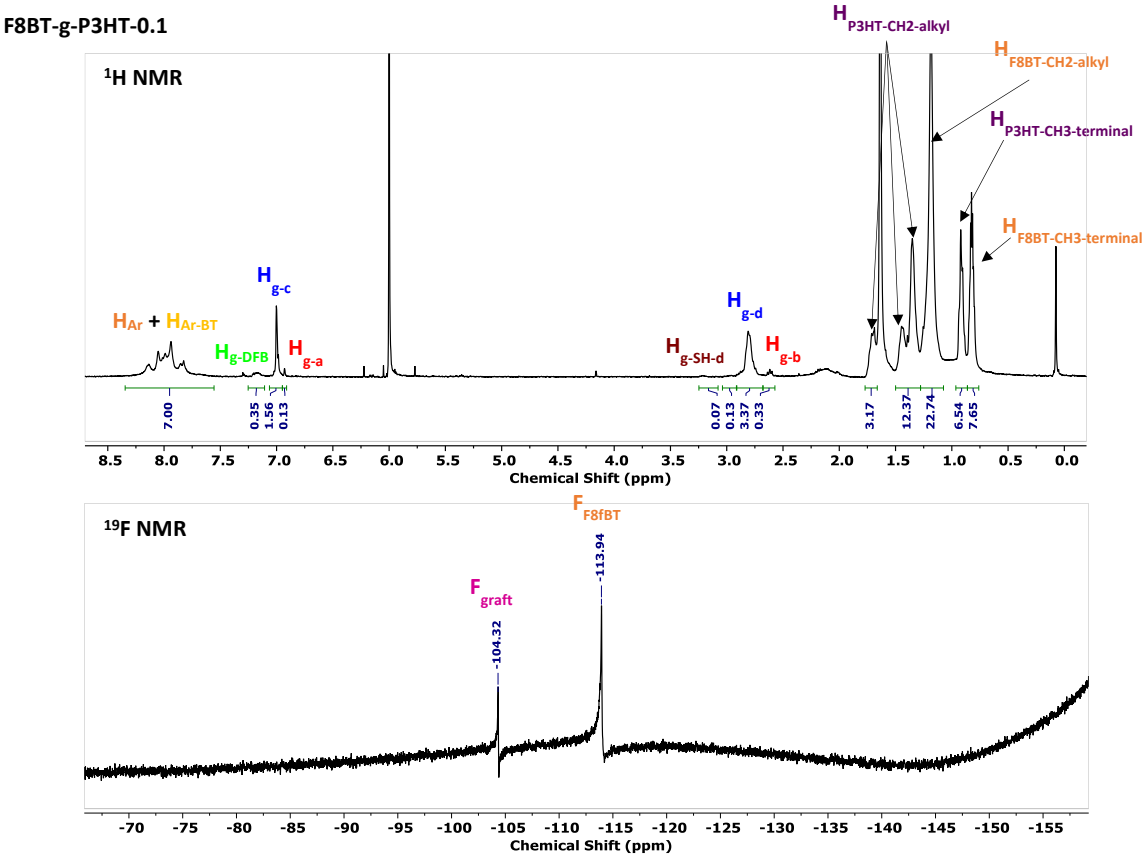


Figure S3.13. ^{1}H NMR (top) and ^{19}F NMR (bottom) of F8BT-g-P3HT-0.1.

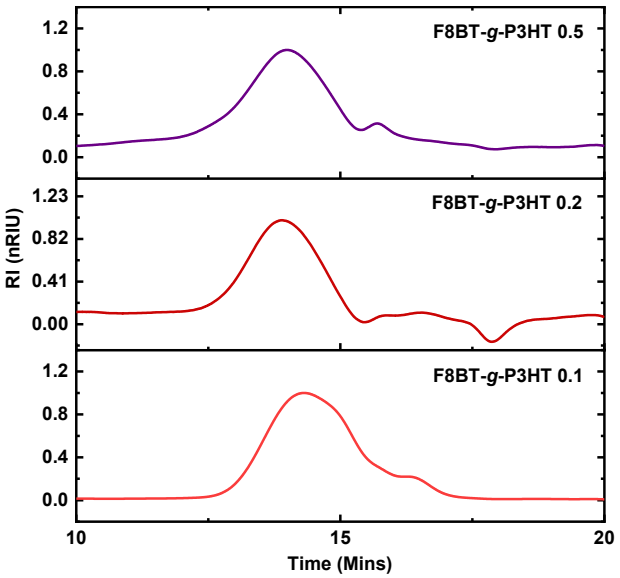


Figure S3.14. GPC trace of F8BT-g-P3HT-0.5, F8BT-g-P3HT-0.2 and F8BT-g-P3HT-0.1 post-purification.

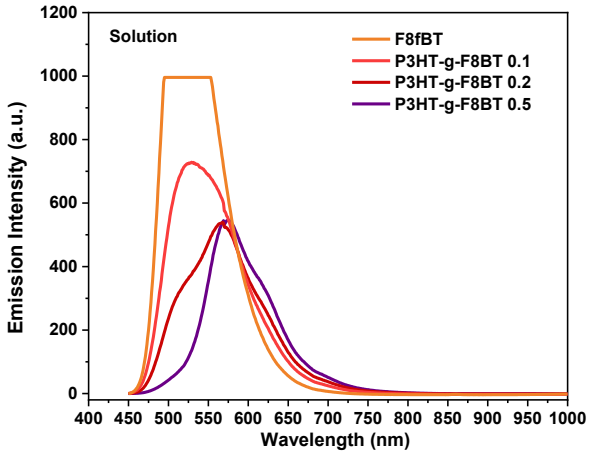


Figure S3.15. PL emission spectra for F8fBT, F8BT-g-P3HT-0.1, F8BT-g-P3HT-0.2 and F8BT-g-P3HT-0.5 in chlorobenzene (5 µM).

Table S3.1. Summary of fluorescence quenching of F8fBT, F8BT-g-P3HT 0.5, F8BT-g-P3HT 0.2 and F8BT-g-P3HT 0.1.

	$\lambda_{em,max}$ (nm)	Emission intensity (a.u.)
Polymer	**film**	**-**
F8fBT	520	>1000 (detector saturated)
F8BT-g-P3HT 0.1	529	724
F8BT-g-P3HT 0.2	566	539
F8BT-g-P3HT 0.5	575	546

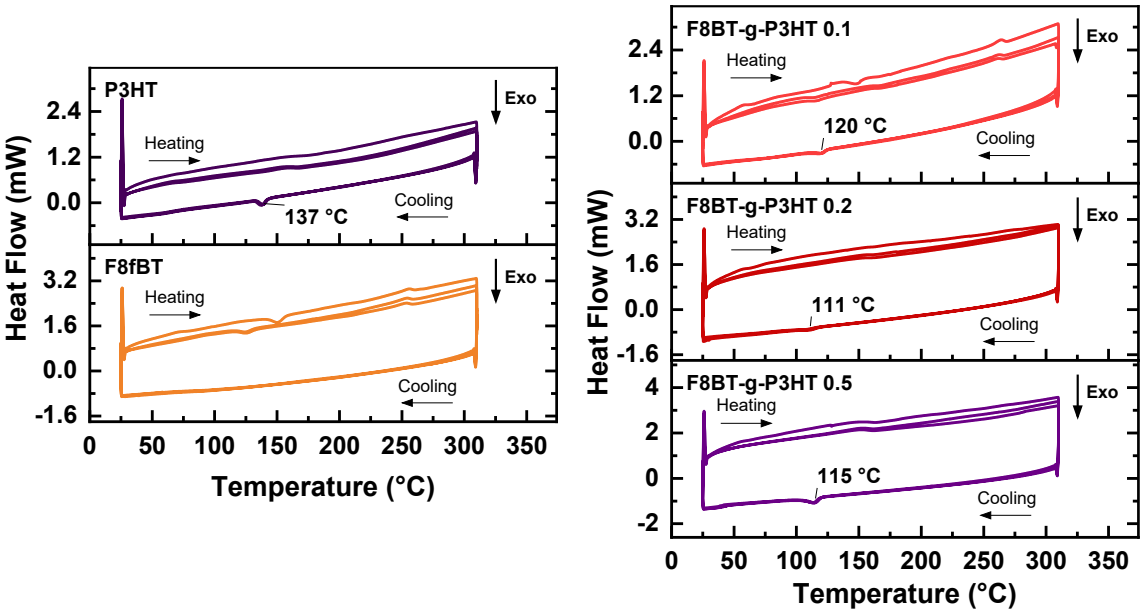


Figure S3.16. DSC traces of F8fBT, P3HT, F8BT-g-P3HT-0.5, F8BT-g-P3HT-0.2 and F8BT-g-P3HT-0.1.

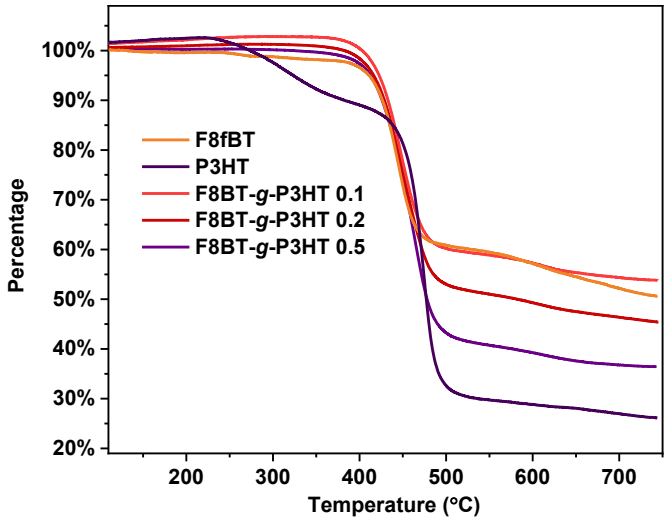


Figure S3.17. TGA curves of F8fBT, P3HT, F8BT-g-P3HT-0.5, F8BT-g-P3HT-0.2 and F8BT-g-P3HT-0.1.

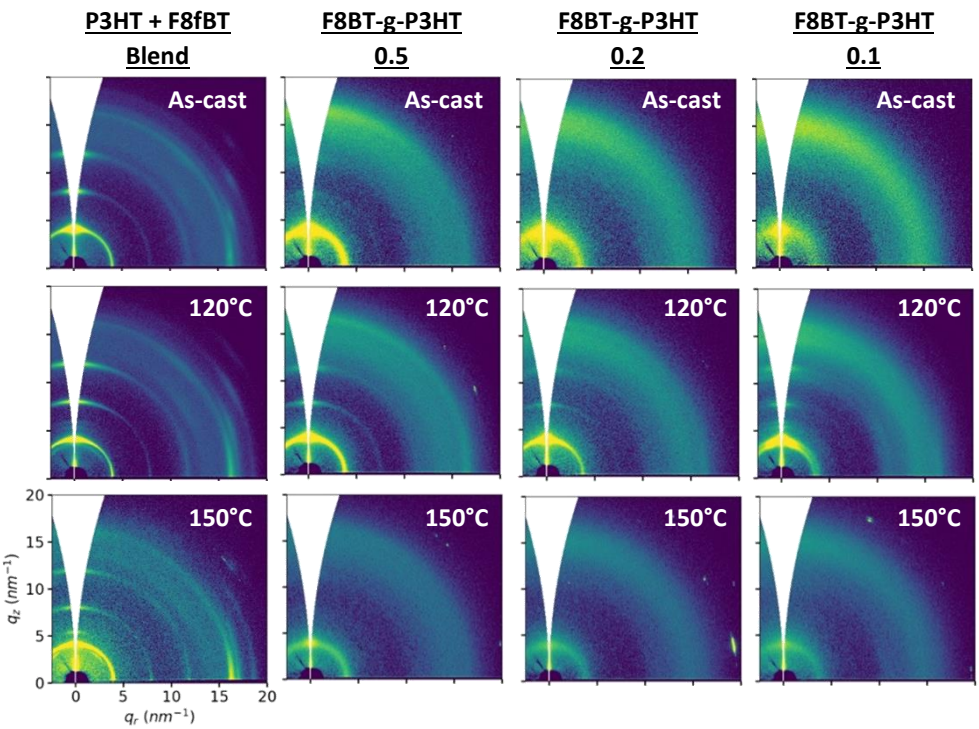


Figure S3.18. GIWAXS images of P3HT:F8fBT (blend), F8BT-g-P3HT-0.5, F8BT-g-P3HT-0.2 and F8BT-g-P3HT-0.1.films as-cast and annealed at 120 °C and 150 °C.

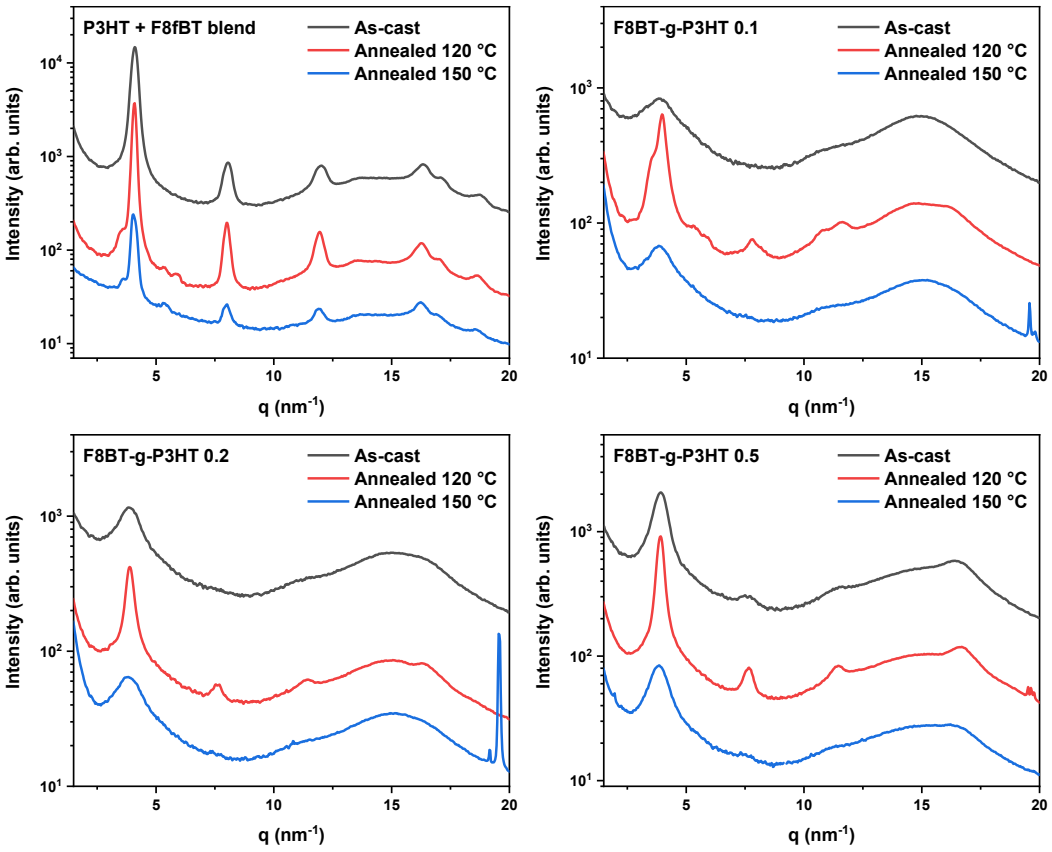


Figure S3.19. GIWAXS diffraction patterns (complete) for P3HT:F8fBT (blend), F8BT-g-P3HT-0.1, F8BT-g-P3HT-0.2 and F8BT-g-P3HT-0.5 films as-cast and annealed at 120 °C and 150 °C.

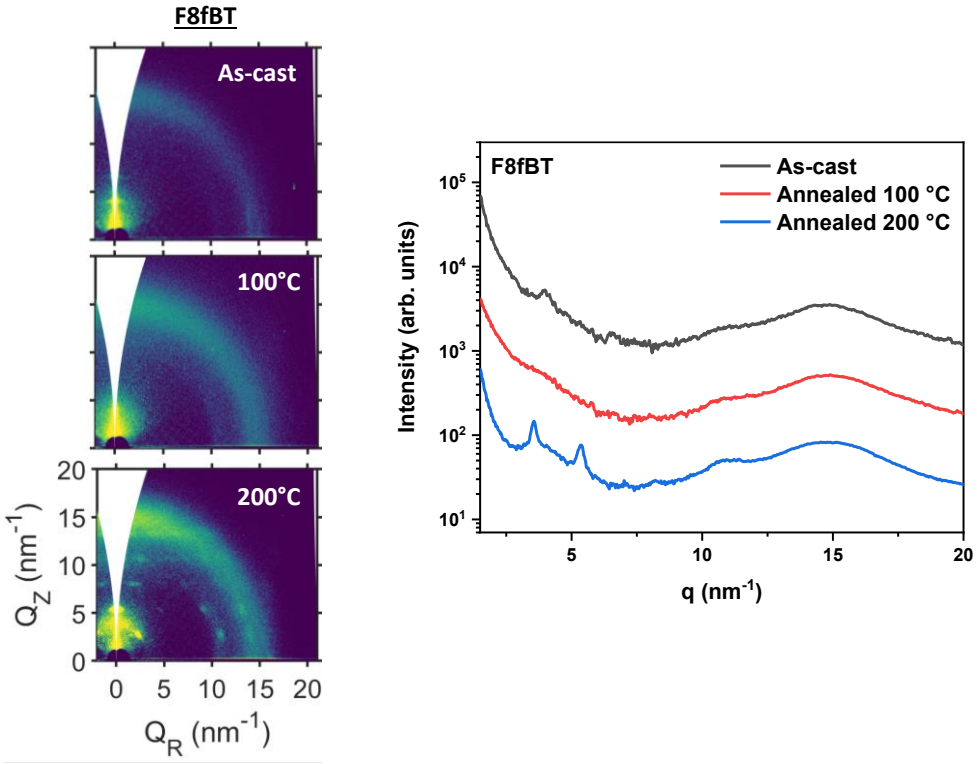


Figure S3.20. GIWAXS images of F8fBT films as-cast and annealed at 100 °C and 200 °C (left) and GIWAXS diffraction patterns (complete) for F8fBT films as-cast and annealed at 100 °C and 200 °C.

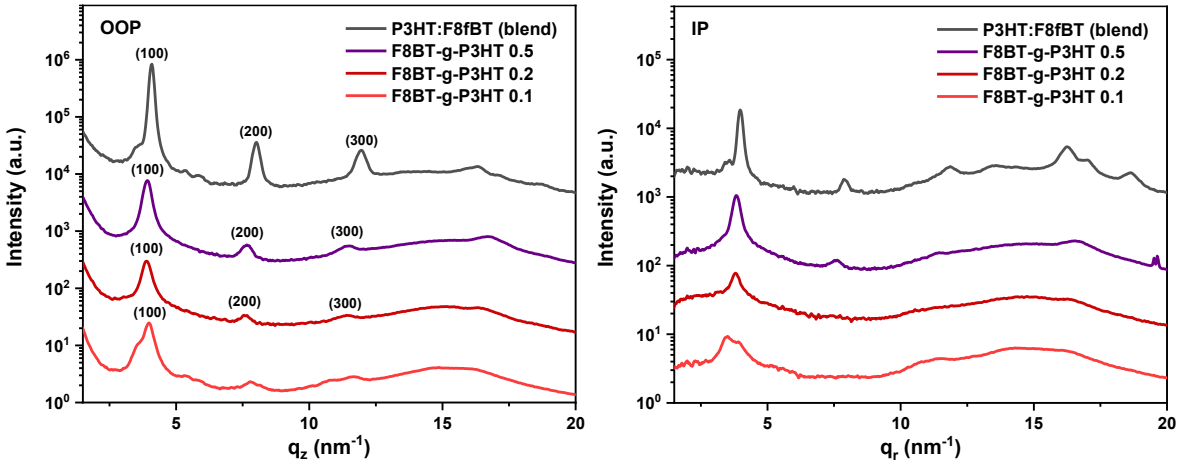


Figure S3.21. GIWAXS diffraction patterns, OOP (left) and IP (right) for P3HT:F8fBT blend, F8BT-g-P3HT 0.5, F8BT-g-P3HT 0.2 and F8BT-g-P3HT 0.1 films annealed at 120 °C.

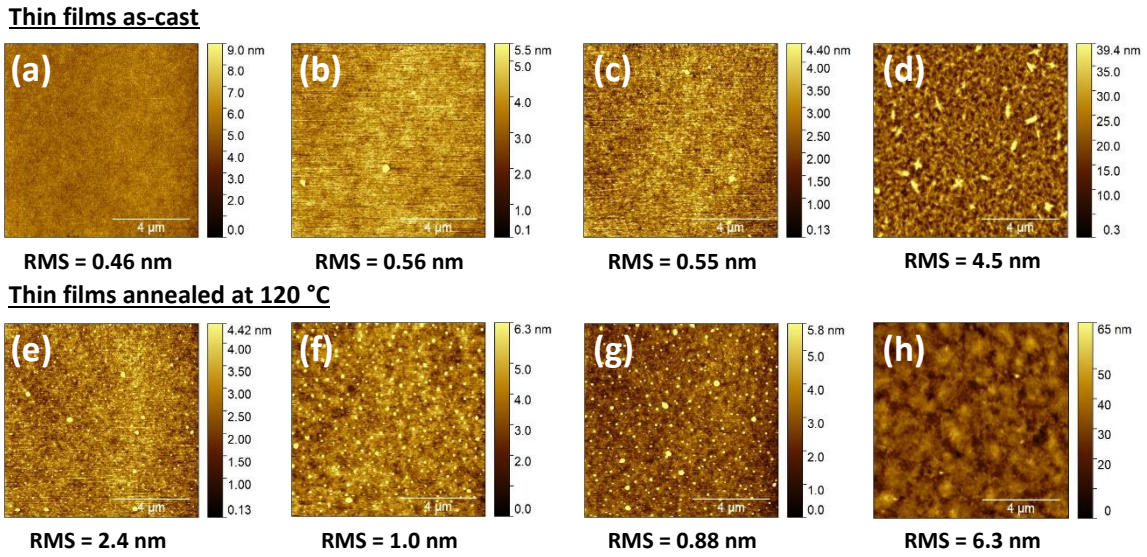


Figure S3.22. AFM images (10x10 µm) of P3HT:F8fBT blend, F8BT-g-P3HT 0.1, F8BT-g-P3HT 0.2 and F8BT-g-P3HT 0.5 thin films, from spin casting on Si wafer. The films were imaged as-cast and after thermal annealing (at 120 °C).

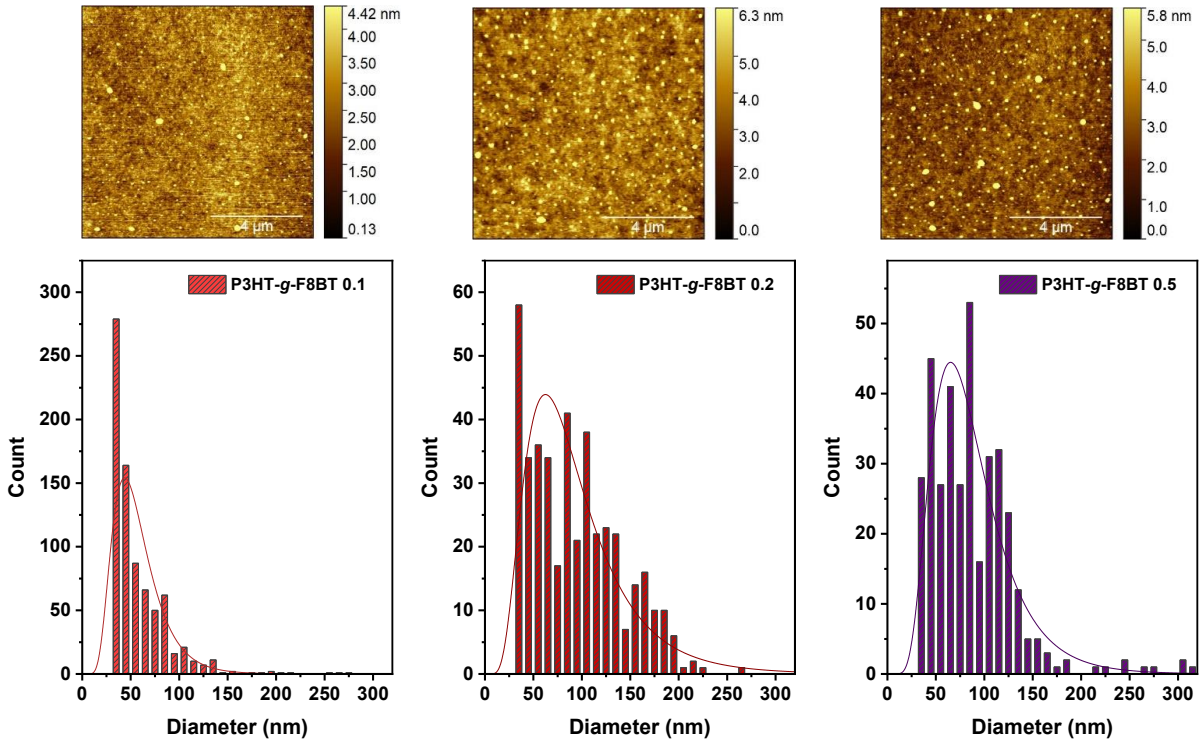


Figure S3.23. AFM images (10x10 µm) and corresponding nanosized aggregate sizes of F8BT-g-P3HT 0.5, F8BT-g-P3HT 0.2 and F8BT-g-P3HT 0.1 thin film annealed at 120 °C.

4 Chapter 4 Appendix:

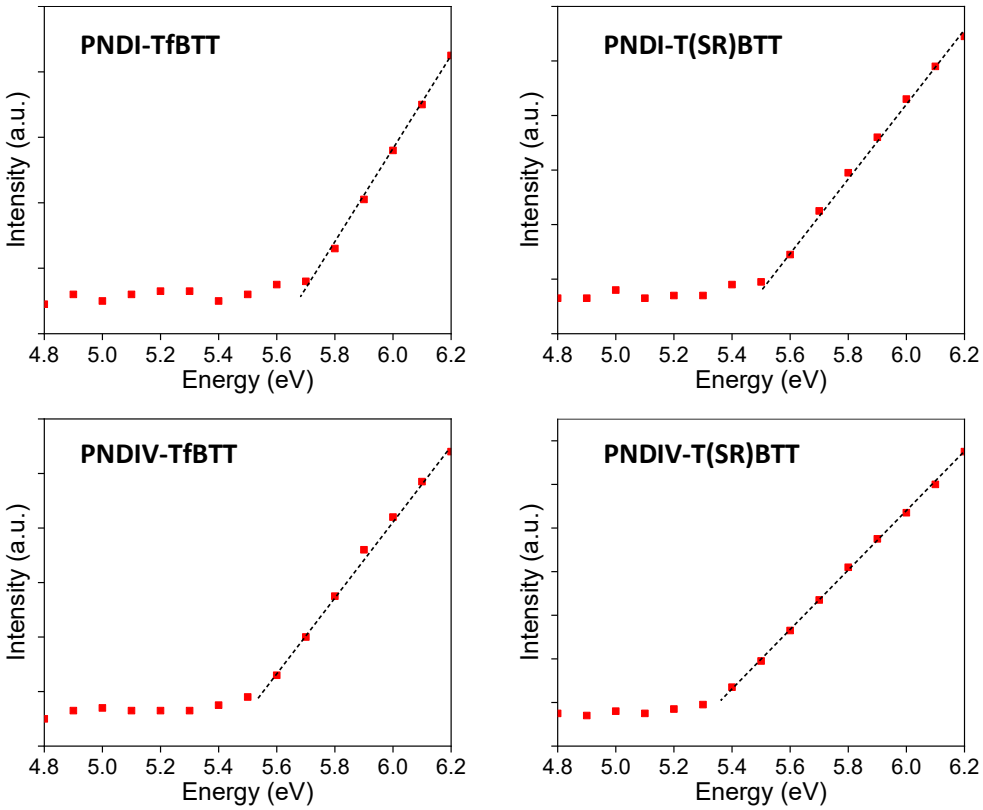


Figure S4.1. PESA measurements for PNDI-TfBTT, PNDIV-TfBTT, PNDI-T(SR)BTT and PNDIV-T(SR)BTT.

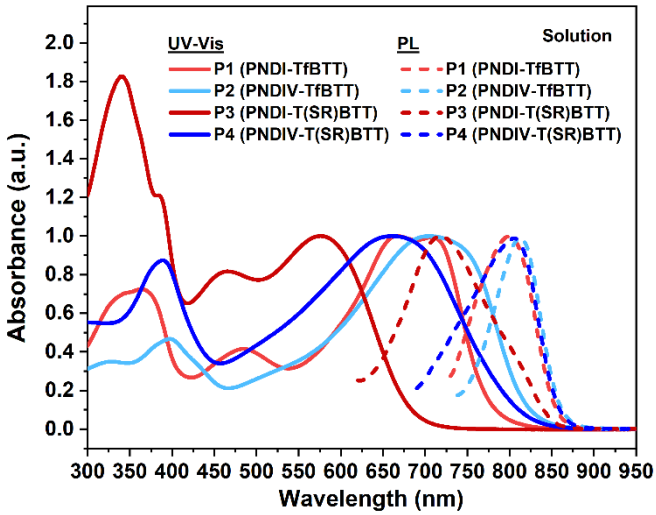


Figure S4.2. UV-Vis absorption and PL emission for PNDI-TfBTT, PNDIV-TfBTT, PNDI-T(SR)BTT and PNDIV-T(SR)BTT.

Table S4.1. Summary of HOMO and LUMO energy levels and dihedral angles within energy minimised structures of PNDI-TfBTT, PNDIV-TfBTT, PNDI-T(SR)BTT and PNDIV-T(SR)BTT calculated using DFT at the B3LYP/6.31G* level.

	HOMO (eV)	LUMO (eV)	Dihedral angle (L→R)	Notes
PNDI-TfBTT	-5.55	-3.51	[1]-41.98 (T), [2] -47.64 (B) [3] 10.03 (T), [4] 7.87 (B) [5] 4.13 (T), [6] 2.50 (B) [7] -41.29 (T), [8] -46.80 (B)	F on the left-hand side of BT
PNDI-T(SR)BTT	-5.54	-3.45	[1] -41.99 (T), [2] -48.29 (B) [3] 16.98 (T), [4] 14.38 (B) [5] 41.79 (T), [6] 39.39 (B) [7] -40.82 (T), [8] -47.88 (B)	SR on the left-hand side of BT
PNDIV-TfBTT	-5.40	-3.51	[1] 18.80 (T), [2] -0.51 (B) [3] 0.38 (T), [4] 0.35 (B) [5] 0.25 (T), [6] 0.25 (B) [7] -0.35 (B), [8] 18.08 (T)	F on the left-hand side of BT
PNDIV-T(SR)BTT	-5.41	-3.43	[1] 18.45 (T), [2] 0.38 (B) [3] -5.11 (T), [4] -4.77 (B) [5] 38.27 (T), [6] 37.53 (B) [7] -4.33 (B), [8] 19.88 (T)	SR on the left-hand side of BT

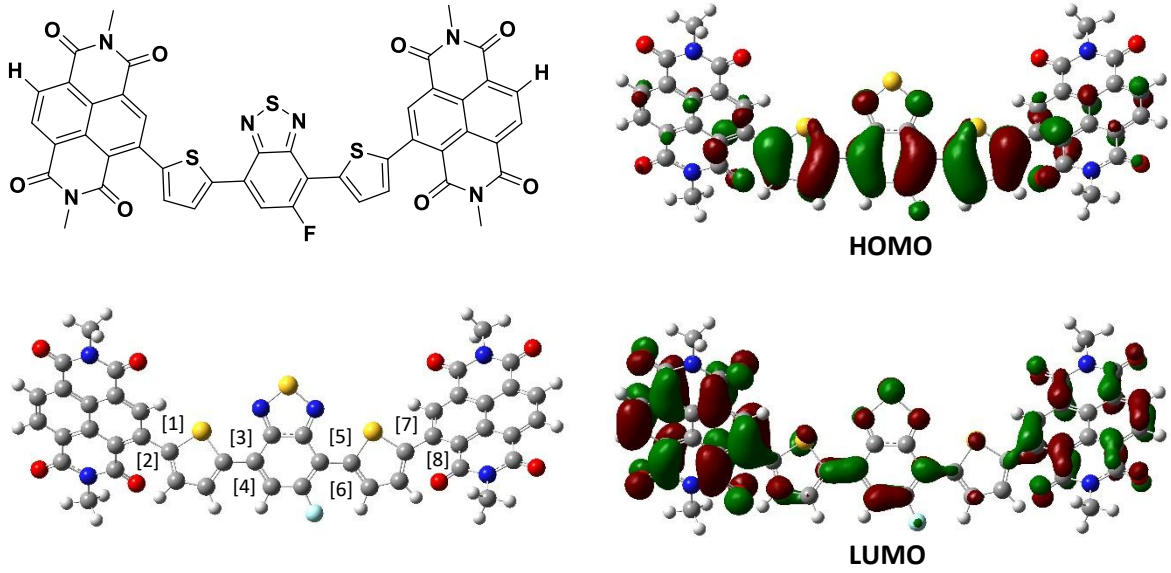


Figure S4.3. (a) Molecular model used for DFT calculations. DFT optimisation of a model of PNDI-TfBTT at the B3LYP/6-31G(d,p) level showing (b) overall backbone geometry (c) HOMO distribution along backbone (d) LUMO distribution along backbone.

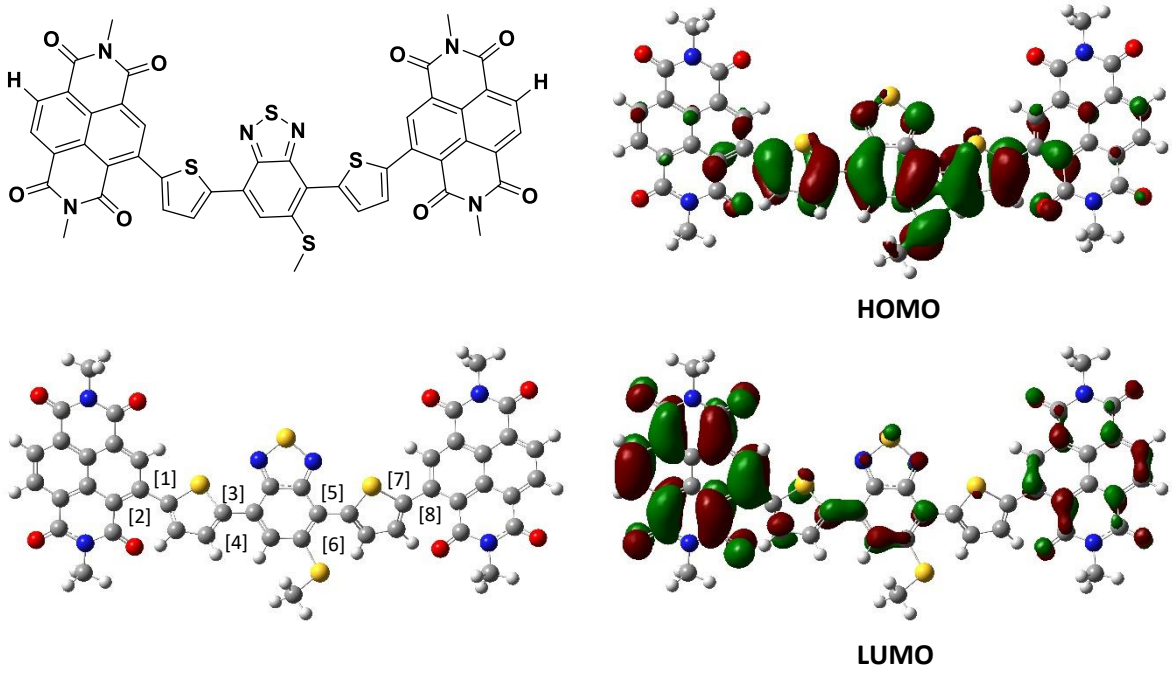


Figure S4.4. (a) Molecular model used for DFT calculations. DFT optimisation of a model of PNDI-T(SR)BTT at the B3LYP/6-31G(d,p) level showing (b) overall backbone geometry (c) HOMO distribution along backbone (d) LUMO distribution along backbone.

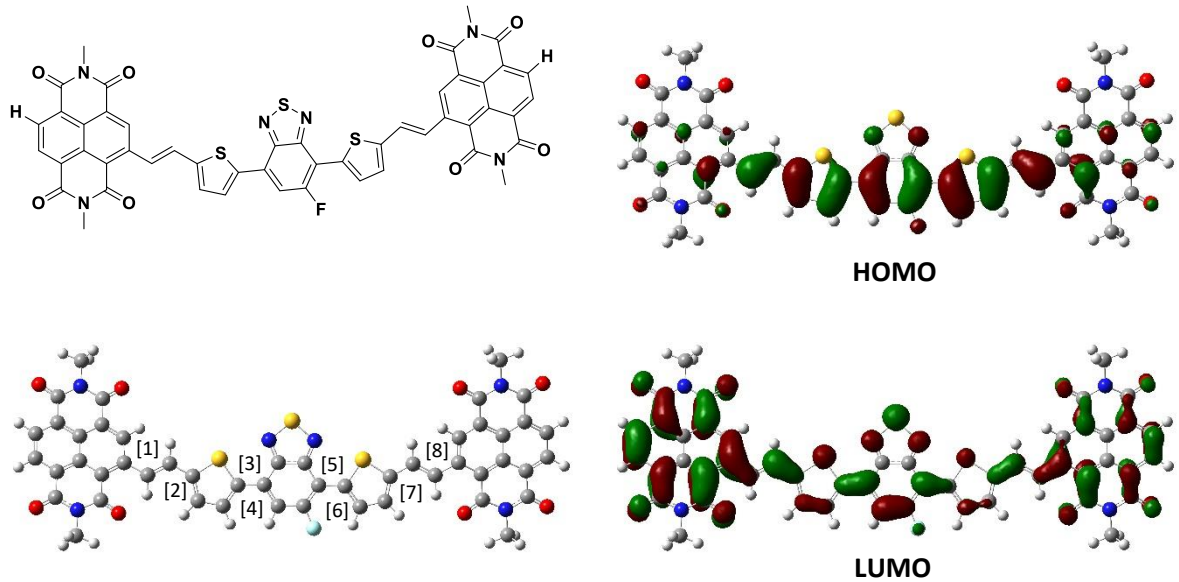


Figure S4.5. (a) Molecular model used for DFT calculations. DFT optimisation of a model of PNDIV-TfBTT at the B3LYP/6-31G(d,p) level showing (b) overall backbone geometry (c) HOMO distribution along backbone (d) LUMO distribution along backbone.

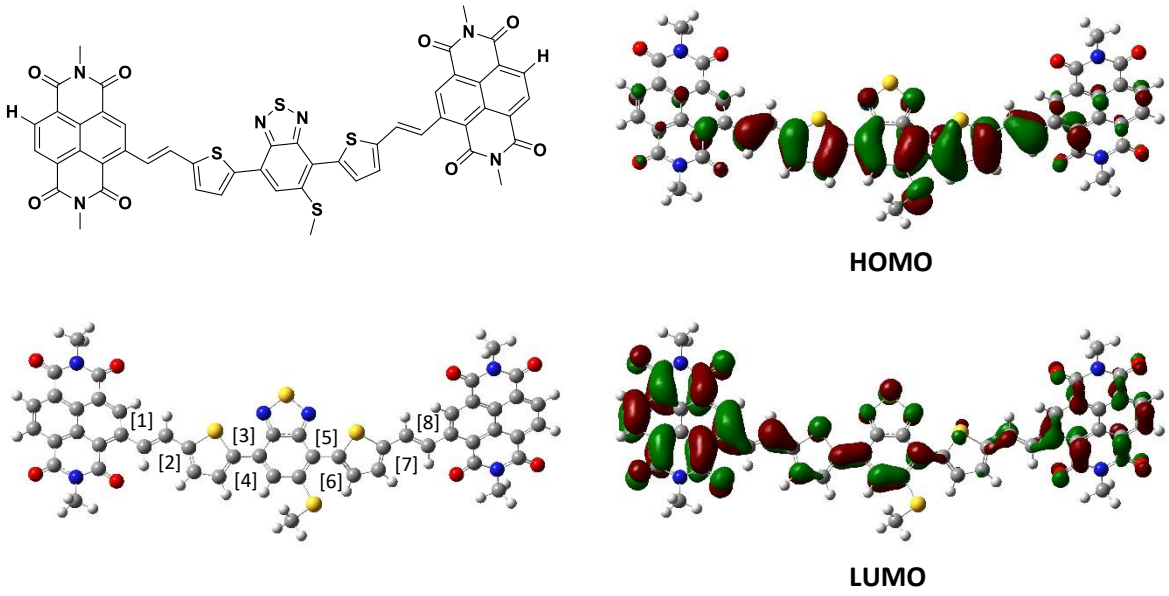


Figure S4.6. (a) Molecular model used for DFT calculations. DFT optimisation of a model of PNDIV-T(SR)BTT at the B3LYP/6-31G(d,p) level showing (b) overall backbone geometry (c) HOMO distribution along backbone (d) LUMO distribution along backbone.

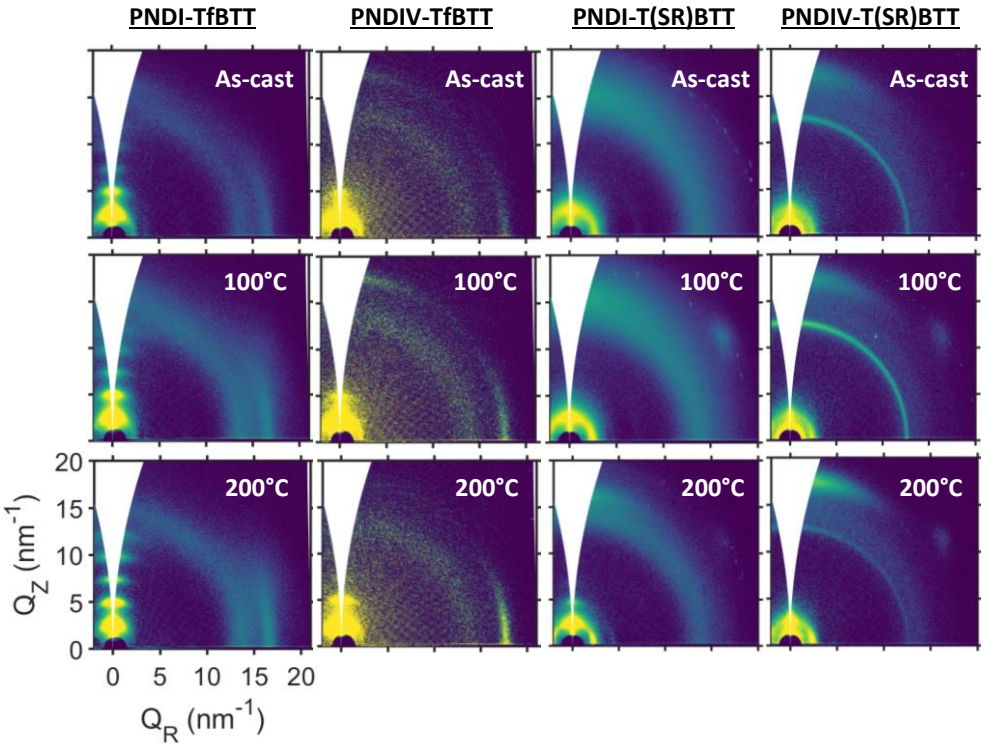


Figure S4.7. GIWAXS images of PNDI-TfBTT, PNDIV-TfBTT, PNDI-T(SR)BTT and PNDIV-T(SR)BTT films as-cast and annealed at 100 °C and 200 °C.

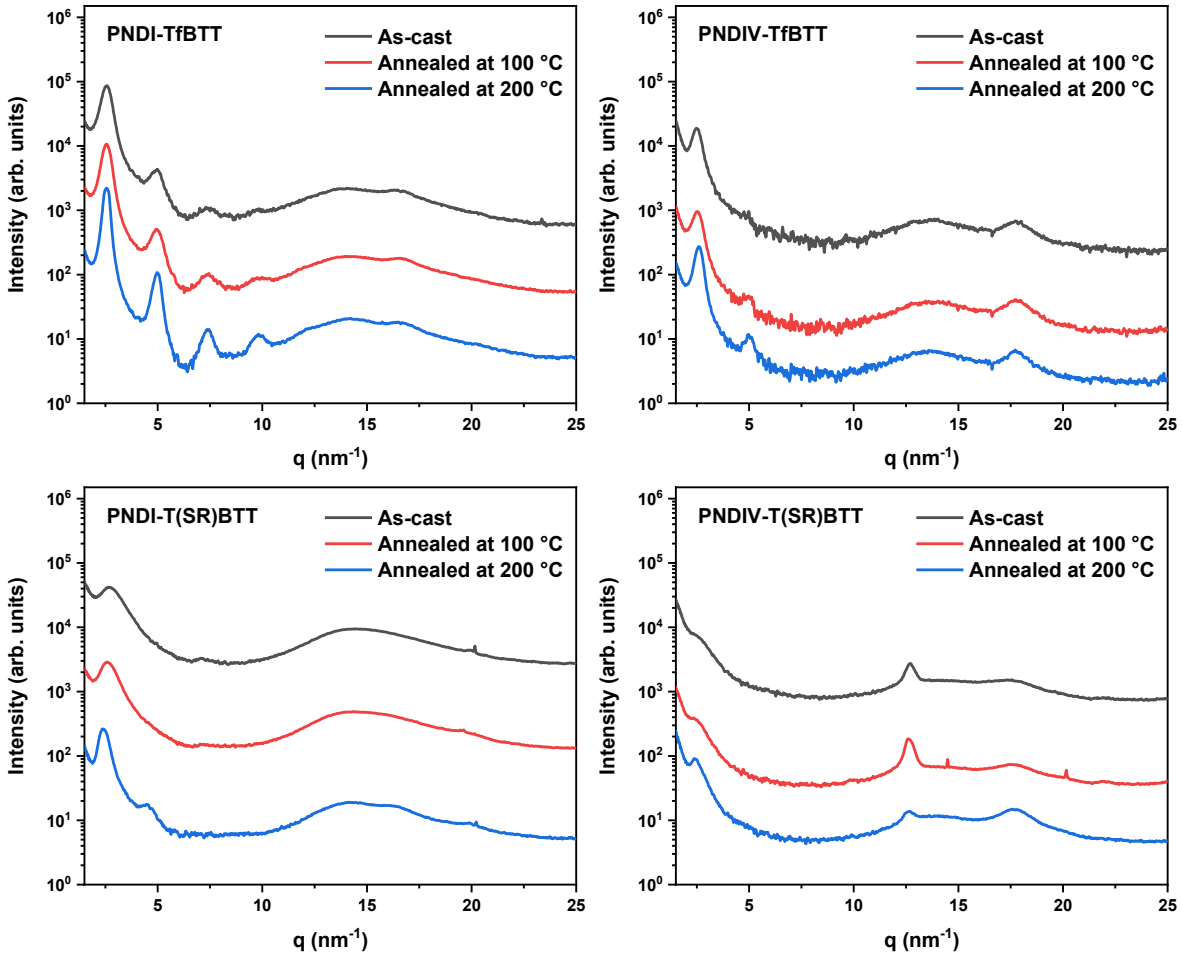


Figure S4.8. GIWAXS diffraction patterns for PNDI-TfBTT, PNDIV-TfBTT, PNDI-T(SR)BTT and PNDIV-T(SR)BTT films as-cast and annealed at 100 °C and 200 °C.

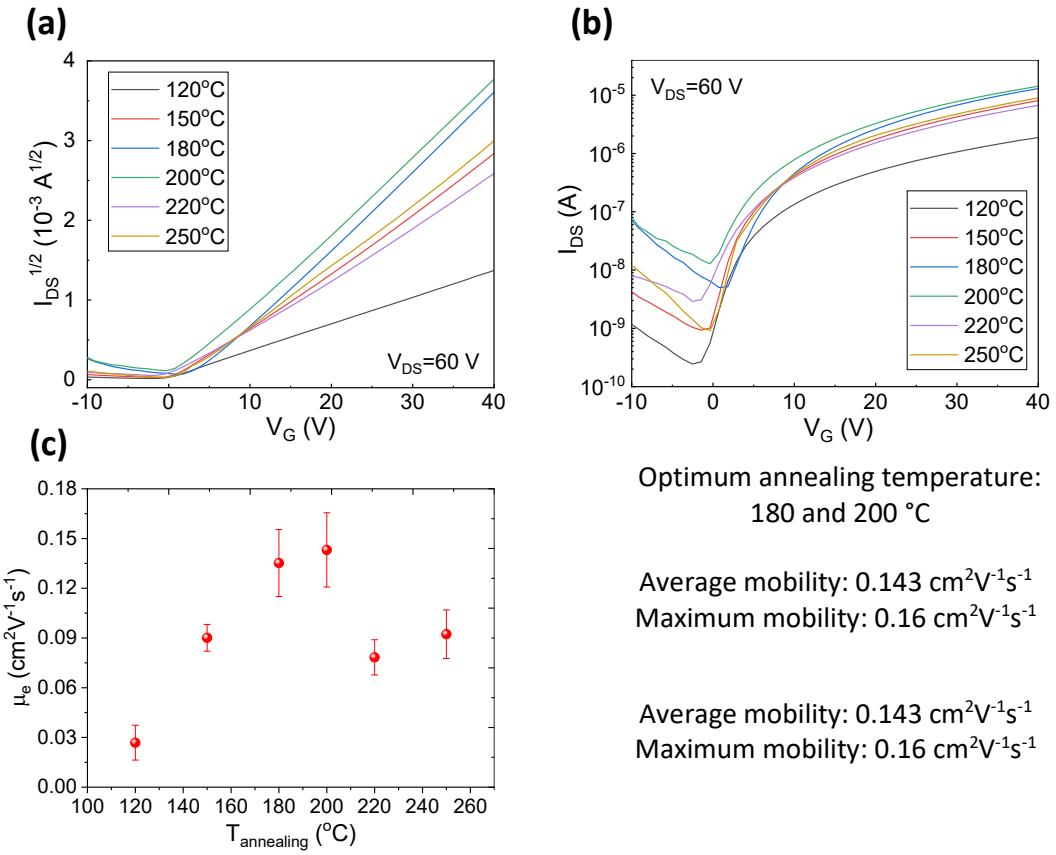


Figure S4.9. Transfer (a,b) characteristics of PNDI-TfBTT OTFT device. (c) Electron mobility vs. annealing temperature of polymer thin film.

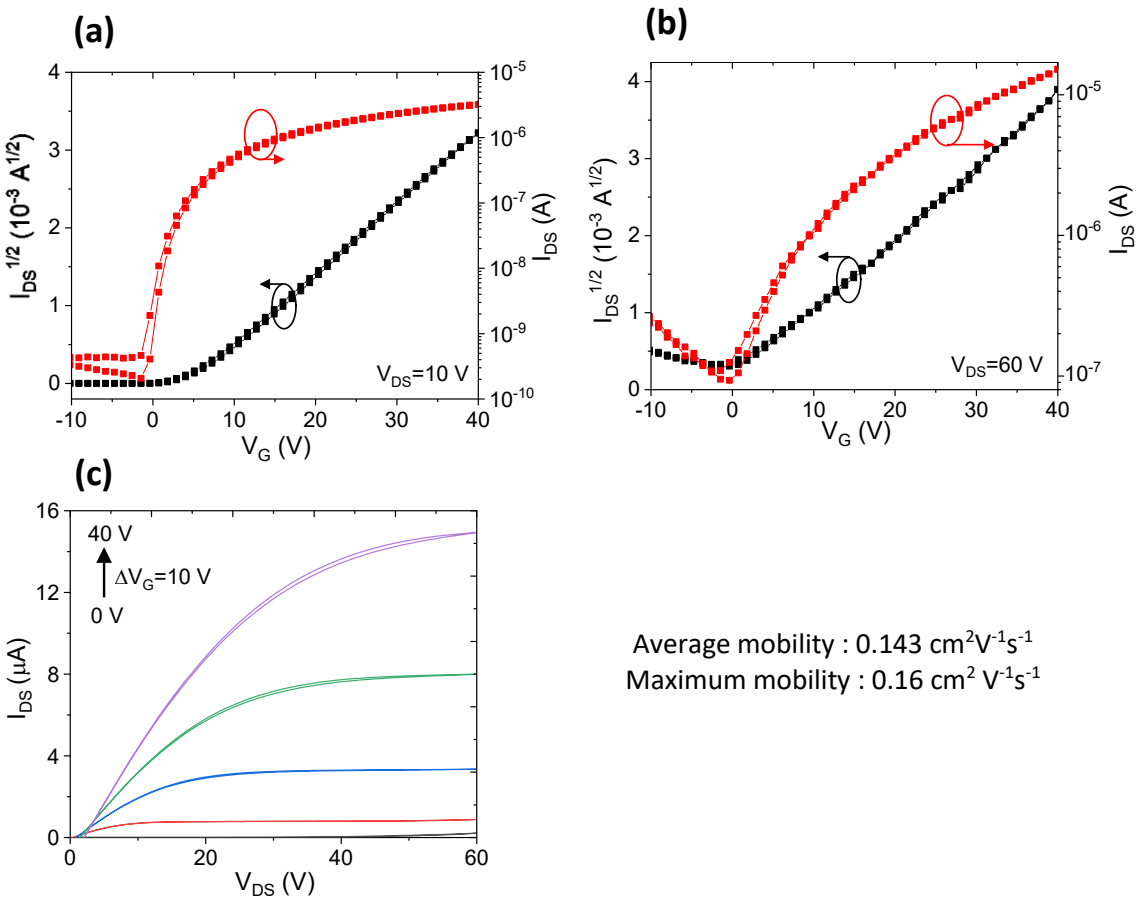
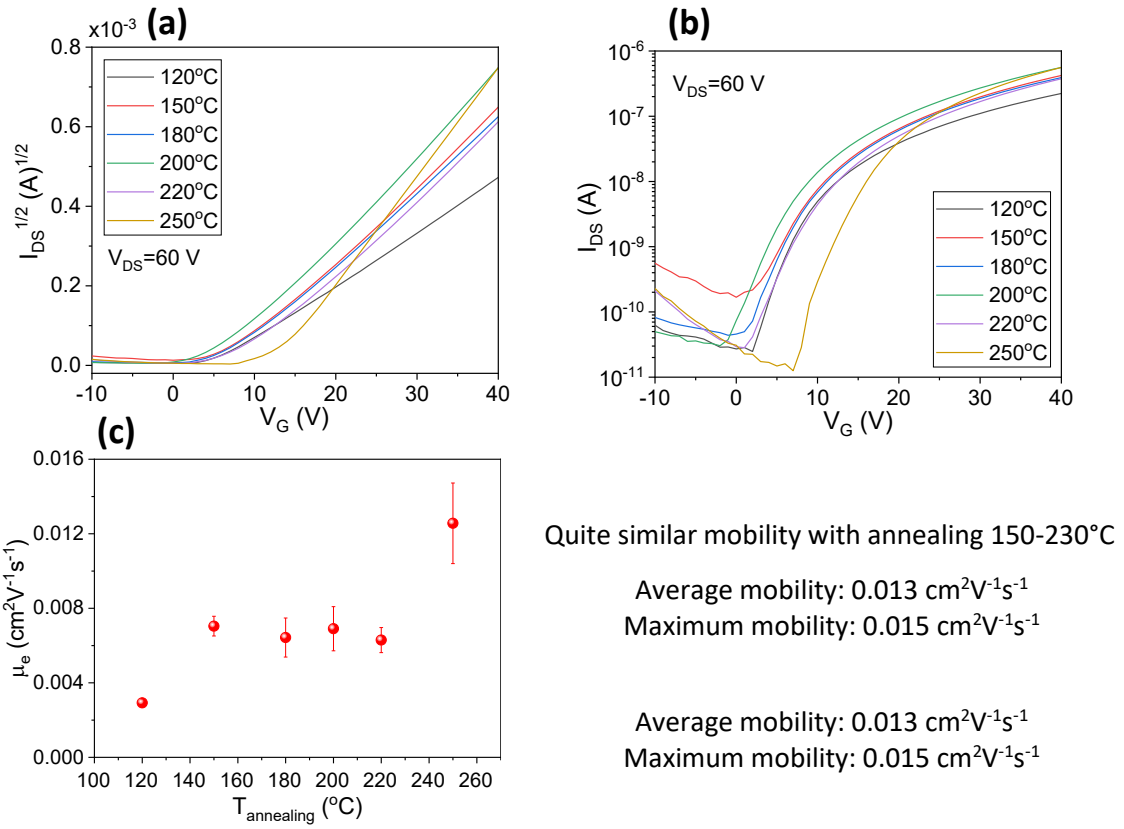


Figure S4.10. Transfer (a,b) and output (c) characteristics of PNDI-TfBTT OTFT device annealed at 200 °C.



Quite similar mobility with annealing 150-230°C

Average mobility: 0.013 $cm^2V^{-1}s^{-1}$
Maximum mobility: 0.015 $cm^2V^{-1}s^{-1}$

Average mobility: 0.013 $cm^2V^{-1}s^{-1}$
Maximum mobility: 0.015 $cm^2V^{-1}s^{-1}$

Figure S4.11. Transfer (a,b) characteristics of PNDI-T(SR)BTT OTFT device. (c) Electron mobility vs. annealing temperature of polymer thin film.

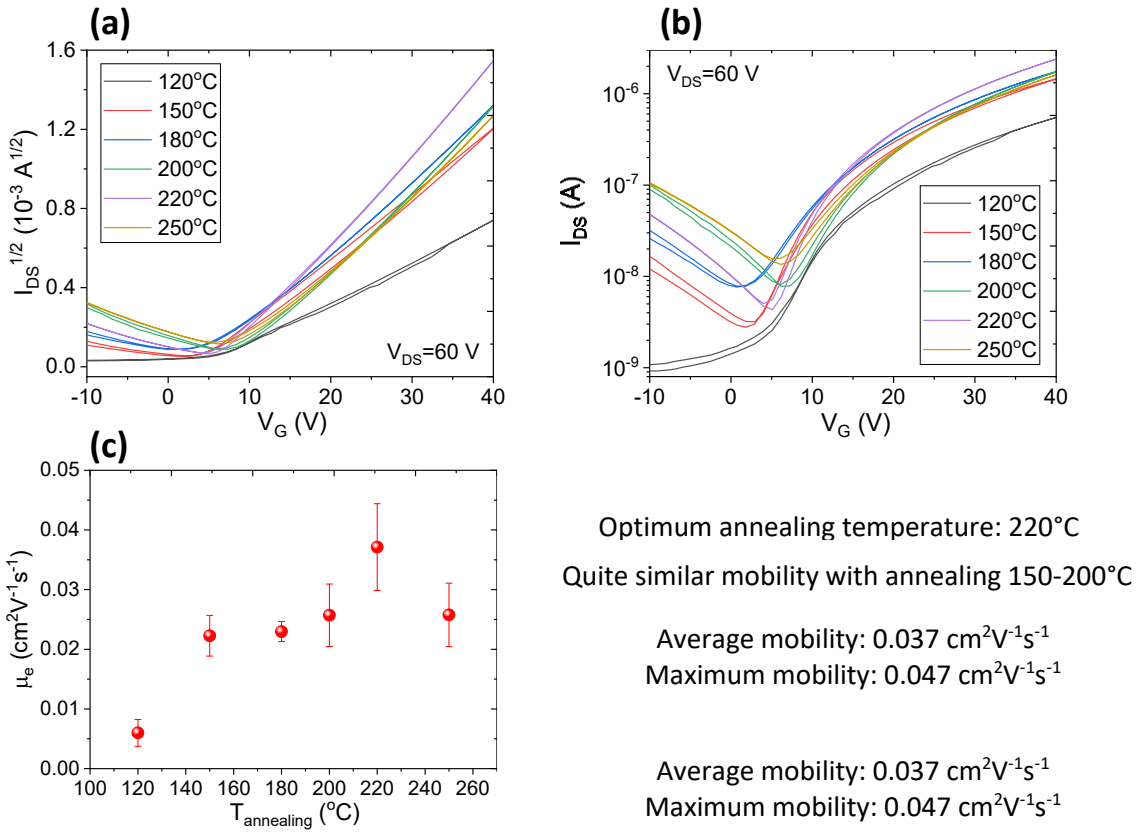


Figure S4.12. Transfer (a,b) characteristics of PNDIV-TfBTT OTFT device. (c) Electron mobility vs. annealing temperature of polymer thin film.

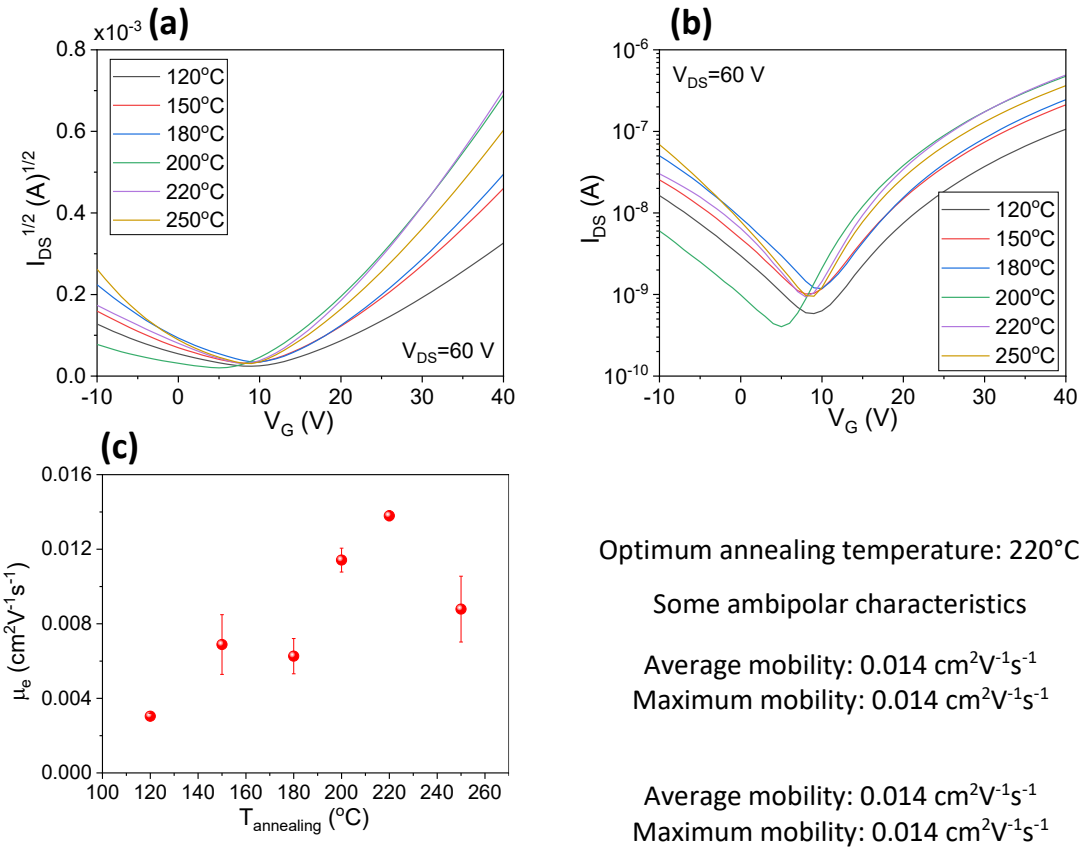


Figure S4.13. Transfer (a,b) characteristics of PNDIV-T(SR)BTT OTFT device. (c) Electron mobility vs. annealing temperature of polymer thin film.

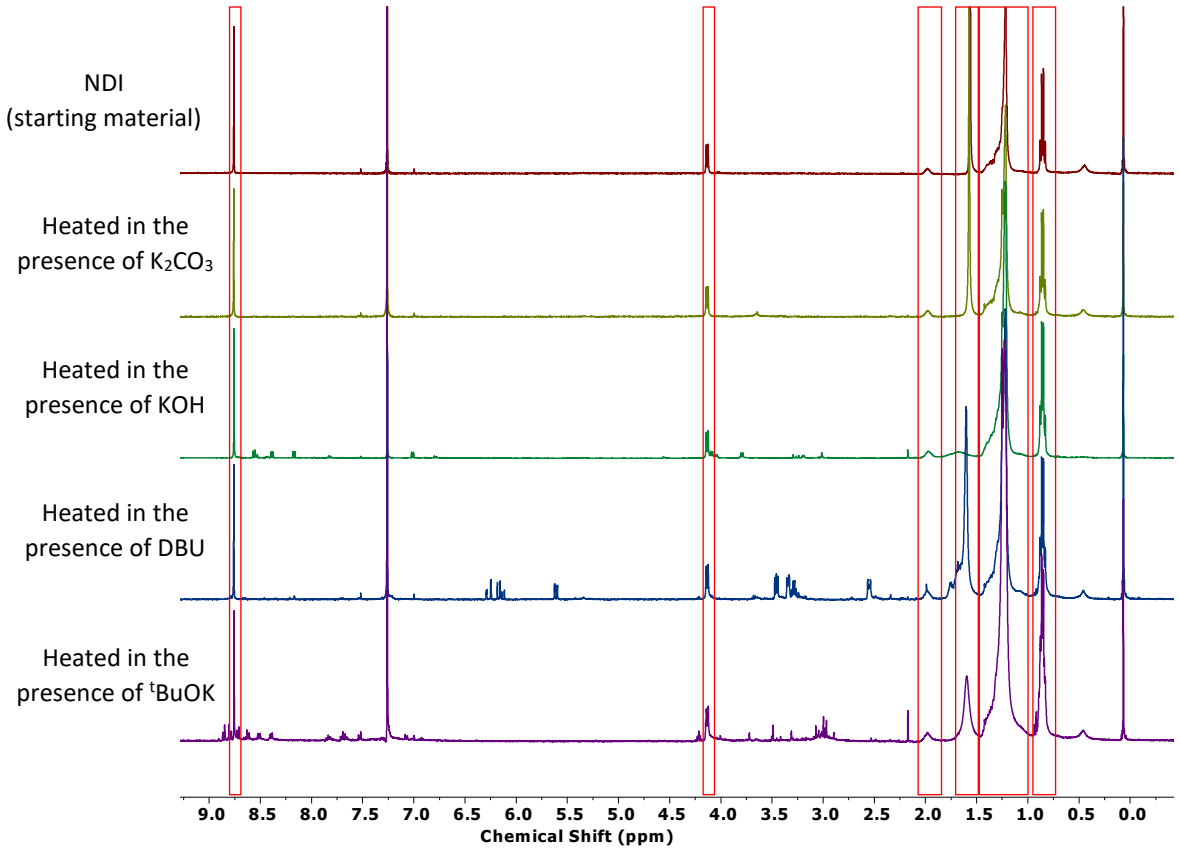


Figure S4.14. ^{1}H NMR of 2,7-bis(2-decyltetradecyl)benzo[lmn][3,8]phenanthroline-1,3,6,8(2H,7H)-tetraone (NDI-2DT), where peaks assigned to NDI are highlighted in red. (a) NDI before exposure to S_NAr reaction conditions. (b-e) NDI after exposure to S_NAr reaaction conditions with K_2CO_3, KOH, DBU, ^{t}BuOK respectively.

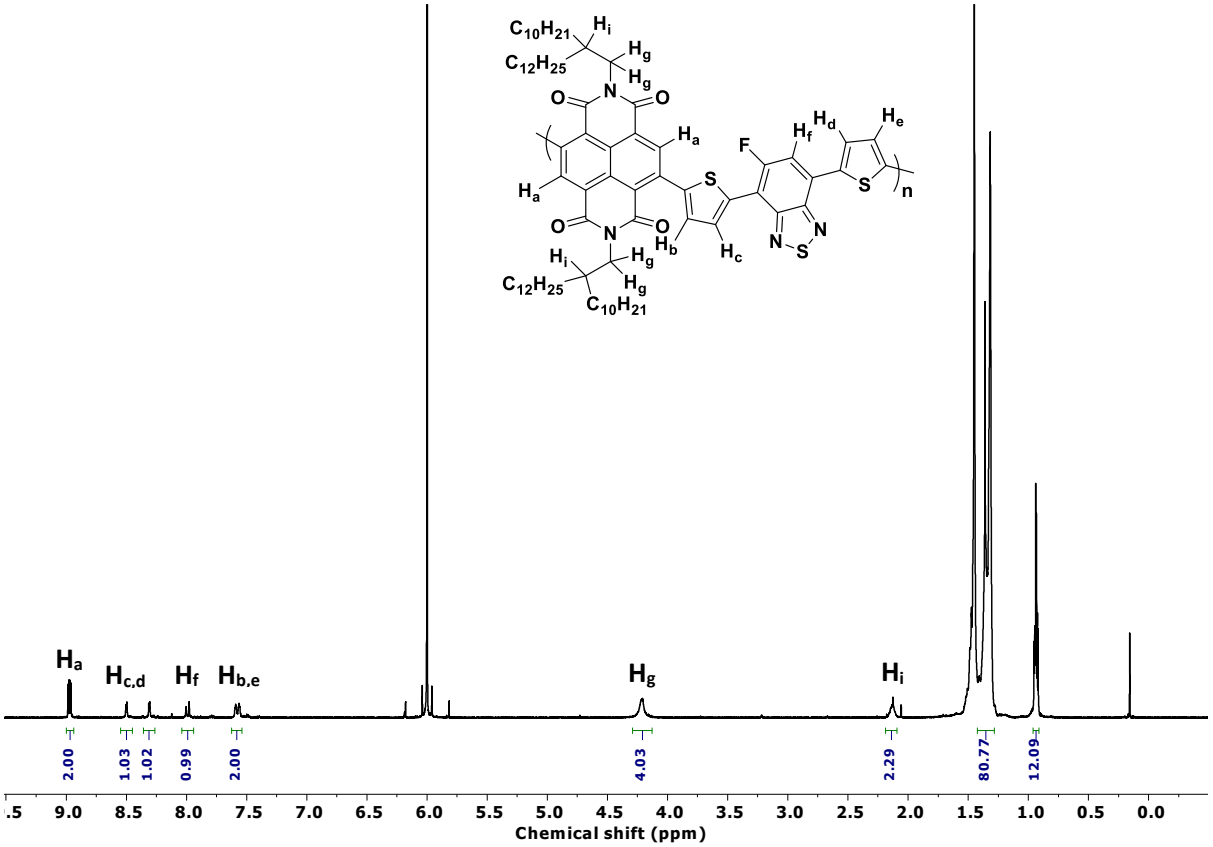


Figure S4.15. ^{1}H NMR of PNDI-TfBTT.

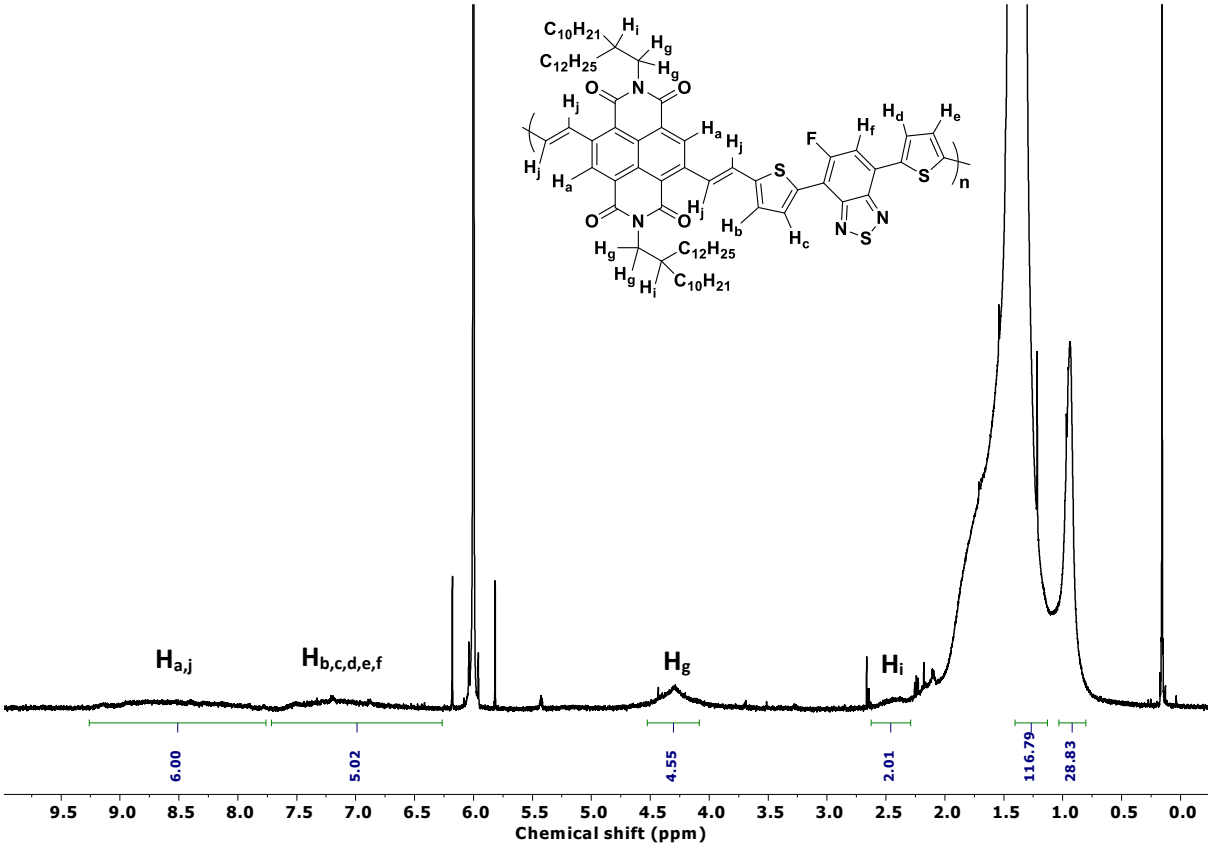


Figure S4.16. ^{1}H NMR of PNDIV-TfBTT.

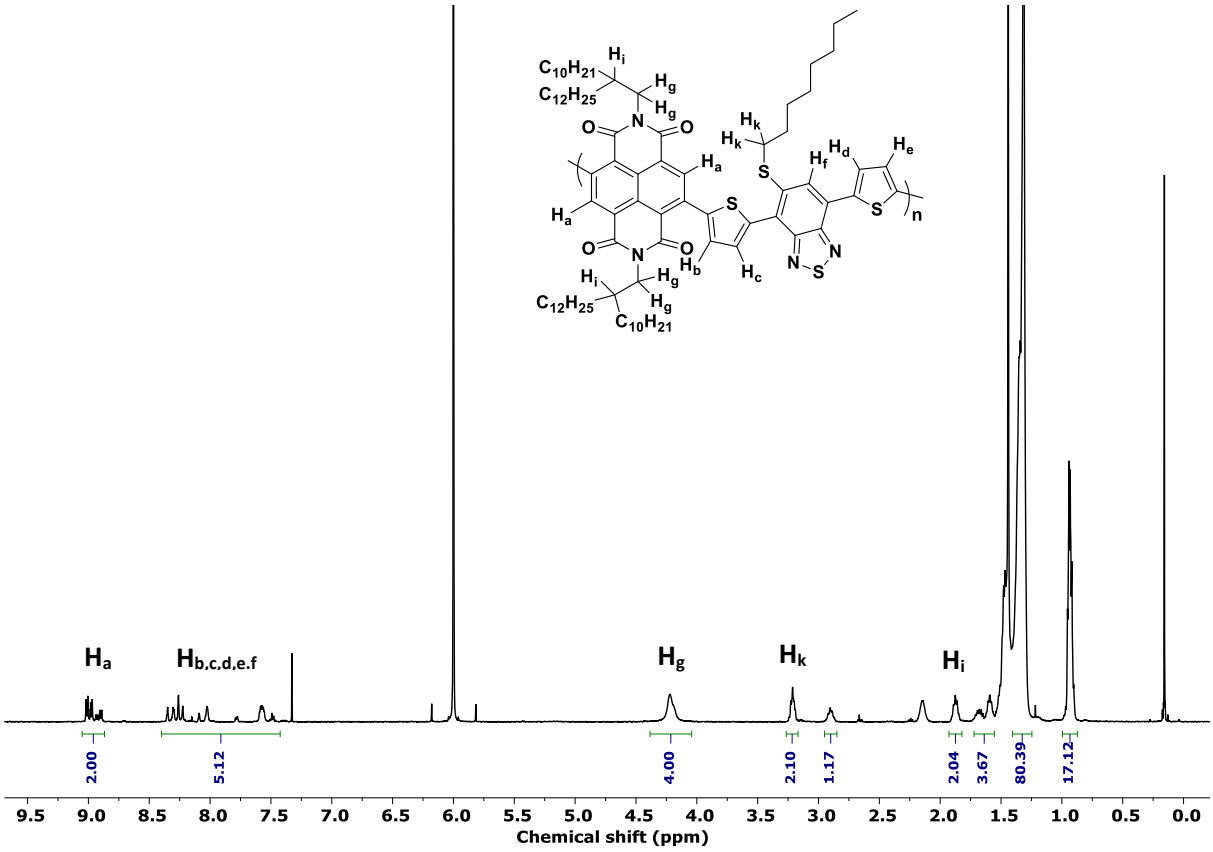


Figure S4.17. ^{1}H NMR of PNDI-T(SR)BTT.

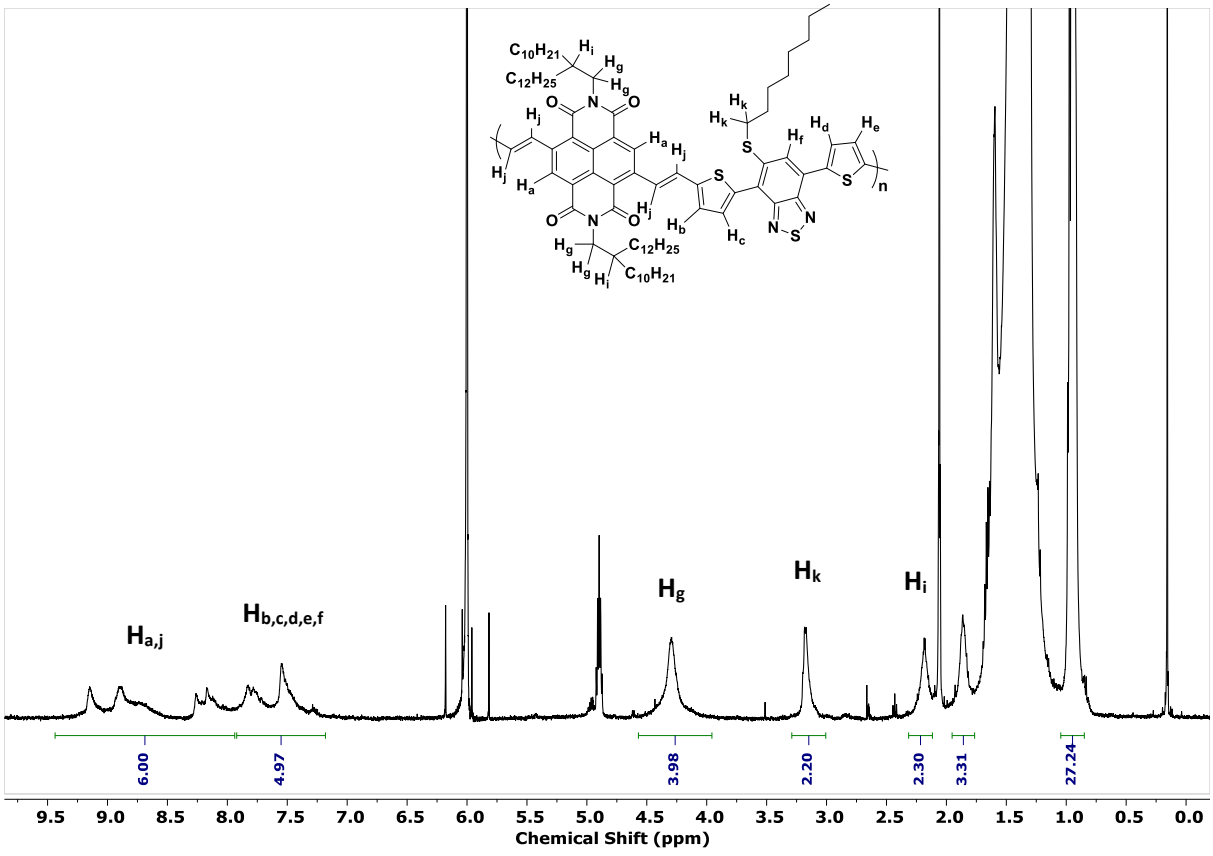


Figure S4.18. ^{1}H NMR of PNDIV-T(SR)BTT.

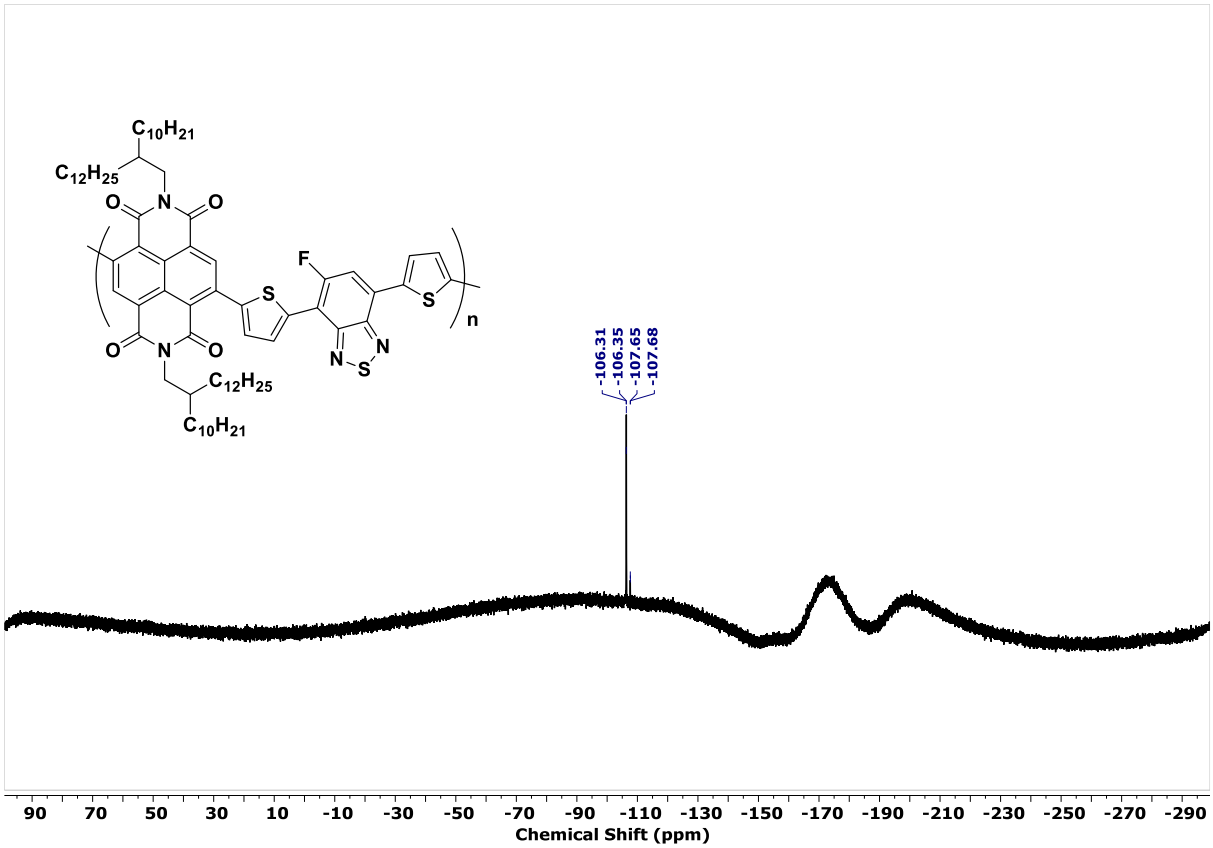


Figure S4.19. ^{19}F NMR of PNDI-TfBTT.

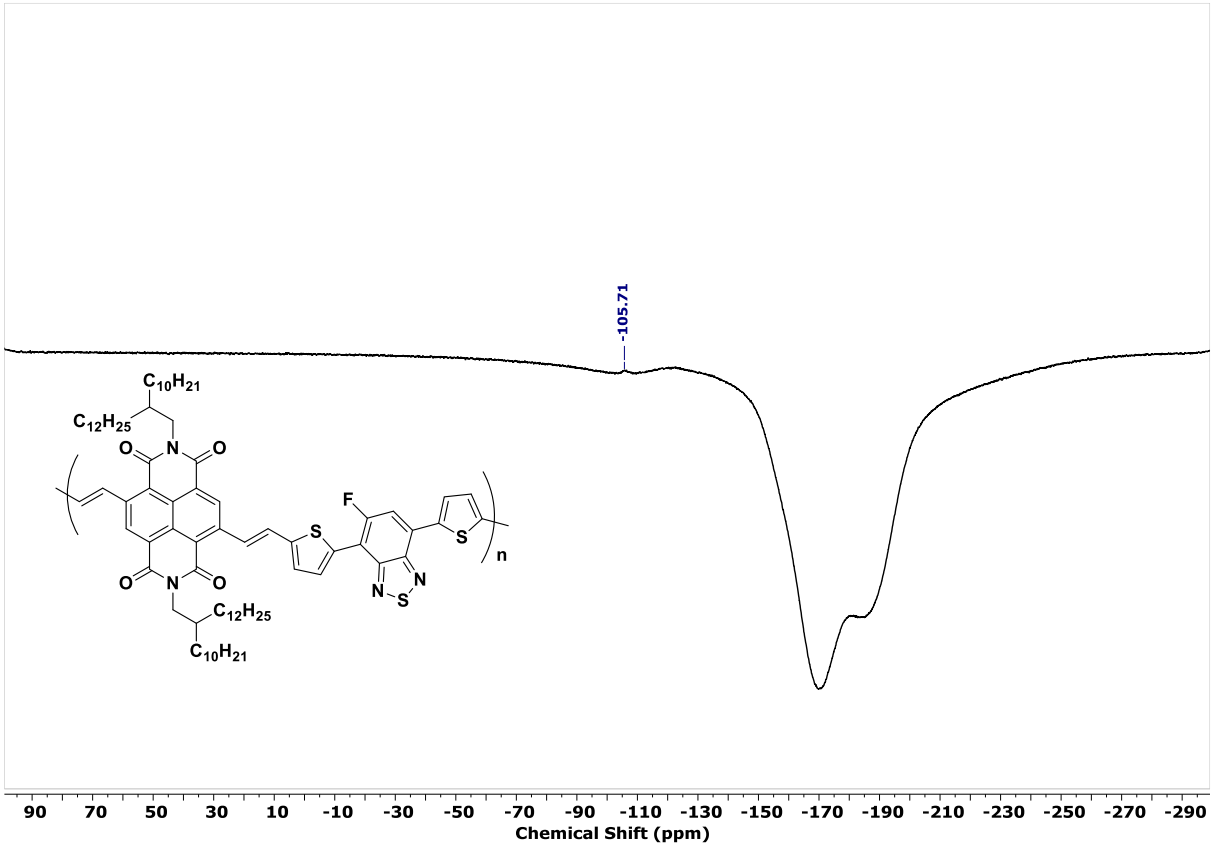


Figure S4.20. ^{19}F NMR of PNDIV-TfBTT.

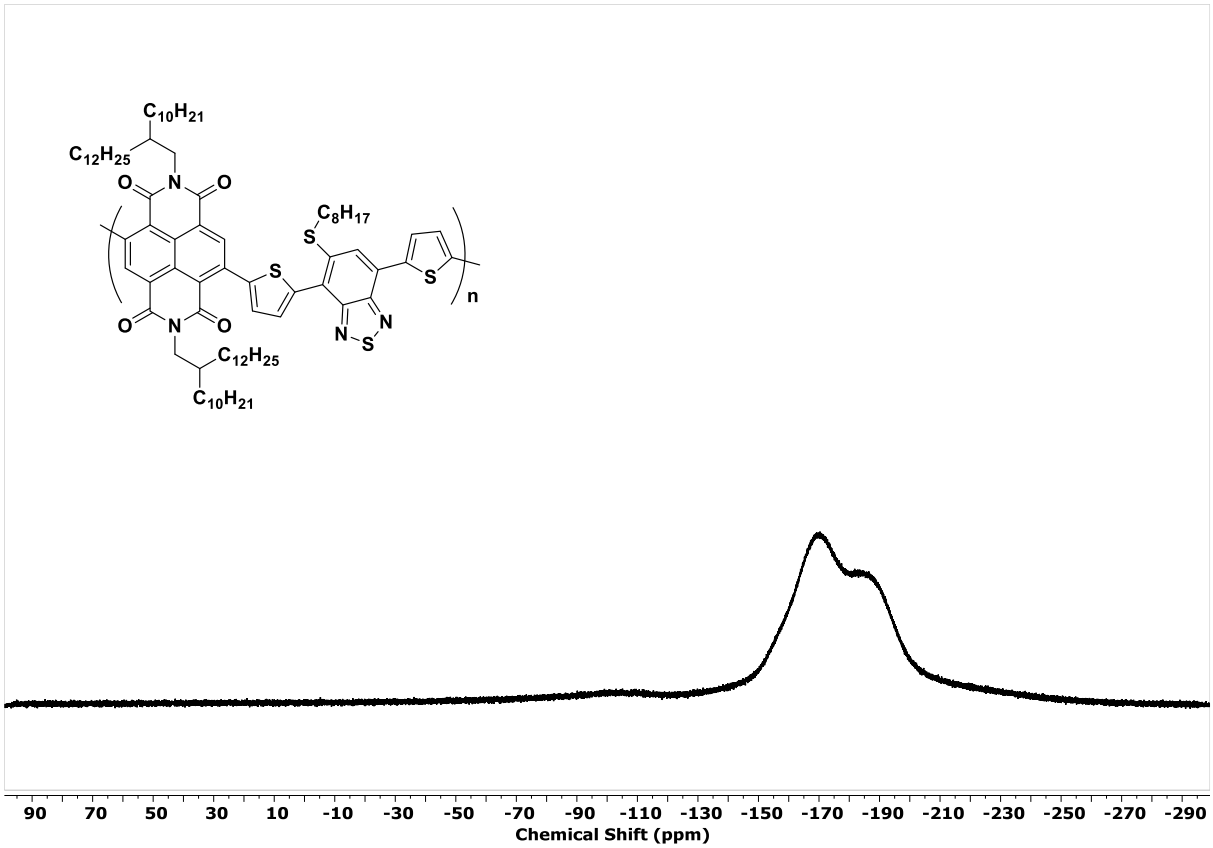


Figure S4.21. ^{19}F NMR of PNDI-T(SR)BTT.

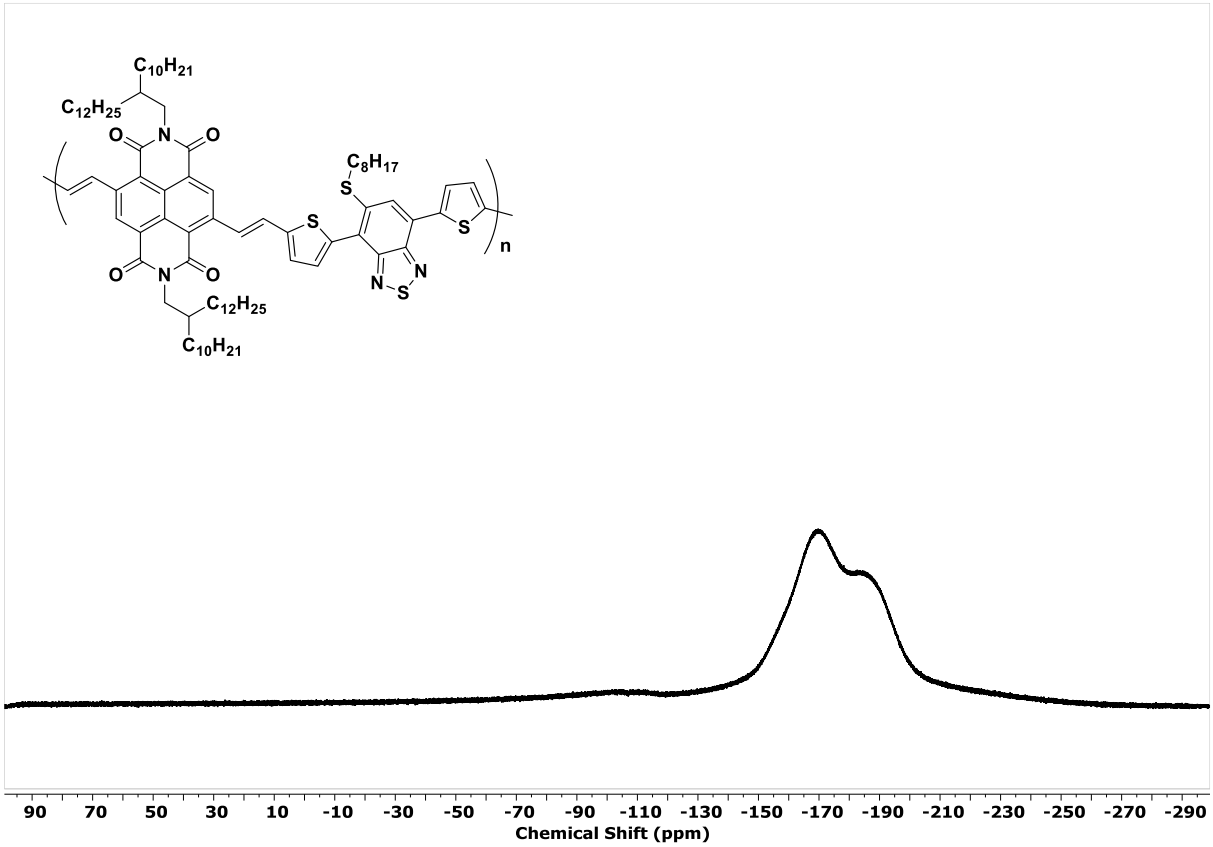


Figure S4.22. ^{19}F NMR of PNDIV-T(SR)BTT.

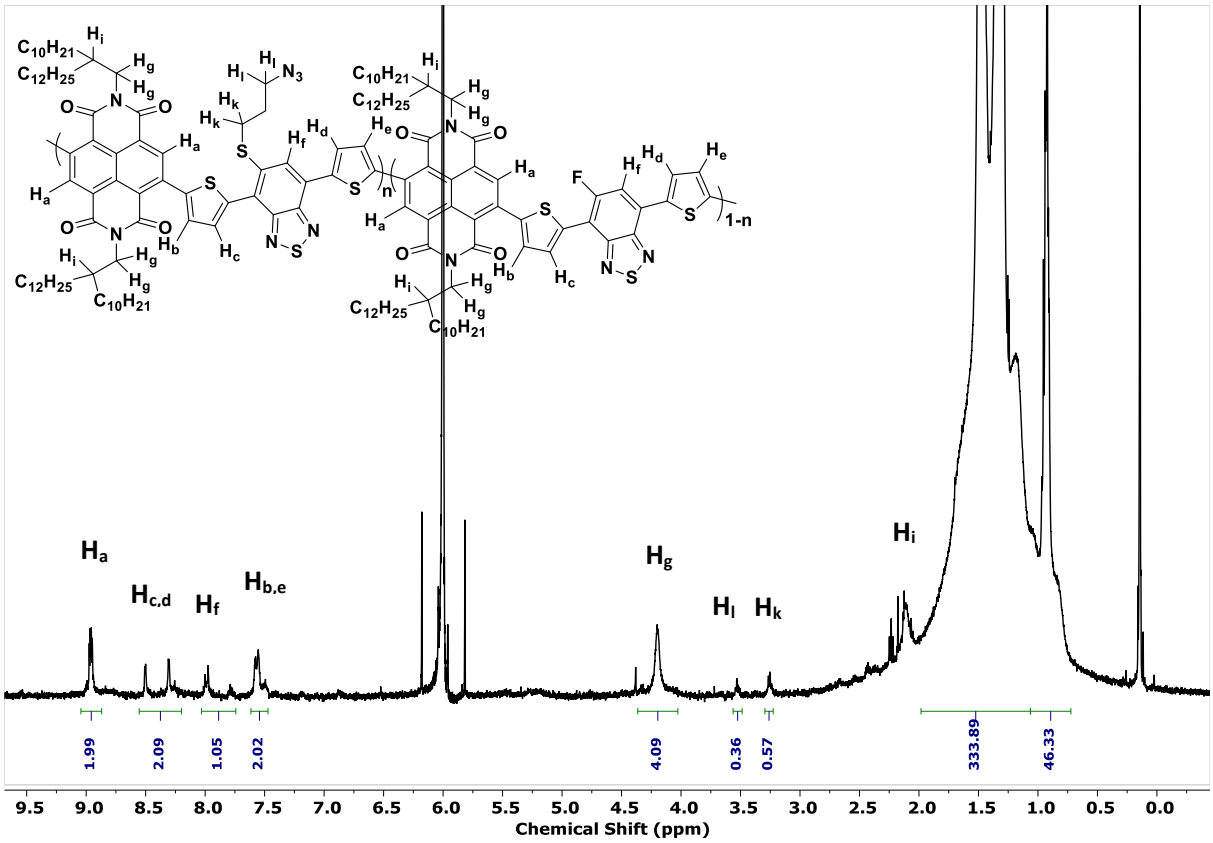


Figure S4.23. ^{1}H NMR of PNDI-T(SAz)BTT-10%.

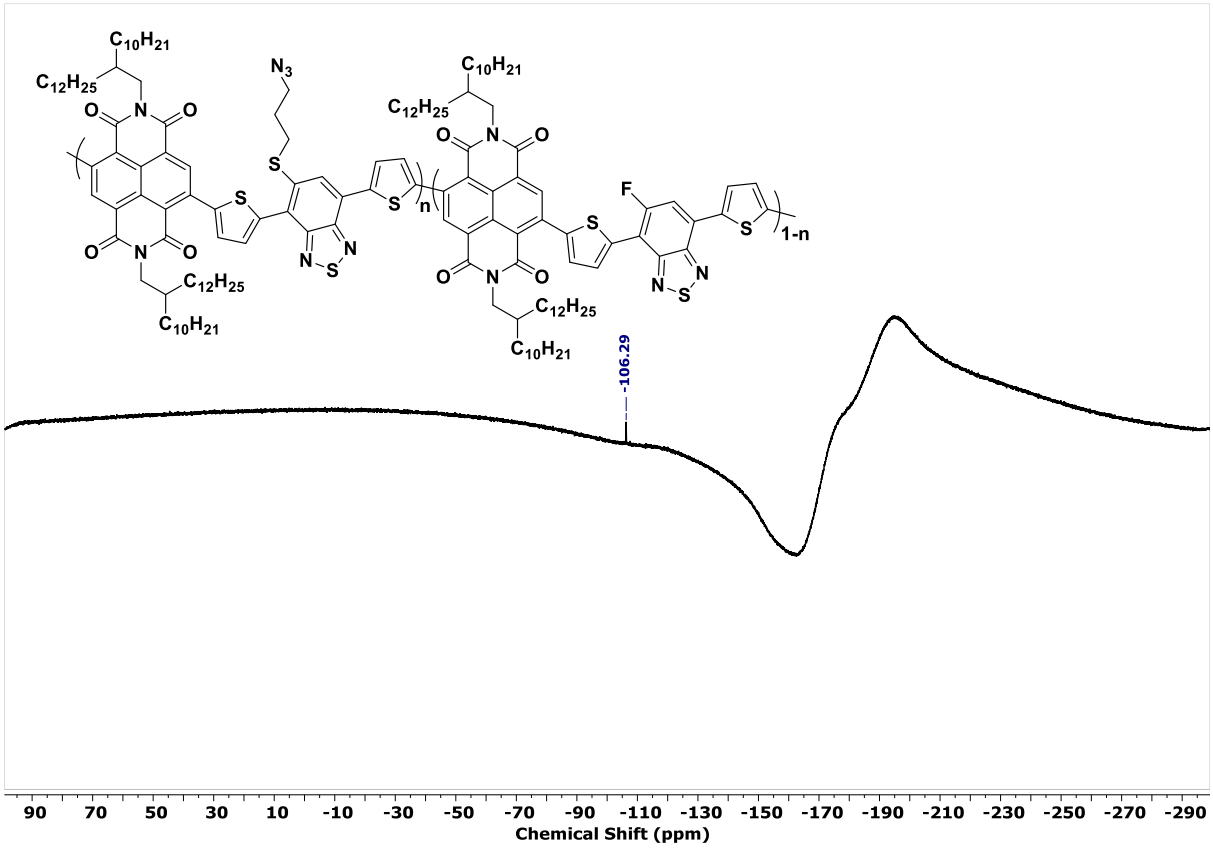


Figure S4.24. ^{19}F NMR of PNDI-T(SAz)BTT-10%.

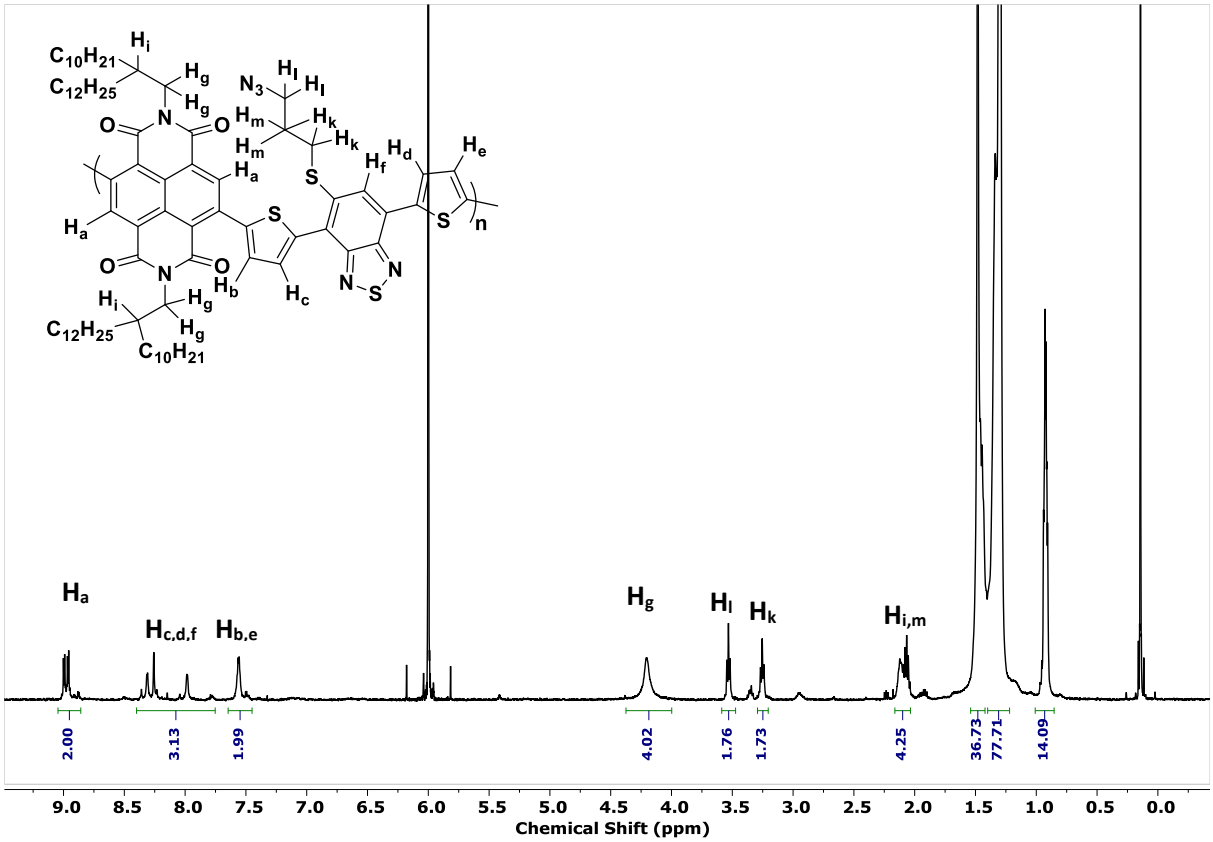


Figure S4.25. ^{1}H NMR of PNDI-T(SAz)BTT-100%.

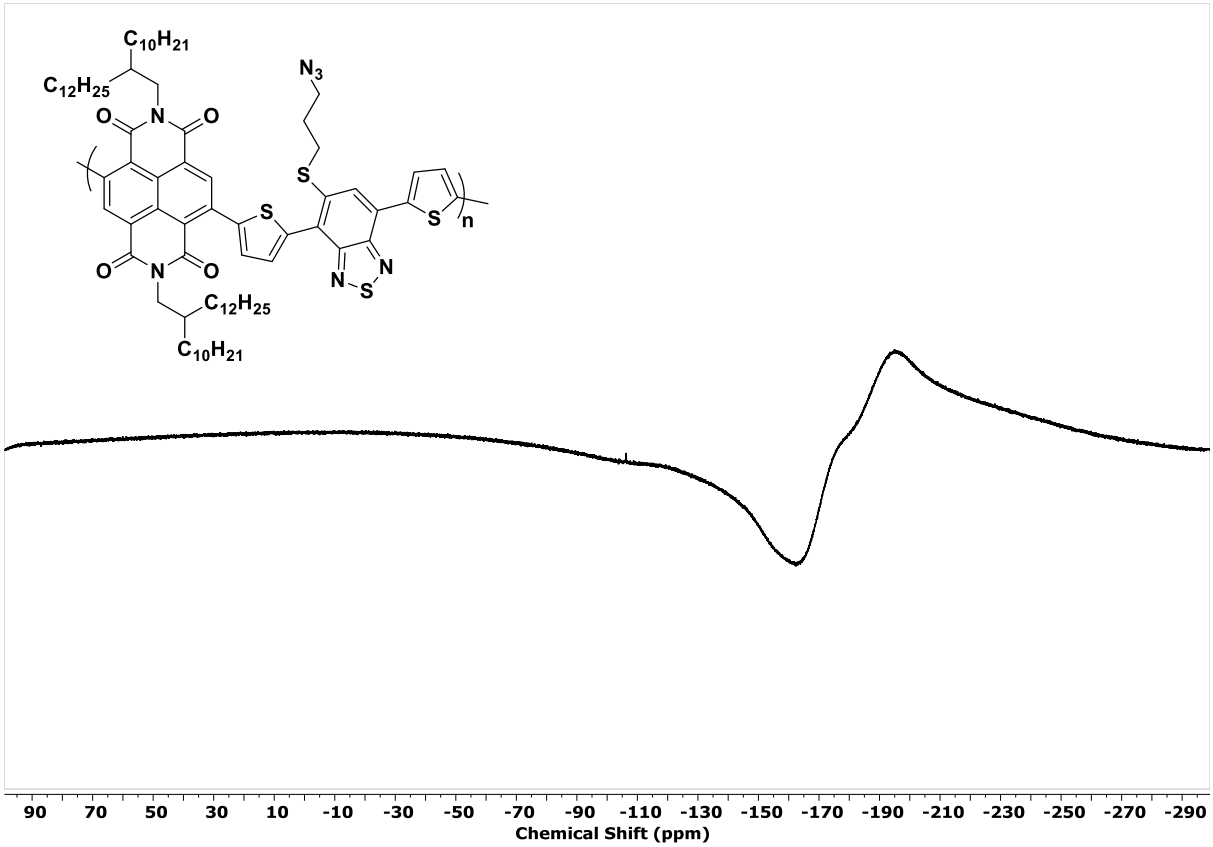


Figure S4.26. ^{19}F NMR of PNDI-T(SAz)BTT-100%.

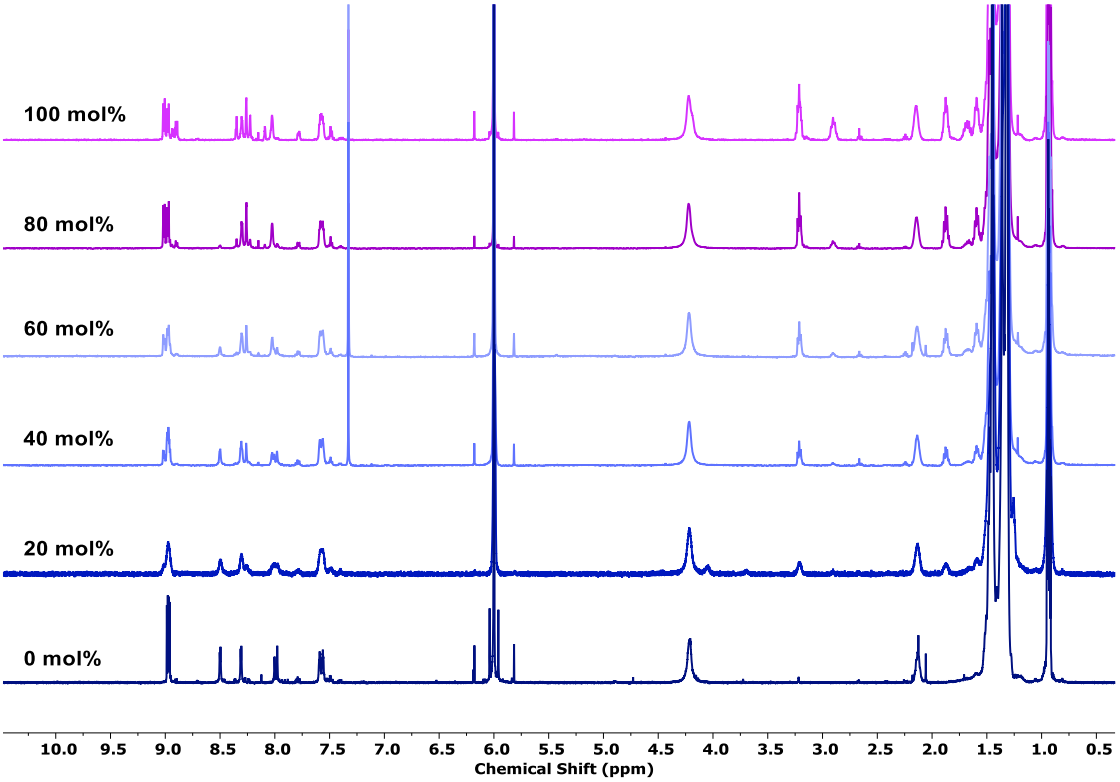


Figure S4.27. ^{1}H NMR spectra for increasing substitution along the PNDI-TfBTT backbone.

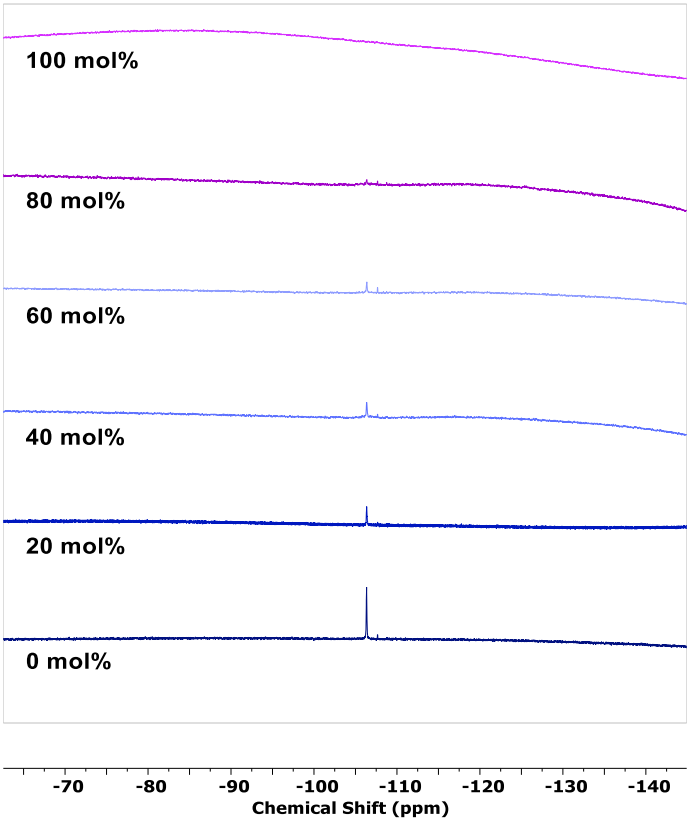


Figure S4.28. ^{19}F NMR spectra for increasing substitution along the PNDI-TfBTT backbone.

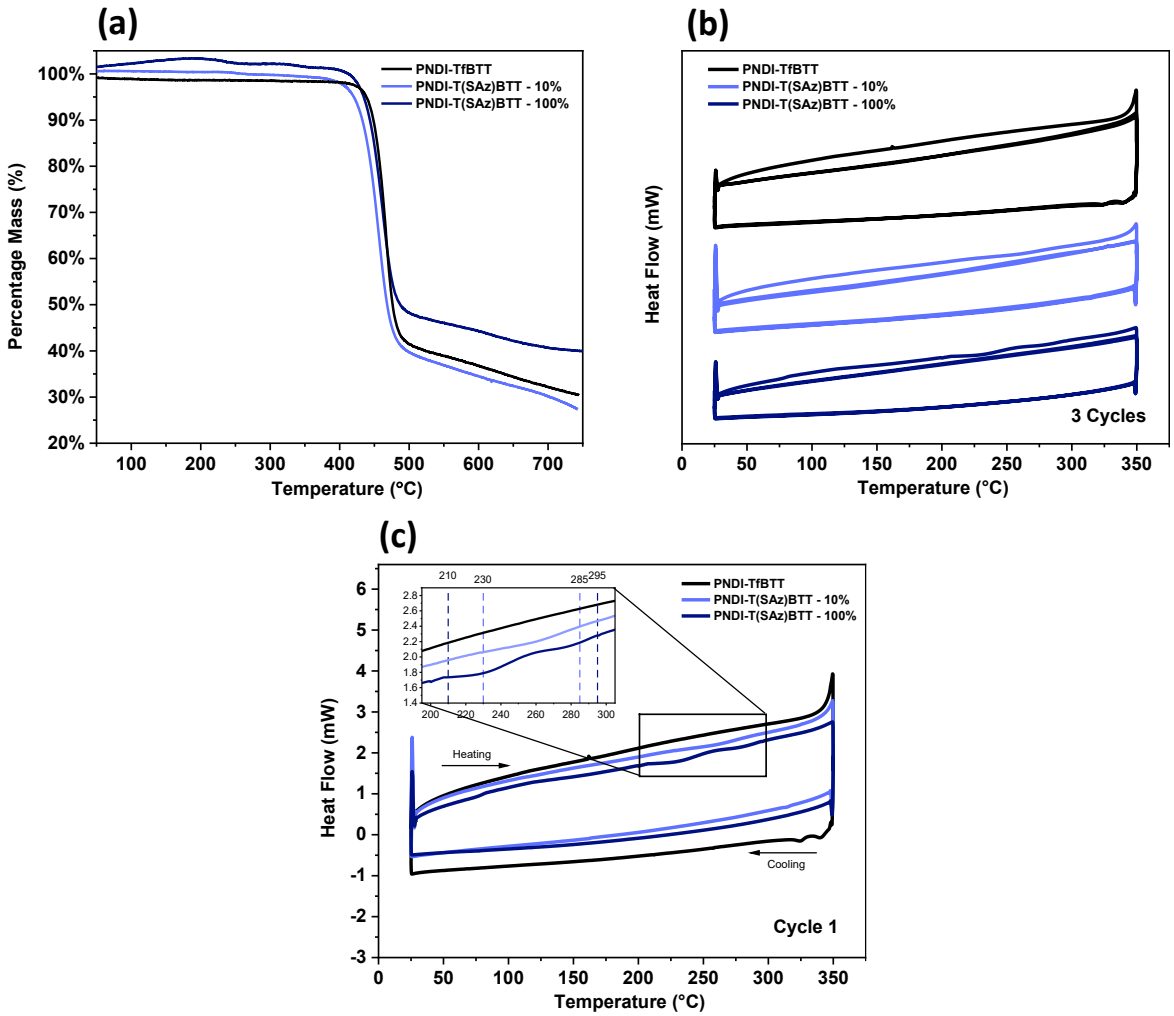


Figure S4.29. (a) TGA data for PNDI-TfBTT, PNDI-T(SAz)BTT-10% and PNDI-T(SAz)BTT-100% carried out in a Nitrogen atmosphere at 5 °C min^{-1} (b,c) DSC data for PNDI-TfBTT, PNDI-T(SAz)BTT-10% and PNDI-T(SAz)BTT-100% carried out in a Nitrogen atmosphere at 10 °C min^{-1}.

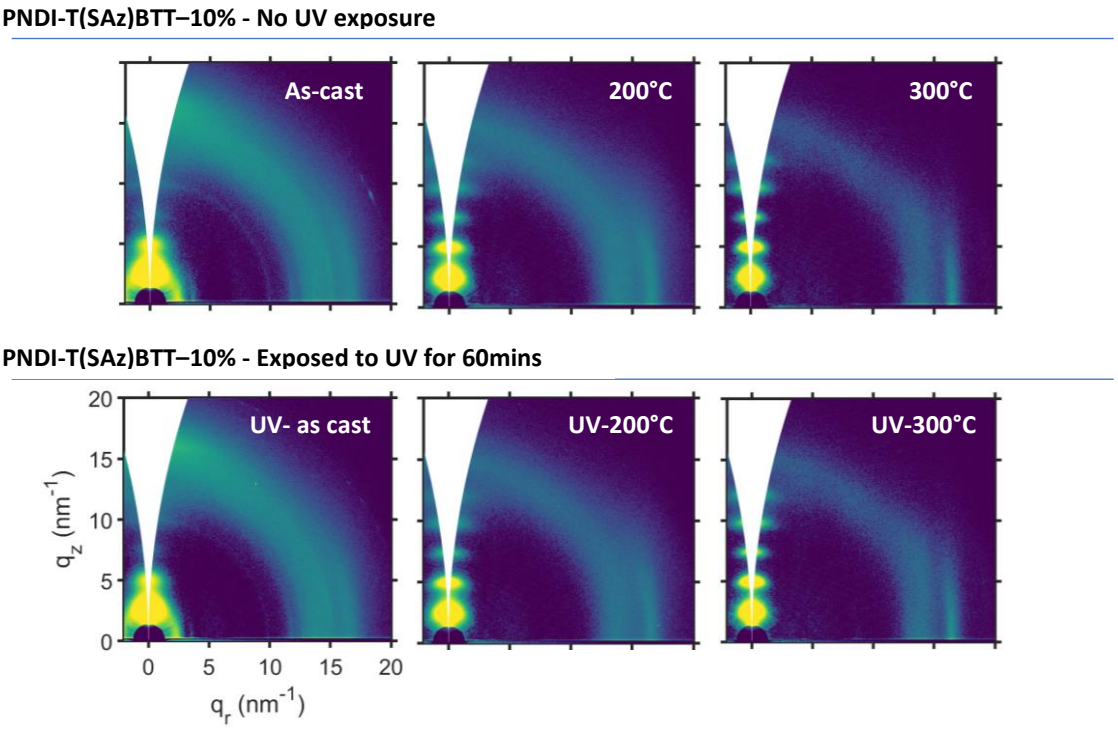


Figure S4.30. GIWAXS images of PNDI-T(SAz)BTT-10% films (a) as-cast (no thermal anneal) and annealed at 200 °C and 300 °C and (b) exposed to UV light (254 nm) for 60 minutes before no thermal anneal (UV only) and annealed at 200 °C and 300 °C.

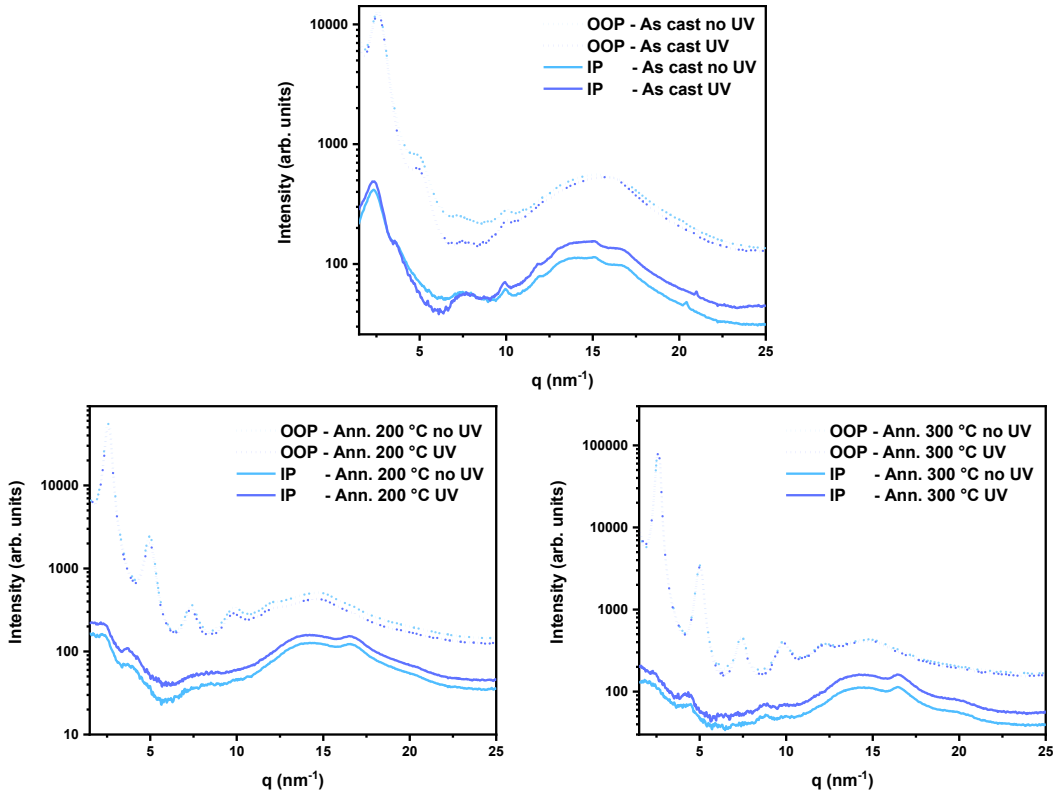


Figure S4.31. GIWAXS diffraction patterns for PNDI-T(SAz)BTT-10% films as-cast and annealed at 200 °C and 300 °C, with and without UV exposure (254 nm) prior to annealing.

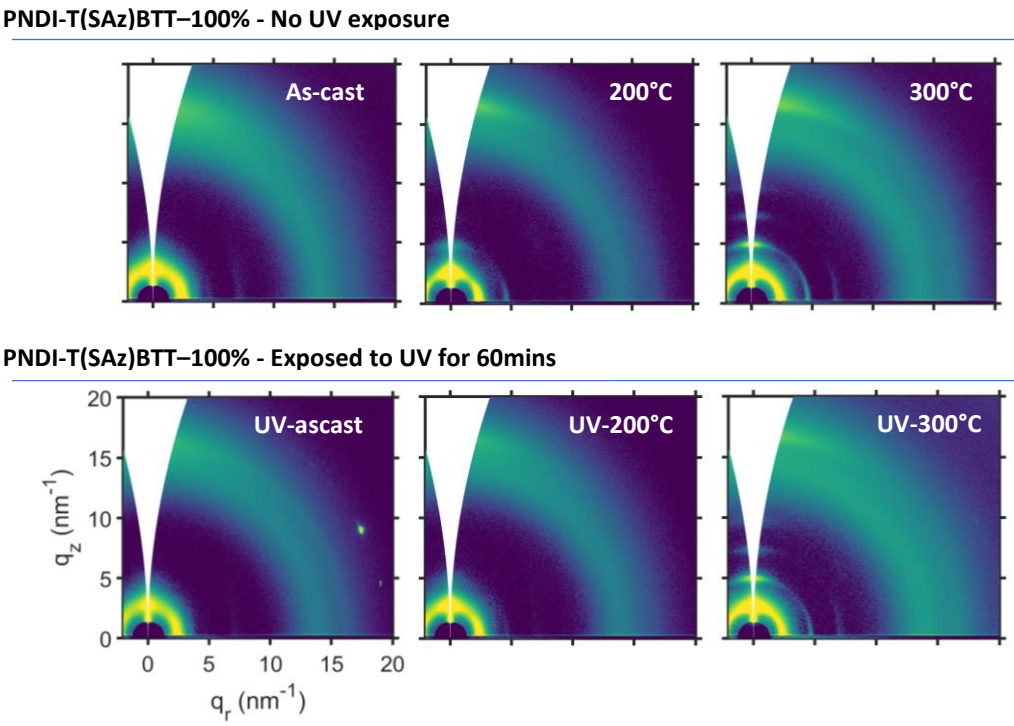


Figure S4.32. GIWAXS images of PNDI-T(SAz)BTT-100% films (a) as-cast (no thermal anneal) and annealed at 200 °C and 300 °C and (b) exposed to UV light (254 nm) for 60 minutes before no thermal anneal (UV only) and annealed at 200 °C and 300 °C.

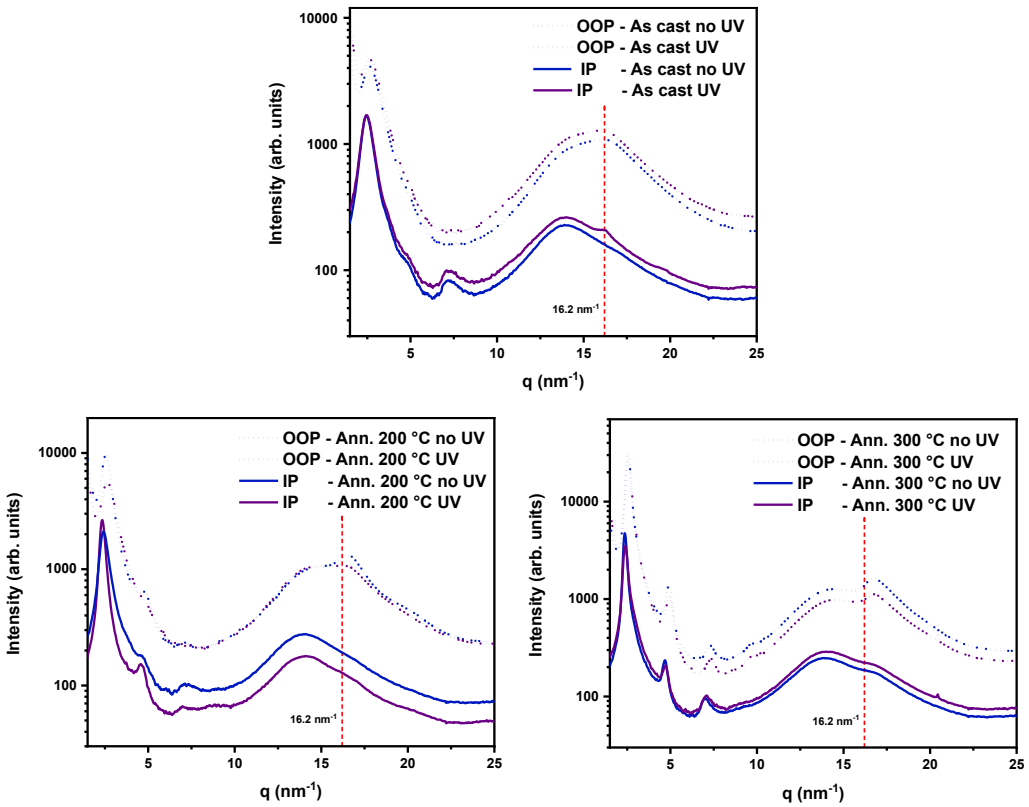


Figure S4.33. GIWAXS diffraction patterns for PNDI-T(SAz)BTT-10% films as-cast and annealed at 200 °C and 300 °C, with and without UV exposure (254 nm) prior to annealing.

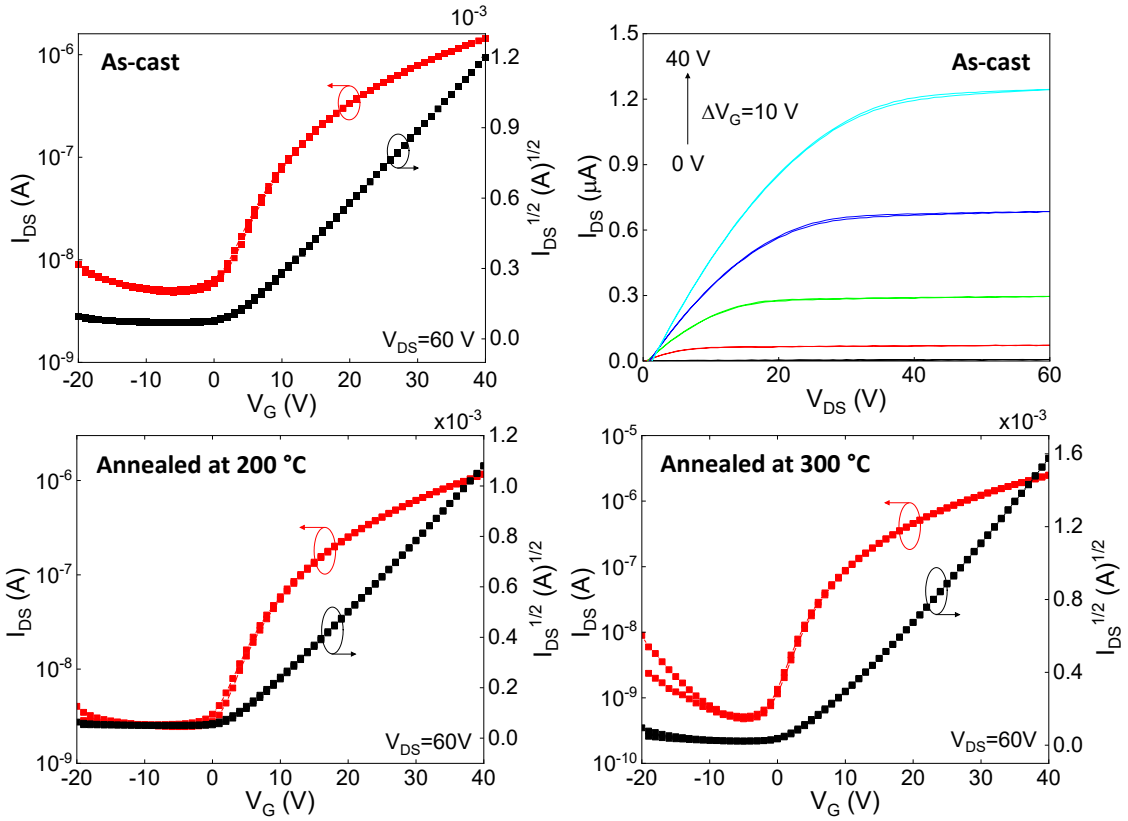


Figure S4.34. Transfer and output characteristics of PNDI-T(SAz)BTT-10% OTFT device.

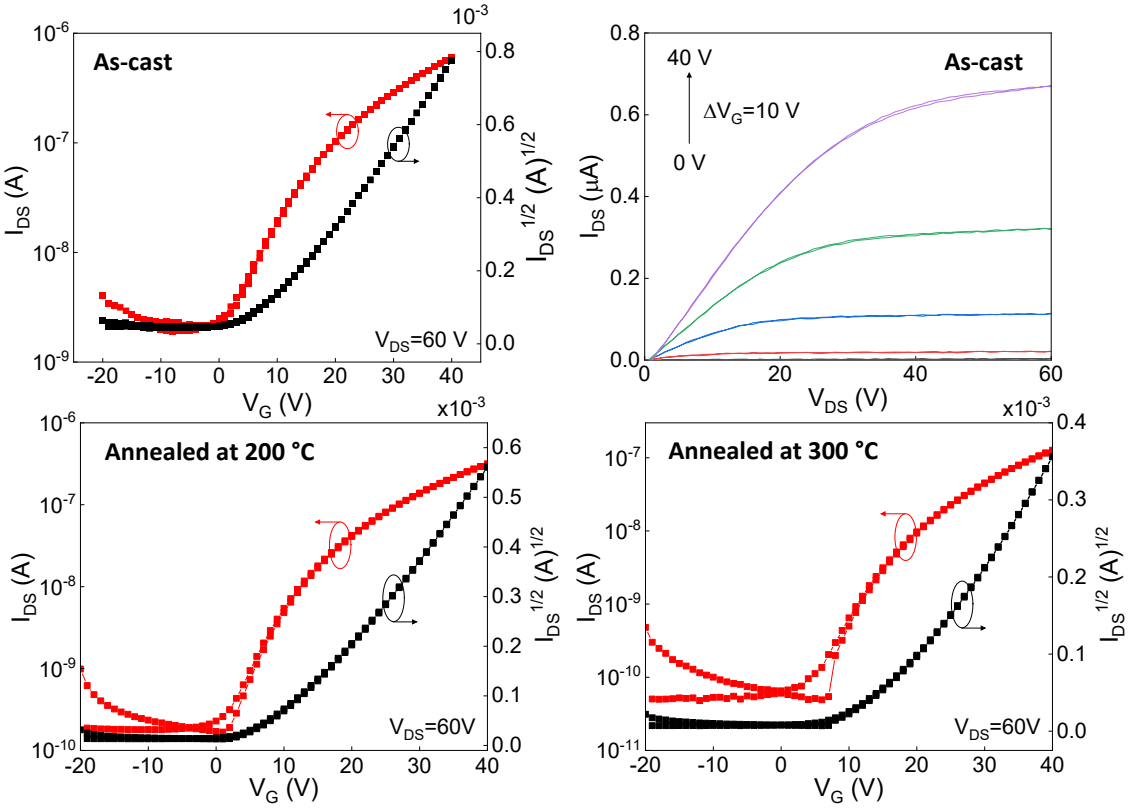


Figure S4.35. Transfer and output characteristics of PNDI-T(SAz)BTT-100% OTFT device.

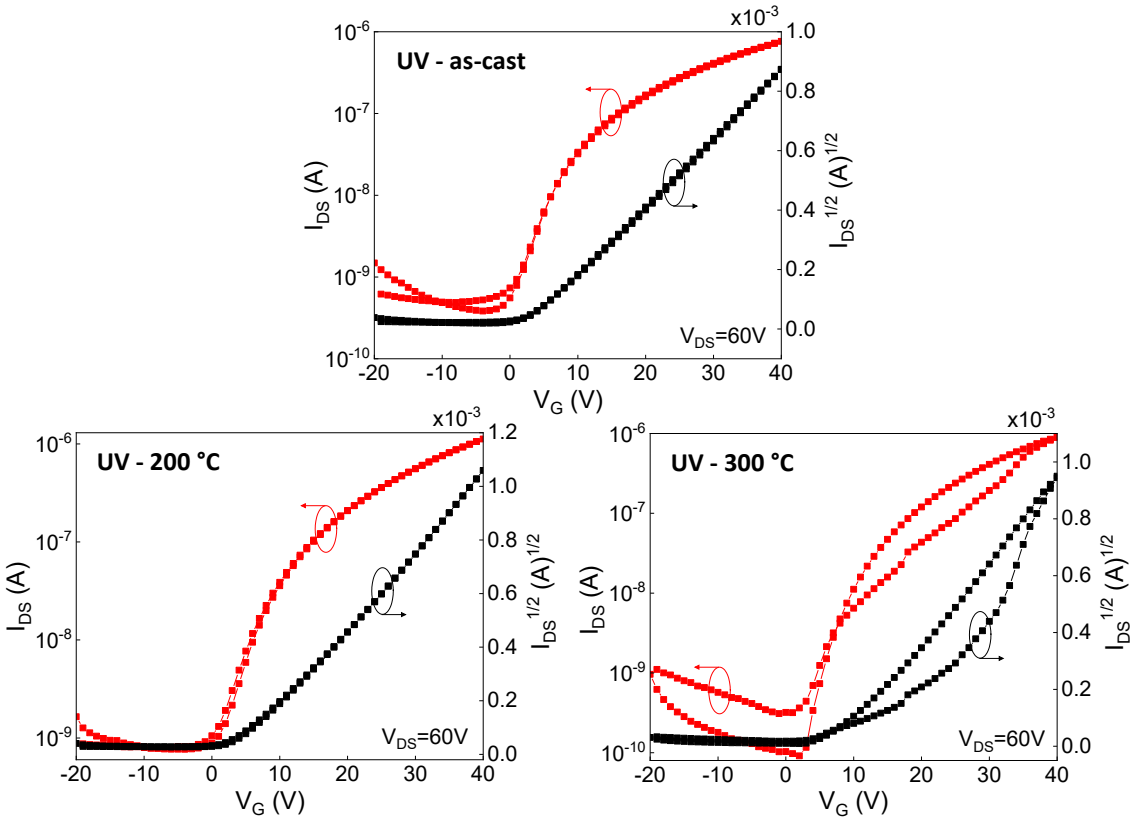


Figure S4.36. Transfer characteristics of PNDI-T(SAz)BTT-10% OTFT device, where thin films have been exposed to UV light.

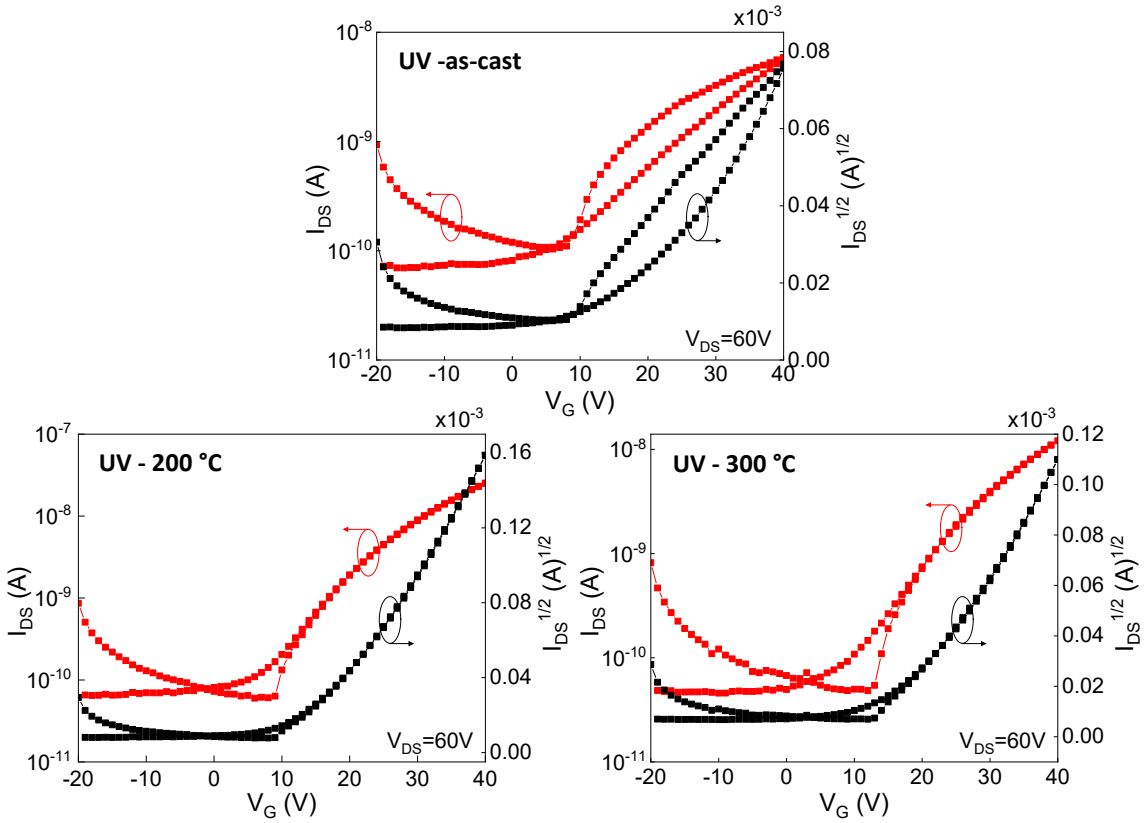


Figure S4.37. Transfer characteristics of PNDI-T(SAz)BTT-100% OTFT device, where thin films have been exposed to UV light.

5 Chapter 5 Appendix:

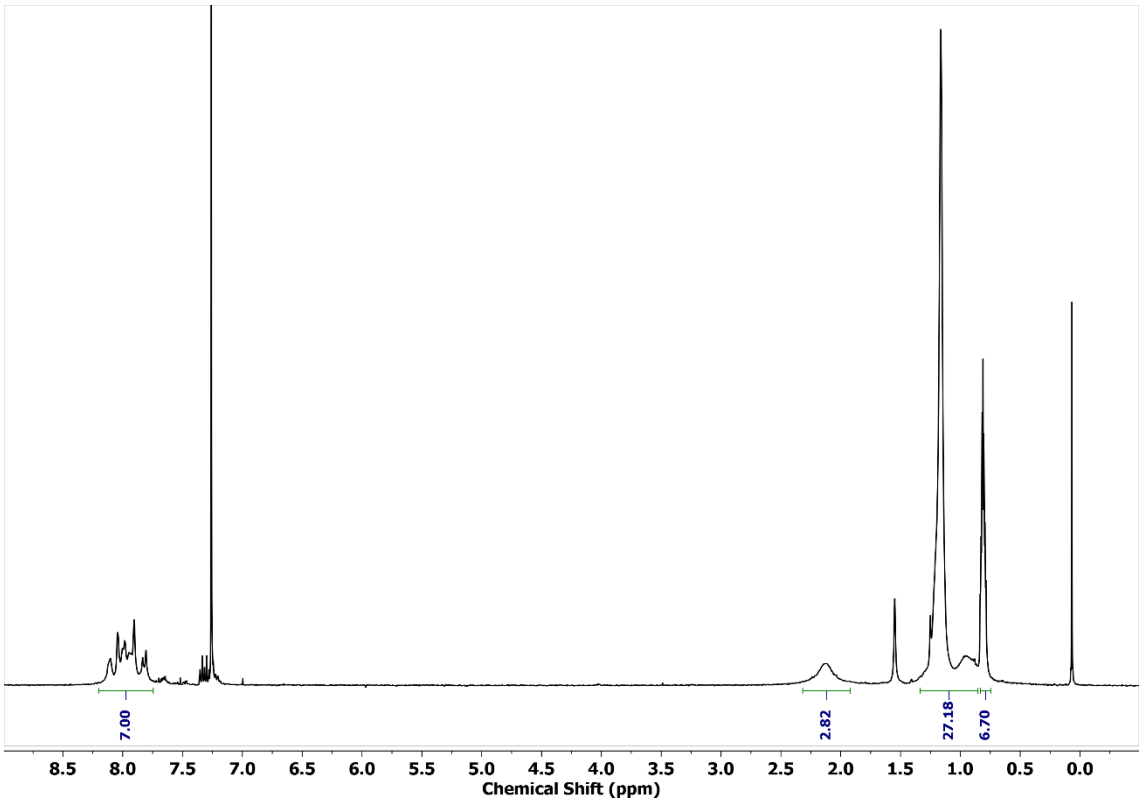


Figure S5.1. ^{1}H NMR of F8fBT.

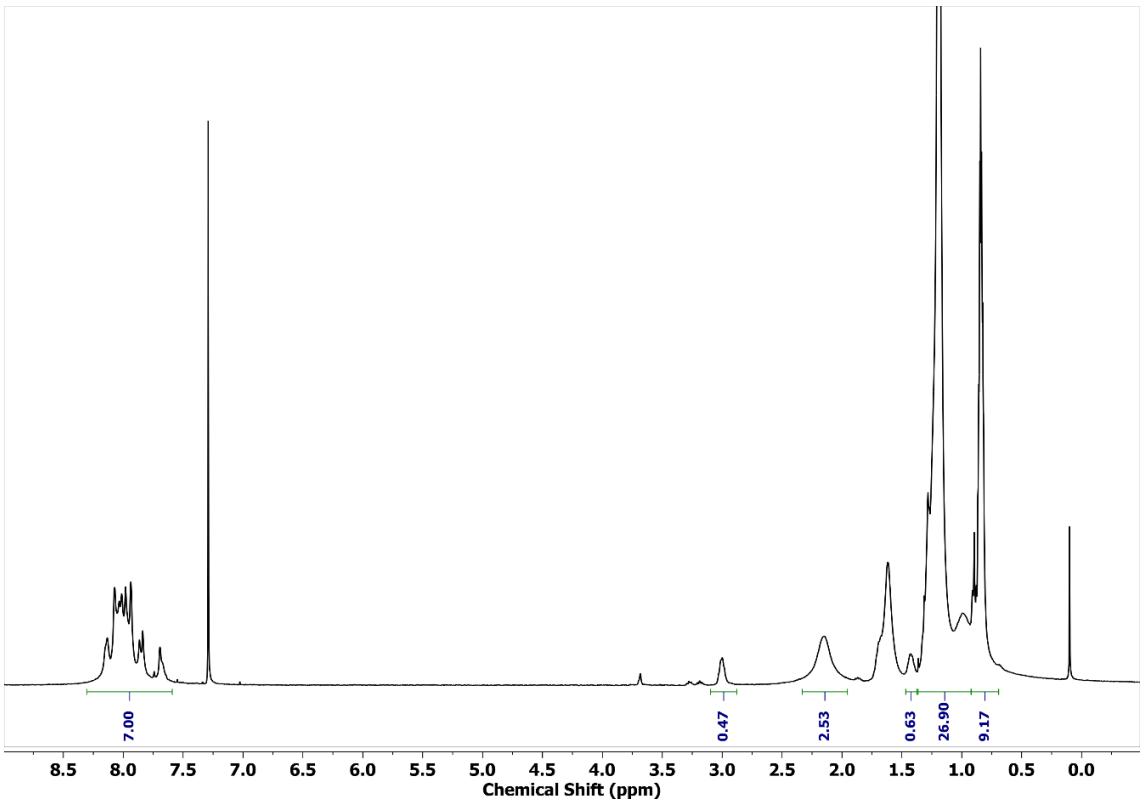


Figure S5.2. ^{1}H NMR of F8BT-SR 0.25.

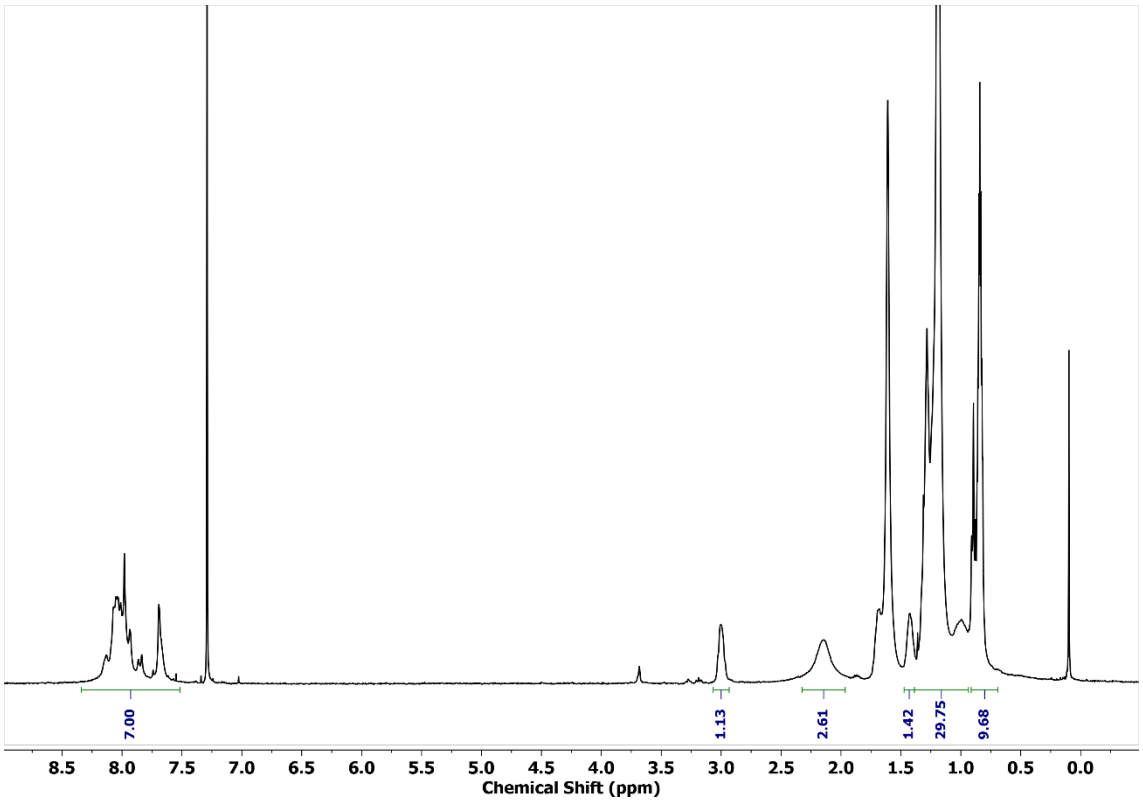


Figure S5.3. ^{1}H NMR of F8BT-SR 0.5.

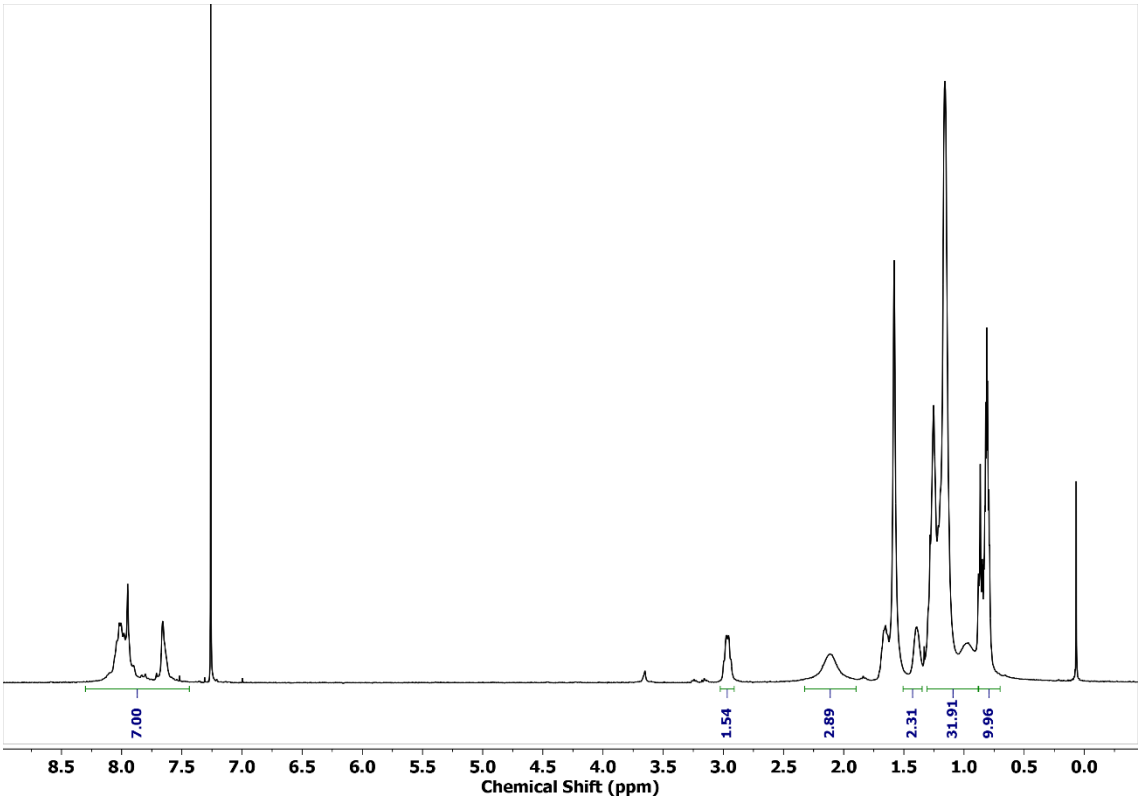


Figure S5.4. ^{1}H NMR of F8BT-SR 0.75.

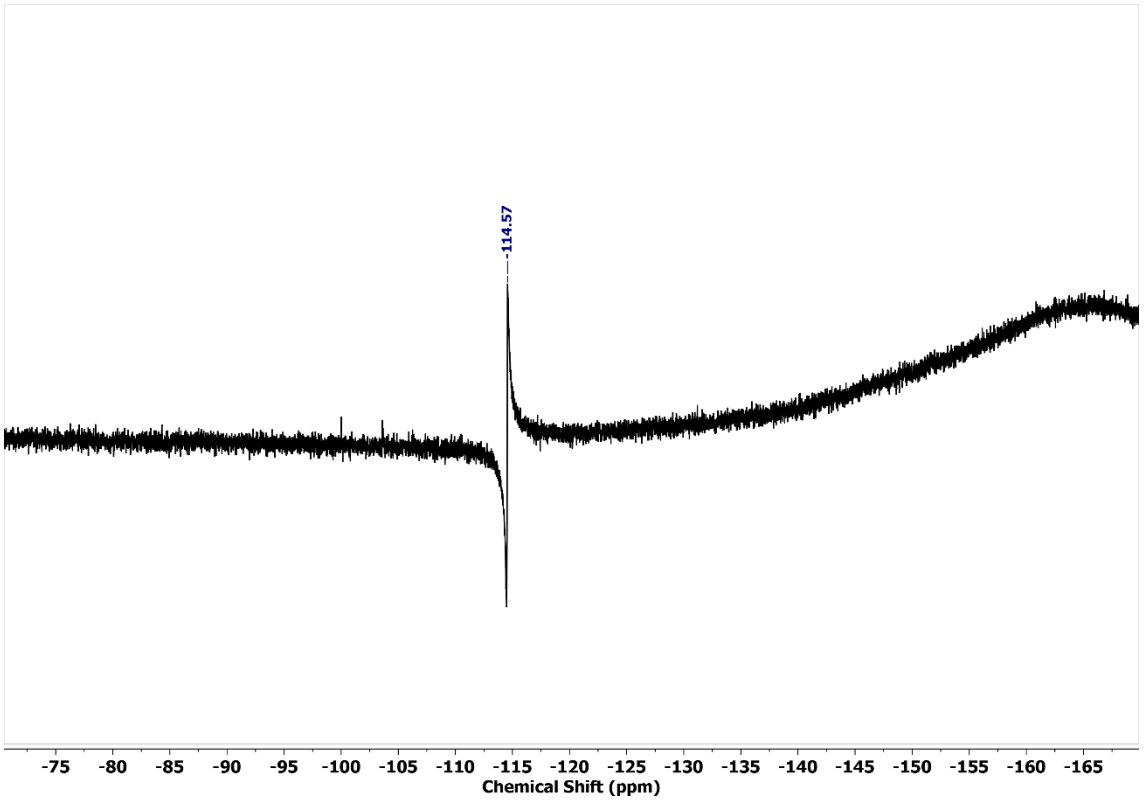


Figure S5.5. ^{19}F NMR of F8fBT.

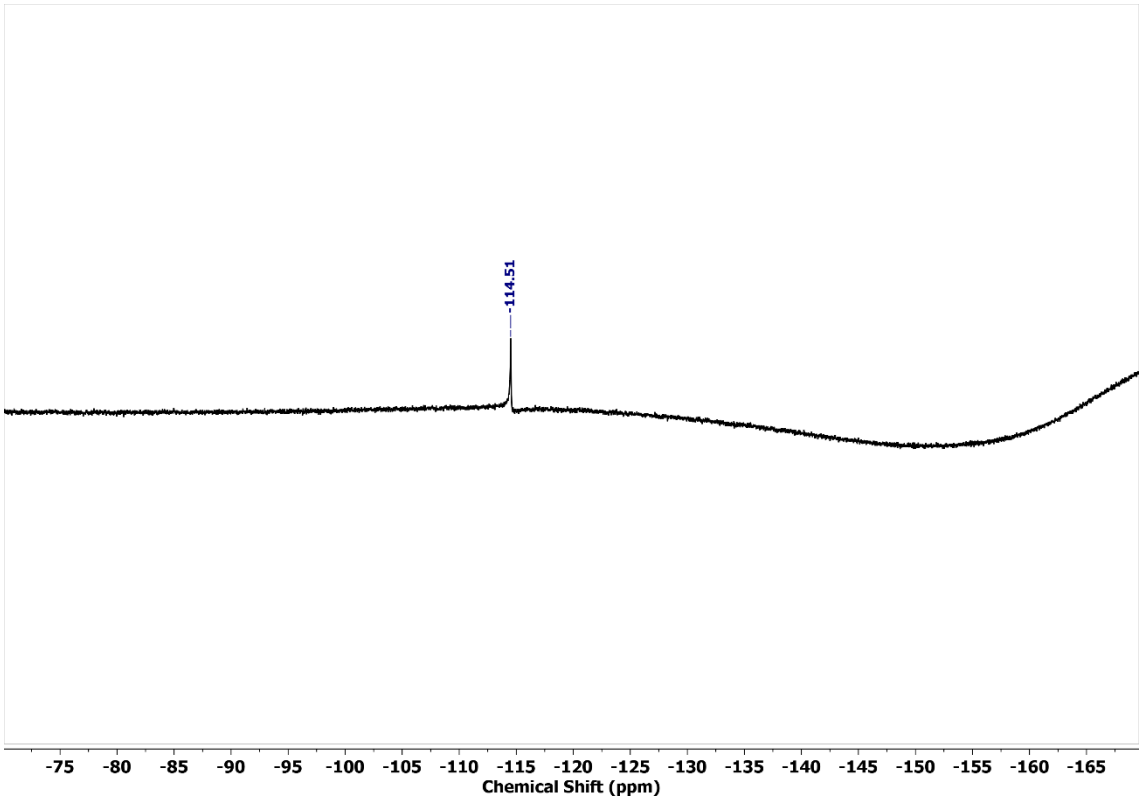


Figure S5.6. ^{19}F NMR of F8BT-SR 0.25.

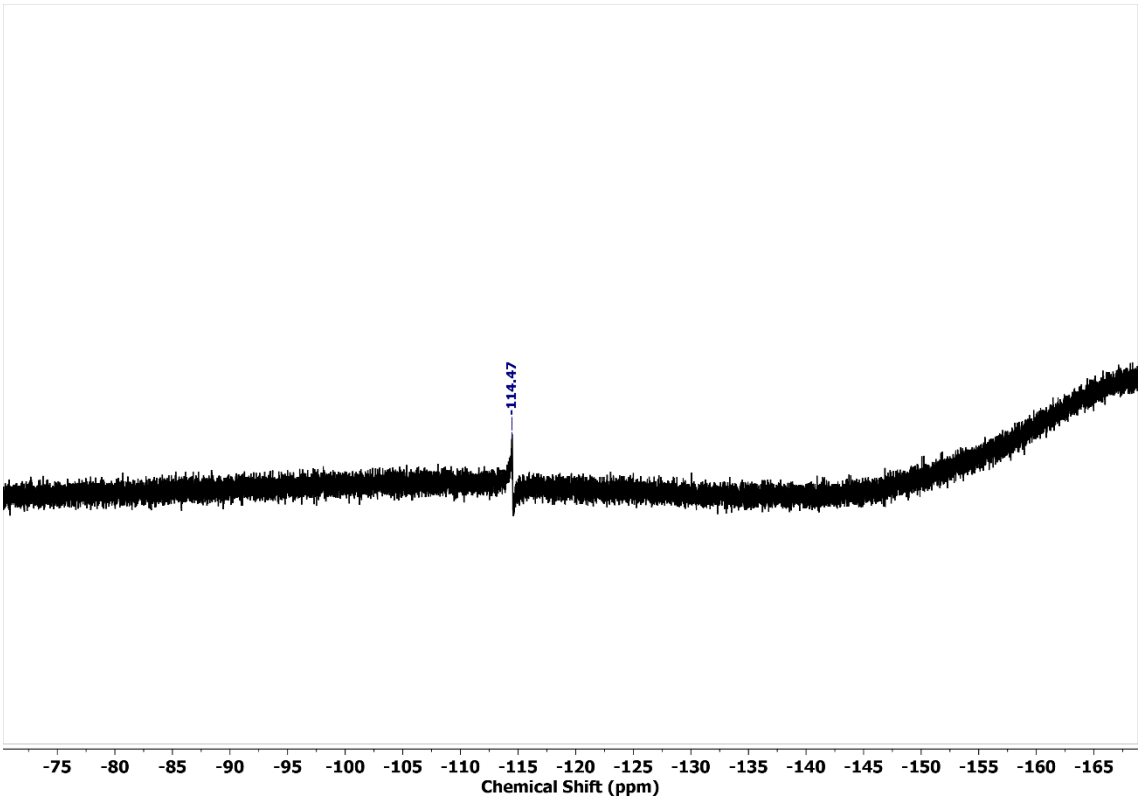


Figure S5.7. ^{19}F NMR of F8BT-SR 0.5.

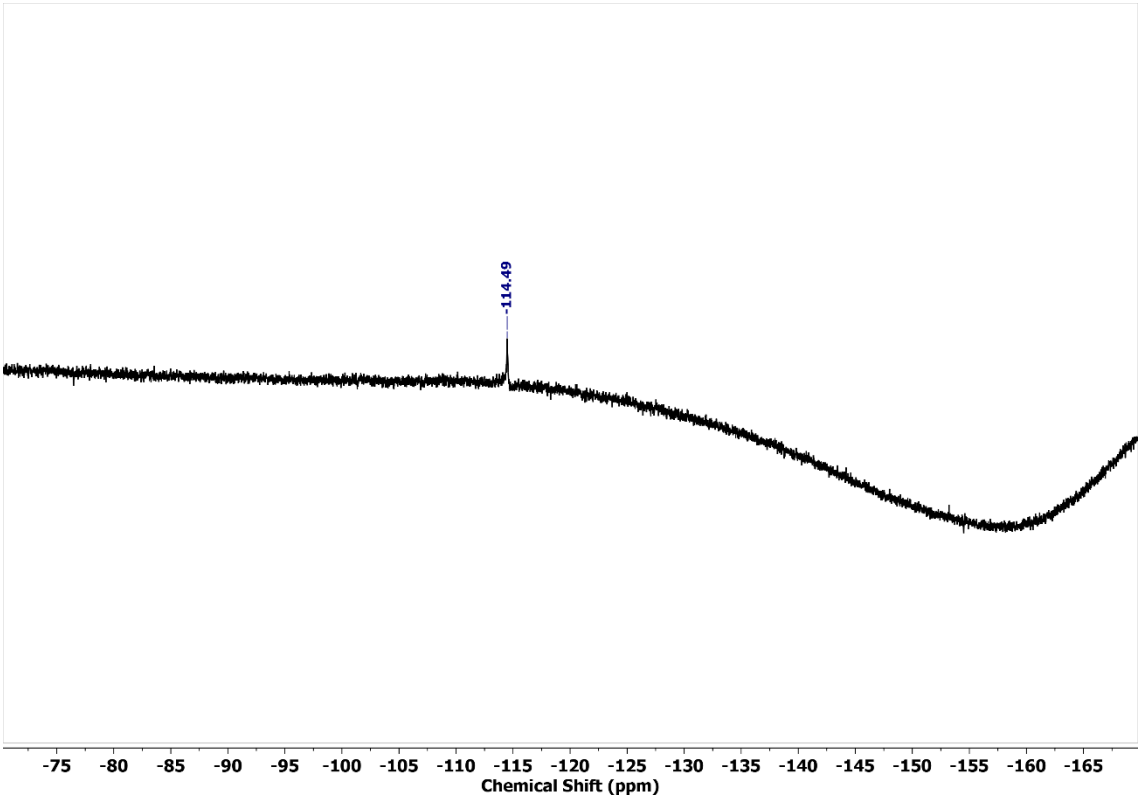


Figure S5.8. ^{19}F NMR of F8BT-SR 0.75.

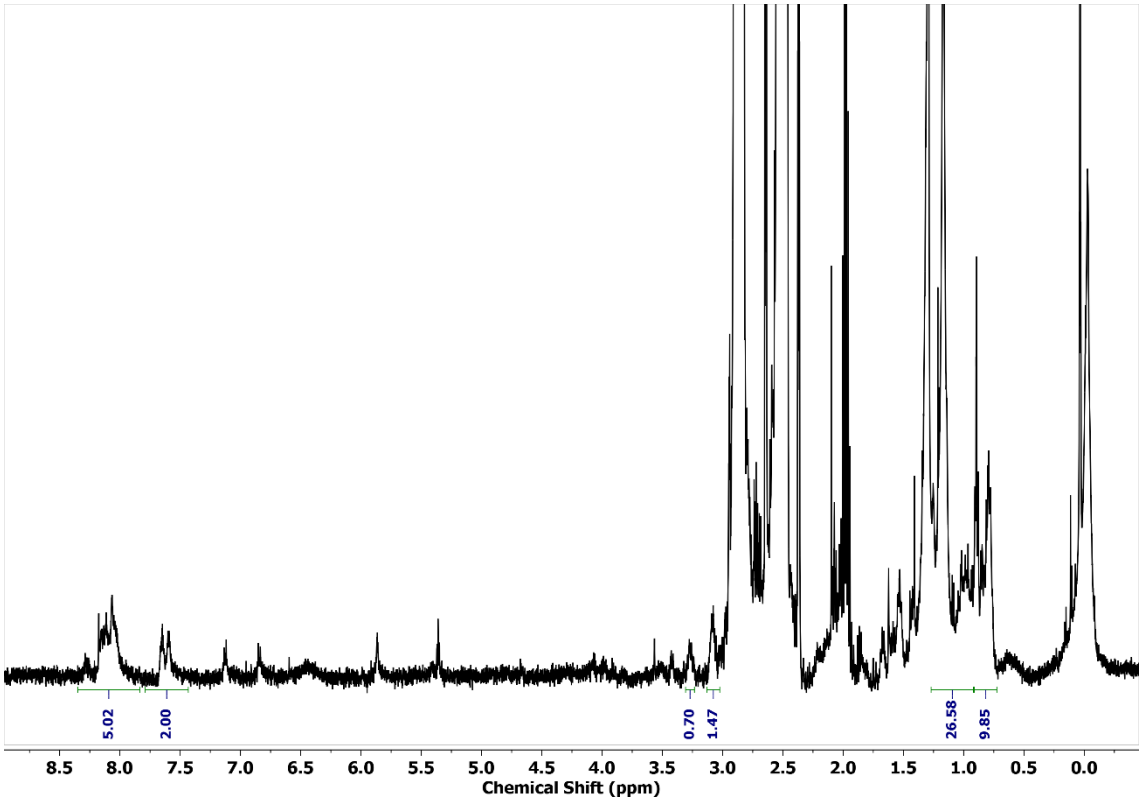


Figure S5.9. ^{1}H NMR of F8BT-SAn 0.25.

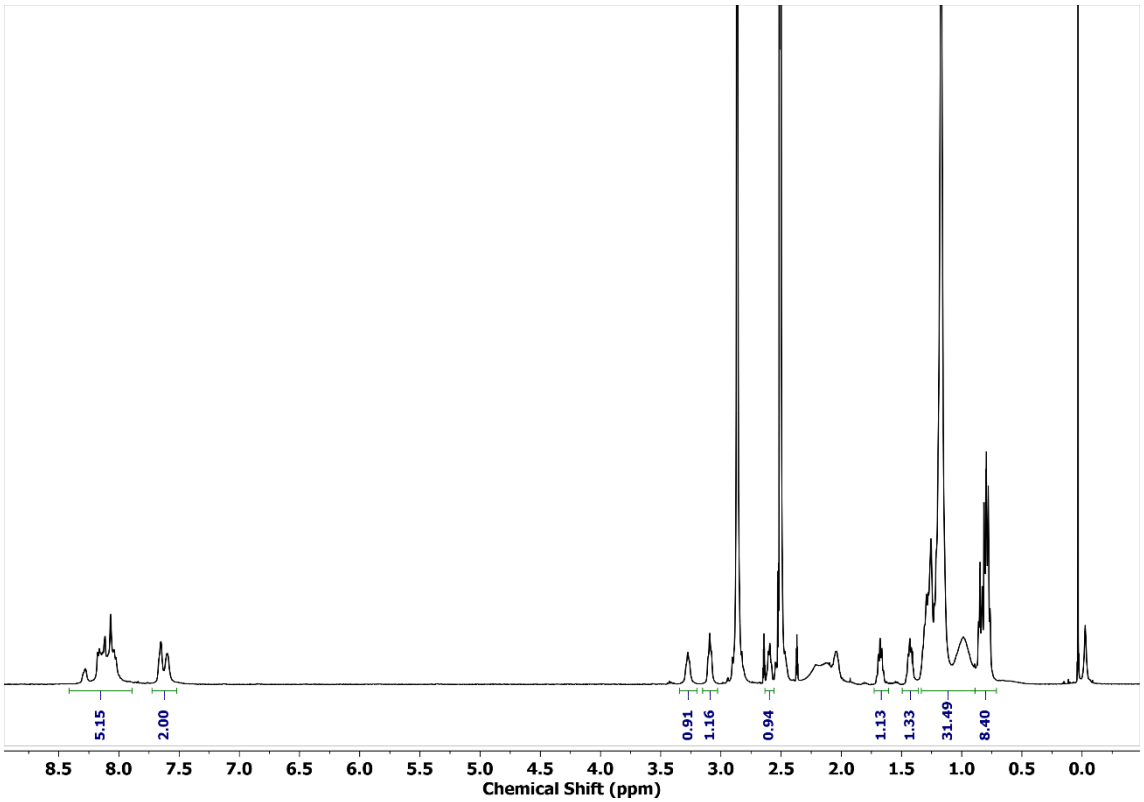


Figure S5.10. ^{1}H NMR of F8BT-SAn 0.50.

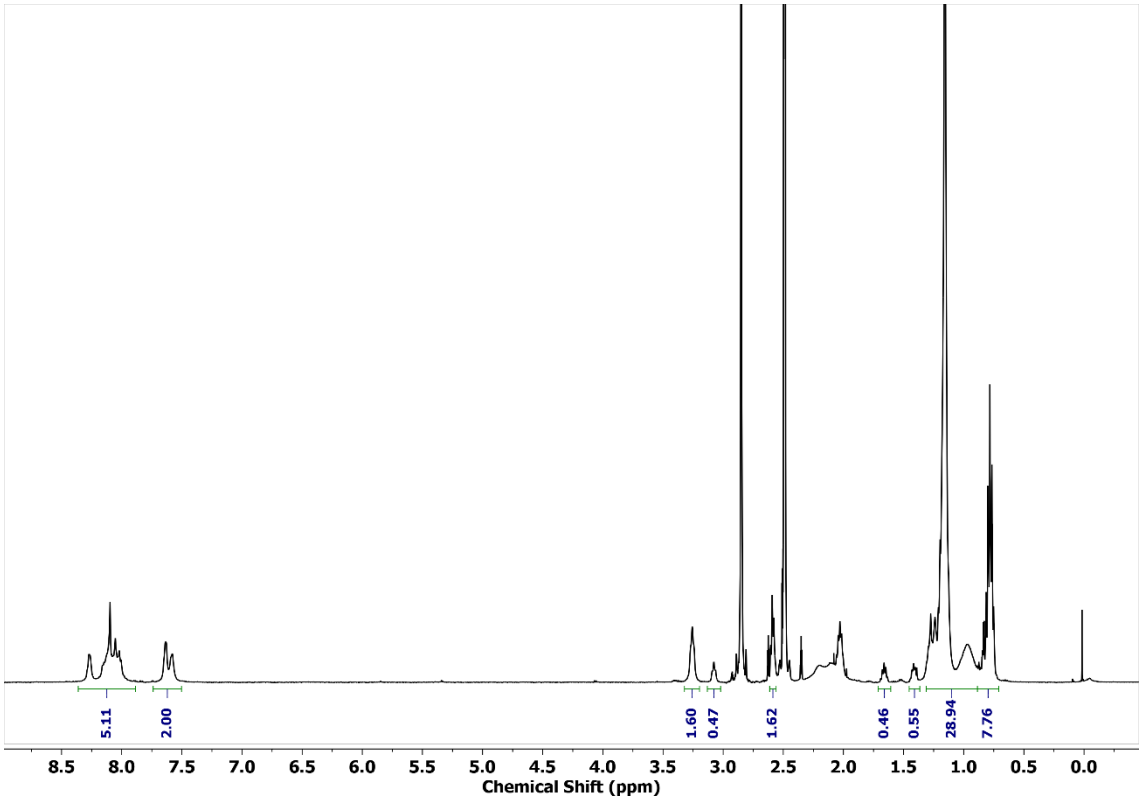


Figure S5.11. ^{1}H NMR of F8BT-SAn 0.75.

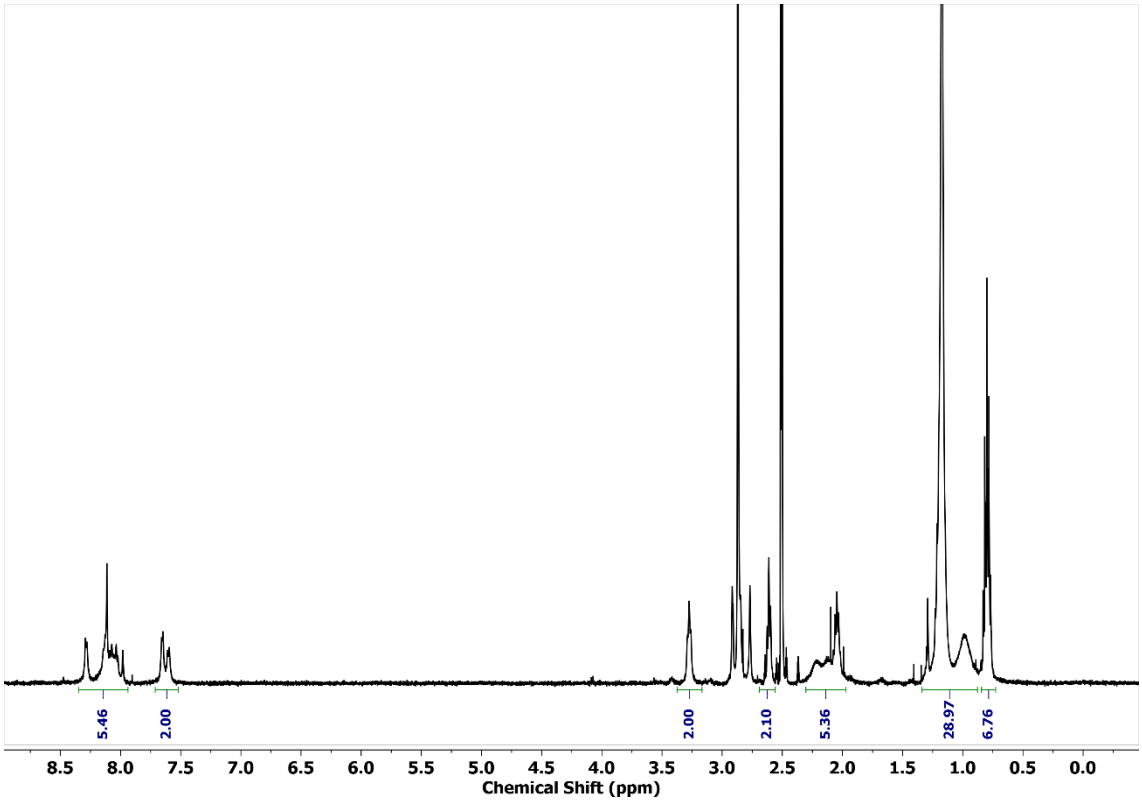


Figure S5.12. ^{1}H NMR of F8BT-SAn 1.00.

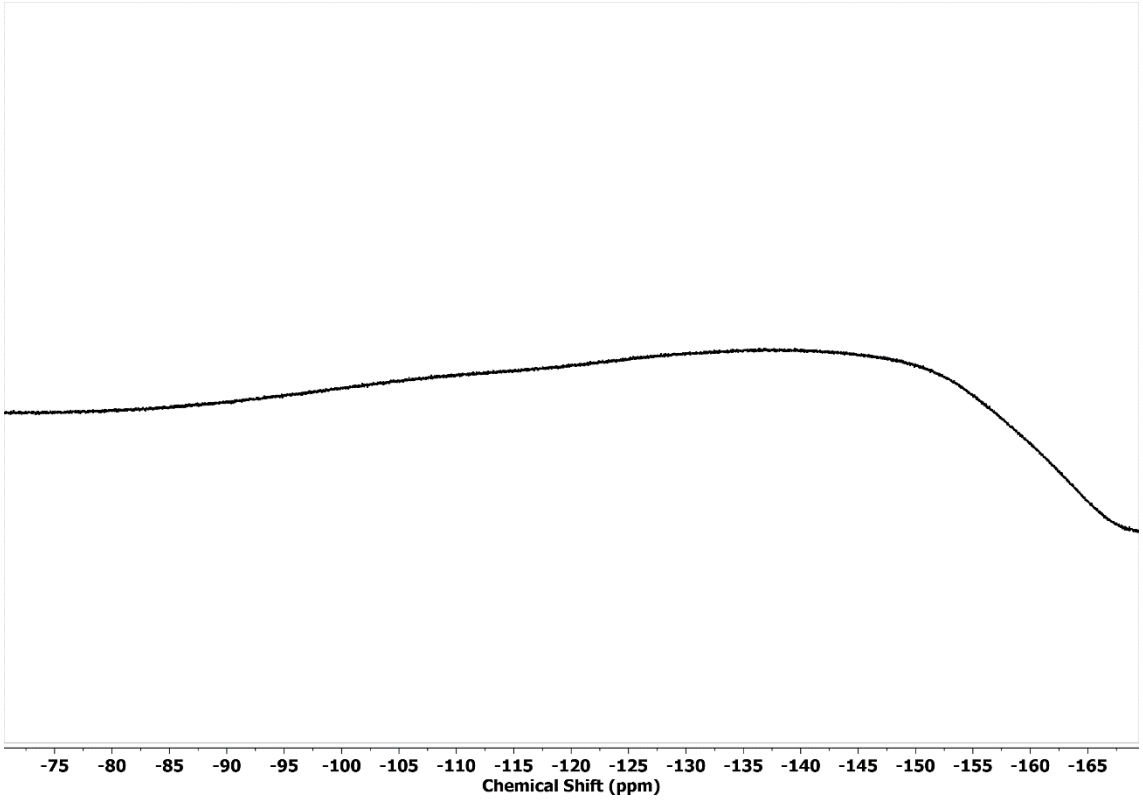


Figure S5.13. ^{19}F NMR of F8BT-SAn 0.25.

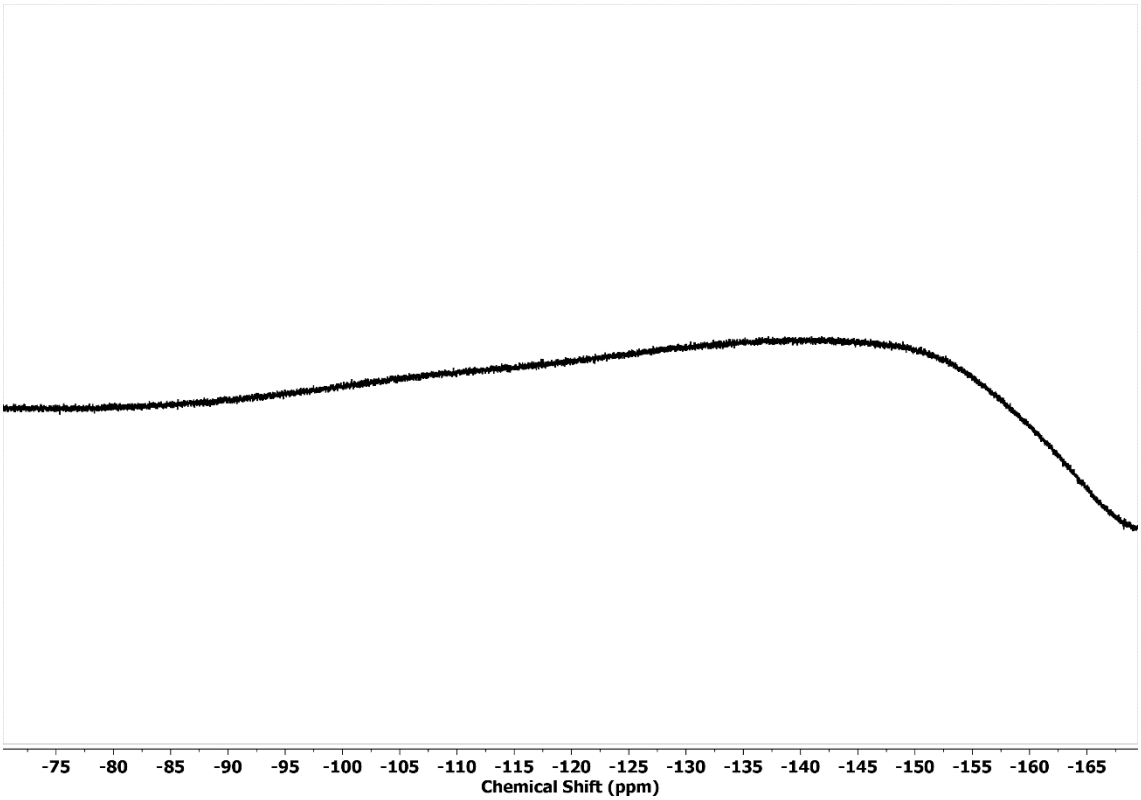


Figure S5.14. ^{19}F NMR of F8BT-SAn 0.50.

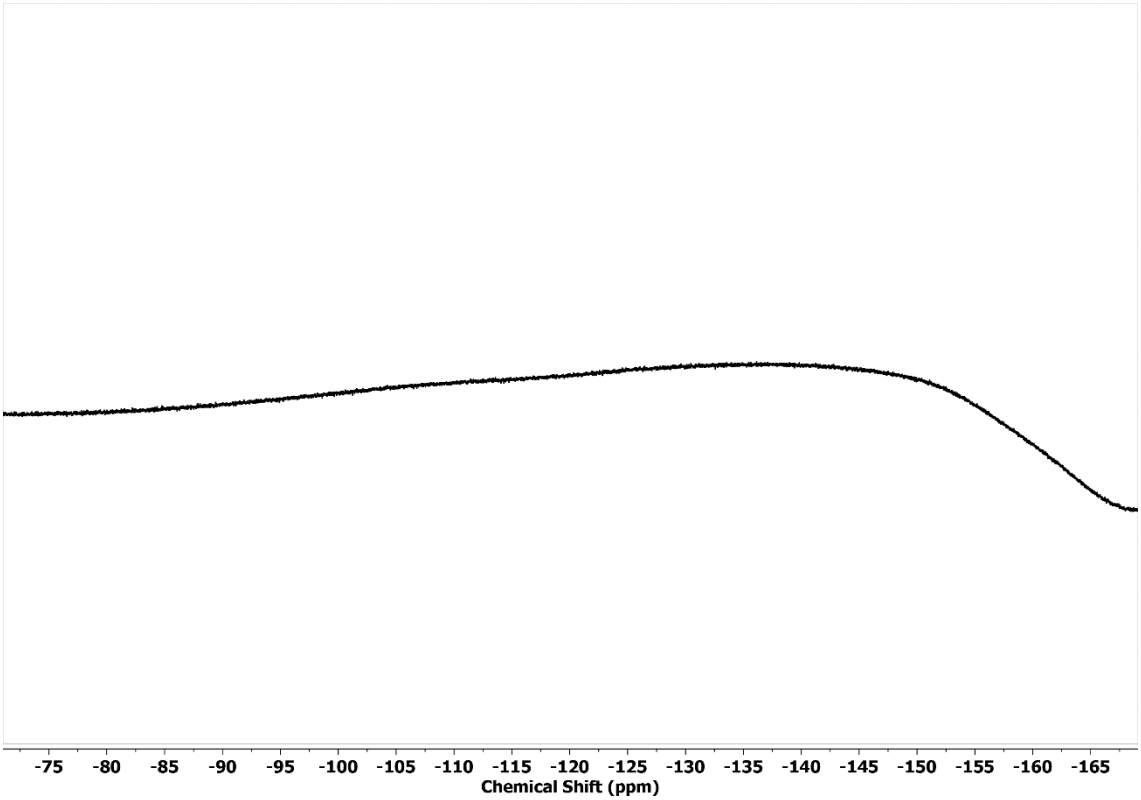


Figure S5.15. ^{19}F NMR of F8BT-SAn 0.75.

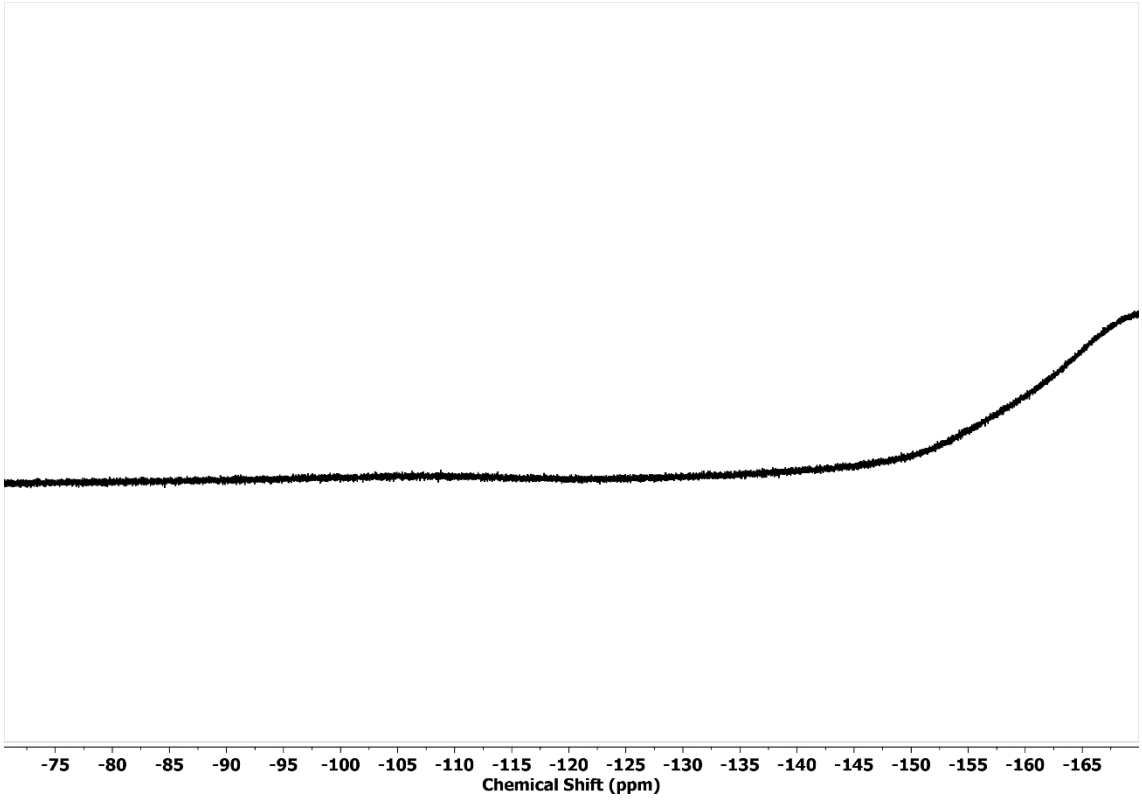


Figure S5.16. ^{19}F NMR of F8BT-SAn 1.00.

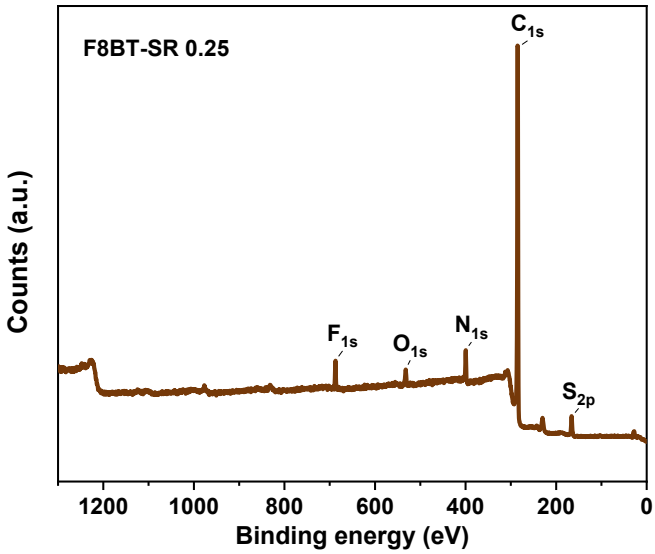


Figure S5.17. XPS survey for F8BT-SR 0.25.

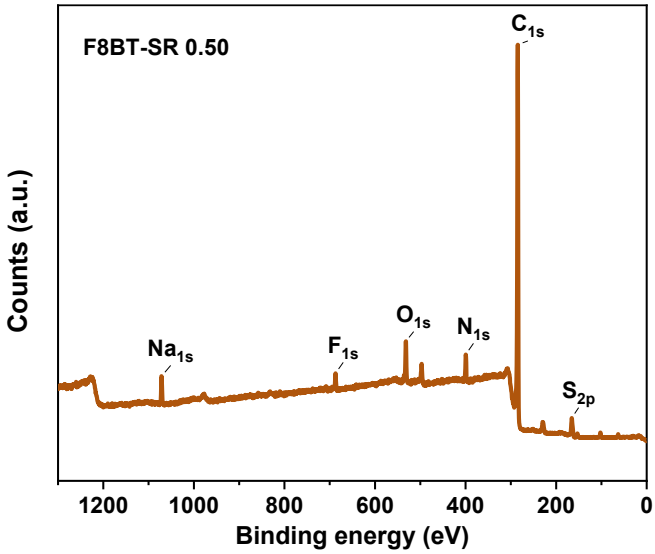


Figure S5.18. XPS survey for F8BT-SR 0.50.

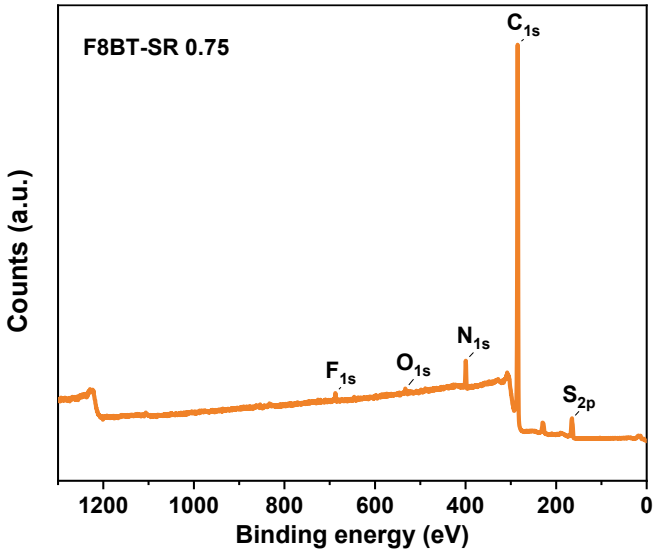


Figure S5.19. XPS survey for F8BT-SR 0.75.

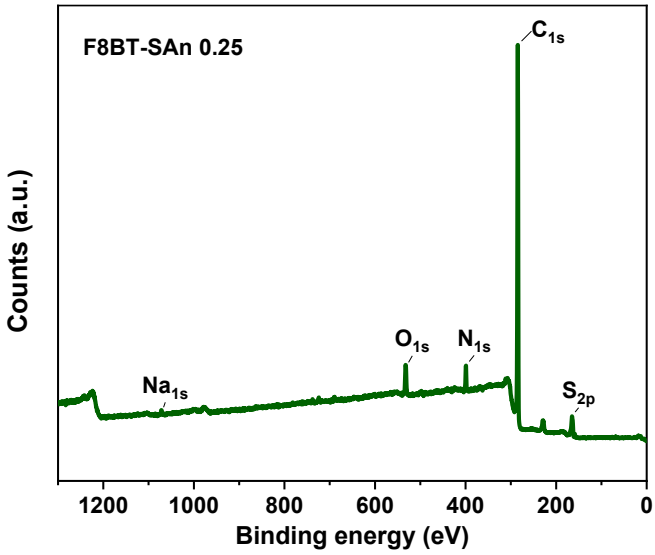


Figure S5.20. XPS survey for F8BT-SAn 0.25.

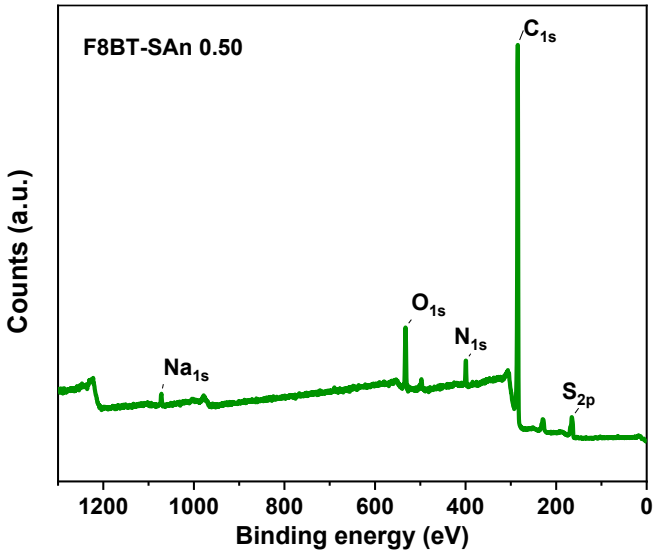


Figure S5.21. XPS survey for F8BT-SAn 0.50.

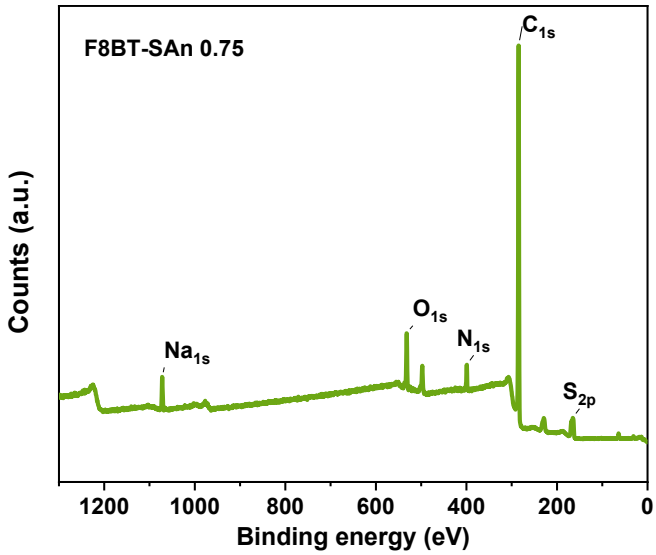


Figure S5.22. XPS survey for F8BT-SAn 0.75.

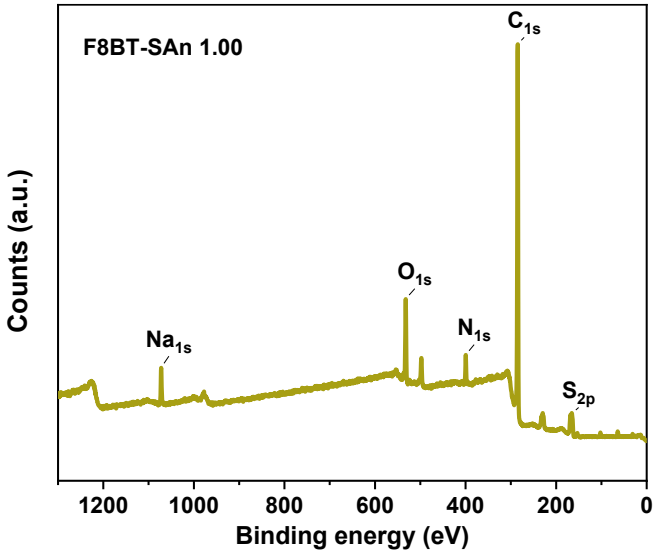


Figure S5.23. XPS survey for F8BT-SAn 1.00.

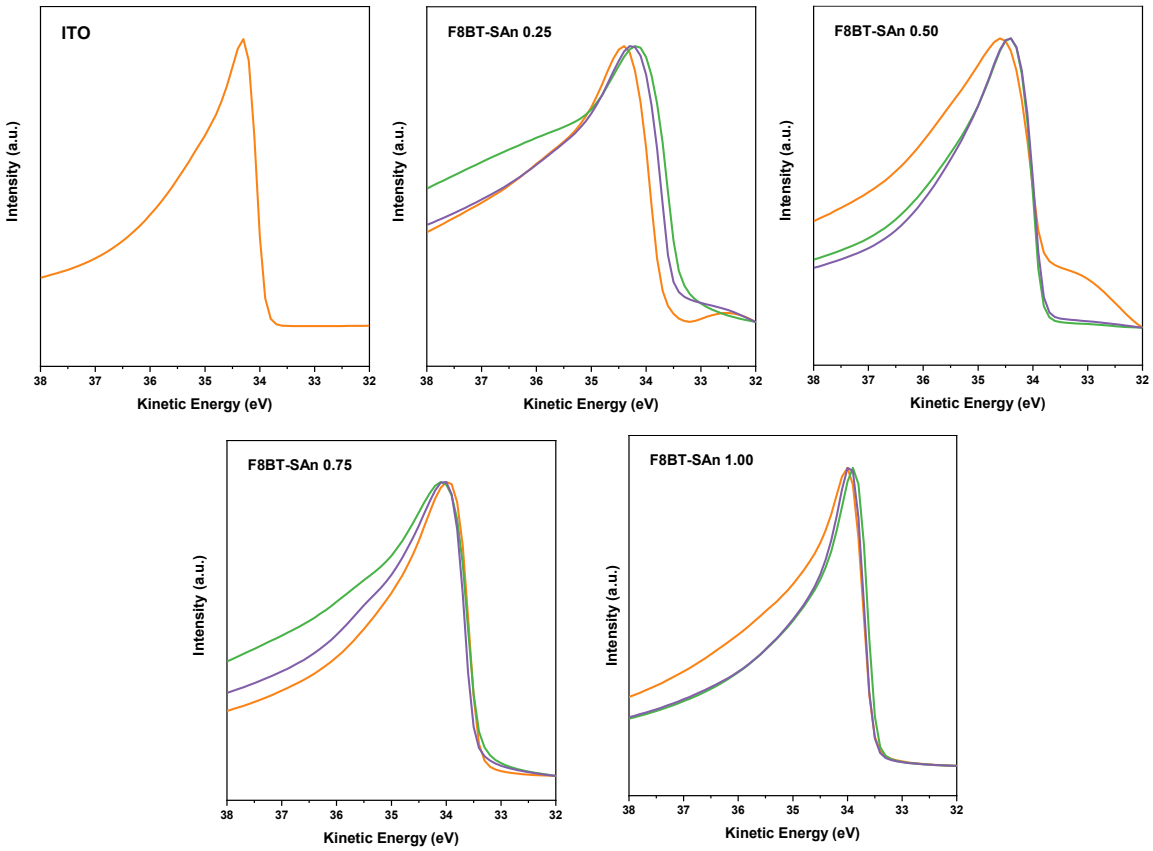


Figure S5.24. Secondary electron cut-off region from XPS measurements of ITO, F8BT-SAn 0.25, F8BT-SAn 0.50, F8BT-SAn 0.75, F8BT-SAn 1.00.

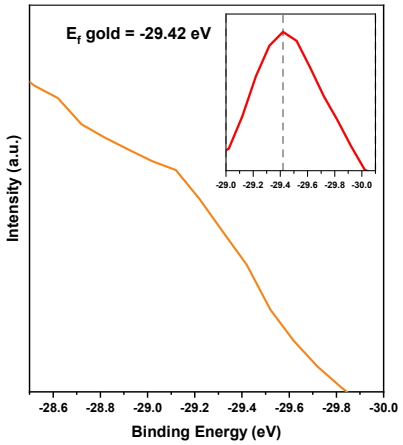
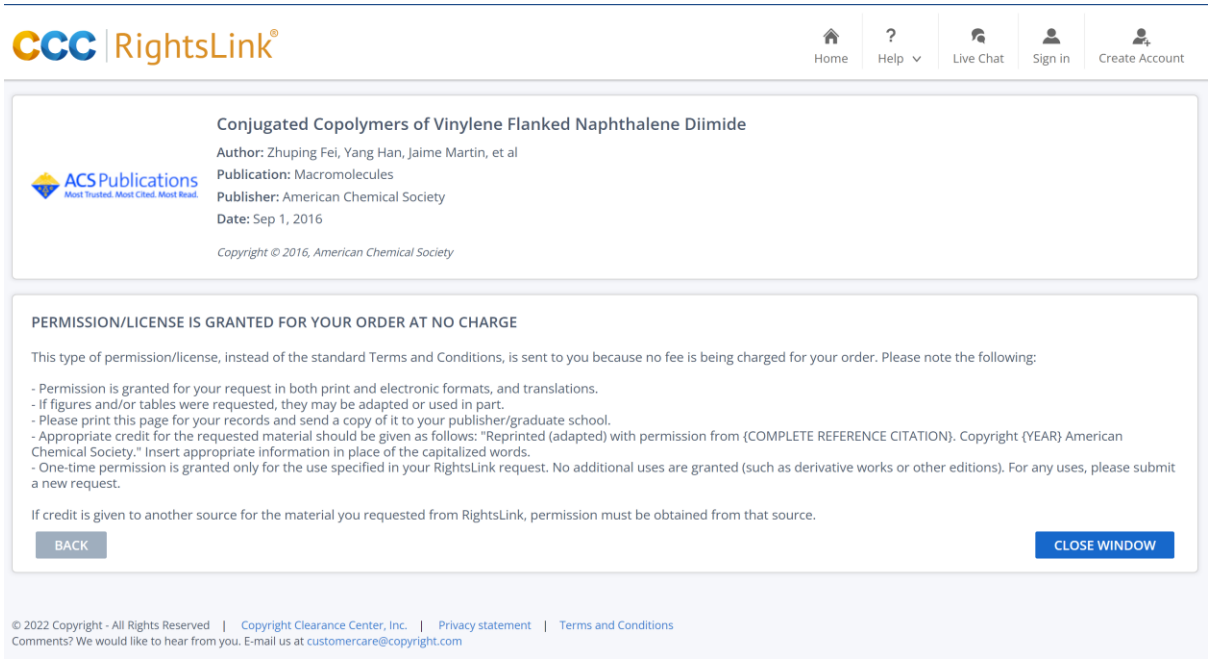


Figure S5.25. Fermi edge region from XPS measurements of gold.

9 Permissions

Permissions for DFT image, Introduction Figure 1.13:



CCC RightsLink®

Home | Help | Live Chat | Sign in | Create Account

ACS Publications
Most Trusted. Most Cited. Most Read.

Conjugated Copolymers of Vinylene Flanked Naphthalene Diimide

Author: Zhuping Fei, Yang Han, Jaime Martin, et al
Publication: Macromolecules
Publisher: American Chemical Society
Date: Sep 1, 2016

Copyright © 2016, American Chemical Society

PERMISSION/LICENSE IS GRANTED FOR YOUR ORDER AT NO CHARGE

This type of permission/license, instead of the standard Terms and Conditions, is sent to you because no fee is being charged for your order. Please note the following:

- Permission is granted for your request in both print and electronic formats, and translations.
- If figures and/or tables were requested, they may be adapted or used in part.
- Please print this page for your records and send a copy of it to your publisher/graduate school.
- Appropriate credit for the requested material should be given as follows: "Reprinted (adapted) with permission from {COMPLETE REFERENCE CITATION}. Copyright {YEAR} American Chemical Society." Insert appropriate information in place of the capitalized words.
- One-time permission is granted only for the use specified in your RightsLink request. No additional uses are granted (such as derivative works or other editions). For any uses, please submit a new request.

If credit is given to another source for the material you requested from RightsLink, permission must be obtained from that source.

BACK | CLOSE WINDOW

© 2022 Copyright - All Rights Reserved | Copyright Clearance Center, Inc. | Privacy statement | Terms and Conditions
Comments? We would like to hear from you. E-mail us at customercare@copyright.com